

2015

Surface Plasmon Resonance Sensing and Characterisation of Nano-Colloids for Nanotoxicology Applications

Hma Salah, Nasih

<http://hdl.handle.net/10026.1/3829>

<http://dx.doi.org/10.24382/1508>

Plymouth University

All content in PEARL is protected by copyright law. Author manuscripts are made available in accordance with publisher policies. Please cite only the published version using the details provided on the item record or document. In the absence of an open licence (e.g. Creative Commons), permissions for further reuse of content should be sought from the publisher or author.

This copy of the thesis has been supplied on condition that anyone who consults it is understood to recognise that its copyright rests with its author and that no quotation from the thesis and no information derived from it may be published without the author's prior consent.

Surface Plasmon Resonance Sensing and Characterisation of Nano-Colloids for Nanotoxicology Applications

By

NASIH HMA SALAH

A thesis submitted to Plymouth University
in partial fulfilment of the degree of

DOCTOR OF PHILOSOPHY

School of Computing, Electronics and Mathematics
Faculty of Science and Engineering
Plymouth University
UNITED KINGDOM

October 2015

Dedication

This thesis is dedicated to my family, especially my dearest wife, who has made astonishing sacrifices to stay beside me all time and help me accomplish my ambitions.

Also, I dedicate it to my astonishing, fantastic and wonderful children, Mohammed, Ayem and Shad. Further dedication of my thesis to everybody who provided assistance I have received either directly or indirectly from them.

Surface Plasmon Resonance Sensing and Characterisation of Nano-Colloids for Nanotoxicology Applications

NASIH HMA SALAH

Abstract

In this research, a Surface Plasmon Resonance (SPR) based sensor system was developed for quick detection of not only silver nanoparticles at low concentrations, but also to a range of individual analytes, according to their optical properties. SPR-based sensors are extremely sensitive to changes in the optical properties of the local environment at this interface, making these instruments highly valuable for surface science and bio-sensing experiments. This has enabled silver in solution (silver nitrate) to be detected from colloidal nanoparticles.

This study involves the theoretical development of an SPR system, where a glass prism and a multi-layered chip are used. The model presented is rigorous and applicable for any multilayer system. With this model, different parameters of the sensor can be selectively altered allowing the user to optimise the sensor's response for a particular analyte and to determine system parameters on the basis of results obtained during experiments. Both theoretical predictions and experimental measurements show that the predicted effective permittivity of silver nanoparticles Ag NPs compared with silver nitrate AgNO₃ enabled the presence of colloidal silver versus silver in solution to be differentiated down to a concentration limit of 0.1 mg l⁻¹.

Different materials were analysed for the compatibility and chemical stability for fabricating biochips. It has been successfully demonstrated that graphene-based SPR sensors are quite promising instruments owing to their improved sensitivity and other beneficial characteristics. Discussion related to different results obtained during experiments is also included together with some recommendations. Opportunities for future research are also mentioned, such as miniaturisation of an SPR sensor system for portable applications so that this technology can be utilised for detection of nano toxicants in the environment.

Table of Contents

DEDICATION.....	I
SURFACE PLASMON RESONANCE SENSING AND CHARACTERISATION OF NANO-COLLOIDS FOR NANOTOXICOLOGY APPLICATIONS.....	II
ABSTRACT.....	II
TABLE OF CONTENTS	III
LIST OF FIGURES	VI
ACKNOWLEDGEMENTS.....	XIX
AUTHOR'S DECLARATION	XX
CHAPTER 1.....	1
1.1 INTRODUCTION.....	1
1.2 BIOSENSORS FOR THE DETECTION OF NANO-PARTICULATES.....	2
1.3 PLASMONICS AND BIOSENSORS.....	3
1.4 AIM AND LAYOUT OF THESIS	5
CHAPTER 2 THEORY AND LITERATURE.....	7
2.1 INTRODUCTION.....	7
2.2 OVERVIEW OF SURFACE PLASMON RESONANCE	8
2.3 NANOPARTICLES AND NANOTECHNOLOGY IN THE SENSING SYSTEM	13
2.4 SPR CONFIGURATIONS	17
2.4.1 <i>Prism Coupling for SPR</i>	18
2.4.2 <i>Grating Coupling for SPR</i>	19
2.4.3 <i>Waveguide Couplers</i>	20
2.4.4 <i>Fibre-Optic Couplers</i>	21
2.5 THE PRINCIPLE OF THE PRISM COUPLING.....	22
2.6 SUMMARY	26
CHAPTER 3.....	27
3.1 NUMERICAL ANALYSIS OF SPR BIOSENSOR.....	27
3.2 BACKGROUND AND REQUIREMENTS OF THE NUMERICAL MODEL	28
3.2.1 <i>SPR Biosensing</i>	28

3.2.2	<i>The Kretschmann configuration</i>	31
3.2.3	<i>Angular Modulation</i>	32
3.3	MATHEMATICAL MODEL FOR NUMERICAL SIMULATION	35
3.4	SIMULATION RESULTS AND DISCUSSIONS	41
3.5	SUMMARY	42
CHAPTER 4	44
4.1	EXPERIMENTAL TECHNIQUES AND SYSTEM DESIGN.....	44
4.2	PHYSICAL VAPOUR DEPOSITION.....	44
4.2.1	<i>Principles of Sputtering</i>	45
4.2.2	<i>RF Enhanced Sputtering</i>	49
4.3	DEVICE FABRICATION (GENERIC)	50
4.3.1	<i>Fabrication Methods</i>	51
4.3.2	<i>Photolithography</i>	52
4.4	SYSTEM DESIGN.....	55
4.4.1	<i>System Design – Mechanical</i>	55
4.4.2	<i>Experimental design of the SPR system</i>	60
4.4.3	<i>Fluidics</i>	62
4.4.4	<i>Electrical and Control</i>	64
4.5	SOFTWARE	67
4.5.1	<i>Architecture and Design of LabVIEW System</i>	67
4.5.2	<i>Software Implementation - User Interface</i>	69
4.5.3	<i>Software Implementation - LabVIEW</i>	72
4.5.4	<i>Software Implementation - Log Files</i>	73
4.6	SUMMARY	74
CHAPTER 5	75
5.1	DEVELOPMENT AND OPTIMISATION OF SPR BIO-SENSING SYSTEM.....	75
5.2	LITERATURE AND THEORY.....	77
5.2.1	<i>Commonly used material systems</i>	77
5.2.2	<i>Properties of Graphene in SPR applications</i>	79
5.2.3	<i>Deposition of Graphene on Ag and Au samples</i>	83
5.3	OPTIMISATION OF PLASMONIC LAYERS	87
5.4	OPTIMISATION OF INTERFACIAL PLASMONIC LAYERS	91
5.5	OPTIMISATION OF GRAPHENE LAYERS	94
5.6	FINAL STRUCTURE.....	95
5.7	SUMMARY	97
CHAPTER 6	98
6.1	DETECTION OF SILVER NANOPARTICLES AND SILVER NITRATE USING THE SPR SYSTEM.....	98
6.2	METHODS	98

6.3 ANALYSIS OF SILVER NANOPARTICLES	99
6.4 EFFECTIVE MEDIUM APPROXIMATION	101
6.5 SIMULATION OF DIFFERENT CONCENTRATIONS OF NANOPARTICLES	103
6.6 EXPERIMENTAL AND SIMULATION OF AG NPs IN COMPLEX MEDIUMS	108
6.7 SUMMARY	114
CHAPTER 7	115
7.1 CONCLUSIONS AND FUTURE WORK	115
7.2 CONCLUSIONS.....	115
7.3 FUTURE WORK.....	117
7.3.1 <i>Encoder Mounting</i>	117
7.3.2 <i>Improving Controlling LabVIEW program</i>	119
APPENDIX A	145
APPENDIX C:	164
APPENDIX D	203
APPENDIX E	209
APPENDIX F	214

List of Figures

Figure 2.1: Spectra of a continuous light source obtained by Wood. The wavelength in nanometres is obtained by multiplying by a factor 10 the numbers shown at the top of the figure. Figure obtained from: (Wood, 1902, Enoch and Bonod, 2012).	9
Figure 2.2: (a) Otto configuration, (b) Kretschmann configuration and (c) multi-layered system. The incident light (p-polarised) undergoes total internal reflection at the prism base where evanescent waves are generated (dotted arrow) to propagate along the metal-prism interface (Salah et al., 2012).....	10
Figure 2.3: Illustrates the SPR sensor layer and the SPPs at an interface between a metal and dielectric.....	12
Figure 2.4: Schematic views of the nanoparticles and bulk size. (a) Quantitative colour phase maps relating structural properties of Au nanoparticles in air with concentrations of 5×10^{-11} (Buzea et al., 2007) (b) Hierarchy of materials from atoms to bulk. Figure obtained from: (Xavier et al., 2012).....	14
Figure 2.5: Melting temperature as a function of pore diameter. The broken line represents the bulk melting point. Figure obtained from: (Roduner, 2006).....	15
Figure 2.6: Variation in nanoparticle size results in altered optical properties of colloidal gold suspensions.	16
Figure 2.7: The stain glass windows of the Gothic cathedrals in France.	17

Figure 2.8: The colour of the 4th Century Roman cup (the Lycurgus Cup) looks green (a) when upon illumination from the outside and (b) looks red upon illumination from the inside. 17

Figure 2.9: Different configuration for SPP modes (a) Kretschmann configuration using a prism coupler, the coupled wave travels between the metal-air interface. (b) Otto configuration, the coupled SPP wave travels in the gold-air gap. (c) Grating coupler, where the grating spacing is comparable in size to the incident wavelength, the SPP couples to the surface of the grating. (d) Waveguide Coupler, the coupled SPP wave travels at the metal-air interface. (e) Fibre optic coupler, where the total internally reflected wavelength can couple with the metallic layer. Figure obtained from: (Abdulhalim et al., 2008). 20

Figure 2.10: (a) Illustration of the charges and the electromagnetic fields, of the SPPs which propagate in x direction with respect to the surface. (b) Field E is exponential decay of the SP wave over the distance from the surface. (c) The dispersion relation of a SP mode, where $\omega = ck$ is the light line. Figure obtained from: (Matsubara et al., 1988). 23

Figure 2.11: (a) The grating coupler employed for excitation of surface plasmons. (b) Wave vector illustration of the input coupler. k_0 and k_{SP} are the wave vectors of the incident light and the surface plasmons, respectively. $G = 2\pi\Lambda$, where Λ is the grating constant. 25

Figure 2.12: (a) Wave vector and ATR from metal surface (b) Dispersion relation of various components of the system, where k_0 is the light line (ω/c). The excitation can be seen as a minima in the Attenuated Total Reflection (ATR) intensity. 26

Figure 3.1: Illustrates the SPR immunoassay technique, (a) Antibody functionalised SPR sensor layer on the top of a conventional glass prism/ gold plasmonic system. (b-d) The sensogram response changing following the binding event. (b) Before and after the binding event, the angles (θ_1 and θ_2) relate to what is shown in (c) and (d). (c) The ATR response over angle, showing before and after binding events how the SPR angle shifts. (d) The transient response from the pre- to post-binding events (Salah et al., 2014).30

Figure 3.2: Kretschmann’s configuration set-up, this contains a glass prism, glass substrates, plasmonic layers and the dielectric sample on top. The incident light is refracted towards the plasmonic layers at an incident angle, the SP evanescent wave is most prominent at the plasmonic-sample environment interface.32

Figure 3.3: (a) The propagations of the incident and reflected light in the Kretschmann configuration. The polarisations of the “S” component, otherwise known as TE mode and the “P” component, otherwise known as TM mode. (b) An example spectra of the reflected amplitude over a range of wavelength, the minima is only observed in TM modes and not a TE. This is because plasmonics are purely Electrical phenomena and not magnetic.35

Figure 3.4: Shows the parameters used in the model, where: $E_0 +$ is the incident energy in the forward direction, $E_0 -$ is the energy travelling backwards from the device (when divided by the incident energy, the Fresnel reflection coefficient can be found). $E_m +$ $1 +$ is the forward propagating transmitted energy (when divided by the incident energy, the Fresnel reflection coefficient can be found) and $E_m + 1 -$ is the backwards

propagating energy, in most systems this is assumed to be 0. \mathbf{j} represents each of the layers, $\mathbf{j} = \mathbf{0}$ and $\mathbf{j} = \mathbf{m} + \mathbf{1}$ are generally assumed to be air.	36
Figure 3.5:Numerical simulations of the real ($\mathbf{n}(\omega)$) and imaginary ($\mathbf{k}(\omega)$) part of the sample's refractive index calculated by the Drude-Lorentz model in Eq. 3.14 and 3.15.	40
Figure 3.6:Compares the reflectivity of the different samples with different real and imaginary components obtained from theoretical calculation.	42
Figure 4.1:Nordico 6 sputtering system with visible target and cathode. This is an example of a sputter up system.....	48
Figure 4.2:Schematic illustration of the Nordico 6" sputtering system, showing all of the mechanical and electrical components of the system, including the vacuum system, gas inlet and RF power supply.	50
Figure 4.3:Ultra-sonication Bath used throughout this thesis.....	51
Figure 4.4:Photolithographic process: (a) BK7 Glass substrate should be cleaned, (b) deposition of photoresist on BK7 glass substrate, (c) apply mask on top of photoresist and expose to UV (d) remove exposed photoresist leaving masked pattern, (e) sputter Gold layer on top of the patterned photoresist and (f) final lift off of resist leaving patterned Gold layer.....	52
Figure 4.5:The mask used for the photolithography process.	53

Figure 4.6: Atomic Force Microscopy line analysis from height scan which shows a uniform layer thickness of 55 ± 1 nm.54

Figure 4.7:(a) The system from the side. (The labels for each element are on the diagrams.)
 (b) The constructed system from the front: The sample pump can be clearly seen at the bottom of the image. The optical scaffolding can also be seen clearly from this angle. .57

Figure 4.8:(a) Mechanical arm designed to hold the laser, (b) mechanical arm designed to support and move, the detector. The bend in the arm is to ensure that the detector and laser can be aligned together from the same central point.58

Figure 4.9:(a) Together and (b) Separated 3D schematic of the designed system (1) Main tube, (2) adjustable screw, (3) holding pin for the structure, (4) a cap for the pin, (5) an arm created for the detector, (6) an arm created for the laser, (7) holding plate for the arm and mechanical spacer (8) second holding place for the arm and mechanical spacer.59

Figure 4.10:The 4-spring based tightening mechanism used to secure the prism, thin-layered system and the micro-fluid channel, 3D design of the base of the mechanism.60

Figure 4.11: Configuration of Prism / Substrate for SPR, the optical properties of the equilateral prism to the glass slide is achieved by using index matching oil and the schematic diagram of the Surface Plasmon Resonance system, showing the incident direction of light from laser at angle (θ) which is collected by the detector. The micro-fluidic flow is shown by blue arrows with the interfacial plasmonic layers between the prism and the sample.61

Figure 4.12: The design of the micro-fluid channel. (a) side view to show the points where the samples can be pumped in and out of the reservoir, (b) top view showing the construction of the reservoir.62

Figure 4.13: The tubing pump REGLO Analog is with 4 tube channels and 8 pump rollers (Speed 2.0 –100 rpm).....63

Figure 4.14: The control system for the system, triangular block corresponds to an amplification of a signal, the circular shapes represent the motors and the rectangles correspond to other key components of the system. The central processing unit is controlling the system using LabVIEW software.....65

Figure 4.15: State machine diagram for program flow, the circles represent different states for the system and the arrows show the flow of the program with the conditions that should be met.....68

Figure 4.16: The User Interface (UI) panel for running the software: (1) simulation data, (2) run simulation and run experiment buttons, (3) angle range, (4) substrate and sample information input, (5) run button for, (6) visual indicators for motor direction, (7) current position of laser and photodiode, (8) most recent values, (9) graph of data, (10) error values, (11) reset button for graph, (12) output file location and (13) current status.70

Figure 4.17: The block overview of the LabVIEW program. (1) Initialisation cluster, (2) delay block, (3) system heart-beat, (4) case structure, (5) status update, (6) while loop box and (7) global stop button.72

Figure 5.1: Surface Plasmon Resonance (SPR) system with sensing cell (a) is the microfluidic chamber with pipe inlets and outlets, (b) is the photodetector, (c) is the laser diode ($\lambda = 664 \text{ nm}$), (d) shows the prism, (e) is the polarizer, (f) is input, (g) is output and (h) is the multilayers plasmonic tunability.....76

Figure 5.2: (a) Group 1B metals interface to glass, where the poor adhesion occurs. (b) Adhesion layer is introduced between the metal and glass, usually Ti or Cr ($\sim 5\text{nm}$) which allows for much better adhesion of metal layer to glass with minimal effect on the optical properties of the metal.....77

Figure 5.3: Biotin-Streptavidin time dependant reaction analysis for different material systems; Graphene with no biotin (blue) , Gold with no biotin (black), gold and biotin (red) and graphene and biotin (green). The graph demonstrated the SPR response over time for the different material systems (Salihoglu *et al.*, 2012).80

Figure 5.4: (a) Raman spectra for single layer graphene on Cu, Au and Ag, showing clearly a strong G-band and no D-band indicating high quality graphene, the 2D-band for Au and Ag is slightly red shifted from the Cu. (b) Optical transmission of Quartz and monolayer, bilayer and trilayer Graphene, showing a drop in intensity of approximately 2% per additional layer. (c) Diagram of the SPR sensor set-up; Kretschmann prism configuration using Au with Graphene transferred on-top. where the laser wavelength is 632 nm. (d) Changes in the SPR, shown as reflection, between standard Au sensor and Au with Graphene, showing 1° shift with the addition of graphene and broadening features of the FWHM. Image: (Salihoglu *et al.*, 2012).82

Figure 5.5: Schematic of the transfer process of SLG. (a) growth of Graphene on Cu foil, (b) coated with photoresist and then (c) PMMA (d) the Cu foil is etched away in Ferric

Chloride to leave Graphene layer on underside of the PMMA and photoresist. (e) the PMMA is placed on the gold layer. (f) the PMMA and photoresist is removed leaving SLG on a Au layer. Figure: (Salihoglu *et al.*, 2012).....85

Figure 5.6: Raman spectra of (a) Au (50 nm)/SLG and (b) Ag (50 nm)/SLG samples, showing G-band at 1580 cm^{-1} and the 2D-band at approximately 2700 cm^{-1} . This was taken using a green laser ($\lambda=514\text{ nm}$).85

Figure 5.7: Comparison between experimentally obtain results (blue) to the output of the theoretical model (red) for (a) Glass/Cr(2 nm)/Ag(50 nm)/H₂O and (b) Glass/Cr(2 nm)/Au(50 nm)/H₂O. The wavelength of the laser is 664 nm.89

Figure 5.8 : (a) Visual representation of the device structure showing the different layers used for the simulation. The wavelength of the laser is 664 nm. (b) Comparison between experimental (blue) and theoretical (red) results for a Glass/Cr (2 nm)/Ag (40 nm)/Au (5 nm)/H₂O system.....90

Figure 5.9 : (a) Simulated ATR of a Glass/Cr (2 nm)/Ag (40 nm)/Au (x nm)/H₂O device for the layer thicknesses (0, 2, 5 and 10 nm) at a wavelength of 664 nm. (b) Corresponding device structure showing the different layers.92

Figure 5.10: ATR response over angle for (a) Glass/Cr(2 nm)/Ag(x nm)/H₂O, (b) Glass/Cr(2 nm)/Ag(x nm)/Au(5 nm)/H₂O, (c) Glass/Cr(2 nm)/Ag(x nm)/Au(5 nm)/Single Layered Graphene/H₂O, (d) Glass/Cr(2 nm)/Au(x nm)/H₂O, (e) Glass/Cr(2 nm)/Au(x nm)/Single Layered Graphene/H₂O, (f) is the FWHM from (a-e) over layer thickness calculated using the Gaussian approximation mentioned in Section 5.3.93

Figure 5.11: (a) Simulation results showing the ATR over angle for different number of graphene layers, (b) (dashed lines) show the Minimum ATR at the resonant angle, solid layers are the resonant angle position, (c) layer structure of BK7 Glass/Cr/Au/Graphene/Sample (d) the FWHM change for the number of Graphene layers and.95

Figure 5.12: Schematic representation of the final system providing with the optimum sensitivity to chemical stability.....96

Figure 6.1: (a) The nanosight graph shows the particle distribution of the Ag NPs in 1 mgL⁻¹ Milli-Q water solution. NanoSight tracking results showing particle / cluster size distribution for 1 mgL⁻¹ solution of Sigma Aldrich < 100 nm Ag NPs. (b) Transmission electron microscope (TEM) image of the Ag nanoparticles, showing residue of PVP used as a stabilising agent during the reduction process. Transmission electron microscopy example image of Ag NPs in 100 mgL⁻¹ Milli-Q water solution. 100

Figure 6.2: (a) The difference in the phase over angle ($\Delta\Phi/\Delta\theta$) overlaid with the ATR for each of the 4 different concentrations, showing a linear shift over angle. The minima of the difference in the phase over angle can be used for a better determination of the resonant angle compared with the ATR. (b) Linearity of the change in resonant angle compared to nanoparticle concentrations. The Ag NP size used in this simulation was 35 nm. 1 mgL⁻¹ of silver relates to 9.54×10^{-5} volume fraction or ~0.01 Vol %. 0.6 % for 62.5 mgL⁻¹, 104

Figure 6.3: SPR - theoretical and experimental results for (a) air and (b) water - with 250 mg L⁻¹ (2.4Vol %) of Ag NPs. 106

Figure 6.4: (a) The change in ATR over time given for AgNO₃ and Ag NPs. (b) scans over angle at time = 0s, 120s and 240s for Ag NPs in CaCl₂. 107

Figure 6.5: (a) ATR change between pure water, AgNO₃ and Ag NPs (62.5 mg L⁻¹), (b) changes in salt concentration with nanoparticles in..... 109

Figure 6.6: The detection of different concentrations of <Size nm> Ag NPs in water and other different saline solutions, Sodium Chloride (NaCl), Calcium Chloride (CaCl₂) and finally the change of Humic Acid with and without Silver Nitrate (AgNO₃). (a) Average resonant angle of each concentration, (b) Average SPR peak intensity, the errors over three measurements are shown as the standard deviation (Red)..... 111

Figure 6.7: change in (a) resonant angle and (b) ATR at the resonant angle over different concentrations of Ag NPs in different complex media (Water, NaCl and CaCl₂)..... 112

Figure 6.8: Different concentrations of Ag NPs in CaCl₂ (Red and Green), showing increase in both angle and ATR at the resonant angle. Also this is compared against 10 mg L⁻¹ of AgNO₃..... 113

Figure 7.1: a) Optical Encoder. b)The entire experimental setup with the left and right encoders mounted is shown in the figure. Encoders are more efficient and have a higher accuracy compared to potentiometers. Hence, the output obtained with the encoders would be more sensitive than using potentiometers. 118

Figure 7.2: Improved LabVIEW program which allows run the system and record the data while introducing the different testing samples to the system. 119

List of Abbreviations

Abbreviations	Full term
UK	United Kingdom
nm	nanometre (0.000000001 metre)
Ag	Silver
Au	Gold
Cr	Chromium
Nm	nanomaterials
NP	nanoparticles
SPR	Surface Plasmon Resonance
SPP	Surface Plasmon Polariton
SPs	Surface Plasmons
SERS	Surface-Enhanced Raman Scattering
ATR	Attenuated Total Reflection
Ag NPs	Silver nanoparticles
AgNO ₃	Silver nitrate
LSPs	Localised Surface Plasmons
RIU	Refractive Index Unit
k_x	Wave vector
k_{SP}	Wave vectors of the surface plasmons
k_0	Wave vectors of the incident light
ε	Dielectric constants
δ_i	Penetration depth
E	Electric Field
L _{SP}	Length of Surface Plasmons
Λ	Grating constant
θ_0	Incident angle
TMM	Transfer Matrix Method and Abeles matrix
FWHM	Full-Width Half-Maxima

SEM	Scanning Electron Microscopy
TEM	Transmission Electron Microscopy
AFM	Atomic Force Microscopy
DLS	Dynamic Light Scattering
mg L^{-1}	milligram per litre
μm	micro metre
PDA	photodiode array
n_0	Refractive index
ω_0	Resonant angular frequency
γ	Relaxation parameter
q	Elementary charge
f_m	Oscillator strength
λ	Wavelength
PVD	Physical Vapour Deposition
RF	Radio Frequency
DC	Direct Current
AC	Alternating Current
Ar	Argon
Xe	Xenon
Ne	Neon
e^-	Electron
SCCM	Standard Cubic Centimetres per Minute
k_B	Boltzmann's constant
P	the pressure of the atmosphere
T	the atmospheric temperature
PTFE	PolyTetraFluoroEthylene
BK7	Glass type
UV	Ultraviolet light
BIA	bio-molecular Interaction Analysis

NI	National Instrument
CPU	central processing unit
PID	Proportional-Integral-Derivative
UI	User Interface
PWM	Pulse-Width Modulation
SLG	Single layer Graphene
PDMS	PolyDiMethylSiloxane
PMMA	Poly(Methyl-MethAcrylate)

Acknowledgements

The foremost thanks and praise go to Allah, the most Compassionate and the Most Merciful, for his gracious guidance on this thesis. I would like to express my gratitude to my supervisors David Jenkins, Richard Handy and Larissa Panina for their guidance and tolerance all the way through. My thesis would not have been successful and possible without the constant support and guidance of them.

In addition, I would also like to thank my family and my wife Jwan Hussein for being there through every step and encouragement that directly or indirectly provided the motivation in completion of this project. Thanks for all of her love, understanding and patience throughout my educational career.

I would like to thank my many friends at Plymouth University, including former Nick Fry and the SolidWork design couldn't have been accomplished without the software provided by Lee Martin.

I also owe a debt of gratitude to the ministry of higher education and scientific research, Kurdistan Regional Government (KRG), KRG- Scholarship Program Human Capacity Development for granting me a three and half –year of the financial support.

Author's declaration

I hereby confirm that this thesis is a result of my original work; none of the materials in this thesis have previously been submitted for any other degree at this or any other university.

This study was financed with the aid of a scholarship from the Ministry of Higher Education and Scientific Research, Kurdistan Regional Government (KRG). Relevant scientific seminars and conferences have been regularly attended, at which work has often been presented;

Publications and Conference Presentations

- I. Nasih Hma Salah, David Jenkins, Larissa Panina, Richard D. Handy and Shakil Awan, Self-Sensing Surface Plasmon Resonance for the Detection of Metallic Nanoparticles, Volume 2 Issue 2, ISSN: 2167 – 5813.
- II. Nasih Hma Salah, David Jenkins, Richard D. Handy, Graphene and its Influence in the Improvement of Surface Plasmon Resonance (SPR) Based Sensors: a Review. 2014.
- III. Nasih Hma Salah, David Jenkins, Larissa Panina, Richard D. Handy and Shakil Awan. Optimisation of Plasmonic Layers for Enhanced Sensitivity of Ag Nanoparticle Detection. To be submitted, *Sensors and Actuators A*.
- IV. Nasih Hma Salah, David Jenkins, Larissa Panina and Richard Handy, Optical detection of low concentrations of toxic nano particles in saline solutions; approximating a pseudo-estuary environment. Presented at SETAC 2014, Basel, Switzerland May 2014.
- V. Nasih Hma Salah, David Jenkins, Larissa Panina and Richard Handy. Detecting Silver Nanoparticles in Aqueous Colloids with Surface Plasmon Resonance – Challenging the Limits of Dynamic Light Scattering. Invited Talk at ICNM'13 2013, BS Abdur Rahman University, Chennai, India, Jan.2013.
- VI. Nasih Hma Salah, David Jenkins, Larissa Panina, Richard D. Handy, P.I. Nikitin and A. Orlov. . Surface plasmon resonance for the detection of non-metallic nanoparticles. Presented at the 23rd Annual Meeting of the Society of Environmental Toxicology and Chemistry, 12-16 May 2013, Glasgow, UK.
- VII. Nasih Hma Salah, David Jenkins, Larissa Panina and Richard Handy. Self-Sensing Surface Plasmon Resonance. Invited talk, International Conference on Nano Devices and Nano Electronics, Chennai, India 21-22 January 2013.

Nasih Hma Salah

Signature:

Date:

Word Count:

CHAPTER 1

1.1 Introduction

The UK relies on large quantities of clean water for day to day living, the average person uses 150 litres of water per day (Waterwise, 2012). However, when the other consumer products that rely on water has been accounted for the average person is said to use approximate by 3,400 litres per day in the UK in 2007 (Waterwise, 2007) which comes from production and transport, of imported food and textiles. Considering there are >60M people in the UK this equates to approximately 0.2 billion litres of water per day. According to the Government, the biggest health risk in the world is due to dirty water which is said to threaten the quality of life and public health. Many factors can pollute water sources, such as factory waste, industrial plants and activities such as fracking and gas extraction. The UK has one of the best clean water supplies in the world; however there is a growing concern over the pollution of drinking water through smaller nanoparticles (< 100 nm), such as silver (Ag) and titanium dioxide (TiO₂); where the health risks are not well understood.

There are currently 438 different confirmed commercial products that include silver nanomaterials (Scholars, 2015), ~10% of these have also been associated with household cleaning products (Scholars, 2015). A high proportion of products that relate to anti-bacterial uses in medicine and dentistry also contain silver nanomaterials (Besinis *et al.*, 2014). These particles will inevitably be transported into the natural environment.

Currently there are no available methods to assess and quantify, the extent of the particles in clean water supplies. A better understanding of the quantities of these pollutants can lead to action to clean, remove or reduce the consumption. Hence, there is an urgent need for improved detection methods for the quantification of NPs in complex samples; to support both environmental and human health risk, assessments (Klaine *et al.*, 2012). Biosensors could be one way to detect particulates in solution, where the affinity and resolution of the biosensor will be the main dependency on the detection limits.

1.2 Biosensors for the detection of nano-particulates

An optical biosensor can be defined as a sensor device that can extract quantitative information from a biochemical reaction using changes in the optical properties. Catalytic, affinity and refractive index based sensors are the three main types of biosensor (Borisov and Wolfbeis, 2008).

Affinity-based techniques use specific bio-recognition events for detecting analytes by measuring changes in the optical response of the sensor. Immunosensors constitute as a subtype of affinity-based biosensors. The Immunosensor technique depends explicitly on the interaction between an antigen and an antibody (Luppa *et al.*, 2001, Sassolas *et al.*, 2008). In this case the active sensor area is usually a functionalised material surface, on-top of an optical system.

The optical properties of a biosensor, for example phase, intensity and polarisation can be changed by small refractive index alterations at the interface between the sensor and analyte. This optical change will affect quantifiable information, such as the reflection and absorption of the device which can be used to compute the refractive index (Manifacier *et al.*, 1976). In general, this method can become inherently inaccurate due

to evanescent decay of the incident light through various layers. Hence, a number of improved methods based on this technique have been founded.

The most widely used method for improving the response is by utilising Surface Plasmon Resonance (SPR) effects in the sensors where the incident wave couples into the metal-dielectric interface depending on the resonant conditions. This will be explained in more depth in Chapter 2. This method relies mainly on small changes in the refractive index resulting variations in the coupling angle, strength of the light beam reflected and the wavelength can be observed (Homola et al., 1999). Another major benefit of using this method is that no labels are required for the detection and the technique is appropriate for real-time measurements.

Different sensor types have been created for a broad range of functions, for example, recognition of disease markers, environmental monitoring and food safety (Homola, 2006, Homola *et al.*, 1999, Homola, 2008). SPR-based sensors have also been used commercially (Liedberg et al., 1995, Healthcare, 2015) such as Biocor .

1.3 Plasmonics and Biosensors

Within the past decade the field of Plasmonics has flourished to become the focus of a growing amount research by both scientists and engineers (Lee, 2009, Enoch and Bonod, 2012), however, the plasmonic phenomena has been around as early as 1902 with the discovery of the so-called Wood's anomalies (Enoch and Bonod, 2012). These anomalies paved the way for research and investigation into Plasmonic phenomena and applications thereof. Researchers are continually developing innovative tools and techniques, that can create nano-sized structures that can manipulate light and electrons, on the nano-scale (Lee, 2009). As a result, SPR technologies has attracted an increasing

amount of interest from researchers; based on its reliability and high performance, compared to existing sensing techniques (Estevez et al., 2014).

Since the implementation in gas sensors, SPR sensing methods have already been applied to a wide range of industrial settings, especially for biochemical detection purposes (Lundström, 2014). In addition, a growing number of researchers are investigating other possible applications for SPR in sensing technology (Estevez et al., 2014). The optical phenomenon that the SPR sensing principle is based on is attributable to p-polarised light beams which excites densely packed charges causing them to oscillate and propagate along the metal–dielectric interface (Maharana and Jha, 2012).

SPR-based biosensors employ Surface Plasmon Polariton (SPP) waves which are particle-like waves confined to a dielectric-metal interface to detect analytes (biomolecules) on the sensor surface (Wu *et al.*, 2010). Any changes in the concentration of the analyte will generate a simultaneous localized change in the effective refractive index at the surface of the metal. Hence, the refractive index change will change the resonance conditions required to excite the SPPs which can be measured optically using the Attenuated Total Reflection (ATR) method.

It is anticipated that SPR enhanced sensing systems with high efficiency, sensitivity, portability, robustness and cost-effectiveness will be developed in the future (Estevez *et al.*, 2014, Lundström, 2014). Since SPR sensing is a label-free technique, it highly depends on the affinity of the analyte to the sensor surface. One must be confident that the analyte has been detected, even if only one molecular binding event has been resolved. This implies that the development of novel interfaces for affinity sensors is crucial if one desires to improve the instrumental resolution.

1.4 Aim and layout of thesis

The aim of this research is not to use nanoparticles for the enhancement of detection sensitivity, but to investigate their use in the self-detection of conducting nanoparticles that are of environmental concern (Shaw and Handy, 2011).

This study targets the development of an alternative SPR-based biosensor design which is based on the Kretschmann configuration of a prism with a multi-layered functional system on top. The detection system will be used to detect very low concentrations of metallic particles of environmental concern, such as, silver nanoparticles. Hence, we propose a self-detection system where the interaction between a dielectric surface and the metallic analyte is quantified. The detection system will acquire and analyse the phase, amplitude and angular information from the sample in real-time. In addition, a mathematical model was constructed to predict the resonant conditions for comparison with the experiments.

The aim of this research is to analyse the feasibility of improved designs of SPR-based sensors aimed at sensing low concentrations of analytes in a solution. Improved design of the sensor system includes the utilisation of a graphene-based multi-layered system. The main advantage of using graphene (Gr) in the SPR-based technique is that it exploits the limitations associated with the Kretschmann configuration and other modulation techniques, such as the sensitivity, insufficient micro-scalability and portability.

Researchers have extensively analysed novel designs of SPR sensors and have shown that it is important to exploit the associated limitations. For this purpose, an innovative SPR sensor design was made. To analyse the efficiency and limitations of these novel sensor designs various tests were conducted.

A mathematical model was created which was used to predict the sensor response and extract parameters such as detection limits and the sensitivity. This will be presented in Chapter 3, along-side experimental data for validity.

Chapter 4 concentrates on how the bio-sensor system was built, including the design and implementation, coding and other experimental techniques used to fabricate and measure the devices.

Then we look at the optimisation (Chapter 5) of the bio-sensing plasmonic system itself by looking at changes in response to different material systems and thickness, where we identify that using graphene can greatly improve the performance of the sensing platform.

Finally we investigated the samples of Ag NPs and AgNO₃ in Water and complex saline solutions (Chapter 6) to show the performance and limitations of the system such as the minimum detection limits, sensitivity and accuracy followed by conclusions and future work.

CHAPTER 2 THEORY AND LITERATURE

2.1 Introduction

The field of Plasmonics has become increasingly important for researchers across a wide range of applications, seeking improved cancer treatments, computer processors and even plasmonic-based lasers (Lee, 2009). This chapter provides a review of the relevant literature concerning Surface Plasmon Resonance (SPR) and graphene based SPR for applications in bio-sensing.

SPR is an established technique for label-free quantification of bio-molecular species, including real time reaction analysis (Liu and Wang, 2009). A typical Kretschmann configuration requires a prism coated with a thin Au film with a thickness of ~50 nm. The configuration is highly sensitive to local relative permittivity changes at, or near, to the interface. More recently researchers have incorporated Au nanoparticles onto the surface of the gold film to enhance the sensitivity by utilising Localised Surface Plasmon Resonance (LSPR) (Estevez *et al.*, 2014, Gao *et al.*, 2010) created a nano-composite aluminium oxide (Al_2O_3) film incorporating Au nanoparticles which was used to detect the interaction between biotin (immobilised to the Au/ Al_2O_3 surface) and streptavidin in a saline solution. This method was able to detect streptavidin concentrations of < 50 nM. Similar work has incorporated Au nanoparticles embedded in a polymer matrix for sensing applications (Hodnik and Anderluh, 2009, Riskin *et al.*, 2010).

A study by Maharana *et al.* (Maharana and Jha, 2012) analysed the unique optical properties of chalcogenide glass and graphene which were used to design a high performance affinity biosensor. In the cases where graphene has been used, the sensitivity of the proposed biosensors increased by more than 100 percent. They corresponded this result with the superior detection provided by chalcogenide glass versus silica glass. The proposed sensor configuration purportedly achieved a detection accuracy that was sixteen times more sensitive compared to other techniques for measuring over the visible spectra. In this regard, Maharana *et al.* reported adequate values for design parameters to achieve superior broadband sensing performance.

In this chapter we introduce the necessary topics needed to understand the results, Section 2.2 gives an overview of the SPR, then Section 2.3 investigates the different types of configurations that can be used to excite Surface Plasmon Polaritons (SPPs) and finally Section 2.5 describes the principles of prism-coupled systems, such as the Otto and Kretschmann configurations.

2.2 Overview of Surface Plasmon Resonance

It was slightly over a hundred years ago, following his observation at the Johns Hopkins University while varying the angle of incidence, Wood came across what he later referred to as anomalies (commonly referred to as Wood's Anomaly) in his reaction spectra using periodic gratings (Wood, 1902). In 1902, Wood was studying the reflectance spectra from P-polarised light (Transvers Magnetic TM) with an optical diffraction grating; this caused the emergence of light and dark spots on the mirror. Hence, the plasmon resonance phenomenon was discovered which was later discussed in detail theoretically by Lord Rayleigh (Rayleigh, 1907) and then the discrepancies

between Rayleigh's theoretical and Wood's experimental observations were explained by Fano (Fano, 1941).

The spectra formed by the optical grating from a constant light source (incandescent lamp) was studied. A few slender lighter and darker, lines can be seen (Fig. 2.1.) which were produced under specific conditions: when the magnetic field was parallel to the periodic grating, the bands were formed under P-polarised light (Wood, 1912). However, there was no description regarding this phenomena at that time, because there was still a lot to be discovered regarding the electromagnetic theory of gratings (Enoch and Bonod, 2012). As a result Wood named them "anomalies" (Wood, 1902) and considered it to be one of the most interesting cases of all time. It is interesting to note that the phenomena, shown in Fig.2.1, was theoretically explained by Ritchie in 1957 (Ritchie, 1957). Although, it was Fano who attributed them to the excitation of surface waves much earlier (1941) (Fano, 1941, Barnes *et al.*, 2003). In regard to the advances in the field of SPR, the main pioneers are believed to be Otto, Kretschmann and Raether (Lundström, 2014). In the late 1960s, they came up with an experimental setup which paved the way for excitation of plasmon waves on metal films (Kretschmann and Raether, 1968, Otto, 1968): These are commonly known as the Otto configuration (Fig.2.2a) and the Kretschmann configuration (Fig.2.2b).

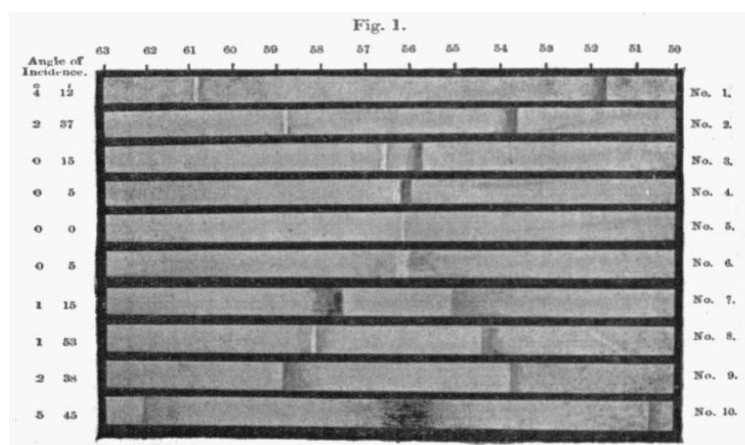


Figure 2.1: Spectra of a continuous light source obtained by Wood. The wavelength in nanometres is obtained by multiplying by a factor 10 the numbers shown at the top of the figure. Figure obtained from: (Wood, 1902, Enoch and Bonod, 2012).

Fig.2.2a shows a configuration first discovered by Otto, the first physicist to demonstrate the existence of SPR (Otto, 1968). Otto placed a prism near a thin film of gold effectively creating a diffraction grating. When the light flowed between the film and the prism, the Otto configuration was formed (Kretschmann and Raether, 1968).

Similarly, in the same year, Kretschmann and Raether also demonstrated SPR by depositing a thin metallic film on a prism (Fig.2.2b). A fluid was spread over the thin film causing SPR to be excited under certain conditions. This resulted in the commonly used Kretschmann's configuration (Otto, 1968). As a result, due to the experimental difficulty of positioning the gold film and its reliability, the Otto configuration did not gain much popularity. Hence, in modern day SPR experiments and commercial sensors, the Kretschmann's configuration is generally considered (Enoch and Bonod, 2012, Oliveira *et al.*, 2012).

SPR, due to its very specific resonant conditions, can be used to pinpoint small changes in the effective refractive index, or the thickness of the surface films. This is due to its high sensitivity to the optical properties of the materials at the interface between the metal and dielectric. In the late 1970s, SPR was exploited in the thin film studies of Pockrand (Pockrand, 1978) and Swalen (Swalen *et al.*, 1980).

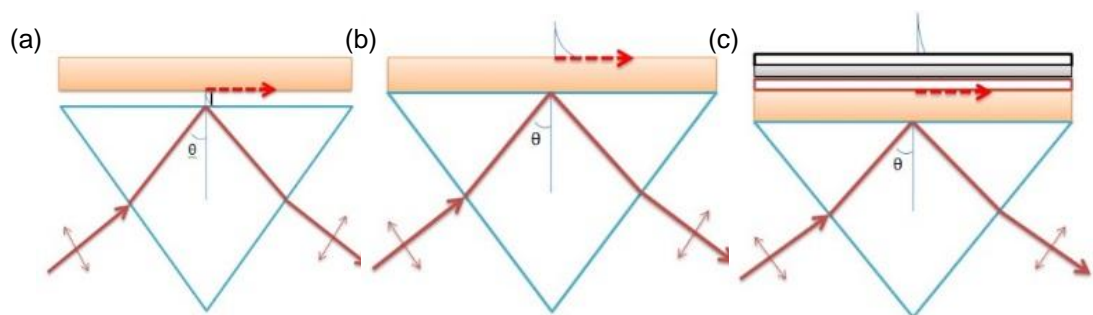


Figure 2.2: (a) Otto configuration, (b) Kretschmann configuration and (c) multi-layered system. The incident light (p-polarised) undergoes total internal reflection at the prism base where evanescent waves are generated (dotted arrow) to propagate along the metal-prism interface (Salah *et al.*, 2012).

The first exploration of SPR in biosensor applications is attributed to the work of Liedberg *et al.* (Van Delden *et al.*, 1997). In 1982 Liedberg *et al.* highlighted a way that SPR can be applied to the study of bio-molecular interactions at surfaces (Van Delden *et al.*, 1997).

SPR first came into use for gas detection in 1982 (Chen and Ming, 2012) and over the past few decades, SPR sensing technology has earned itself a reputation for the detection of chemical and biological analytes (Huber *et al.*, 1999) and also for medical diagnostics (Jorgenson and Yee, 1993) and environmental monitoring (Weiss *et al.*, 1996). Raether (Raether, 1988) defines Surface Plasmons (SPs) as:

“electromagnetic surface waves that have their intensity maximum in the surface and exponentially decaying fields perpendicular to it”.

They are mainly divided into two categories, Propagating Surface Plasmons, more commonly known as Surface Plasmon Polaritons SPPs and (LSPs). In order for SPPs to be excited at a metal dielectric planar interface, a number of approaches can be used, such as, the Kretschman (Liedberg *et al.*, 1995, Otto, 1968) and Otto (Otto, 1968), configurations, metal–dielectric waveguides (Homola, 2006), metallic diffraction gratings (Chen and Ming, 2012) and fibre optic coupling (Homola, 2006). Unlike SPPs, LSPs are generally associated with metallic nanoparticles, where LSPR can occur under certain condition. However, these are localised to the surface of the particle and they are not propagating waves (Maier, 2007). Therefore, a strong enhancement in the electric field within a few nano-meters of the surface (near-field) can be induced. This has resulted in their extensive use in applications such as Surface-Enhanced Raman Scattering (SERS) (Estevez *et al.*, 2014), fluorescence enhancement (Petryayeva and

Krull, 2011), refractive index sensitivity (Roh *et al.*, 2011) and bio-molecular interaction analysis (Boozer *et al.*, 2006).

Nowadays, after a century has passed since Wood's creation, Plasmonics are now an essential component of nano-photonics which can be described as the manipulation of light on the nanoscale. Various telecommunications business have benefited from plasmonic stimulation for super-lensing (Fehrenbacher *et al.*, 2015), or production of compressed, high-velocity, low-energy and intervention-free optical devices (Monzón-Hernández *et al.*, 2004). Thus, the ability to describe the metal using the free-electron model is necessary to describe the behaviour of the SPP waves. Fig. 2.3 illustrates the SPPs at an interface between a metal and dielectric. As the energy transfer is ultra-sensitive to the coupling conditions, the refractive index of the dielectric layer can be accurately determined by monitoring the angle of the reflected light, along with the intensity and/or phase. The SPR condition occurs at a unique angle, obtained by identifying the minima in the reflected beam after total internal reflection, this is also complimented by a 180° phase shift.

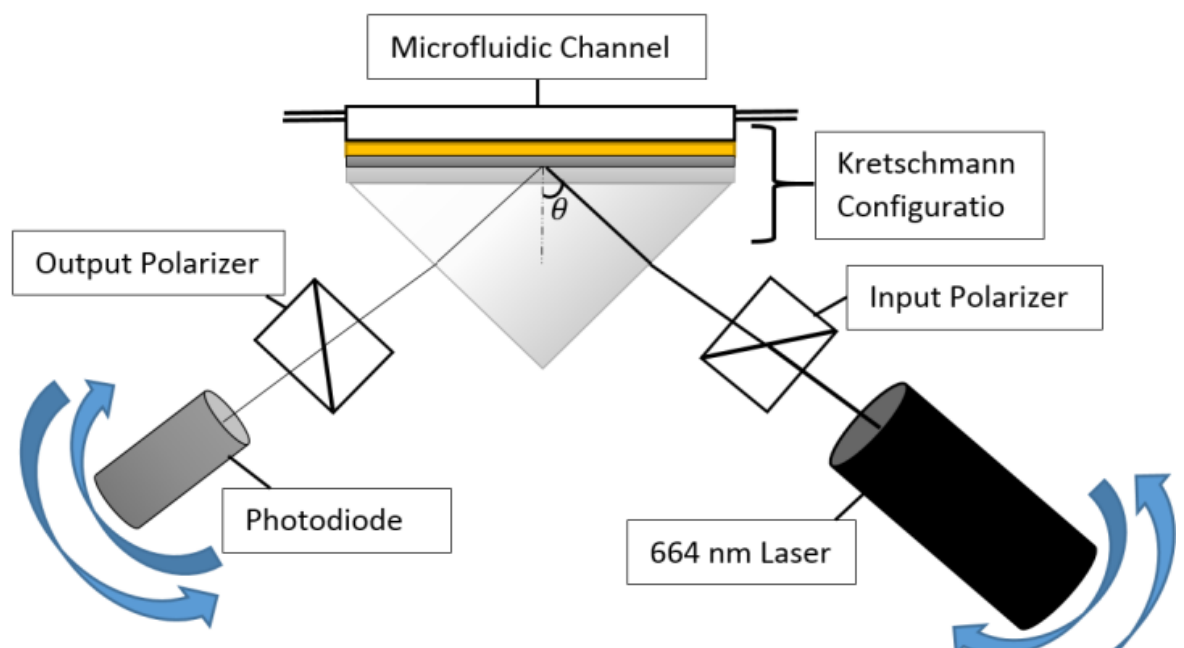


Figure 2.3: Illustrates the SPR sensor layer and the SPPs at an interface between a metal and dielectric.

Silver (Ag) and Gold (Au), are the most frequently used metals in these configurations, due to their resonance peaks within the visible spectra. Theoretically, a higher sensitivity can be achieved using Ag due to the smaller resonance peak width in thin films. However, Au is the most suited metal for cell culture, due to its biocompatibilities, in SPR-based biosensor applications (Liu and Wang, 2009).

2.3 Nanoparticles and nanotechnology in the sensing system

Nanotechnology has paved the way to provide tools that are required to create functional materials, nano-devices and complex systems. This includes taking control of the material on an atomic, or molecular scale and also through making use of novel properties and phenomena. The National Nanotechnology Initiative (Initiative, 2012) states that:

“Nanotechnology is science, engineering and technology conducted at the nanoscale which is about 1 to 100 nanometres.”

A nano-particle can be 'loosely' defined as an object where all three dimensions are less than 100 nm (Garcia, 2011). The term 'ultrafine particles' is often used to refer to nano-particles that are physically and chemically, heterogeneous (Hosokawa *et al.*, 2007), such as, volcanic ash and soot.

The nano-particles are fabricated with the intention of bearing some particular features, for example, shape, size and chemistry. Some examples can be found in aerosols, colloids, or even powders (Sattler *et al.*, 2010). The surface area has a huge impact on the behaviour of the nanomaterial, it is one of the main factors that can result in higher levels of reactivity and strength (Chan, 2007). Bakalova *et al.* (Bakalova *et al.*, 2004) stated that:

“Nanomaterials or Nanoparticles show characteristics that are not completely free from the effects of quantum particles that pass by and not quite the properties exhibited by bulk materials”.

Bulk and nano-scale materials exhibit different phenomena to each other, due to the number of atoms and the restriction of charges on the surface (surface and quantum confinement). The physical properties of bulk materials are normally referred to as their constants, but their properties will change significantly when the material is confined to the nano-scale (Buzea *et al.*, 2007).

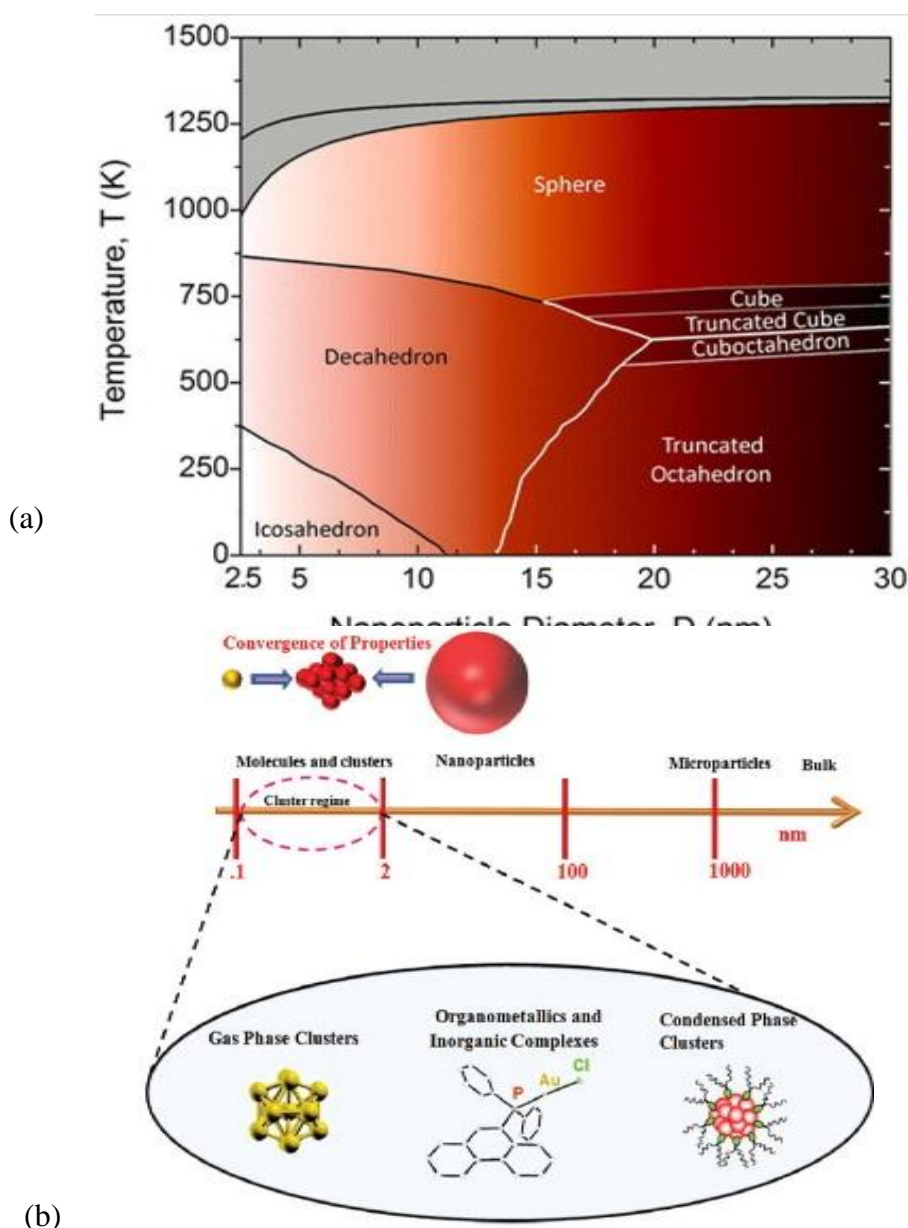


Figure 2.4: Schematic views of the nanoparticles and bulk size. (a) Quantitative colour phase maps relating structural properties of Au nanoparticles in air with concentrations of 5×10^{-11} (Buzea *et al.*, 2007) (b) Hierarchy of materials from atoms to bulk. Figure obtained from: (Xavier *et al.*, 2012).

The size of the nanoparticle can affect the sintering and melting temperatures depending on their shape (González *et al.*, 2012); the smaller the nano-particle the lower the melting point (as seen in Fig. 2.4a and Fig. 2.5). It is expected that composite materials containing spherical particles with radii less than 100 nm, can achieve optimal magnetic permeability (Roduner, 2006). Nano-particles have been used throughout history, however, the effects have never been fully understood until recently. Now, scientists are aware that this is due the surface area to volume ratio which determines the luminescence peak for the nano-particles. Through understanding this process, techniques have been developed, an example would be the use of nano-spheres as biological tags and can also be used in the development of pharmaceuticals (Nouailhat, 2010).

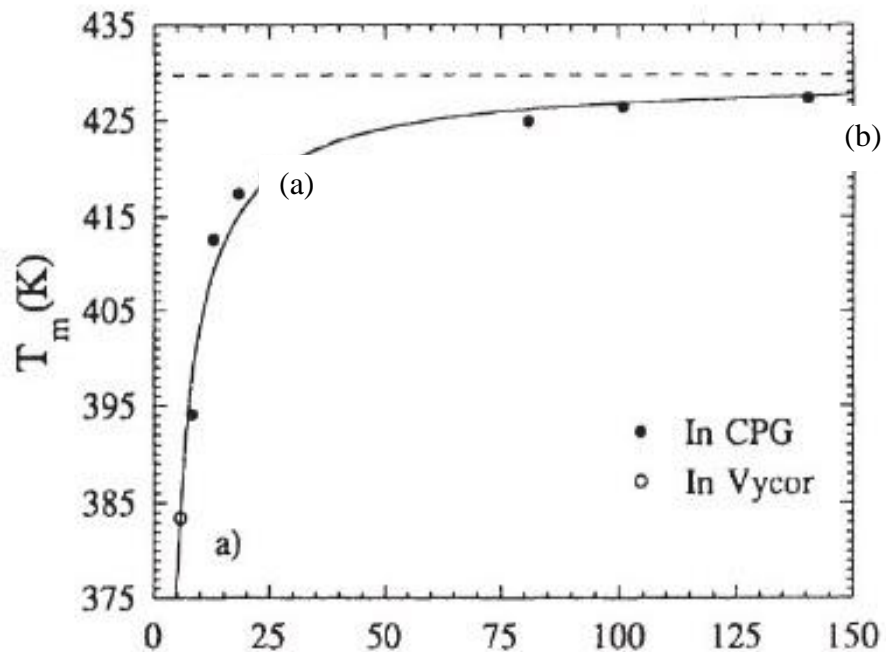


Figure 2.5: Melting temperature as a function of pore diameter. The broken line represents the bulk melting point. Figure obtained from: (Roduner, 2006).

When a material is reduced to nano-sized particles, surface sites available significantly increase which is why nanoparticles are of significance. Since nanomaterials have tuneable properties, they will continue to be of importance as they have always been in

the past in the development of novel technologies. The electromagnetic and chemical properties of metallic nanomaterials can especially be altered by modifying their size, shape and environment. Figure 2.6 represents an instance of the tunability of the optical properties of dissolved particles; the colour of metallic nanoparticles is produced by light scattering and absorption.

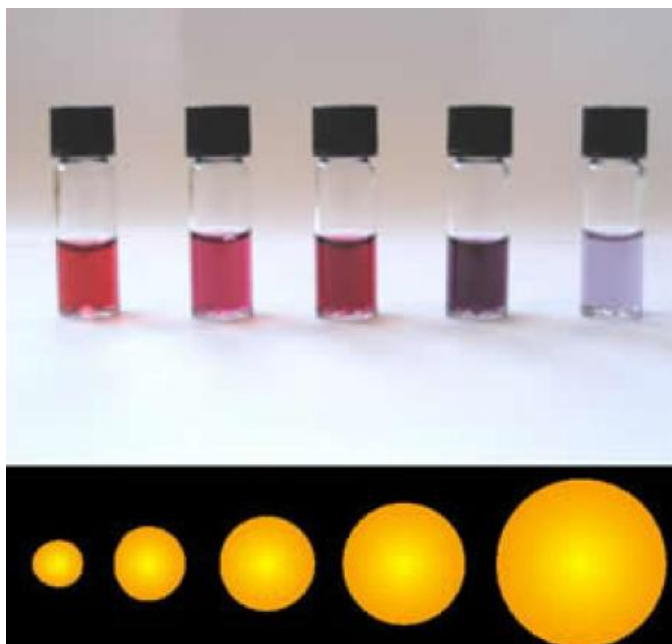


Figure 2.6: Variation in nanoparticle size results in altered optical properties of colloidal gold suspensions.

Nanomaterials have been widely utilized in art for the longest of time. Employing gold and silver nanoparticles integrated into the glass to give the panes several shades are the stain glass windows of the Gothic cathedrals in France Figure 2.7.

Figure 2.8 depicts the Lycurgus Cup, going back to the 4th century AD which integrates silver and gold nanoparticles into the glass to give the cup a dichroic characteristic. The cup looks green when it is illuminated from the outside by white light, as the particles scatter bluish-green light. However, the cup looks red when the light is placed inside the cup and the particles inside the glass absorb the green light and the remaining colours of the white light seem to be reddish-orange and are transmitted.



Figure 2.7: The stain glass windows of the Gothic cathedrals in France.



Figure 2.8: The colour of the 4th Century Roman cup (the Lycurgus Cup) looks green (a) when upon illumination from the outside and (b) looks red upon illumination from the inside.

2.4 SPR Configurations

In order for SPR to be excited at a metal-dielectric interface, there is a need for the incident light to be P-polarised (Transverse Magnetic polarisation) (Maier, 2007) and its wave vector must match that of the Surface Plasmon (SP). Oliveira *et al.* assert that:

''This can be done either by passing the light through a medium with a refractive index higher than that of the dielectric medium at the boundary at which the SP is to be excited, or by using diffraction effects''.

As a consequence, when it comes to SPR-based sensors, couplers appear to be essential (Oliveira *et al.*, 2012).

2.4.1 Prism Coupling for SPR

Kretschmann and Raether (1968) came up with a prism-based configuration to excite Surface Plasmon Polaritons SPPs (Kretschmann and Raether, 1968). The Kretschmann configuration is taken as the most common setup (Lundström, 2014). As can be seen in Fig. 2.9a, directly on top of a prism surface, a metal film is deposited which is illuminated (typically with a single wavelength laser) through the prism at an angle of incidence greater than the critical angle for total internal reflection. At the interface between the prism and the metallic film (e.g. Au), the light beam is confined to the interface at certain conditions. As a result, the Surface Plasmons (SPs) are excited at the sample-metal surface of the metal film as evanescent waves.

The Otto configuration (Otto, 1968), is illustrated in Fig. 2.9b. In order for photons to tunnel through the air gap between the metal and prism, they should be very close to each other. This configuration can be very useful for studying SPR effects with bulk materials (Otto, 1968). However, applications where fluids and solutions are concerned, this configuration is no longer effective, due to the gap between the metal and prism being occupied by a dielectric material.

A variety of different approaches have been in use for measuring SPR in prism-based sensor configurations, the most popular parameters used include: angular (Gwon and Lee, 2010), wavelength (Oliveira *et al.*, 2012), intensity (Chien and Chen, 2004), phase (Oliveira *et al.*, 2012) and polarisation-state measurements (Daghestani and Day, 2010). Unlike single-point measurements, such as the intensity and phase approaches, the angular and wavelength approaches have earned themselves a reputation for yielding

more reliable information (Estevez *et al.*, 2014). This is due to their reliance on multi-point measurements. Zhang *et al.* (Zhang *et al.*, 2003) stated that both of them have been demonstrated in multi-channel, high-density (array) formats, in which SPR can be excited in a large number of locations. In order to extract information about the sample at each particular location, the light reflected from that location has to be analysed. Although the angular-measurement approach has been used in various commercial SPR instruments (Lundström, 2014), Zhang *et al.* (Zhang *et al.*, 2003) asserted that:

“The best sensitivity (refractive-index resolution) obtained therewith being better than 3×10^{-7} refractive-index unit (RIU)”.

The relative sensitivity of the phase-measurement and the intensity-measurement approaches have been the subject of some debate (Ran and Lipson, 2006).

2.4.2 Grating Coupling for SPR

To overcome the wave-vector mismatch, a periodical metal-dielectric grating, comparable in size to the wavelength required. The wave vectors from the diffraction grating are larger in magnitude than the incident light. A light beam is directed towards a medium, where there is a periodic grating, when the light beam reaches the grating it is diffracted and can be coupled in the interface direction or between the metal-dielectric (Fig. 2.9c) (Abdulhalim *et al.*, 2008). Substrate-metal SP modes can be sufficiently coupled providing the metal film thickness and the grating corrugation depth are adequately matched.

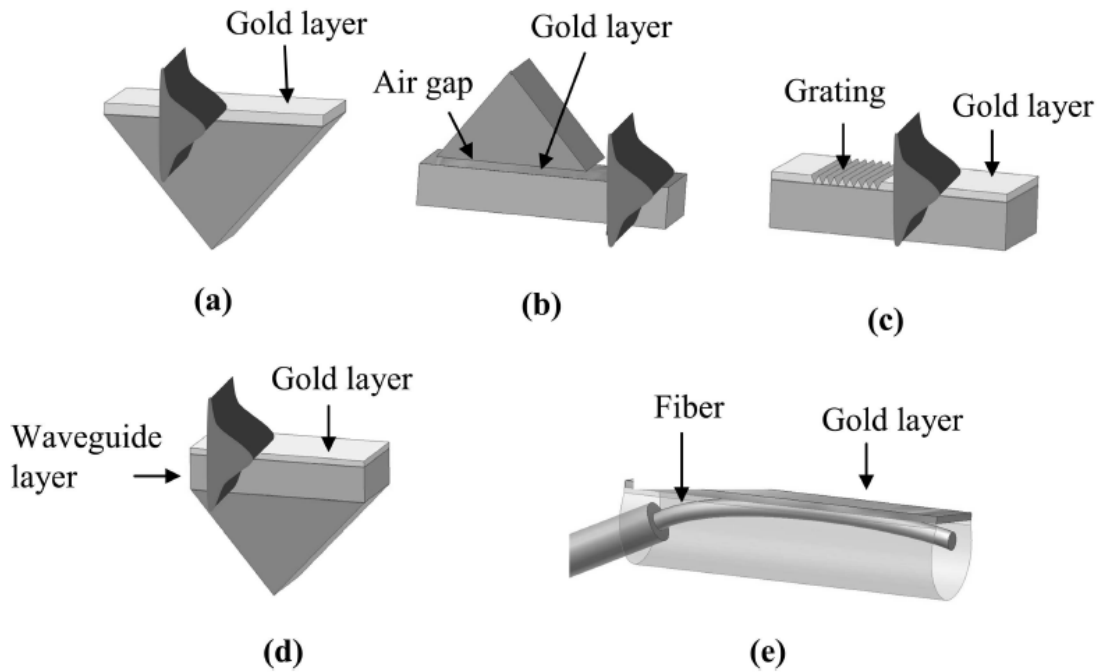


Figure 2.9: Different configuration for SPP modes (a) Kretschmann configuration using a prism coupler, the coupled wave travels between the metal-air interface. (b) Otto configuration, the coupled SPP wave travels in the gold-air gap. (c) Grating coupler, where the grating spacing is comparable in size to the incident wavelength, the SPP couples to the surface of the grating. (d) Waveguide Coupler, the coupled SPP wave travels at the metal-air interface. (e) Fibre optic coupler, where the total internally reflected wavelength can couple with the metallic layer. Figure obtained from: (Abdulhalim et al., 2008).

The main benefit of the grating-coupled SPR sensors is the possibility of producing them with the aid of mass replication technologies, particularly injection molding and hot embossing. Oliveira *et al.* (Oliveira *et al.*, 2012) and Dostálek *et al.* (Dostálek *et al.*, 2005) believe that this technology could pave the way for the production of low-cost, high-throughput, SPR platforms for label-free monitoring of bio-molecular interactions.

2.4.3 Waveguide Couplers

The waveguide configuration bears a close resemblance to that of the Kretschmann configuration. According to Homola et al. (Homola, 2006):

“The light is guided by either a single or multi-layer (slab or channel) waveguide to a region with a thin metal over layer”.

In the regions where there is a metal-waveguide interface, the light will evanescently decay through the metal layer (Fig. 2.9d). The SP is excited at the outer interface of the metal layer as long as it is phase-matched with the guided mode. The waveguide-coupled SPR sensor benefits from nearly the same level of sensitivity as the prism-coupled SPR sensor configuration (Homola *et al.*, 1999). The control of the optical path, the small sizes and ruggedness in the sensor system, should be emphasised as some of the key features of using optical waveguides.

2.4.4 Fibre-Optic Couplers

Fig. 2.9e shows the configuration of a Fibre-optic coupled SP sensor. Abdulhalim *et al.* (Abdulhalim *et al.*, 2008) have described this configuration:

“SPR sensors with fibre-optic couplers operate using either wavelength or intensity interrogation on an SPR active sensing area that is located either at the end of the fibre or in the middle of the fibre where the cladding of the optical fibre core is partially removed”.

Defects or bends in the optic-fibre suggest that mode conversion and polarisation changes, need to be taken into consideration (Abdulhalim *et al.*, 2008), these can be seen as a disadvantage to this configuration. Therefore, the stability of the signal may be limited. In order to avoid modal conversion, Homola *et al.* (Homola *et al.*, 1999) suggested the use of a single-mode optical fibre, however, the polarisation instability still persists. According to Piliarik *et al.* (Piliarik *et al.*, 2003), SPR-based sensors that use polarisation-maintaining fibres have also been used. As a result of the evanescent field within an optical fibre, a standing charge density wave can be excited at the metal surface (usually Au). The relative permittivity of the thin metal film and the sample, influences the SP on the metal surface.

Wavelength interrogation operation, is when the light, at a specific wavelength and incident angle, couples to the SP vector. A minimum will be observed in the reflectance

spectrum when the light is absorbed, or diffracted along the metal-dielectric interface. When a sample is introduced on the metal film, it will cause a change in the effective refractive index at the metal-dielectric interface, therefore the resonant conditions for the SPR conditions can be found by scanning a range of wavelengths. Intensity interrogation operation describes the change in the intensity that is measured which occurs as a result of refractive index variation adjacent to the metal surface. According to Homola *et al.* (Homola *et al.*, 1999), sensor resolutions have been reported for the two types of operations, they are 8×10^{-5} RIU and 5×10^{-5} RIU, specify respectively. Fibre-optic couplers can allow for the production of a miniaturized probe with a limited interrogation area. This is believed to be their main attraction. This is mainly because it allows sensing under inaccessible and harsh circumstances (Homola *et al.*, 1999, Hassan *et al.*, 1999).

2.5 The principle of the prism coupling

Surface plasmons refer to electromagnetic surface waves that propagate along a metallic surface (Ritchie, 1957, Stern and Ferrell, 1960). Fig. 2.10a shows SPPs at the interface between a dielectric medium and metal surface. They can be described as a collective oscillation of the free charges present at the metal surface which produces an electromagnetic field with both, the perpendicular and parallel, components with respect to the interface. Because of the evanescent nature of the fields, the waves are bound to the surface.

Eq. 2.1 demonstrates the field distribution along the surface, where E_0 is the incident energy, k_x is the wave vector along the interface between the metal-dielectric and k_z is the wave vector perpendicular to the surface originating from the interface. In the equation the '+' applies when $z > 0$ and the '-' applies when $z < 0$; this is due to the SPP

mode being bound to the surface. Fig. 2.10b shows the exponential decay of the field in the z direction which is caused by the imaginary k_z component of Eq. 2.1. (Raether, 1988, Barnes et al., 2003).

$$E = E_0 e^{\pm i(k_x x \pm k_z z - \omega t)} \quad (2.1)$$

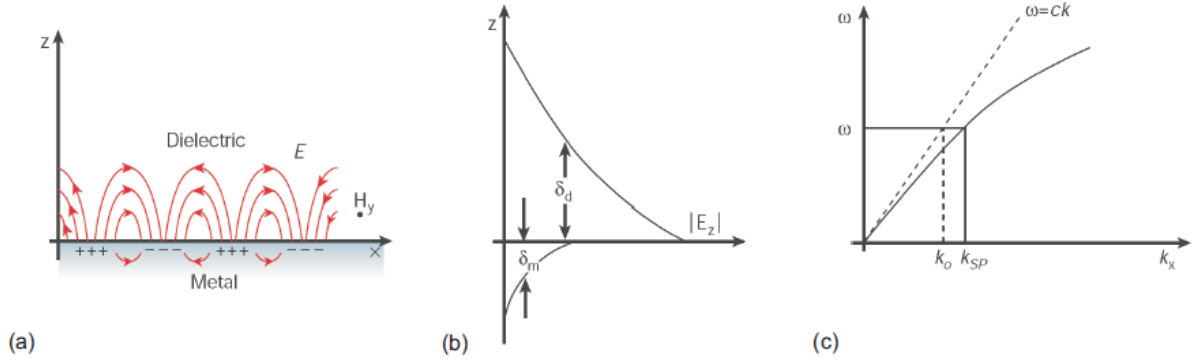


Figure 2.10:(a) Illustration of the charges and the electromagnetic fields, of the SPPs which propagate in x direction with respect to the surface. (b) Field E is exponential decay of the SP wave over the distance from the surface. (c) The dispersion relation of a SP mode, where $\omega = ck$ is the light line. Figure obtained from: (Matsubara et al., 1988).

The Eigen frequency of the surface plasmons is linked directly to the wave vector k_x . The dispersion relation of SPs at the interface of air and metal is shown in Fig. 2.10c (Raether, 1988, Barnes *et al.*, 2003). It is evident that the SP modes always exist ahead of the light line ($\omega = ck$), hence the SPPs are non-radiative. A light-plasmon coupler is required to overcome the momentum difference, in order to excite the surface plasmons with light.

$$k_x = \frac{\omega}{c} \left(\frac{\epsilon_m \epsilon_d}{\epsilon_m + \epsilon_d} \right)^{1/2} \quad (2.2)$$

Eq. 2.2 shows the components of the k_x wave vector, where ϵ_d and ϵ_m are the dielectric constants of the dielectric medium and the metal, respectively. Assuming that the imaginary part of the metal is much less than the real part ($\epsilon_m'' \ll |\epsilon_m'|$) and the

dielectric medium is purely real (non-absorbing), the complex wave vector along the interface, $k_x = k'_x + ik''_x$, is given in Eq. 2.3 and Eq. 2.4.

$$k'_x = \frac{\omega}{c} \left(\frac{\epsilon'_m \epsilon_d}{\epsilon'_m + \epsilon_d} \right)^{1/2} \quad (2.3)$$

$$k''_x = \frac{\omega}{c} \left(\frac{\epsilon'_m \epsilon_d}{\epsilon'_m + \epsilon_d} \right)^{3/2} \frac{\epsilon''_m}{2(\epsilon'_m)^2} \quad (2.4)$$

To ensure k'_x is a real positive number, the requirements that ϵ'_m needs to be negative, but also needs to be larger than that of the dielectric medium ($|\epsilon'_m| > \epsilon_d$), should be fulfilled. The momentum difference provided by the coupler allows us to couple to the surface plasmons with light. The internal absorption is determined by k''_x .

The wave vectors of surface plasmons i.e. k_{zm} and k_{zd} are imaginary due to the relations $\epsilon'_m < 0$ and $\omega/c < k_x$. Hence, the field amplitude of the SP normal to the surface reduces exponentially ($\exp(-|k_{zi}| \cdot |z|)$).

$$\delta_i = \frac{\lambda}{2\pi} \left(\frac{\epsilon'_m + \epsilon_d}{\epsilon_i^2} \right)^{1/2} \quad (2.5)$$

Eq. 2.5 gives the penetration depth (δ_i) of the electric field (Sambles *et al.*, 1991).

Calculating the skin depth in the metal ($z < 0$), $i=m$. For the dielectric medium ($z > 0$), $i=d$. The exponential decay of the field E_z on both sides of the surface is shown in Fig. 2.10b, where the penetration depth is much smaller for the metallic side of the interface.

The intensity of SPs propagating along a smooth surface reduces to $e^{-2k''_x x}$, due to the imaginary vector k''_x . The length of the SP (L_{SP}) is given in Eq. 2.6 and described the length the SP travels before being reduced to $1/e$. The upper size limit for any photonic-based system using SPPs is decided by the propagation length of the SP.

$$L_{SP} = (k''_x)^{-1} \quad (2.6)$$

The interaction among the Surface Plasmons directed by the two interfaces cannot be overlooked, when a metal film is fabricated on a dielectric medium and the film thickness is similar to the penetration depth of the surface plasmons. This interaction causes development of a thickness-dependent dispersion relation.

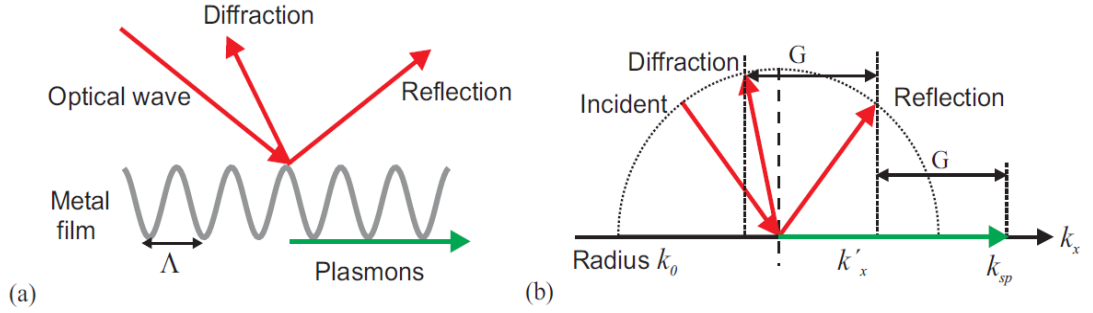


Figure 2.11:(a) The grating coupler employed for excitation of surface plasmons. (b) Wave vector illustration of the input coupler. \mathbf{k}_0 and \mathbf{k}_{SP} are the wave vectors of the incident light and the surface plasmons, respectively. $\mathbf{G} = \frac{2\pi}{\Lambda}$, where Λ is the grating constant.

The production of SPPs at a metal-dielectric interface needs the parallel wave vector (k_x , Eq. 2.7) component of the excitation field to equal the SP vector (k_{SP} , Eq. 2.8). Two experimental techniques have been used to reach this relationship. These methods are grating coupling and Attenuated Total Reflection (ATR) (Raether, 1988).

When the light ($k_0 = \frac{\omega}{c}$) hits the grating with a periodic grating constant Λ and an incident angle θ_0 , its surface wave vectors takes on the form $k_x \sin(\theta_0 \pm mG)$, where $G = \frac{2\pi}{\Lambda}$ and $m =$ an integer value greater than 0. Excitation of SPP modes can only be possible by fulfilling the following relations (Eq. 2.7 and Eq. 2.8).

$$k_x = \sqrt{\epsilon_d} \frac{\omega}{c} \sin \theta_0 \quad (2.7)$$

$$k_x = k_0 \sin \theta_0 \pm mG = k_0 \sqrt{\frac{\epsilon_m}{\epsilon_m + 1}} = k_{SP} \quad (2.8)$$

Where $\epsilon_d = 1$ is the dielectric constant of vacuum. A grating coupler along with a k -vector diagram is shown in Fig. 2.11. By changing the grating constant (Λ) one can tune the criteria for the SPP mode. The resonance can be observed through the minima in the ATR (Fig. 2.12).

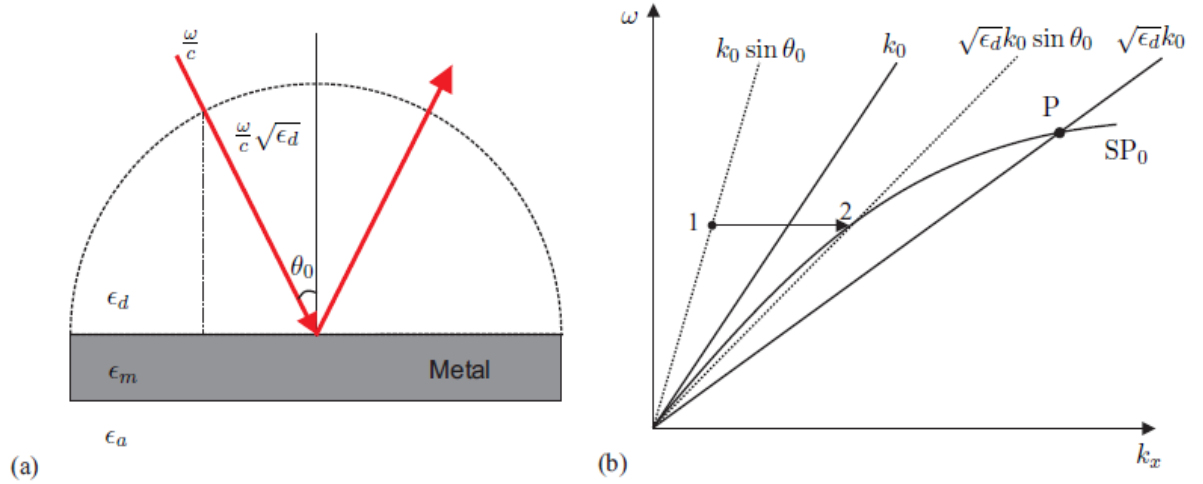


Figure 2.12:(a) Wave vector and ATR from metal surface (b) Dispersion relation of various components of the system, where \mathbf{k}_0 is the light line (ω/c). The excitation can be seen as a minima in the Attenuated Total Reflection (ATR) intensity.

2.6 Summary

In this chapter we looked at the problems, outlined in Chapter 1, in more depth drawing from the literature (Section 2.1 and Section 2.2). Then, consider at ways in which we could solve this problem using SPR based sensing system; looking at different configurations for exciting the plasmons (Section 2.3). In Section 2.4 we view in more depth at the Kretschmann configuration as the best candidate for the specific application. We will now construct a mathematical model for predicting the SPR response from a multi-layered system.

CHAPTER 3

3.1 Numerical Analysis of SPR Biosensor

Due to the complex nature of the Surface Plasmon Resonance (SPR) biosensors, numerical analysis of an N-layered system, based on the Kretschmann's configuration, has been conducted (Daghestani and Day, 2010, Born and Wolf, 1999, Salah *et al.*, 2012). This allows for the analysis of SPR conditions with varying materials, number of layers and their thicknesses in order to optimise the resolution and sensitivity. We created a numerical model using the Transfer Matrix Method (TMM, also known as Abeles matrixes) which is based on Fresnel's complex amplitudes for the transmission and reflection. The numerical analysis of device structures for use as SPR biosensors will be used for the development of the experimental devices. The proposed system uses an angle interrogation method, where the angle is varied and measured until a minima is detected in the reflection; better known as the SPR angle. The minimum angle shift detected can be used to determine concentrations of analytes in solution from the change in the effective refractive index of the solution (or sample).

The two most important parameters which can be obtained from the numerical analysis is firstly the Full-Width Half-Maxima (FWHM) of the SPR peak that describes the *resolution* of the sensing system (Verma *et al.*, 2011) where the smaller the FWHM the higher the resolution of the sensor. The other is the *sensitivity* of the system which is based on how much the SPR angle shifts with changing the refractive index (Maharana

and Jha, 2012); the more the peak shifts for a change in refractive index, the more sensitive the sensing system is.

In this chapter, a description of the requirements of the model will be discussed, relating to similar work found in the literature, followed by a detailed description of the methods involved in the numerical analysis. This will be followed with results based on different material systems and layer thicknesses. These results and the limitations of the system, will then be discussed with comparison with similar methods in the literature.

3.2 Background and Requirements of the numerical model

Here we will discuss the requirements of the numerical model, starting with SPR biosensing applications, where the advantages and disadvantages of this technique are described. Then a detailed description of the Kretschmann configuration will be given, leading into methods of measuring the SPR conditions. Then follows a description of the system requirements, such as the analytes to be detected, the range of concentrations and the materials that will be investigated to support these requirements.

3.2.1 SPR Biosensing

Due to their high sensitivity (Lahav *et al.*, 2008, Jha and Sharma, 2009) and reliability (Maharana and Jha, 2012), SPR based sensors are commonly used in bio-sensing application. The main benefit of using the SPR technique, is that it allows for label-free detection of low concentrations of analyte (Liu and Wang, 2009). The SPR method relies on changes in the refractive index on the metal-sample interface of the sensor where a change in the refractive index changes the SPR conditions. By detecting this change it is possible to obtain information, such as the presence, concentration or purity of an analyte. In most cases, the change in refractive index is measured by determining

the SPR angle (angular interrogation method) of multi-layered optical system which contains the analyte at the interface. Other methods include wavelength, phase and intensity interrogation (Homola *et al.*, 1999).

In this work, the angular interrogation has been concentrated on due to its higher sensitivity (Alleyne *et al.*, 2007) compared with the wavelength and intensity interrogation techniques and its simplicity compared with phase interrogation techniques (Salazar *et al.*, 2013). The advantage of SPR sensing devices is that they are unaffected by interference from light scattering within the sensing medium. This is due to a small sensing area, given by the penetration depth of the SPR which has been approximated to be between 200 and 300 nm (Raether, 1988). Only particulates within the area closest (< 300 nm) to the metal film cause a significant change in the SPR response. This is advantageous if the refractive index of the analyte suspended in solution is of interest.

A wide range of SPR based sensors are in use that generates a signal specific to the fluctuation in the refractive index at the surface of the sensor. In particular the SPR based sensing technique is employed for Immunoassays (Mullett *et al.*, 2000), where it is used to measure specific antibody-antigen reactions. By using this technique the antibodies are immobilised on top of the metallic surface (usually gold due to the ease of conjugation with antibodies (Mullett *et al.*, 2000)), this enables the antigens to be passed into the chamber using a fluidic stream (As shown in Fig.3.1a). This creates local specific binding sites for the antigens; where the binding event causes a change in the effective refractive index and hence the SPR conditions as shown in Fig.3.1(b-d).

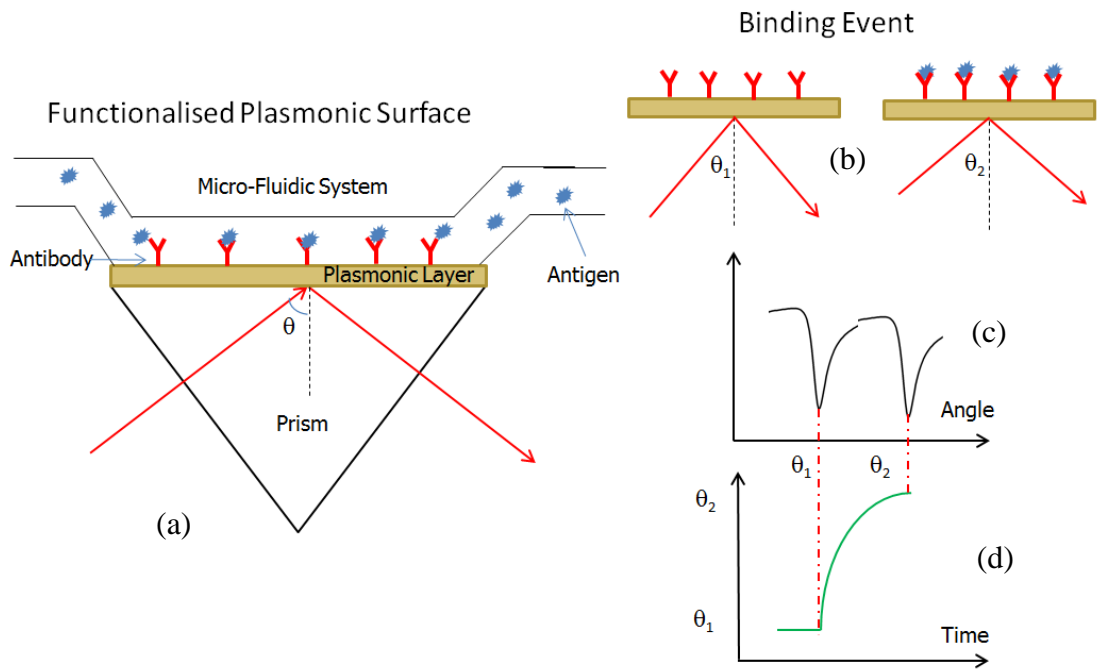


Figure 3.1: Illustrates the SPR immunoassay technique, (a) Antibody functionalised SPR sensor layer on the top of a conventional glass prism/ gold plasmonic system. (b-d) The sensogram response changing following the binding event. (b) Before and after the binding event, the angles (θ_1 and θ_2) relate to what is shown in (c) and (d). (c) The ATR response over angle, showing before and after binding events how the SPR angle shifts. (d) The transient response from the pre- to post-binding events (Salah et al., 2014).

The most common SPR sensor system is based on the Kretschmann configuration (Kretschmann and Raether, 1968) which is extensively used for chemical and bio-molecular sensing with high sensitivity (Maharana and Jha, 2012). A demonstration of how the Kretschmann configuration can be used for detecting analytes in solution can be seen in Fig. 3.1. The thiol groups, from the disulphide bridge, of the antibodies create a covalent bond to the surface of the gold film (or any other thiol-rich surface), immobilising them in an evenly spaced manner (Neves-Petersen *et al.*, 2006). This allows them to be densely packed on the surface of the sensor, hence creating specific antigen binding sites (Neves-Petersen *et al.*, 2006).

3.2.2 The Kretschmann configuration

The Kretschmann prism configuration describes a multi-layered system on-top of a glass prism. This allows incident rays of light to couple into Surface Plasmon (SP) mode which is specifically bound to an interface. Very fine films of metals, such as silver or gold, are usually used for SPs, due to their optical properties. The film thickness after deposition can be easily controlled; as it has been widely researched (F. A. W. , 2013). The metal films are deposited onto a glass substrate which is optically coupled to a prism. A material is known to support SP waves when the real component of the dielectric permittivity is negative (experiment, 2012). Other metals, such as Vanadium, Chromium, Cobalt, Nickel, Platinum, Palladium, Aluminium, Tungsten, Copper and some semiconductors can also demonstrate SP phenomena (Wang *et al.*, 2013).

The amount of light that is coupled to the SP mode is determined by the physical conditions of the surrounding materials, this also has an effect on the SP conditions, where these can be tuned. The top dielectric in Fig. 3.2 is labelled as the sample environment; this is where the analyte of this study will be presented. As shown in Fig. 3.2, the Surface Plasmon Polariton (SPP) is bound to the interface between the sample environment and the plasmonic layers, although the SP modes will appear at all interfaces between materials due to coupling effects. Under certain conditions an electric field (\mathbf{E}) is generated at the interface which quickly decays in the adjacent materials, this can be described as high density electron gas which oscillates and it is the oscillation that propagates.

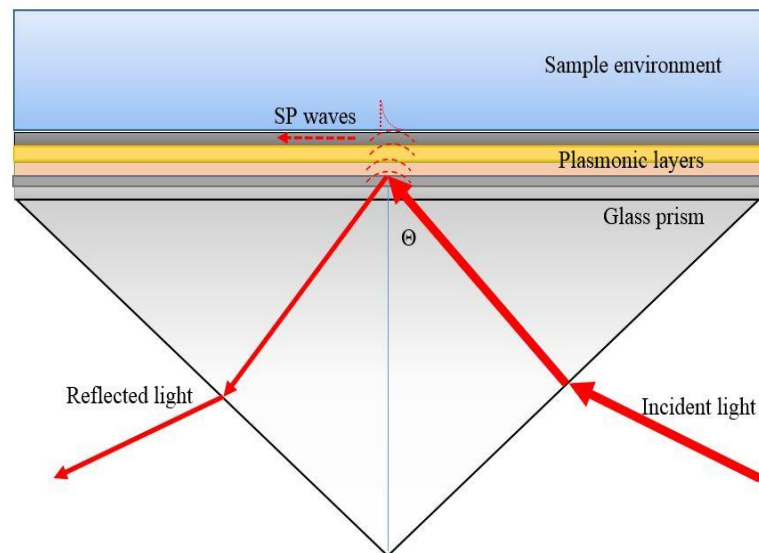


Figure 3.2:Kretschmann's configuration set-up, this contains a glass prism, glass substrates, plasmonic layers and the dielectric sample on top. The incident light is refracted towards the plasmonic layers at an incident angle, the SP evanescent wave is most prominent at the plasmonic-sample environment interface.

3.2.3 Angular Modulation

Several analytical methods can be used to detect the presence of silver nanoparticles and characterise their suspensions. These techniques include electron microscopy techniques, such as Scanning Electron Microscopy (SEM) and Transmission Electron Microscopy (TEM). Atomic Force Microscopy (AFM), light scattering and filtration methods have been used (Besinis *et al.*, 2014), however each of these techniques has certain limitations. For instance, most of these techniques are time consuming, costly and sample preparation can be laborious and techniques such as the light scattering method are not specific enough (Bradford *et al.*, 2009). Additionally, their efficiency is further compromised when NPs exist in biological and other complex environmental solutions (Hackenberg *et al.*, 2011).

Dynamic Light Scattering (DLS), also known as photon correlation spectroscopy is an experimental tool used to detect colloidal particulates, such as Ag NPs in solution (Tomaszewska *et al.*, 2013). The basic principle is that light from a laser is focused onto a small section of the sample, whereby the light is scattered by the particulates. The

scatter angle is correlated to the particle size which enables the particle size distribution to be found by exploring different angles. In this work we are concerned with metallic nanoparticles (Ag NPs) in low concentrations ($< 50 \text{ mg L}^{-1}$). It is probably that both clusters and mono-dispersed nanoparticles, will be present. Compared to the proposed SPR method, DLS is better suited to determining the particle size and shape. When the concentration of the analyte reaches a certain low limit, such as 10 mg L^{-1} , the measurements can be indeterminate. DLS can be used to detect particles from around 0.1 nm to $10 \text{ }\mu\text{m}$, even when a limited range of particle sizes are present. DLS enables the extraction of useful information such as an inferred concentration (Tomaszewska et al., 2013).

To quantify the size and size distribution, AFM, SEM or STEM may also be used. In a recent paper by Tomaszewska *et al.* (Tomaszewska *et al.*, 2013), DLS was used to determine the size distribution for particulates, for both singular mono-dispersed and mixtures of varying size mono-dispersed nanoparticles with promising results. When particles with 10 nm , 55 nm and 80 nm radii were present the DLS spectrum clearly identified all of them. DLS cannot directly determine concentration, but it does have a concentration limit; where the size and shape of the particulates can be determined. However, measuring the concentration or detecting the presence of silver nanoparticles, at the very low environmental levels remains a significant challenge.

Angle modulation applied in SPR measurement has proved to be the most extensively used approach for detecting changes in the SP wave-vector in a sensing arrangement (Wang *et al.*, 2013). The angle of the incident light compared to the surface of the prism can be measured and controlled with high accuracy, making this a good method for use in bio-sensing applications. There are different ways to implement this modulation technique using the Kretschmann configuration: The sensor can be mobilised with respect to the fixed laser source using a rotating stage (Guo, 2012). Alternatively the

sensor system can be fixed and the use of a goniometer to move the laser and detector in unison can be used (Guo, 2012). In this study, we make use of both methods. The approach of angle modulation is used in commercial SPR sensing systems, where they use a photodiode array (PDA) for detecting light (Guo, 2012).

It has been established that an angular resolution of 0.001° can be achieved with the best arrangements for angle modulation (Ray *et al.*, 1997). Realistically, the achievement of this resolution is challenged by a number of factors, such as divergence, refraction and spectral broadening. This has been shown to limit the resolution to approximately 0.01° (Ray *et al.*, 1997). The required analyte is detected by examining the SPR coupling angle that can be determined through the SPR response curve.

$$S = \frac{\partial \theta_{\text{SPR}}}{\partial n_a} \quad (3.1)$$

$$\text{DA} = \frac{1}{\text{FWHM}} \quad (3.2)$$

The nature of the reflectance curve, such as the FWHM, can be used to determine the performance of the SPR sensor (Maharana *et al.*, 2014). The sensitivity (Eq. 3.1) is determined by how much the resonant angle (θ_{SPR}) shifts with change of refractive index (n_a). The width (FWHM) of the peak determines how precisely the sensor can detect the resonant angle (Eq. 3.2). Therefore, the system performance can be analysed from its SPR response.

Fig. 3.3a Shows the path of the incident and reflected light in the Kretschmann configuration. The amplitude of the reflected wave will reach minima only under p-polarisation, as can be seen in Fig. 3.3b. Only P-polarised light allows coupling into Plasmon modes because the electric field vector of the light is normal to the surface of the metal film.

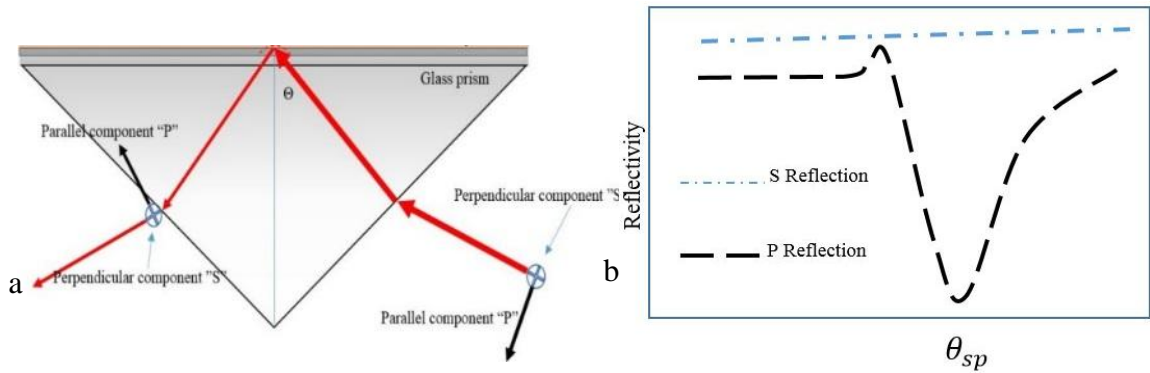


Figure 3.3:(a) The propagations of the incident and reflected light in the Kretschmann configuration. The polarisations of the “S” component, otherwise known as TE mode and the “P” component, otherwise known as TM mode. (b) An example spectra of the reflected amplitude over a range of wavelength, the minima is only observed in TM modes and not a TE. This is because plasmonics are purely Electrical phenomena and not magnetic.

Researchers have studied different interrogations methods such as phase, intensity and angular interrogations (Salah et al., 2012, Zhang, 2013). So far, the determination of the real component of the refractive index of an absorptive sample through these interrogations have been reviewed theoretically without integrating a graphene layer as a sensor layer (Yan *et al.*, 2011, Sharma and Gupta, 2007, Kurihara and Suzuki, 2002).

3.3 Mathematical Model for Numerical Simulation

We created a numerical model using the Transfer Matrix Method (TMM) which is based on Fresnel’s complex amplitudes for the transmission and reflection at each boundary (interface). This mathematical model would predict the Surface Plasmon Resonance angle and the shape of reflection vs angle curve for a multi-layered system with a set concentration of analyte which in this case are Ag nano-particles. The model will predict the sensor response and will help to optimise the detection resolution, sensitivity and linearity.

Fig. 3.4 shows a multi-layered system, where j denotes the layer index. This system can be modelled using the TMM, where a 2×2 Abeles matrix describes the propagation of

light through the layers. Each layer has a thickness (h_j) which can be characterised by the complex refractive index ($n_j = n + ik$) and the angle of incidence (θ_j). The latter is related to the angle of incidence in the system: $\sin \theta_j = n_0 \sin \theta_0 / n_j$, where n_0 is the refractive index of the ambient medium. The Abeles matrix for each layer is constructed using two parameters β_j (Eq. 3.3) and p_j (Eq. 3.4), for P-Polarised light.

$$\beta_j = \frac{2\pi}{\lambda} h_j n_j \cos \theta_j \quad (3.3)$$

$$p_j = \frac{\cos(\theta_j)}{n_j} \quad (3.4)$$

The transfer matrix can be derived directly from the Maxwell equations for macroscopic electromagnetism (Born and Wolf, 1999), where specific boundary conditions are set at each layer interface. Because of these boundary conditions the following assumptions are made:

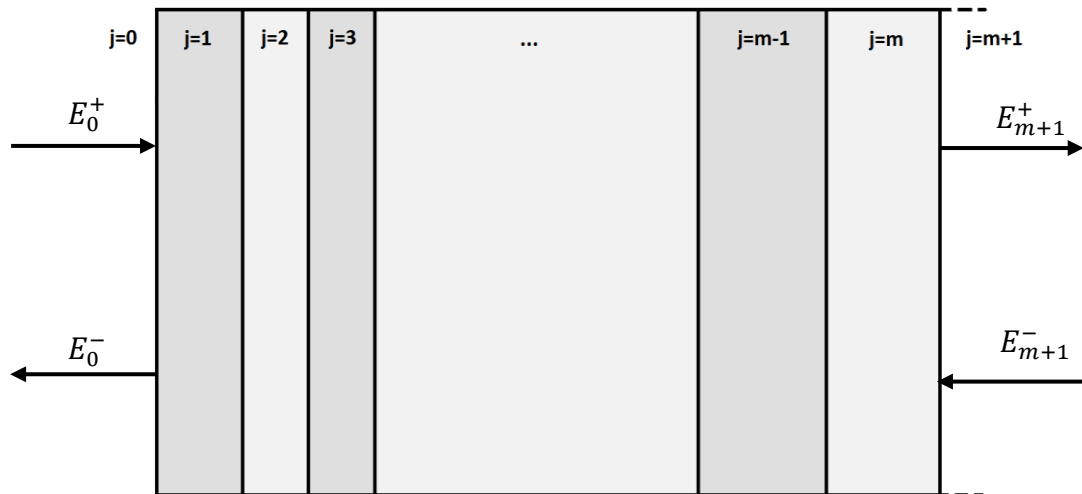


Figure 3.4: Shows the parameters used in the model, where: \mathbf{E}_0^+ is the incident energy in the forward direction, \mathbf{E}_0^- is the energy travelling backwards from the device (when divided by the incident energy, the Fresnel reflection coefficient can be found). \mathbf{E}_{m+1}^+ is the forward propagating transmitted energy (when divided by the incident energy, the Fresnel reflection coefficient can be found) and \mathbf{E}_{m+1}^- is the backwards propagating energy, in most systems this is assumed to be 0. \mathbf{j} represents each of the layers, $\mathbf{j} = \mathbf{0}$ and $\mathbf{j} = \mathbf{m} + \mathbf{1}$ are generally assumed to be air.

- Each of the layers is infinitely wide, as just the height of the layer is taken into consideration.
- The transfer matrix approach only considers homogenous and isotropic films.
- Only plane waves can be considered.
- It cannot handle diffusion between two adjacent layers and assumes the interface to be perfectly flat.

With these assumptions the transfer matrix of layer j is written as shown in Eq. 3.4.

$$\hat{M}_j = \begin{pmatrix} \cos(\beta_j h_j) & \frac{i}{p_j} \sin(\beta_j h_j) \\ ip_j \sin(\beta_j h_j) & \cos(\beta_j h_j) \end{pmatrix} \quad (3.4)$$

A full derivation from Maxwell's equations can be found in **Appendix A**. The TMM allows the propagation of light through a stratified medium to be described. The full characteristic matrix \hat{M} (Eq. 3.5) of the system is found by multiplying the matrices \hat{M}_j .

$$\hat{M} = \left(\prod_{j=1}^m \hat{M}_j \right) \quad (3.5)$$

The Fresnel coefficients for reflection (r) and transmission (t) for the whole system can then be extracted from Eq. 3.6.

$$\begin{pmatrix} 1 + r \\ (-1 + r)p_0 \end{pmatrix} = \hat{M} \cdot \begin{pmatrix} t \\ -t \cdot p_{m+1} \end{pmatrix} \quad (3.6)$$

The characteristic matrix \hat{M} can be described by its individual elements, as shown in Eq. 3.7.

$$M = \begin{bmatrix} M_{11} & M_{12} \\ M_{21} & M_{22} \end{bmatrix} \quad (3.7)$$

The conversion from the transfer matrix to the scattering matrix can be found from Eq. 3.6 and Eq. 3.7, where now the Attenuated Total Reflection ATR can easily be found by calculating the difference between the reflected energy (\mathbf{E}_0^-) and the incident energy (\mathbf{E}_0^+). This is shown from the matrix elements in Eq. 3.8 and the total transmission is shown in Eq. 3.9 (Pettersson *et al.*, 1999) written for $p_0 = p_{m+1}$.

$$S = \begin{bmatrix} S_{11} & S_{12} \\ S_{21} & S_{22} \end{bmatrix} = \begin{bmatrix} -\frac{M_{21}}{M_{22}} & \frac{1}{M_{22}} \\ M_{11} - \frac{M_{12}M_{21}}{M_{22}} & \frac{M_{12}}{M_{22}} \end{bmatrix} \quad (3.8)$$

$$\begin{bmatrix} E_0^+ \\ E_0^- \end{bmatrix} = \begin{bmatrix} S_{11} & S_{12} \\ S_{21} & S_{22} \end{bmatrix} \begin{bmatrix} E_{m+1}^+ \\ E_{m+1}^- \end{bmatrix} \quad (3.9)$$

Where E_0^+ , E_0^- , E_{m+1}^+ and E_{m+1}^- relate to the energies shown in the fig.3.3 for the multi-layered system. This is what describes the internal scattering energies of the device which enables us to obtain the Reflection and Transmission coefficients (Eq. 3.10 and Eq. 3.11)

$$R_{TOT} = |r|^2 = \left| \frac{E_0^-}{E_0^+} \right|^2 = \left| \frac{S_{21}}{S_{11}} \right|^2 \quad (3.10)$$

$$T_{TOT} = |t|^2 = \left| \frac{E_{m+1}^+}{E_0^+} \right|^2 = \left| \frac{1}{S_{11}} \right|^2 \quad (3.11)$$

Using this method for a set wavelength, layer thicknesses and refractive indices, it is possible to sweep through the incident angle and reveal local minima in the spectra when the SPP conditions are met. This enables us to explore different structures to determine the response in each case before building the sensors.

Furthermore, it has been assumed that the Drude-Lorentz model can be used to describe the absorptive properties of the sensed medium (due to the presence of absorptive particles). The dielectric constant can be expressed as shown in Eq. 3.12 (Kurihara and Suzuki, 2002).

$$\epsilon_s(\omega) = \epsilon_s^{ba} + \frac{\omega_p^2}{\omega_0^2 - \omega^2 - i\omega(\gamma)} \quad (3.12)$$

In Eq. 3.12: ω refers to the frequency of incident light, ϵ_s^{ba} corresponds to $\omega \rightarrow \infty$, (equilibrium state ignoring the effects of positive or negative charges or external fields), ω_0 refers to the resonant angular frequency and γ is the relaxation parameter which relates to the FWHM of the resonant peak. Oscillator damping (ω_p^2), Eq.3.13, refers to the parameter proportional to the quantity of absorptive particles.

$$\omega_p^2 = \sqrt{\frac{Nq^2}{m\epsilon_0}} \quad (3.13)$$

N is the number of free charges, q is the elementary charge; m is the mass of the charge with the effective mass. You are only able to obtain the result for the first oscillation mode using this technique. If you want other resonant modes f_m is the oscillator strength and the incorporation of this into Eq. 3.12 is shown in Eq. 3.14 and Eq. 3.15 shows the relationship between Eq. 3.14 and the complex refractive index.

$$\tilde{\epsilon}(\omega) = \tilde{\epsilon}(\omega \rightarrow \infty) + \sum_{m=0}^M \frac{f_m \omega_p^2}{\omega_m^2 - \omega^2 + i\omega\gamma_m} \quad (3.14)$$

$$\tilde{\epsilon}(\omega) = \epsilon_{real}(\omega) + i\epsilon_{imag}(\omega) = \tilde{n}(\omega)^2 \quad (3.15)$$

The calculated $n(\omega)$ and $k(\omega)$ are shown in Fig. 3.5 using the parameters $\gamma_m = 4.9009 \times 10^{14}$ rad/s, $\omega_p^2 = 3.8373 \times 10^{28}$ rad²/s² and $\omega_0 = 2.8999 \times 10^{15}$ rad/s (Zhang, 2013). It is clear from the figure that at the centre frequency (ω_0), the imaginary part $k(\omega)$ are greatest. On the other hand, the minimum and maximum of the real part $n(\omega)$ is found at FWHM of the absorption peak. These trends have been earlier reported by some researchers, thereby indicating that the Lorentz model is reliable.

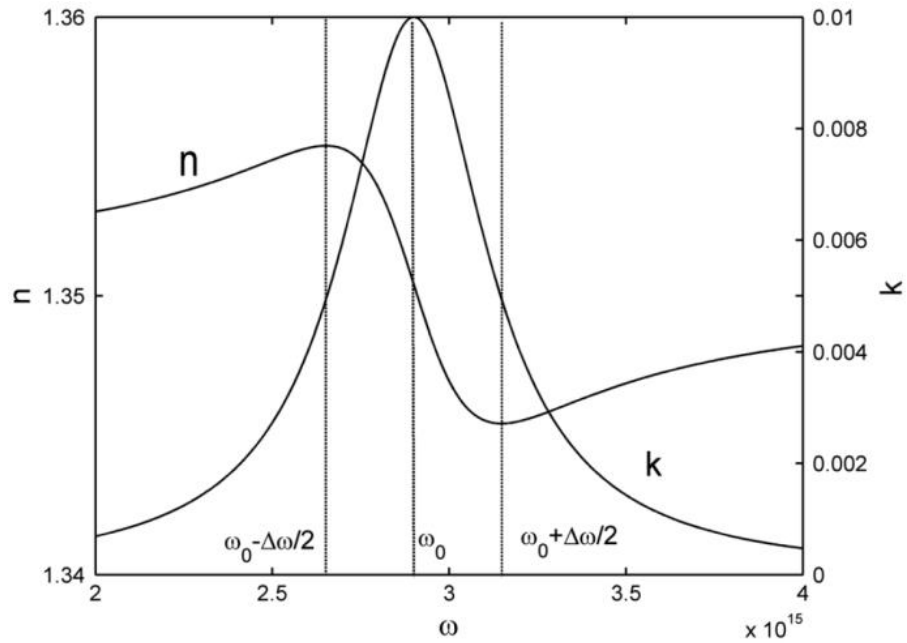


Figure 3.5: Numerical simulations of the real ($\mathbf{n}(\omega)$) and imaginary ($\mathbf{k}(\omega)$) part of the sample's refractive index calculated by the Drude-Lorentz model in Eq. 3.14 and 3.15.

From the graph above it can be stated that the real component of the refractive index at absorption maximum frequency is not affected by the reduction or increase in the absorption. At $\omega = \omega_0$, there is maximum change in $k(\omega)$ and it is still much smaller as compared to $n(\omega)$; Δk smaller than Δn . Therefore, the imaginary and real components of the refractive index can be treated independent, here $n(\omega)$ alters because of different background dielectric constant $\epsilon_s^{ba}(\omega \rightarrow \infty)$.

As a result, the change in SPR signal of the real component is evaluated with particular imaginary component though it is not constant for varying angular frequency. The SPR signal drawn from the change in both real and imaginary components must be split when ω_p^2 is altered. The determination of the real component of the refractive index ($n(\omega)$) in SPR bio-sensing applications will be discussed in the next section.

3.4 Simulation Results and Discussions

Fig. 3.6 shows that change in real component of the refractive index of the absorbing medium has an effect on the reflectivity and resonance angle. This study produced results which corroborate the findings of (Akimoto *et al.*, 1999, Durou *et al.*, 1973, Kotsev *et al.*, 2003); and similar findings were obtained in the case of transparent medium (Zhang, 2013). This system has the arrangement of Cr (2 nm)/Ag (40 nm)/Au (5 nm)/Gr (0.33 nm) for detecting the absorptive media, where the Graphene (Gr) is single-layered.

Here chromium acts as an adhesion layer, silver as a plasmonic layer, gold as a protective layer and graphene is used to enhance the sensitivity of the SPR system. By using a 5 nm protection layer of gold on top of the silver layer, the optimized thicknesses of the silver film is 40 nm. Otherwise without the Au protection layer, the optimized thickness is 50 nm for Ag with one layer of graphene. When a number of simulated results were compared, it became clear that as the thickness of the Ag decreases, the maximum absorption increases.

As shown in Fig. 3.6, the intensity interrogation has been realised by obtaining a range of linear measurement values which have been obtained by sweeping the incident angle. The relation between the SPR reflection and the fixed real component of the refractive index, as well as the changing imaginary components. Furthermore, when the imaginary part is more dominant than the real part, the change in the resonant angle is much lower and therefore the sensitivity of the sensor is much less. This is supported by Fig. 3.6 The higher the imaginary component of the refractive index, the broader the SPR peak will be. This can lead to errors in the determination of the resonant angle which would rise in equivalent noise conditions.

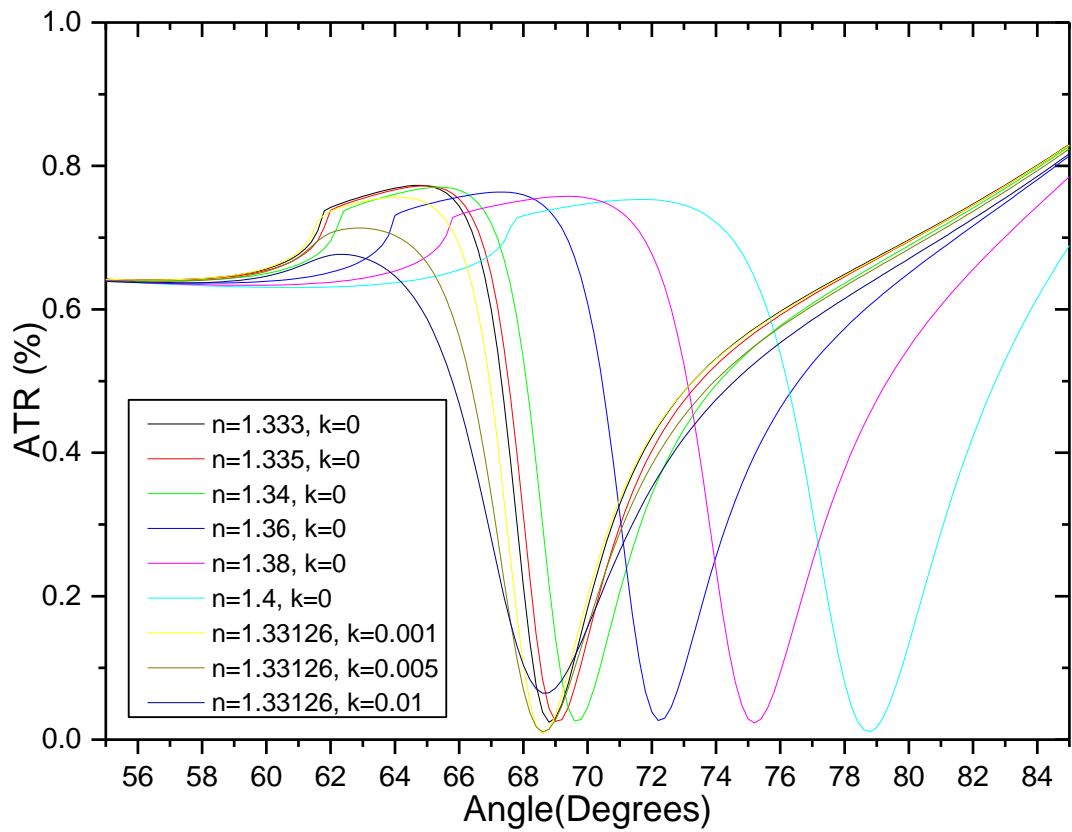


Figure 3.6: Compares the reflectivity of the different samples with different real and imaginary components obtained from theoretical calculation.

3.5 Summary

In this chapter, SPR sensors using two interrogations for the determination of the real component of the refractive index of the sample are evaluated by numerical simulation. In comparison with the analysis of transparent media (materials without imaginary part of the refractive index within the visible range), the sensitivity has been demonstrated to increase by the use of both intensity and angular interrogation.

However, in the case of intensity and angle interrogations, such a wavelength must be selected which evades the absorption bands ($k(\lambda) \ll n(\lambda)$). Furthermore, in the case of these interrogations, the sensitivity gets adversely affected if the same thickness of plasmonic film which has been optimised for non-absorptive sample is employed for an absorptive sample. Yet, it is worth mentioning that the thickness of multi-layered thin film affects the sensitivity of both interrogation methods. It can be stated that optimal

thickness reduces with the increase in absorption of the sample. In other words, once the optimization of thickness of plasmonic film has been done efficiently, maximum resolution is demonstrated by the SPR sensor.

CHAPTER 4

4.1 Experimental Techniques and System Design

Designing, developing and using a new instrument for a specific task is time consuming, requiring many different engineering based skills. During this research, a large proportion of the time was taken to assemble the system in order to achieve the best possible results. This Chapter is focused on the design considerations, as well as some of the techniques used in order to reach our goal.

Section 4.2 covers Physical Vapour Deposition (PVD) which deposition methods used throughout this work and Section 4.3 covers how we prepared and fabricated the devices for the system. The design considerations and development of the entire system are discussed in Section 4.4 and Section 4.5.

4.2 Physical Vapour Deposition

An appropriate coating technique is needed for the fabrication of thin metal films. For this purpose, a Physical Vapour Deposition (PVD) technique commonly known as sputtering is used. This technique enables the growth of very thin layers (1-2 nm up to 2 μm). An advantage of this technique is that it is used for making thin metal layers from materials, such as gold, silver and chromium which are difficult to deposit using other techniques. In most cases, when using PVD, the deposited film does not contain contamination from other materials, unlike other techniques, for example, electro-

plating which can result in the formation of deposited layers containing contaminants (Mattox, 2010, Sullivan and Dobrowolski, 1993, Sullivan and Dobrowolski, 1992).

Evaporation is another PVD technique, where the source material is resistively heated using a resistive coil or crucible. The source material evaporated, before it is condensed on the surface of the substrate. This technique requires a high vacuum as the atmosphere pressure is proportional to the evaporation rate (Buzea and Robbie, 2005); due to the mean free path of the vapour. An advantage of evaporation is the higher purity of the deposited film, due to the high vacuum needed. However, it suffers from poor step coverage (Bunshah et al., 2001) and becomes difficult to evaporate materials that have high melting temperatures. Sputtering requires a mid to high vacuum ($\sim 10^{-7}$ mBar) and generally achieves better adhesion to the substrate (Buzea and Robbie, 2005) whilst maintaining a high purity. One of the main disadvantages of sputtering is the sputtering rate which is usually much lower than other PVD techniques. Also, the plasma may cause some damage to the sample through the implantation of the inert gas atoms that are usually used (Bunshah et al., 2001).

A number of different sputtering techniques can be utilised depending on the power sources available, such as microwave, electron-beam, ion-beam, Radio Frequency (RF) and Direct Current (DC) (Chen and Chang, 2003). In the next section, we shall look at the sputtering mechanisms and then focus on RF sputtering technique which has been used in this project.

4.2.1 Principles of Sputtering

To grow a thin film of a given material, sputtering is used. This works by bombarding a source material (target) with ionised particles which breaks away the atoms that are then directed towards the substrate to form a uniform layer.

The sputtering chamber is usually filled with an inert gas, such as Argon (Ar), Xenon (Xe), or Neon (Ne). High energy electrons collide with the inert gas to form an ion. For example, if the chamber is filled with Argon atoms then electron collides with Argon, it knocks out an electron (secondary electron emission) from the outer shell which ionises the argon ($Ar + e^- \rightarrow Ar^+ + 2e^-$). The Argon atoms are accelerated towards the cathode (target). When they collide with the surface of the source material, if the kinetic energy of Ar^+ is higher than the binding energy of the target, an atom is released in the direction of the anode (substrate). During this process, free electrons can recombine with the ions; and this will result in the emission of a photon. The photon will have energy which due to the laws of the conservation of energy; can be defined as the energy difference between the incident energy and the ground state. Due to the excess energy from the bombardment of the target, it will start heating. This is why water-cooling is usually employed to ensure that the source material does not get too hot.

To have control of the plasma, the pressure needs to be regulated as well as the flow of the inert gas into the chamber. The flow of gas is measured in Standard Cubic Centimetres per Minute (SCCM). Eq. 4.1 describes the mean free path (λ_m) of particles, where k_B is Boltzmann's constant; T is the atmospheric temperature; P is the pressure of the atmosphere and d is the sum of the average radii of the two colliding particles. In the case of Argon and electrons colliding, d would be equivalent to the radius of Argon only. To obtain good plasma, the mean free path of inert gas atoms must be sufficiently short to ensure collisions; for this reason a vacuum pressure of 10^{-4} mBar is used, where the pressure can be correlated to the inert gas flow.

$$\lambda_m = \frac{k_B T}{\sqrt{2} \pi d^2 P} \quad (4.1)$$

The base pressure of the system is usually $2 - 4 \times 10^{-7}$ mBar which is maintained using oil based Diffusion pumping set-up. The base pressure will rise depending on the

inert gas flow introduced hence it will decrease the mean free path of the gas particles and electrons. However, you need to ensure the pressure is low enough to enable the mean free path of the source material is long enough to reach the substrate without too many collisions. This trade-off between the SCCM, sputtering power and pressure is what will determine the deposition rate of the system. Generally, for Argon, flow rates of approximately 20 SCCM are used, where 1 SCCM = $2.7 \times 10^{19} \text{ cm}^{-3}$. The dependence of this relationship can be shown using Eq. 4.2, where P is pressure (Pa), V is the volume; n/V is the molar concentration (mol m^{-3}), R is the gas constant (for Argon, $R = 208 \text{ (J kg}^{-1} \text{ K}^{-1})$) and T is the temperature (K). Therefore the pressure of the system will be the sum of the base pressure and the gas pressure.

$$P = \frac{n}{V} \cdot RT \quad (4.2)$$

The most common process gas is Argon (~99.95% pure) which is used to create an inert atmosphere. When sputtering, it is required that the target material is extremely pure, usually 99.99% pure or more. Several things can happen during particle collisions with the target: The ion causes an atom to be ejected from the source material; Ar atoms can get implanted in the target (usually when the Ar atom has not been ionised); the structure of the target can be altered; secondary electron emission can occur when an electron collides with the surface. The ion can be neutralised or reflected from the surface.

These systems contain electrodes (anode and cathode) which are structured specially for each individual system. Moreover, these electrodes are positioned facing each other and the adjustable gap between them is usually 5 to 10 cm the gap. Insulation of these electrodes from one another and from the chamber is done electrically using PolyTetraFluoroEthylene (PTFE) mounting ring for isolation. The anode which is attached to the sample holder, can be left floating, where the voltage will increase

depending on the applied sputtering power. Conversely, a tuning network can also be employed similar to the one that is employed for the cathode.

A sputter down system (Fig. 4.1) refers to sputter coating machines, where the cathode is positioned above the anode. On the other hand, a sputter up system refers to sputter coating machines, where the cathode is positioned below the anode. There are other, less common systems, such as sideways sputtering systems; where the electrodes are positioned on either side of the chamber.

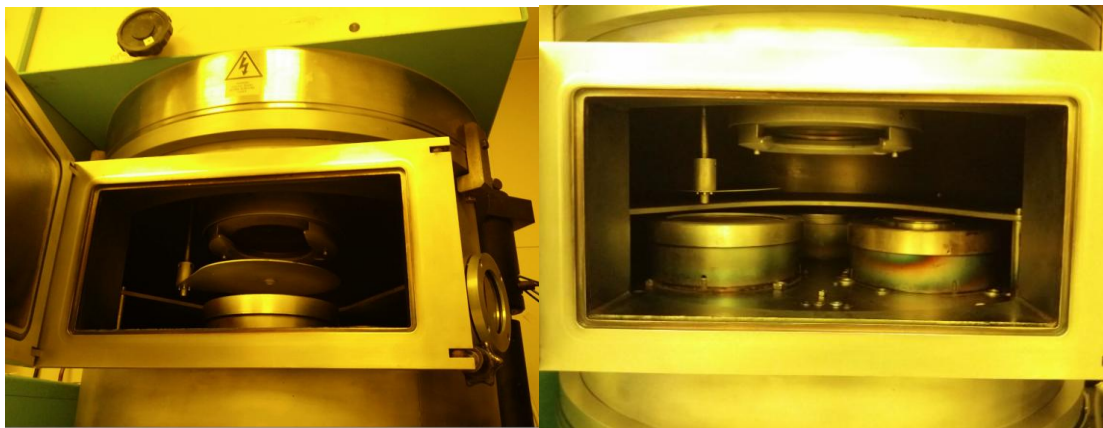


Figure 4.1: Nordico 6 sputtering system with visible target and cathode. This is an example of a sputter up system.

When the target material reaches the substrate in atomic, or molecular, form, there is a chance that it may undergo ejection. However, two particles can unite to make a doublet which is less mobile and more stable compared to single atoms, for this reason there is a lower probability of re-emission. Eventually, triplets and quadruplets are generated. After this, the nucleation stage proceeds, where islands of the target material develop. The islands form single crystalline, or polycrystalline, structures which eventually coalesce or agglomerate.

Several advancements have been made in this field to improve the deposition rate, film quality and uniformity. Examples of these include magnetically enhanced cathodes (Morrison Jr, 1981), bias sputtering (Kawakami et al., 1999) and substrate heating

(Glocker, 1993). The benefits of using these advancements can include; improved film adhesion, step coverage and film density. It can also lead to decreased resistivity and therefore, improvements in the purity of the film. An example of this would be using negative biasing on the anode (substrate), where a small bias voltage of -90 V, at a power of 300W (-75 V for a power of 200 W), can reduce contamination and improve film quality (Mattox, 2010, Buzea and Robbie, 2005, Sullivan et al., 2000).

4.2.2 RF Enhanced Sputtering

A Nordico 6" sputtering system is used in the present work; Fig. 4.2 provides a schematic illustration of this system. There are three targets (Au, Ag and Cr), each having a 15.2 cm diameter and one substrate holder. A relay switch is used to select the target required; each is independently linked to a power source. A rotatable shutter is positioned in-between the anode and cathode so that targets surface can be etch-cleaned prior to deposition. A RF power supply is used with the Nordico 6" system, An advantage of using a RF source is that it is easier to maintain the conditions for a plasma and it stops the targets from heating so much (Roman, 2004, Mapps et al., 1997).

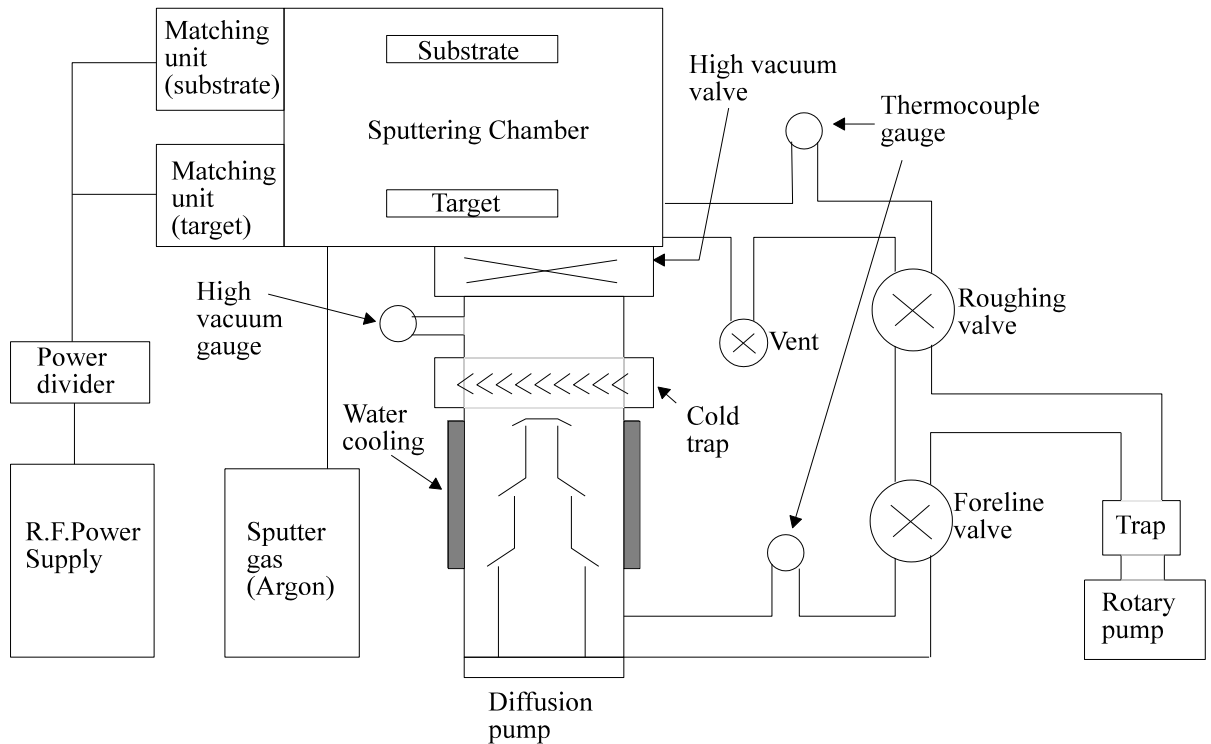


Figure 4.2: Schematic illustration of the Nordico 6" sputtering system, showing all of the mechanical and electrical components of the system, including the vacuum system, gas inlet and RF power supply.

Generally, in most RF powered sputtering systems, a frequency of 13.56 MHz is used and is attached to the matching network using cable which acts as a transmission line, equivalent in length to a multiple of quarter of the wavelength. This is to ensure maximum power throughput from the source is achieved. The RF power source of the system is attached to the cathode and Alternating Current (AC) bias provided to the target surface. This results in the acceleration of electrons and ions in the plasma towards target surface as they are greatly affected by the electric field.

4.3 Device Fabrication (Generic)

To understand how the devices are fabricated, this section provides a basic process used to create a test device comprising of a BK7 glass substrate of thickness (100 μm) with a thin gold film deposited using the sputtering technique described in Section 4.2.1. The gold film was fabricated to be 40-50 nm in thickness. The fabrication process involves a

basic cleaning process, the deposition of the thin film and then the characterisation of the film to ensure that it is as expected.

4.3.1 Fabrication Methods

A BK7 glass slide (Fisher Scientific total area 400 mm²) is used as a substrate. Originally the glass slides had a thickness of 0.1 mm, however they were too fragile to work with and this led to 0.5 mm thick slides being chosen for the substrate.

To remove surface contaminants from the substrate which helps increase the sputtered film quality, a cleaning process is used. The cleaning process consists of washing the substrate in solvents using an ultrasonic bath (Fig. 4.3). The samples are sonicated for 20 minutes at 60°C before being washed with acetone, followed by ethanol, to remove any surface contaminants. The substrates are finally rinsed using de-ionised water, then dried using nitrogen before being annealed at 110°C for 30 minutes to evaporate any remaining solvents. The gold layer is deposited on the substrate using the RF sputtering technique outlined in Section 4.2.1. The Argon is leaked into the vacuum chamber at a rate of 4 SCCM and 200 W Direct Current (DC) is used as a power source. The vacuum pressure during sputtering was approximately 4×10^{-7} mbar. Then by adjusting the sputtering time with respect to deposition rate the layer thickness can be controlled and thicknesses between 1 and 100 nm are easily achievable.



Figure 4.3: Ultra-sonication Bath used throughout this thesis.

4.3.2 Photolithography

To calibrate the sputtering of the metallic layers on the BK7 glass using the sputtering system a standard photolithographic process was chosen. This will create a pattern on the substrate which can then be measured using profilometry or Atomic Force Microscopy (AFM). Using this information we can calibrate the sputtering rate and uniformity of the film under certain conditions.

Photolithography is a several step process, Fig. 4.4 shows the basic steps. Fig. 4.4b demonstrated the BK7 substrate with the positive photoresist spun on. Following this a patterned mask (Fig. 4.4c) is used with Ultraviolet light (UV) illumination to breakdown the irradiated parts of the photoresist. This can then be removed using a developer solution leaving the mask pattern in photoresist on the surface (Fig. 4.4d). Then the material can be sputtered on top of this, as well as the substrate, as shown in Fig. 4.4e. Finally the photoresist is removed leaving just the opposite of the pattern in the sputtered material on the surface (Fig. 4.4f).

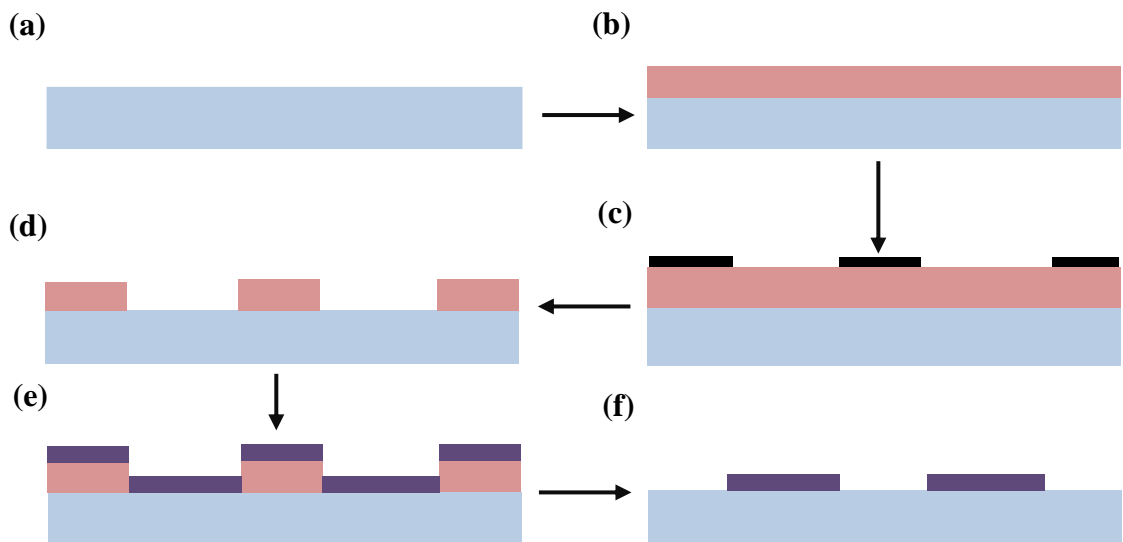


Figure 4.4:Photolithographic process: (a) BK7 Glass substrate should be cleaned, (b) deposition of photoresist on BK7 glass substrate, (c) apply mask on top of photoresist and expose to UV (d) remove exposed photoresist leaving masked pattern, (e) sputter Gold layer on top of the patterned photoresist and (f) final lift off of resist leaving patterned Gold layer.

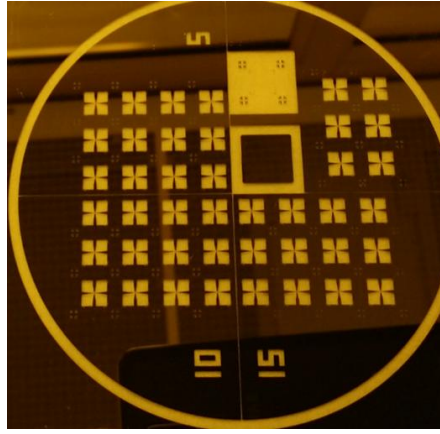


Figure 4.5: The mask used for the photolithography process.

The substrate needs to be thoroughly cleaned as described in Section 4.3.1. Also, before the photoresist can be applied, the substrate needs to be pre-baked, typically at 100°C for one minute. A positive photoresist (Shipley S1813) is used, which is spun to form a 1 μm thick layer on the BK7 glass. To achieve this thickness, specific spin parameters were used: 20 seconds of spinning time at 3000 RPM with maximum acceleration. The remaining solvent was then removed by thermally drying the layer for 60 seconds at 110°C.

Contact Lithography is when the mask is in contact with the sample and illuminated from above allowing maximum exposure where the mask is most transparent to UV (400 - 350 nm). In this case the mask (shown in Fig. 4.5) was laid on top of the photoresist and given a dose of light of 90 mJ cm^{-2} which is the suggested dose for a layer thickness of 1 μm . Using Eq. 4.3, we can determine the exposure time needed to give the correct dose, where T is the exposure time in seconds, I_0 is the intensity of the exposure light (mW cm^{-2}) and E_d is the exposure dose (mJ cm^{-2}).

$$T = \frac{I_0}{E_d} \quad (4.3)$$

After exposure to UV for the duration set by the dosage needed, a developer solution is used to remove the UV softened photoresist leaving the pattern of the original mask.

The developer solution used was Shipley MICROPOST MF-319. The sample was left to develop in the solution for the optimum time of 40 seconds. These samples were then dried using nitrogen before the gold layer was deposited using the sputtering system.

When the sputtering is complete, the residual photoresist needs to be removed. The Shipley 1165 positive resist remover was used, where the sample was left in the solution for 40 - 60 seconds before being rinsed with de-ionised water. The sputtered layer can now be studied using techniques such as AFM (Fig. 4.6 Showing 55 ± 1 nm layer).

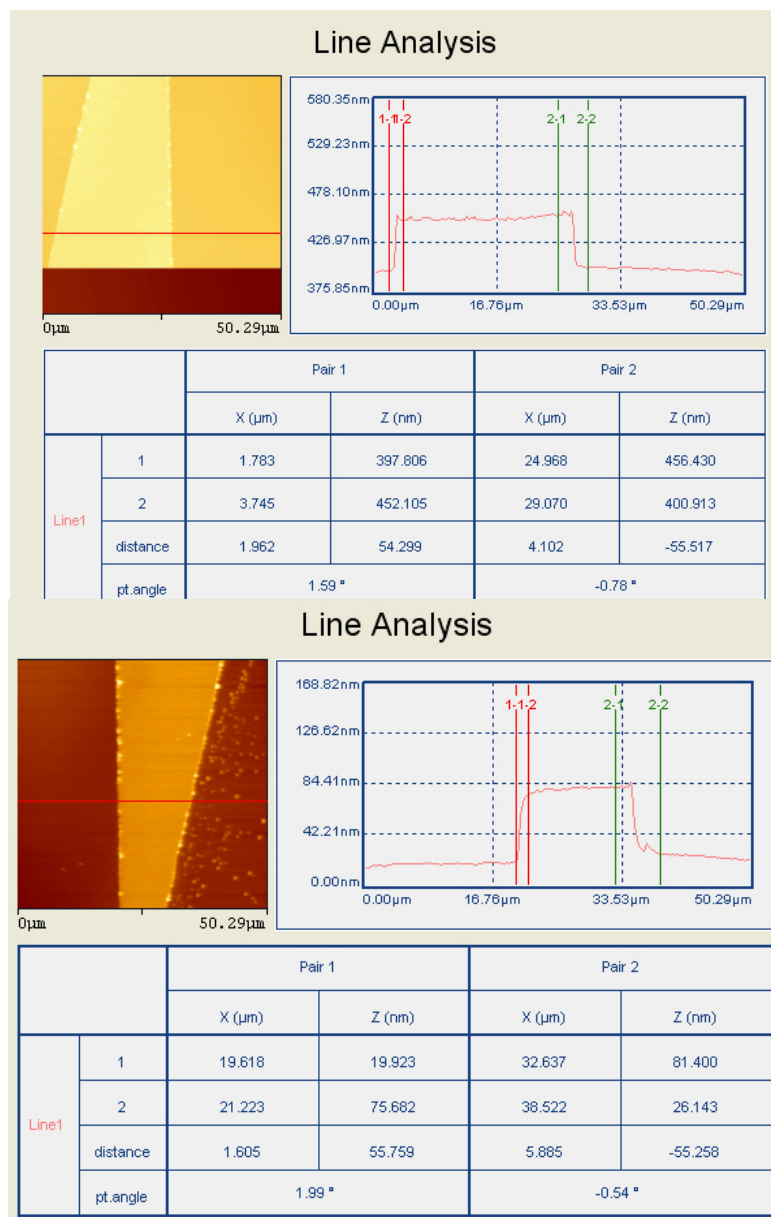


Figure 4.6: Atomic Force Microscopy line analysis from height scan which shows a uniform layer thickness of 55 ± 1 nm.

4.4 System Design

The goal is to design and build a small, automated and portable system to take to the field whereby it is possible to scan and collect data and make measurements, giving real time results instead of bringing sample from field to the lab and do so. The system is controlled by LabVIEW and in the homemade system, it is possible to scan a wide range of angles from 30-90° which is more than the current literature (Homola et al., 1999, Schuck, 1997, Homola, 2008) and commercial systems (Willems and Van Duynne, 2007, Schuck, 1997), have achieved.

The SPR resonance angle with respect to Air or gas and liquid are (40 – 43°) and (70 – 75°), respectively. The duration of the full scan of the whole range with our system is around 8 minutes. The Kretschmann's configuration employing multi-layered made of prism (BK7), Chromium (Cr), Silver (Ag), Gold (Au) and Graphene (Gr) has been considered. Furthermore, a microfluidic channel was designed and built for sample delivery. The effective permittivity of the liquid or gas sample was measured using the Surface Plasmon Resonance (SPR) angle with a laser (664 nm, Red) and a single cell silicon photodiode.

4.4.1 System Design – Mechanical

To achieve the required specification, the SPR measurement system had to be designed to give a maximal range of angles without compromising the system sensitivity and resolution. The system was designed and built at Plymouth University. Fig. 4.7 shows a view of the system from the side (Fig. 4.7a) and the front (Fig. 4.7b). The system is mounted on an optical table (Photon Control). Optical Micro Bench is used for the optical components and for additional structural support, (Fig. 4.7a). There are two legs (Fig. 4.7b). These are used to support the main rod (Fig. 4.7b) which is used as a central point for the geometric alignment of the system. The system requires the laser to

be aligned with the detector after the beam has been reflected from the metal-dielectric sample interface. To achieve this, two arms have been designed independently, one for the laser ((6) in Fig. 4.8a and Fig. 4.9) and one for the detector ((5) in Fig. 4.8b and Fig. 4.9). The laser used during the experimental work was a 35 mW semiconductor laser (664 nm). The polarisation of the laser was done by using an extinction ratio of 500:1. The photo-detector with a low noise coefficient of 1×10^{-14} ($\text{W}/\sqrt{\text{Hz}}$) with an active area of 3.2 mm^2 , showed good linear response over the visible spectrum, where the current output was directly proportion the light intensity.

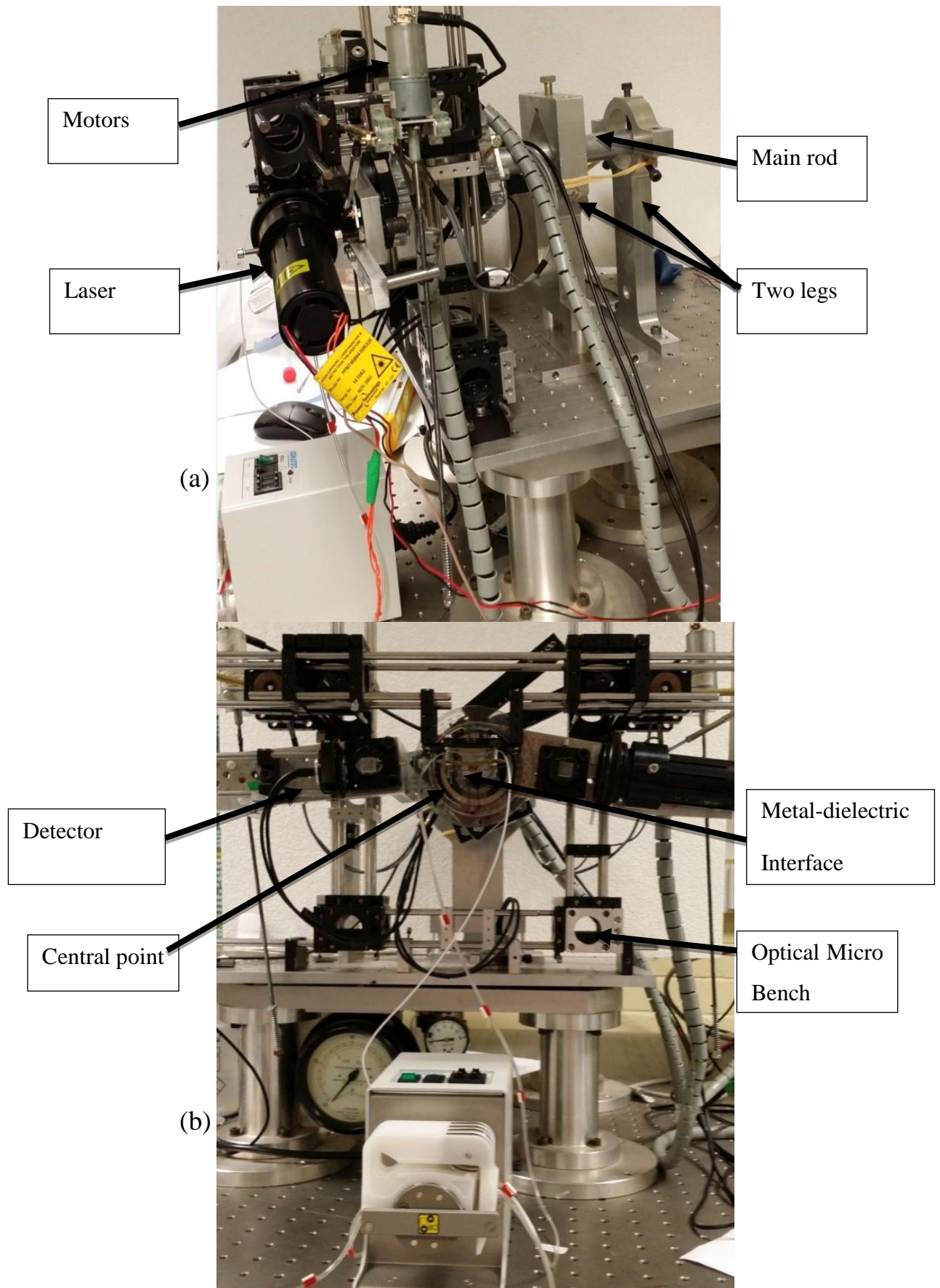


Figure 4.7:(a) The system from the side. (The labels for each element are on the diagrams.) (b) The constructed system from the front: The sample pump can be clearly seen at the bottom of the image. The optical scaffolding can also be seen clearly from this angle.

The configuration of the arms and the pivot, for these have been designed and are shown in Fig. 4.8. They have been designed to allow 10 cm spacing from the laser and detector, to the centre of the main rod. These arms have been secured to the main rod with the use of ball-rings. The swinging arms of the instrument met at the central point of the plate. On one of the swing arms, a photo-detector is attached and on the other one, a laser is fixed. On the exterior surface of the hemispherical plate, angular marks were scribed. In addition to this, indexing of the swing arms allows the exact determination of the position of arm within 0.02° accuracy.

The detector and laser are able to achieve a range of angles between 30° and 90° in relation to the sample. They are designed to move synchronously using a motor with an M4 threaded bar rod of length 300 mm (Fig. 4.7b). The arms are connected with an elbow joint to a potentiometer (Fig. 4.7a). This creates a closed feedback system for controlling and measuring the position of the laser/detector relative to the sample surface and allows for an angular resolution of 0.02° . A full design for all parts from SolidWorks can be found in **Appendix B**.

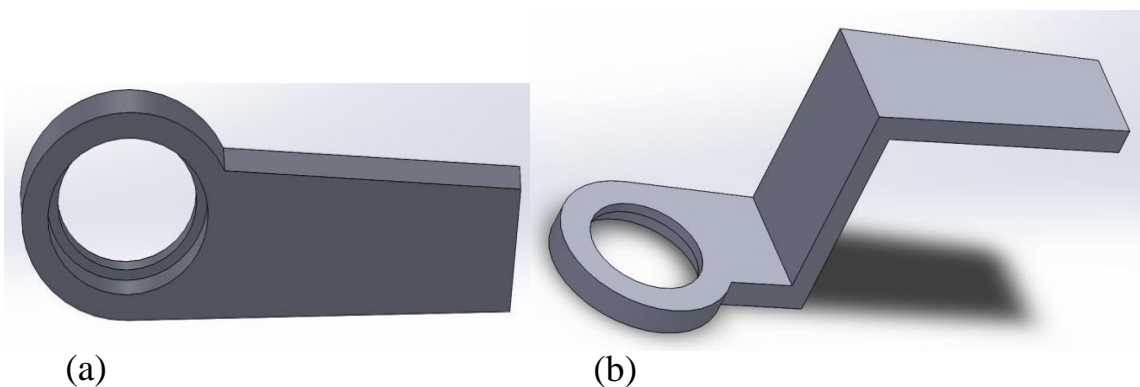


Figure 4.8:(a) Mechanical arm designed to hold the laser, (b) mechanical arm designed to support and move, the detector. The bend in the arm is to ensure that the detector and laser can be aligned together from the same central point.

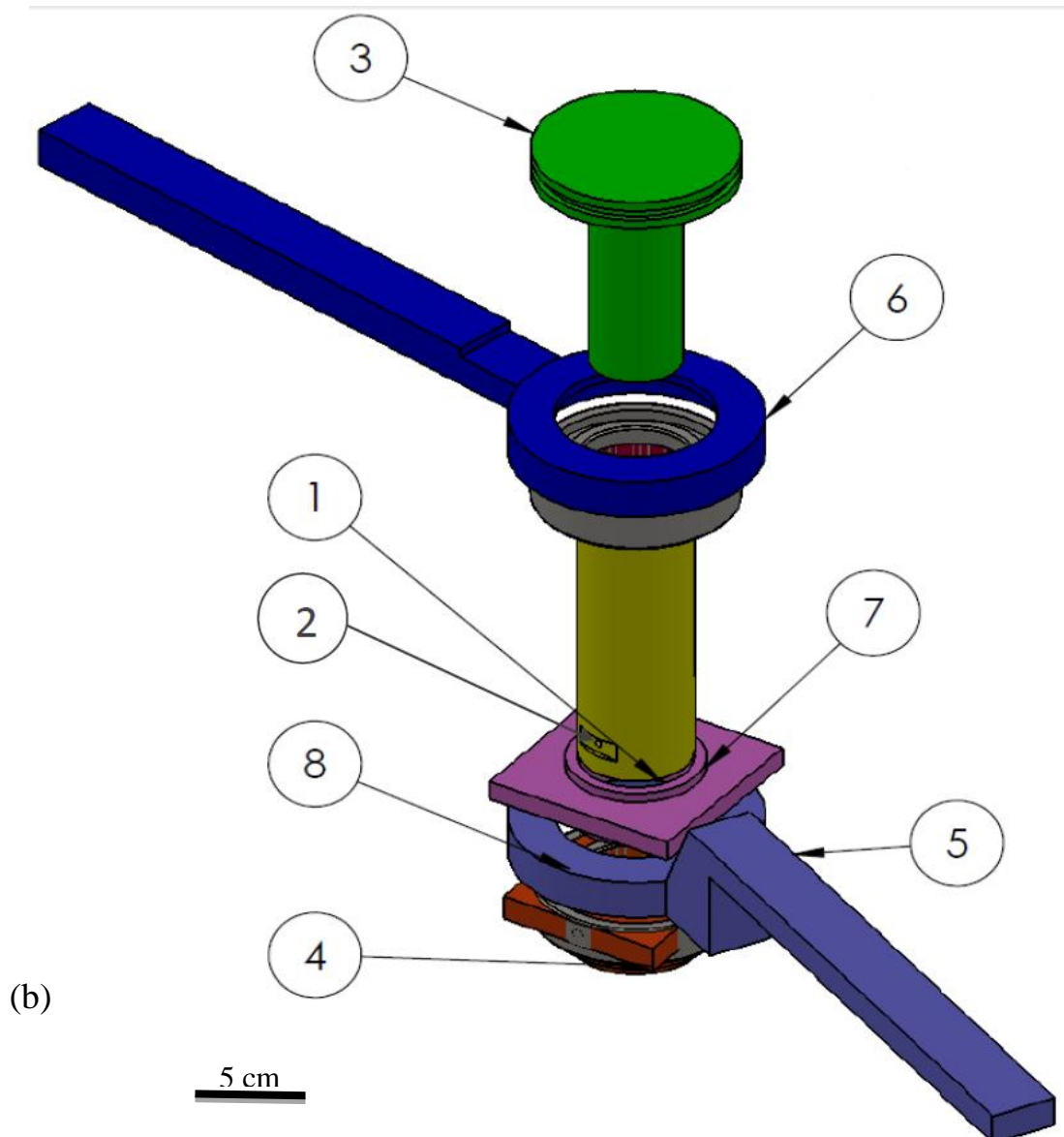
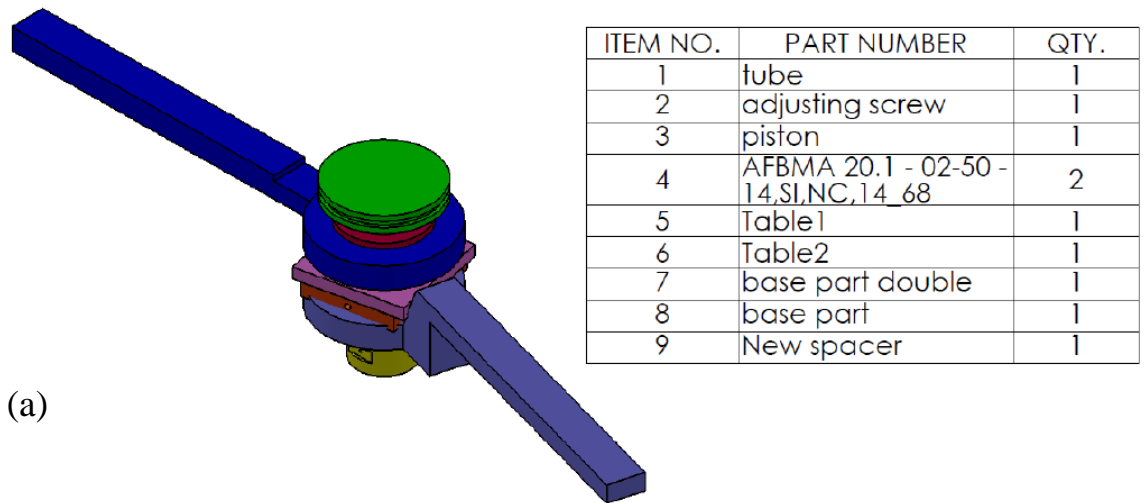


Figure 4.9:(a) Together and (b) Separated 3D schematic of the designed system (1) Main tube, (2) adjustable screw, (3) holding pin for the structure, (4) a cap for the pin, (5) an arm created for the detector, (6) an arm created for the laser, (7) holding plate for the arm and mechanical spacer (8) second holding place for the arm and mechanical spacer.

The laser is positioned to face one side of the glass prism (Fig. 4.7a), and the detector to the other, to enable the measurement of the SPR angle for a liquid, or gas, sample. The laser passes through a polarised lens and a beam splitter (Fig. 4.7b) before and after the sample, this is done to minimise interference from external sources. The system is controlled and data acquisition is done by National Instruments LabVIEW, this will be explained further in Section 4.5. The glass prism is mounted onto the micro Bench using a 4-spring based tightening mechanism, (Fig. 4.10).



Figure 4.10: The 4-spring based tightening mechanism used to secure the prism, thin-layered system and the micro-fluid channel, 3D design of the base of the mechanism.

4.4.2 Experimental design of the SPR system

During this study, the structure of an instrumental platform for Surface Plasmon Resonance (SPR) system was designed followed by its construction. The structure was based on the Kretschmann configuration which uses an evanescent field for optical excitation of the surface plasmon waves. The SPR sensing platform was constructed on an optical bench and using standard mechanical parts and mounts (optical micro-benches). The schematic diagram of the system is shown in Fig. 4.11.

Optical components, a rotational translation stage for controlling angle of incidence and reflectance of the laser beam have been shown in Fig. 4.11. The laser light source passes through a polariser; allowing just p-polarised light through, the same at the detector end

also which was used to minimise external interferences. The plasmonic layers were fabricated using PVD techniques discussed in Section 4.2. Data acquisition software was written using National Instrument (NI) LabVIEW which is also used to run, control, operate and drive the entire system. In addition to this, various sample compartments and a flow cell were made to facilitate measurements under controlled flow or in a conned liquid volume.

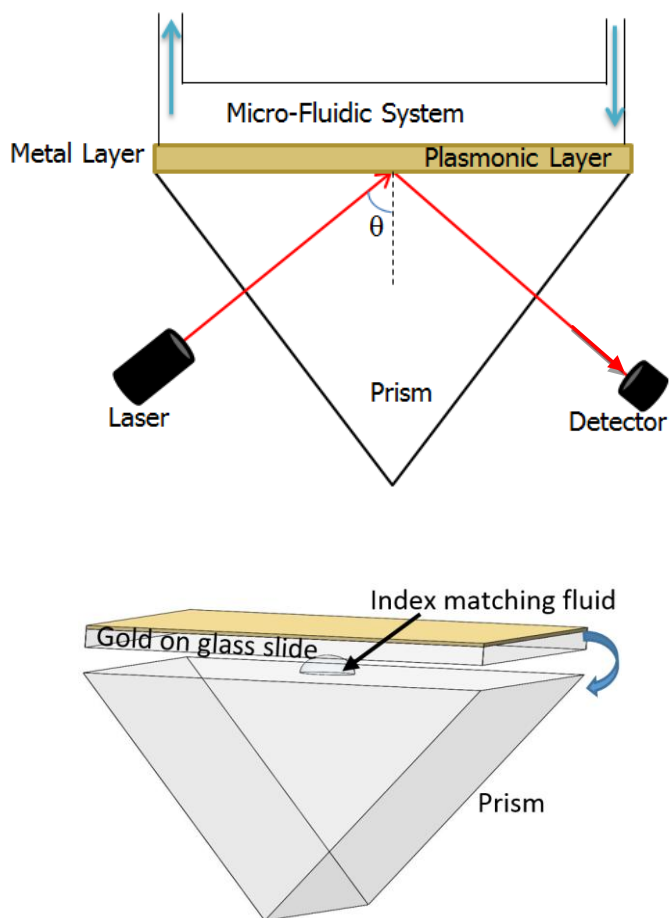


Figure 4.11: Configuration of Prism / Substrate for SPR, the optical properties of the equilateral prism to the glass slide is achieved by using index matching oil and the schematic diagram of the Surface Plasmon Resonance system, showing the incident direction of light from laser at angle (θ) which is collected by the detector. The micro-fluidic flow is shown by blue arrows with the interfacial plasmonic layers between the prism and the sample.

This system is generic and can be adapted for various conditions encountered in bio-sensing applications, however, the work conducted in this thesis was designed for laboratory use only. A right angle glass (Schott BK7) prism (Edmund Scientific)

(15 × 15 × 15 mm) was used throughout this work, where the real part refractive index (n) of the prism was 1.51. BK7 is a widely used material for glass substrates which is the reason for selecting the BK7 prism as the refractive index at the interface needs to be equal to avoid reflection/refraction. As shown in Figure 4.11, the glass slide with the gold film on is optically matched to the prism through index matching oil (Cargille Laboratories, 1.519 RIU at 559 nm).

4.4.3 Fluidics

There are some essential characteristics of the flow system that need to be considered when designing for a bio-molecular Interaction Analysis (BIA) system. The overall volume of the liquid handling system should be minimum to reduce the amount of sample consumed. Another consideration in this type of application is that the substance should be fed in and extracted at the same rate. Therefore, the measurement area of the sample compartment must be kept at minimum. Structure of the cuvette and flow system which has been used in this project is shown in Fig. 4.12.

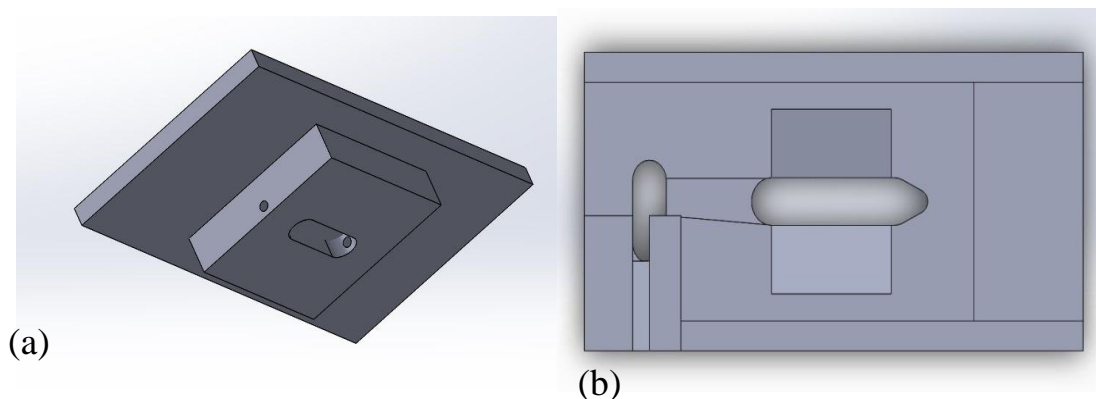


Figure 4.12: The design of the micro-fluid channel. (a) side view to show the points where the samples can be pumped in and out of the reservoir, (b) top view showing the construction of the reservoir.



Figure 4.13: The tubing pump REGLO Analog is with 4 tube channels and 8 pump rollers (Speed 2.0 –100 rpm).

The micro-fluid channel (Fig. 4.12) was designed to be used with a one-channel liquid pump (Fig. 4.13). This enables liquid samples to be pumped into the system, creating the metal-dielectric interface needed for SPR. The pumping system had been implemented to enable removal of the liquid sample and cleaning of the metallic surface with Deionised water.

The diameter and depth of the flow cell were 1 mm and 1 mm respectively. The thin layered system, consisting of Cr, Ag, Au and G layers, is sandwiched between the prism and the micro-fluidic channel using applied pressure. Plastic tubing with 1 mm diameter was used to add liquid to the micro-fluidic chamber. This tubing was attached to the treaded fittings on end of the flow cell. In all experiments, the liquid samples were added to the flow cell using a pump (REGLO Analog Pump, Fig. 4.13) which has a range of pump speeds from 0.003 – 35 mL/min.

Flow for the analogue version is controlled by setting the pump speed (RPM). Speed is adjustable from 2 – 99 % in 1 % steps via a 2-digit potentiometer. Analog input and output controls via contact closure include: speed control (0 - 5 or 0 - 10 V; 0 - 20 or 4 – 20 mA), speed output (4-channel: 0-5 kHz), start/stop and rotation direction. The combination of pump speed (RPM) and the ID of the selected tubing determines actual flow rate per channel.

4.4.4. Electrical and Control

The electrical design of the system plays an important role in the collection of data and control of the system. At the core of the system LabVIEW is used. The system requires control of the inputs and outputs and data acquisition is also used to allow for data logging and mathematical manipulation of the results in real time. In this section we shall describe the construction of the electronics and overall control design used to run and acquire data from the system. This includes an in-depth description of the closed loop feedback system used to maximise the accuracy of the measurements.

Fig. 4.14 demonstrates the control system used: The potentiometers are linear with a range from 1 k Ω to 1 M Ω (Tolerance \pm 20%), over a 300 $^\circ$ aperture. The motors are 12 V DC geared servo motors which provide a maximum torque of 0.33 N.cm and a maximum speed of 300 RPM. The source is a single crystal silicon based laser (Laser 2000 PM-655-5) arranged in a Fabry-Pèrot configuration. The laser provides a continuous wave output (0 - 35 mW) at a wavelength (λ) of 664 nm. The detector used is a silicon photodiode (Hamamatsu S1336-44BK); at 664 nm, the photo-diode produces photosensitivity of 0.35 A/W. The photo-diode chosen provides a large active region of 3.2 mm 2 that has a low noise coefficient of 1×10^{-14} (W/ $\sqrt{\text{Hz}}$). Hence, we are able to use the raw amplified data directly from the detector without any filtering.

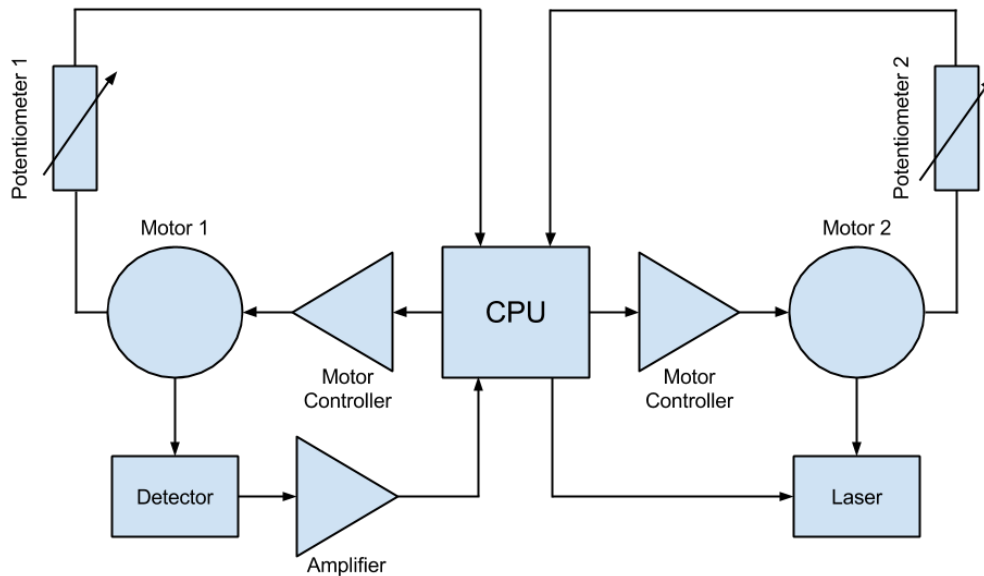


Figure 4.14: The control system for the system, triangular block corresponds to an amplification of a signal, the circular shapes represent the motors and the rectangles correspond to other key components of the system. The central processing unit is controlling the system using LabVIEW software.

It can be seen in Fig. 4.14 that the CPU is at the core of the system. The CPU is running LabVIEW which logs the data from the detector and the potentiometers, whilst controlling the motors and laser. The system requires the laser to be moved around a range of angles, in relation to the surface of the sample. To achieve this, the accuracy of the measured angle is paramount; hence, a closed feedback loop is used with Proportional-Integral-Derivative controller (PID controller).

The CPU controls the speed and duration of the motors. The motors control the movement of the detector and laser with the use of the threaded rod specified in Section 4.4.1. The elbow joints, also described in Section 4.4.1, are connected to the potentiometers; as the laser, or detector, move the potentiometer changes resistance. The raw data from the detector is fed through an amplifier back into the CPU for data logging and analysis of the results.

The positions of both the laser and the photo-detector are calibrated by finding the maximum reflection intensity. After calibration they are synchronously moved together;

using the potentiometers for positional feedback. The change in resistance of the potentiometer will be equivalent for both the laser and detector motors. The accuracy of the angle measurements is determined by the potentiometers.

$$\text{Accuracy of Measurement} = \frac{\theta_a R_{\text{Res}}}{(R_{\text{Max}} - R_{\text{Min}})T} \quad (4.4)$$

Eq. 4.4 shows how we calculated the accuracy of measured angle ($^{\circ}/s$) using the potentiometers, where θ_a is the total aperture (300°). R_{Min} and R_{Max} are the minimum and maximum resistances ($1 \text{ k}\Omega$ and $1 \text{ M}\Omega$ respectfully). R_{Res} is the resolution of the device used to measure the resistance of the potentiometers and finally T is the sample period of the measurements. Using this we obtained an accuracy of approximately $0.02 \text{ }^{\circ}/s$.

The motor utilises Pulse-Width Modulation (PWM) to control the speed with a maximum of 300 RPM at 100 % using PWM it is possible to control the motors with a better accuracy. For example, if a duty cycle of 0.1 is used, then the overall speed will be approximately 30 RPM. This would correlate to a movement speed equivalent to $180 \text{ }^{\circ}/s$. It uses an internal gearbox to reduce the speed of the motor which allows for better accuracy in the movements.

The raw information from the detector is amplified and collected through the use of data acquisition methods in LabVIEW; it is important to note that the signal from the detector is not filtered or altered in another way. LabVIEW collects the data from the detector after amplification and exports it into a data file to be used for mathematical manipulation and data representation later on. This shall be discussed at the same time as the LabVIEW control system in Section 4.5.3.

4.5 Software

As described in Section 4.4.4, the experimental setup consists of 2 DC motors, angular feedback from potentiometers, (device for phase and intensity and phase angle and intensity is read from SPR7280 device), a laser and a photodiode. This section describes the software that has been developed, using LabVIEW. LabVIEW uses a GBIB interface and PCIe (NI) card for data acquisition and motor control shown in Section 4.5.2. We have created a User Interface (UI), which is used for controlling the motors and providing a front end for the overall system control and data manipulation. The software also runs a simulation of the model (discussed in Section 3.3) alongside the experiment, so that results can be directly compared.

4.5.1 Architecture and Design of LabVIEW System

The software is required to be event driven and respond to user input in real-time, hence state machine architecture has been chosen, shown in Fig. 4.15. The pre-initialisation state (Pre-init in Fig. 4.15) makes all of the control variables changeable by the user. When the experiment is running, the user can no longer edit these variables; this ensures that both the simulation and the experiment can run uninterrupted and avoid corruption of data.

The initialisation state (init in Fig. 4.15) collects the user inputs, and will continue to collect the information until 'run' has been selected. When 'run' is selected the program will move onto the next state. The post-initialisation state (Post-init in Fig. 4.16) uses the information provided by the user to enable and disable variables dependent on the controls needed while the simulation, or experiment, is running.

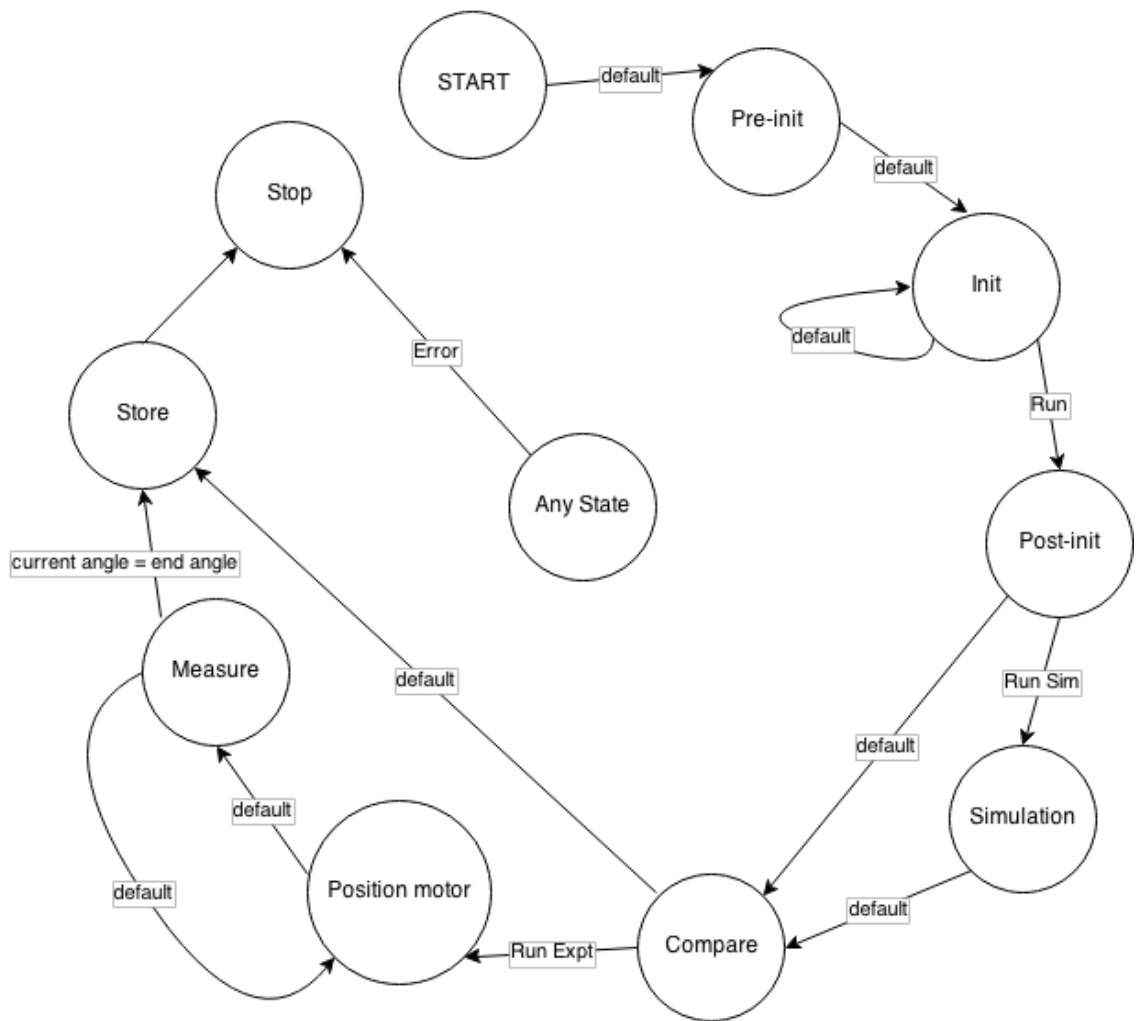


Figure 4.15: State machine diagram for program flow, the circles represent different states for the system and the arrows show the flow of the program with the conditions that should be met.

If the user has selected to run a simulation, then the program will move to the simulation state (Fig. 4.15). In this state the user parameters will be used and the simulation will be run for a range of angles and resolution previously specified in the (pre-init or init state). If the results from the simulation or if a simulation is not run, then the information from the post-init state are passed onto the compare node (Fig. 4.15). This node loads data from previous simulations, or experiments and plots it onto a graph with the live data collected from the experiment, or the data passed from the simulation.

The position motor state (Fig. 4.15) controls the movement of the motors. The current system design uses the data from the potentiometers to create a Proportional-Integral-Derivative (PID) controller system. However, this will be replaced with (absolute

encoders). At each position where a measurement needs to be taken, the data acquisition state is reached (measure in Fig. 4.15). At this point the Attenuated Total Reflection (ATR) is measured with respect to the current angle. Furthermore, the phase angle and intensity of the laser is measured by the SPR7280 device and the data is acquired by the software also. This information is plotted onto a graph which shows the ATR with respect to the angle after the data has been collected.

Once the scan has been complete and the final position of the motors is such that satisfies the final angle required then the data collected is stored into a log file. The log file has the file extension .txt and is tab delimited which can be opened with most standard software packages (Microsoft Excel, Matlab etc.). This is the function of the store node (Fig. 4.15) which also stored an image of the graph plotted during the experiment, or simulation. The user creates a working directory, after this has been done folder and file, names are generated automatically based on the materials being tested. A new log file is generated every time the simulation, or experiment, is executed. After this has completed the program moves to the stop state (Fig. 4.15), where all the data acquired is released, it closes all references and then displays any errors occurred during the execution of the program. This is before terminating the program safely.

4.5.2 Software Implementation - User Interface

The User Interface (UI) for the system is the main control interface; this is controlled in the background by LabVIEW software which will be explained below. This section focuses on the UI and the functionality of the program from a top level. The entire UI can be seen in Fig. 4.16.

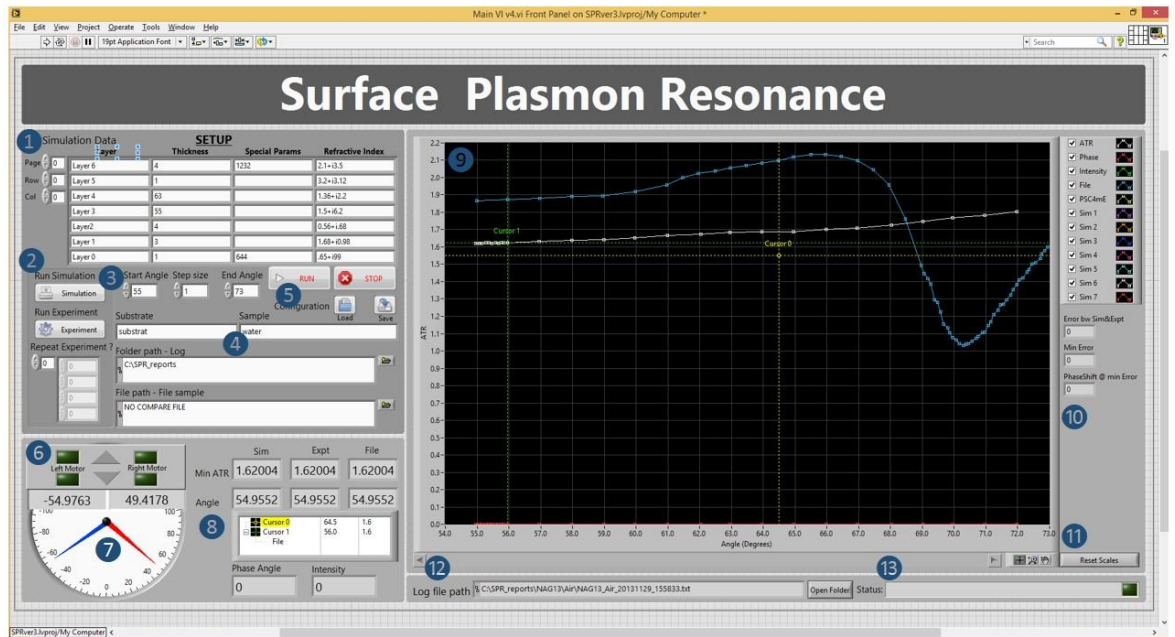


Figure 4.16: The User Interface (UI) panel for running the software: (1) simulation data, (2) run simulation and run experiment buttons, (3) angle range, (4) substrate and sample information input, (5) run button for, (6) visual indicators for motor direction, (7) current position of laser and photodiode, (8) most recent values, (9) graph of data, (10) error values, (11) reset button for graph, (12) output file location and (13) current status.

Fig. 4.16 (1) shows the area where the user can enter parameters for running a simulation. This would include the layer name, thickness and the wavelength of the laser (nm), Special Params and the refractive index of each material at the specified wavelength.

The buttons to run either the simulation, or an experiment can be seen in Fig. 4.16 (2), if the run simulation box is pressed, the program uses the parameters from the simulation inputs (Fig. 4.16 (1)) and then runs the simulation. If the run experiment button is pressed the program will interface with the hardware and initiate the experiment. The repeat experiment box automatically repeats the experiment after a time delay (m) which should be specified by the user.

The input for the angle range for the experiment is shown in Fig. 4.16 (3), this requires a start angle, an end angle and a step size, all proved in degrees ($^{\circ}$). At each value of this variable a data point is created either from simulation, or experimental, results. The

information, such as the substrate and sample used in the experiment, should be entered into the relevant boxes; shown in Fig. 4.16(4). This information is then used to automatically create a file name for the log file. The folder path specifies the working directory, where the output files will be stored upon completion.

Once the user has configured all of the parameters specified in Fig. 4.16 (1-4), the run button Fig. 4.16 (5) should be pressed. This then disables the control parameters and starts executing the code (Init state in Fig. 4.15). The stop button can be used to stop the experiment, or simulation at any time. The load button can load previously saved configurations for simulation, or experiment, the save button will save the parameters entered by the user.

The visual indicators Fig.4.16 (6) are used to determine the direction of travel of the motors when an experiment is being conducted. Below these indicators there is a graph (Fig. 4.16 (7)) that visualises data of the motor positions. This is only valid if the experiment switch has been pressed (true), this will not change if you are only running a simulation.

Fig. 4.16 (8) shows a table which corresponds to the values for the position of the cursors on the graph (Fig. 4.16 (9)). The graph, along with the cursor table can be used for comparing the simulations to old experimental data. The graph displays the ATR, phase and intensity with respect to incident angle. Next to the graph there are error values (Fig. 4.16 (10)), these display the error between the simulation and experimental, the minimum error of the reflected light and then the phase shift at the minimum error. Fig. 4.16 (11) is a reset switch for the graph, it resets the zoom centres the graph and makes all points visible.

Furthermore, the file name and path is shown in a text box at the bottom of the window (Fig. 4.16 (12)). There is also a status bar Fig. 4.16 (13), which keeps updating while

the program is executing with the current status, this is also useful for troubleshooting and understanding what is happening within the system.

4.5.3 Software Implementation - LabVIEW

In this section we shall look at the LabVIEW block diagram of the program (Fig. 4.17).

This is the highest level you can obtain through programming with ready programmed blocks that you can just drag and drop to build a working program. This is advantageous for detailed and complex programming requirements. We shall now breakdown the system into its core parts as specified by the numbers in Fig. 4.17.

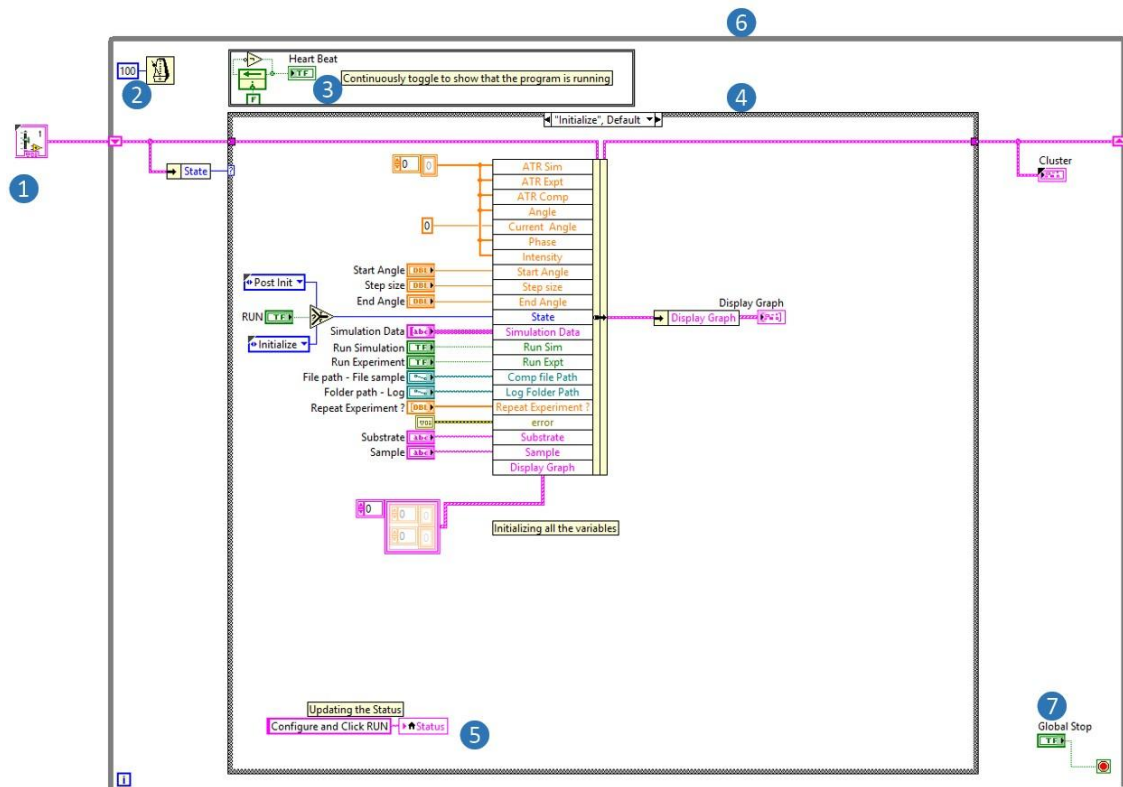


Figure 4.17: The block overview of the LabVIEW program. (1) Initialisation cluster, (2) delay block, (3) system heart-beat, (4) case structure, (5) status update, (6) while loop box and (7) global stop button.

Fig. 4.17 (1) shows the initiation cluster; this contains all of the parameters that will be used within the program. This cluster is used to group all the variables into a single block which makes the program easier to read. There are two main loops with a timer

(Fig. 4.17 (2)) providing a delay between each loop iteration. The number specified in the timer relates to a time in milliseconds (ms).

To ensure that the programming is running and has not crashed or halted, a heartbeat signal within an infinite loop is used (Fig. 4.17 (3)). The status of this heartbeat signal is output onto the UI in the form of a flashing visual indicator next to the status bar in Fig. 4.16 (13).

Fig. 4.17 (4) shows the case structure, this consists of different cases (assumedly based on one or two of the initial parameters fed in), each case corresponds to a different state of the state machine diagram shown in Fig 4.15. Fig. 4.17 only demonstrates the case for the initialisation state. Now the same needs to be done for each other case, as well as explanation of what is happening in each of the cases maybe, such as mathematical manipulation and control parameters. It just seems pointless to go into this much depth with the UI and not the actual program, also show what is inside the parameters box.

The status box (Fig. 4.17 (5)) updates itself for every change of state; as shown in Fig. 4.15. This information is then output onto the user interface (Fig. 4.16 (13)). The whole program structure is encased into a continuous while loop (Fig. 4.17 (6)), this will only exit if the loop is broken from inside. There is also a global stop (Fig. 4.17 (7)) button for the program; as specified in Fig. 4.16 (5). This button will safely interrupt the program, before releasing all the acquired resources.

4.5.4 Software Implementation - Log Files

As we mentioned earlier in this section, the program generates a log file which is saved using a name generator based on the substrate and sample. In this section we shall look

at how the file names are generated for the data and graph files and how the parameter data is presented in the log file.

Once the working directory is chosen by the user; the log files and graphs, are stored in folders starting with the substrate name, then the sample name, followed by an experimental, or simulation, folder and a final folder named 'log files'. All data file outputs are in '.txt' (ASCII) format, where all the data stored in the files is two dimensional, and stored as blocks of characters separated with a tab spacing. When opened as a '.txt' file, the blocks of characters are treated as strings.

The file name for both the parameters and graphs are generated by using the following information:

- Experimental or Simulation
- Substrate Name
- Sample Name
- Date (YYYYMMDD)
- Time (HHMMSS)
- .txt/.jpg

The file name takes the form Exp Substrate Sample Date Time.txt), where the Exp represents experimental and will change to Sim if it is for simulation data. The file extension will also change from the graph to the data log file. Therefore, the data and the corresponding graph will have the same name, apart from the file extension that will change from '.txt' to '.jpg'.

Every experimental, or simulation, log file will not overwrite previous log files, as its name will be unique. This is because of the file name containing the data and time of the acquirement of the data, hence, extra care must be taken to ensure that the system time and date does not change.

The log files are built using a 2 dimensional data system; each row in the file represents a different set of parameter values and each of the 14 columns represent a different parameter:

1. Time (seconds with millisecond resolution)
2. Angle
3. ATR simulation value
4. ATR experimental value
5. ATR file path (for comparison)
6. ATR difference ($|\text{Simulation} - \text{Experiment}|$)
7. Phase shift (at the minimum error value)
8. Minimum error value (after phase shift)
9. Phase
10. Intensity
11. Angle at minimum ATR (Simulation)
12. Minimum ATR value (Simulation)
13. Angle at minimum ATR (Experimental)
14. Minimum ATR value (Experimental)

4.6 Summary

In this chapter we discussed the experimental techniques used throughout this work including PVD techniques (Section 4.2), device fabrication and photolithography (Section 4.3). Then we showed the development of the experimental set up, including the Electrical and Mechanical design (Section 4.4) and then the data acquisition and software (Section 4.5). In the next chapter we look at the optimisation of the sensing system to find the optimum set-up for maximum sensitivity.

CHAPTER 5

5.1 Development and Optimisation of SPR Bio-Sensing System.

In Chapter 3 we discussed the development and use of a model that predicts the Attenuated Total Reflection (ATR) for a system of thin films on a prism which is based on the Kretschmann configuration, discussed in Chapter 2. Chapter 4 showed the experimental techniques and the system design for the real-time measurement of such a system. In this chapter we look at the development of the sensing sample and the optimisation of the materials system used. In order to achieve maximum resolution, based on the change in resonant angle with change in refractive index and also highest sensitivity (lowest error) which is based on the Full-Width Half Maxima (FWHM) of the resonant peak, a carefully designed materials system needs to be realised.

The two most important parameters are the Full-Width Half Maxima (FWHM) of the SPR peak which describes the resolution of the sensing system (Verma *et al.*, 2011) and the sensitivity of the system which is based on the shift in resonant angle over a change in refractive index (Maharana *et al.*, 2014). The idealistic sensing system will have a very small FWHM and large changes of the resonant angle with change of the refractive index. To achieve this, a meticulous design of the plasmonic layers needs to be realised.

Fig. 5.1 shows a multi-layered system for controlling the response of the SPR. Careful selection of the materials used in this part of the system will ensure that

we can achieve maximum performance. In this chapter we will describe the route that we took to experimentally and theoretically build an optimum sensing system with the specific application of sensing Ag NPs in mind.

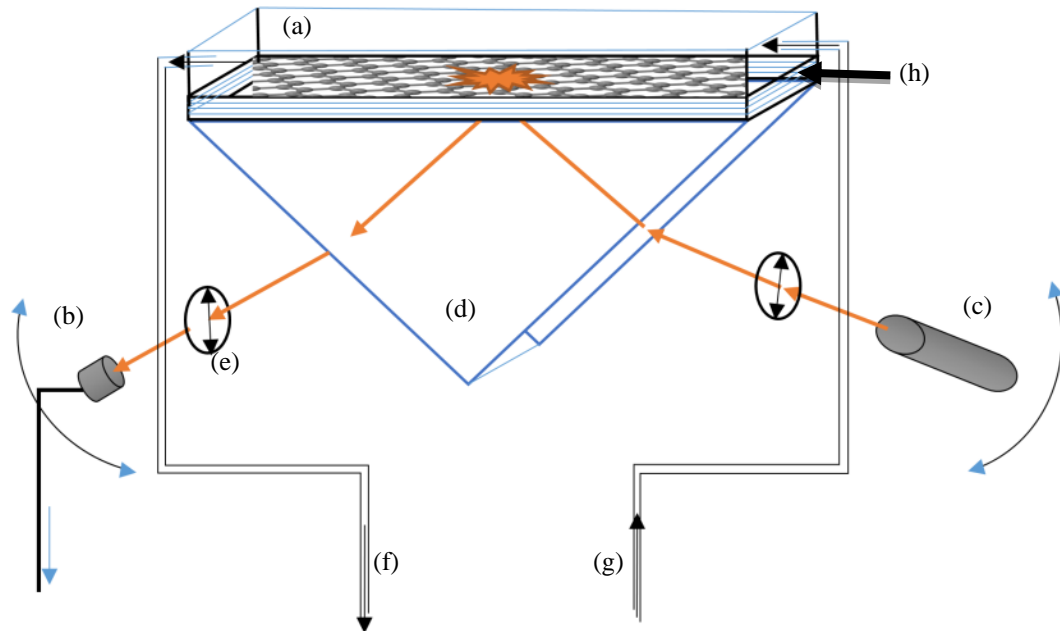


Figure 5.1: Surface Plasmon Resonance (SPR) system with sensing cell (a) is the microfluidic chamber with pipe inlets and outlets, (b) is the photodetector, (c) is the laser diode ($\lambda = 664 \text{ nm}$), (d) shows the prism, (e) is the polarizer, (f) is input, (g) is output and (h) is the multilayers plasmonic tunability.

Section 5.2. will give an introduction into commonly used materials and their advantages and disadvantages within this sensing arrangement shown in Fig. 5.1.

Then we will look at the uses of graphene and how it can be used to increase the performance of the sensing system, leading onto some deposition techniques for monolayer and multi-layered graphene. Section 5.3. will describe the steps taken to optimise the system in terms of different materials used, different layer thicknesses, followed by the optimisation of the number of Graphene layers (Section 5.5.). Finally, we will show the optimum design and discuss the sensitivity and resolution of the system and where the limitations are. Chapter 6 will then give an in-depth study of the detection of Ag nanoparticles (NPs) in

water and other complex solutes, such as silver nitrate (AgNO_3), using the optimised sensing system.

5.2 Literature and Theory

5.2.1 Commonly used material systems

The SPR based sensor systems require an active plasmonic layer, such as Gold (Au) or Silver (Ag), to enable the Plasmon Resonance. Au and Ag are the most commonly used materials due to their Surface Plasmon Resonances appearing within the visible spectra (Maier, 2007). Au has a much broader plasmon response compared with Ag, which suggests that Ag would give a higher resolution Surface Plasmon Resonance (SPR) response compared with Au. However, studies have shown that Ag is not chemically stable and this is the reason why Au is the preferred material for SPR bio-sensors (Maalouli *et al.*, 2011, Szunerits *et al.*, 2008). Au is usually the preferred material for such systems, owing to its stable chemical and optical characteristics. However, Au films have not proved to be efficient in developing highly sensitive SPR sensors, whereas Ag films appear to be the most suitable candidate since plasmon coupling demonstrates sharper angular resonance as compared to Au thereby improving the sensitivity of the sensor (Choi and Byun, 2010).

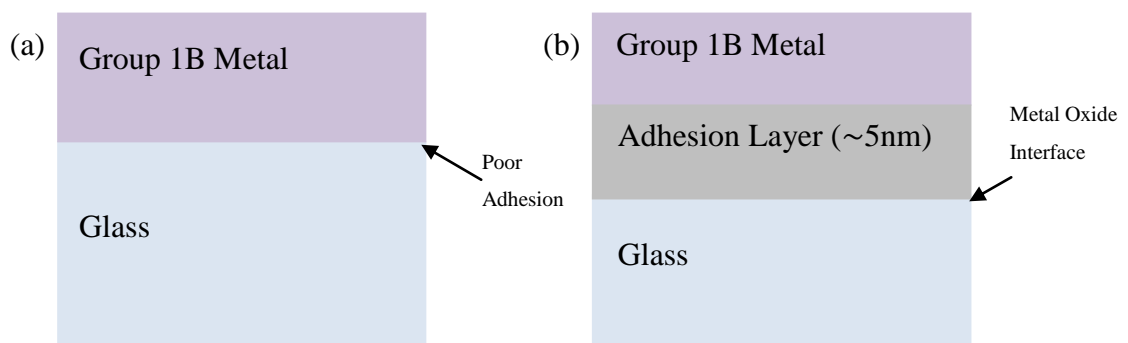


Figure 5.2: (a) Group 1B metals interface to glass, where the poor adhesion occurs. (b) Adhesion layer is introduced between the metal and glass, usually Ti or Cr ($\sim 5\text{nm}$) which allows for much better adhesion of metal layer to glass with minimal effect on the optical properties of the metal.

Another well-known problem with plasmonic materials such as Au and Ag is the adhesion to glass. It is well known that group 1B metals (Copper (Cu), Ag and Au) do not have strong adhesive properties to dielectric materials such as silicon dioxide (SiO₂) (Benjamin and Weaver, 1961, Vogt *et al.*, 1994, Hoogvliet and Van Bennekom, 2001). This means that these metals have poor adhesion to glass substrates (Fig. 5.2a) which is due to group 1B metals not having a high affinity for oxygen (Benjamin and Weaver, 1961). The hydroxyl groups which develop on the surface of the glass, require an oxide bond to form strong adhesion, hence, it is necessary to consider a thin (~2 to 5 nm) adhesive layer (Fig. 5.2b) such as Chromium (Cr) or Titanium (Ti) which have been shown to form covalent oxide bonds at the surface with the hydroxyl groups causing much stronger adhesion (Hoogvliet and Van Bennekom, 2001, Benjamin and Weaver, 1961). The most commonly used transition metals for adhesion are Cr and Ti due to the stable oxides that they can form at the boundary (Hoogvliet and Van Bennekom, 2001). However, Ti has been shown to diffuse along the grain boundary quickly and it quickly oxidises at the surface of the gold (Vogt *et al.*, 1994) making Cr the logical choice.

Limitations in the sensitivity of SPR biosensors utilising Au have been reached which is why there has been a significant effort to improve SPR based bio-sensors by using Ag (Maalouli *et al.*, 2011, Szunerits *et al.*, 2008, Lockett *et al.*, 2008, Salihoglu *et al.*, 2012). However, Ag oxidises over time which changes the optical and chemical properties of the material which decreases the sensitivity over time (Salah *et al.*, 2012). Hence, a solution is required to stop the oxidation process and improve the chemical stability of Ag films.

Maalouli et al. (Maalouli *et al.*, 2011) used a 5nm hydrogenated amorphous silicon carbide (α -SiC:H) capping layer on top of the silver plasmonic layer which protects the silver layer from oxidising and at the same time increasing the sensitivity of the system. Other groups (Salihoglu *et al.*, 2012, Szunerits *et al.*, 2008) have used other metal oxides, such as Tin Oxide (SnO₂) and Indium Tin Oxide (ITO) (5-10 nm), to cap the Ag films which have also shown improvements in the sensitivity. Lockett et al. (Lockett *et al.*, 2008) used a similar technique to Maalouli's (Maalouli *et al.*, 2011), where they used a thin amorphous carbon (α -C) layer. In this chapter I will discuss the use of a thin layer (\sim 5 nm) of Au on top of silver which can give improvements in the sensitivity as you would expect when using Ag, but also keeping some of the advantageous properties of Au (Section 5.3) (Salah *et al.*, 2012).

Another method to address the stability of Ag and the sensitivity of the system, is to introduce mono-layered or few-layered graphene (Choi and Byun, 2010, Song *et al.*, 2010, Kravets *et al.*, 2013, Verma *et al.*, 2011). The issue of sensitivity is addressed by adding a graphene layer to the SPR sensor. Graphene has been shown theoretically (Salah *et al.*, 2014) to improve the sensitivity of the SPR sensor response. One to a few layers of graphene on top of the protective gold film changes the SPR response significantly (Salah *et al.*, 2014).

5.2.2 Properties of Graphene in SPR applications

Graphene, since its discovery in 2004 (Novoselov *et al.*, 2004), has gained significant research interest due to its optical, electrical and mechanical properties (Charlier *et al.*, 2008). Graphene can be described as a two dimensional, one atom thick, layer of sp² hybridised carbon which naturally forms a honeycomb lattice

structure (Geim and Novoselov, 2007). The aromatic nature of graphene (Popov *et al.*, 2012) allows for π - π^* stacking with biomolecules making it a strong binding site for biomolecules, making it a good choice for real-time reaction-based bio-sensing systems, such as the well-known Biotin-Streptavidin reaction (Fig. 5.3) (Song *et al.*, 2010). Graphene-based SPR sensors offers many improvements to other common arrangements.

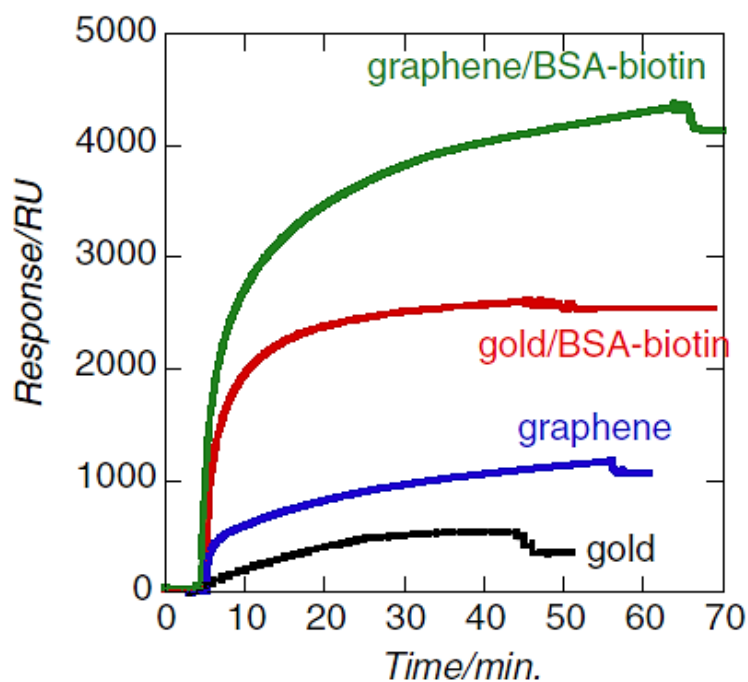


Figure 5.3: Biotin-Streptavidin time dependant reaction analysis for different material systems; Graphene with no biotin (blue) , Gold with no biotin (black), gold and biotin (red) and graphene and biotin (green). The graph demonstrated the SPR response over time for the different material systems (Salihoglu *et al.*, 2012).

One of the main improvements is the enhancement in the adsorption potential of organic molecules due to the strong π - π^* stacking. The addition of graphene provides a protective surface for the plasmonic layer, as it significantly reduces oxidation of the metallic surfaces (Chen *et al.*, 2011). However, it also suppresses the SPR slightly having adverse effects on the sensor response (Salihoglu *et al.*, 2012).

One of the most important parameters that concerns the use of Graphene in sensing applications is the complex refractive index which determines the optical response and changes in the SPR conditions according to the number of layers of graphene (L). The complex refractive index, according to Wu *et al.* (Wu *et al.*, 2010) and later by Szunerits *et al.* (Szunerits *et al.*, 2013), can be found using Eq. 5.1, where $C_g = 5.446 \mu m^{-1}$ is given by the opacity measurements made by Nair *et al.* (Nair *et al.*, 2008), λ_0 is the wavelength of interest and must be given in μm for the units to balance.

$$\tilde{n} = n + ik = 3 + i \frac{C_g}{3} \lambda_0 \quad (5.1)$$

Another parameter that is needed for the simulations is the thickness of the graphene layers which is given by $d = L \times 0.34 \text{ nm}$ (Wu *et al.*, 2010). The percentage absorption per layer can also be estimated using the fine structure constant (α), where the opacity is given as $(1 - T) = \pi\alpha$. $\pi\alpha$ is given in Eq. 5.2 (Nair *et al.*, 2008), where e is the electron charge, \hbar is planks constant divided by 2π and c is the speed of light.

$$\pi\alpha = \frac{\pi e^2}{\hbar c} \approx 2.3\% \quad (5.2)$$

This is in agreement with experimentally obtained results by Salihoalu *et al.* (Salihoglu *et al.*, 2012) shown in Fig. 5.4b. They found that Graphene on quartz showed a linear drop of approximately 2% per layers of graphene over the visible region.

Salihoalu *et al.* (Salihoglu *et al.*, 2012) also used Graphene in bio-sensing applications, first they used a transfer technique using a PolyDiMethylSiloxane (PDMA) mould which will be explained in Section 5.2.3. The Graphene was

grown using Chemical Vapour Deposition (CVD) using Cu as a catalyst. They then used a PMMA mould to transfer the Graphene from the Cu to the Au or Ag.

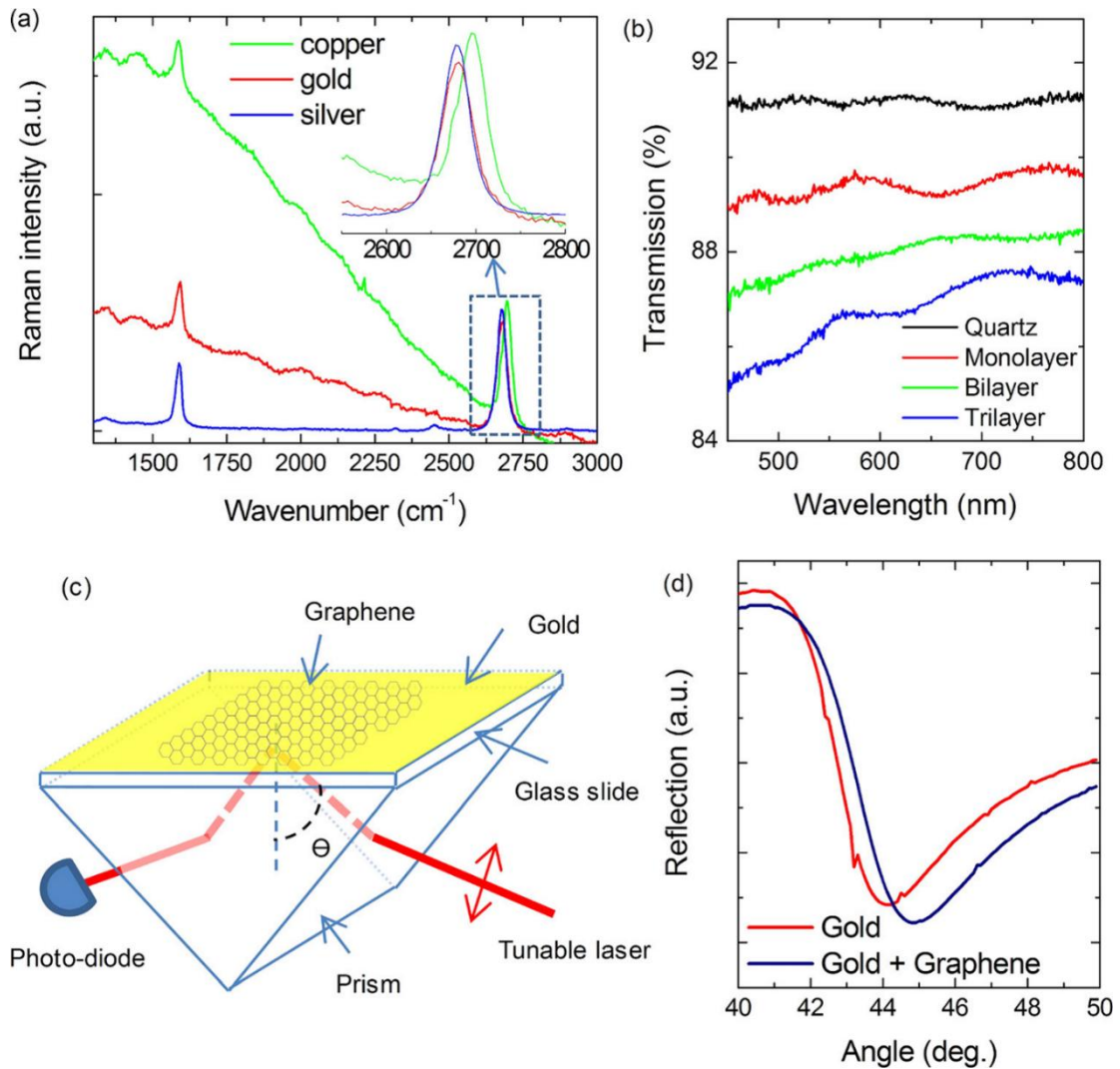


Figure 5.4: (a) Raman spectra for single layer graphene on Cu, Au and Ag, showing clearly a strong G-band and no D-band indicating high quality graphene, the 2D-band for Au and Ag is slightly red shifted from the Cu. (b) Optical transmission of Quartz and monolayer, bilayer and trilayer Graphene, showing a drop in intensity of approximately 2% per additional layer. (c) Diagram of the SPR sensor set-up; Kretschmann prism configuration using Au with Graphene transferred on-top. where the laser wavelength is 632 nm. (d) Changes in the SPR, shown as reflection, between standard Au sensor and Au with Graphene, showing 1° shift with the addition of graphene and broadening features of the FWHM. Image: (Salihoglu *et al.*, 2012).

Fig. 5.4a shows the Raman spectra for Graphene on each of the different materials showing a slight red shift occurring, which they discussed, could be due to the transfer technique. Also they note that the Graphene is of high quality, stating that there is no defect peak (D-band) in the Raman spectra for any of the samples, only

the G-band and 2D-bands are visible. Fig. 5.4c shows their arrangement for the experiment, having a tuneable laser and photo-diode for measurement of the ATR in angle interrogation mode. Fig. 5.4d shows a comparison between plane Au and Au with graphene showing a 1° shift in the resonance minima and also they showed that by introducing Graphene the FWHM of the peak widens which in turn lowers the sensitivity of the system.

Due to a large research effort made in the deposition of Graphene, the use of graphene for SPR bio-sensor applications is becoming feasible. This also leads to being able to coat suitable surfaces with a specific number of Graphene layers in a controlled manner (Verma *et al.*, 2011). Graphene has been shown to improve the sensitivity and response of different photonic-based sensing systems (Kravets *et al.*, 2013, Choi and Byun, 2010, Vasic *et al.*, 2013, Szunerits *et al.*, 2013, Echtermeyer *et al.*, 2011, Grigorenko *et al.*, 2012), whilst also making it possible to use chemically unstable materials such as Ag to realise high performance SPR bio-sensors. We will now look at the method used to deposit Graphene layers onto Ag and Au using CVD and transfer techniques.

5.2.3 Deposition of Graphene on Ag and Au samples.

Depositing the metallic layers on glass is a well refined process, throughout this work we have used the physical vapour deposition technique (Section 4.2) to deposit the metallic layers on the borosilicate glass (BK7) substrate. However, depositing Graphene, whilst controlling the number of layers, proves to be more demanding. A transfer technique, outlined by Salihoglu *et al.* (Salihoglu *et al.*, 2012) which uses the Chemical Vapour Deposition (CVD) technique, is used for the deposition of Graphene onto Au and Ag films.

Single layer Graphene (SLG) can be grown on Cu foil by means of CVD (Bae *et al.*, 2010, Li *et al.*, 2009). In this case a 35 μm thick piece of Cu foil is first heated in a quartz chamber to approximately 1000°C for 20 minutes to reduce the oxidised surface. Carbon is adsorbed onto the surface of the Cu from a precursor gas; a mixture of Hydrogen (H_2) and Methane (CH_4). The precursor is released into the low vacuum chamber (~ 7 mBar) at a rate of 15 SCCM for a duration of 20 minutes. The carbon atoms then nucleate via grain propagation to form a SLG crystal (Bae *et al.*, 2010, Li *et al.*, 2009) (Fig. 5.5a).

Poly(Methyl-MethAcrylate) (PMMA) was used to cover the photoresist described creating a stamp which can be transferred from one substrate to another (Fig. 5.5c). The Cu substrate was etched away to leave the resulting PMMA stamp ready to transfer to the Au or Ag (Fig. 5.5d). The stamp is then positioned onto the target material before being placed in acetone to dissolve the PMMA and photoresist (Fig. 5.5e and Fig. 5.5f respectfully). Once the PMMA has finished being dissolved, the resulting Graphene sheet is bound to the Ag or Au layer, after drying, the sample is heated to 180°C for 20 minutes to flatten out any wrinkles (Pirkle *et al.*, 2011).

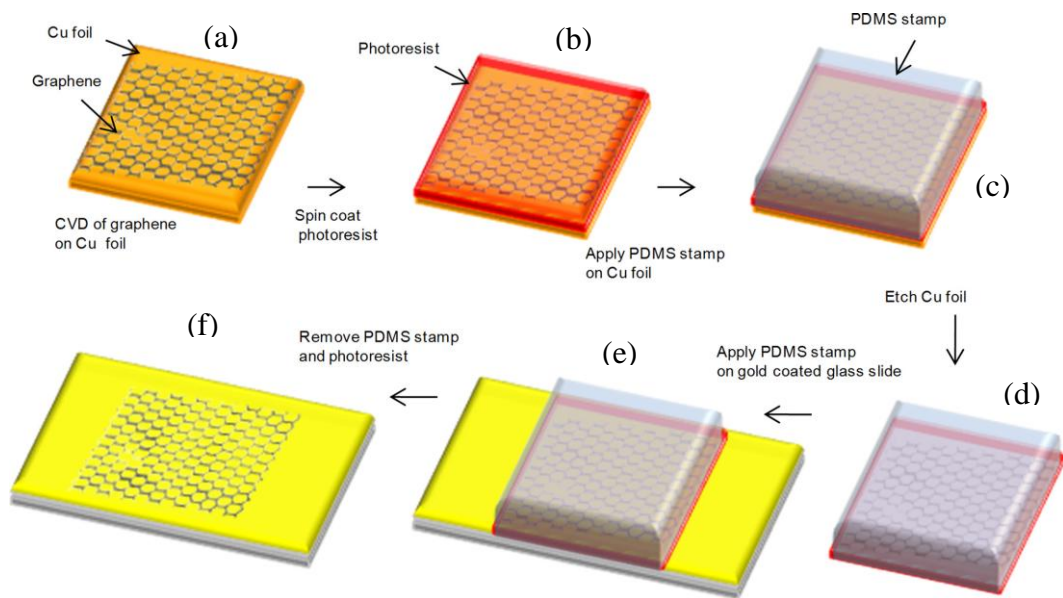


Figure 5.5: Schematic of the transfer process of SLG. (a) growth of Graphene on Cu foil, (b) coated with photoresist and then (c) PMMA (d) the Cu foil is etched away in Ferric Chloride to leave Graphene layer on underside of the PMMA and photoresist. (e) the PMMA is placed on the gold layer. (f) the PMMA and photoresist is removed leaving SLG on a Au layer. Figure: (Salihoglu *et al.*, 2012).

To check the quality of the resulting SLG film Raman spectroscopy was used for sample containing Au (Fig. 5.6a) and Ag (Fig. 5.6b) layers. The results were obtained using the Horiba Confocal Raman microscope, where a green laser ($\lambda=514$ nm) was used. Ferrari (Ferrari, 2007) has gone into great depth to analyse Raman spectra for Graphene and other forms of carbon, addressing the significance of each of the peaks and how they relate to the quality of the Graphene layer.

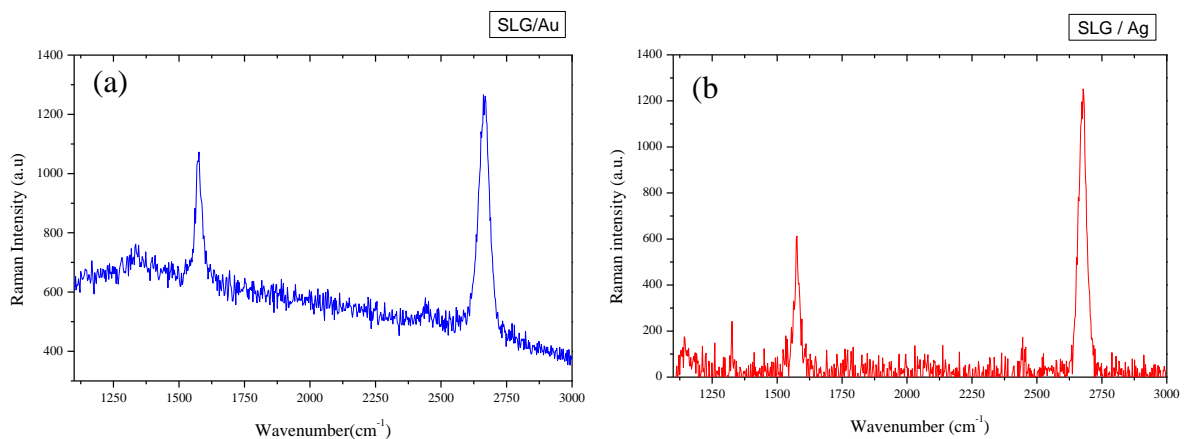


Figure 5.6: Raman spectra of (a) Au (50 nm)/SLG and (b) Ag (50 nm)/SLG samples, showing G-band at 1580 cm^{-1} and the 2D-band at approximately 2700 cm^{-1} . This was taken using a green laser ($\lambda=514$ nm).

According to Ferrari, SLG can be visibly identified using Raman spectroscopy which comes down to three distinct and unique peaks. The first the G-band which is found at 1580 cm^{-1} which is due to bond stretching of the sp^2 carbon in the hexagonal ring structure (Ferrari, 2007). The second is the 2D peak which can be observed around 2700 cm^{-1} which for pristine single layered graphene appears as a single peak with small FWHM. The third is the D-band which has been shown to be a measure of the disorder in Graphene sheets and does not appear in high quality SLG (Ferrari, 2007).

Observations were made concerning the G and 2D bands with increasing number of layers. The G peak increases in energy as the number of layers increases. The 2D peak splits into four bands, predominantly due to splitting of the electronic bands from the π - π^* stacking of the Graphene layers (Ferrari and Basko, 2013, Ferrari, 2007).

The Raman spectrum of graphene is unique and the layer characteristics are identified by the D and 2D bands of the observed Raman spectrum, one appears at $\sim 1580\text{ cm}^{-1}$ which is called the G band and the other at $\sim 2700\text{ cm}^{-1}$ which is called the 2D band. In ordered SLG sheets the intensity of the 2D band is usually around 2-4 times larger than the G band, as the number of layers increases the intensity of the G band increases and hence the ratio between the two falls.

Fig. 5.6a shows the Raman spectra for SLG on Au, where the G and 2D peaks can be clearly seen indicating that there is just a single layer of Graphene present. Fig. 5.6b shows the spectra for SLG on Ag, the intensity of the 2D to G peak is greater than that of the Au, and there is no visible D peak which would suggest that the Graphene layer on the Ag is of a slightly higher quality than that transferred on to

the Au sample. However, they are both of high quality and the Raman spectra have shown that we have achieved SLG sheets on the required materials.

Due to the delocalised electrons on the surface of the Gr sheets, this can aid the SPR of the system making the device more sensitive. From the Raman spectra the high quality graphene suggests that we would have a high density of delocalised electrons on the surface which should in turn improve the SPR response achieving a better detection sensitivity. We will now discuss how the plasmonic layers were optimised to achieve the maximum resolution and sensitivity for the bio-sensing application.

5.3 Optimisation of plasmonic layers

In order to simulate the effects of different materials, thicknesses and geometry of the SPR sensor, we first need the optical properties of each of the materials. The refractive indices of the materials used (Cr, Ti, Ag and Au) are shown for 664 nm wavelengths in Table 5.1. The chosen wavelengths correspond to the wavelengths of the lasers that we have used. The complex refractive index of Graphene was approximated using an approximation given by Bruna *et al.* (Bruna and Borini, 2009). Bruna *et al.* defined the relationship between the refractive index and wavelength for single layered graphene as $n = 3$ and $k = C_1 (\lambda/n)$, where $C_1 \cong 5.446 \mu m^{-1}$, λ is the wavelength in μm and n is the real part refractive index. a is fine structure constant and d is layer thickness, therefore the extinction coefficient is given by:

$$k = -\frac{\lambda}{4\pi n d_1} \ln(1 - \pi a) \cong C_1 \frac{\lambda}{n} \quad (5.3)$$

Table 5.1. Refractive index for the materials (Cr, Ti, Ag, Au and Graphene) used in the modelling of the SPR sensor for 664 nm wavelengths.

Material	Complex Refractive Index
Chromium (Cr)	3.48 + i4.36
Titanium (Ti)	2.29 + i3.05
Silver (Ag)	0.14 + i4.15
Gold (Au)	0.17 + i3.15
Graphene (Single Layer)	3.00 + i1.21
BK7 Glass	1.52 + i0.00
Refractive index matching gel	1.50 + i0.00

The FWHM of the curves were calculated using Origin (Origin is an industry-leading scientific graphing and data analysis software), by taking the area of the SPR peak. We can approximate the FWHM from the area of the curve based on the peak being Gaussian like; this is not the most accurate method, however as we are only interested in the *relative* change in relation to a reference this method can be used.

$$FWHM \cong \frac{2\sqrt{2 \ln(2)} A}{\sqrt{2\pi} h} \quad (5.4)$$

We will now verify the model given in Chapter 3 with experimentally obtained results to show how accurate we are able to estimate the SPR response from a multi-layered system. It is stated in the literature (Homola et al., 1999) that Ag films in SPR sensors exhibits a much smaller FWHM compared with the use of Au. For this reason, a Glass (BK7)/Cr (2 nm)/Ag (50 nm) sensor was constructed and also one where the Ag is replaced with gold. Fig. 5.7 shows the results from this experiment. Fig. 5.7a shows the Ag system for the experimental and simulation results, showing a very good agreement in the peak position, however

the FWHM from the experimental curve is much smaller than the model. This means that any simulations done with Ag will most likely perform better in experiments in terms of the accuracy.

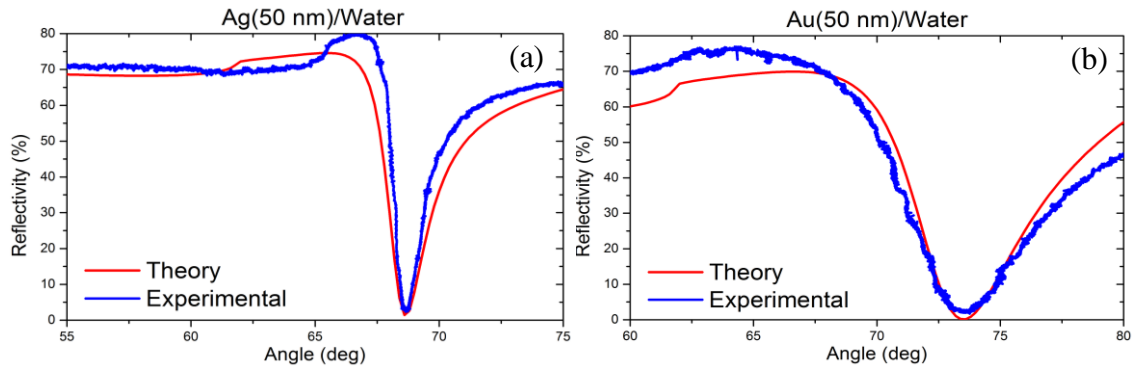


Figure 5.7: Comparison between experimentally obtain results (blue) to the output of the theoretical model (red) for (a) Glass/Cr(2 nm)/Ag(50 nm)/H₂O and (b) Glass/Cr(2 nm)/Au(50 nm)/H₂O. The wavelength of the laser is 664 nm.

Fig. 5.7b shows the same system but with Au instead of Ag. The SPR peak in the experiment seems to be a bit larger than the modelling, especially in terms of the FWHM, where the experimentally obtained one is much larger than in the simulation. This means that any experimental devices using Au will most likely perform with less accuracy than the simulation would suggest.

Comparing the first set of results, we would expect that having a system of both Ag and a much smaller layer of Au, the results to be better in terms of accuracy (smaller FWHM) and the peak position to be the same. Fig. 5.8a shows the device structure used for the experimental and simulations, where the literature states that because Ag is not a chemically stable surface, due to oxidisation, Au is usually preferred. In this study we capped the Ag with a thin layer of Au to protect the Ag, while keeping the improved sensitivity.

Fig. 5.8b shows the results of this, using a 5 nm layer of Au on top of a 40 nm Ag layer, where the experimentally obtained results seems to have a much smaller

FWHM than the simulation suggests which is advantageous when trying to optimise the layer thicknesses.

This section has provided evidence to suggest that the mathematical model, shown in Chapter 3, can be used to predict the SPR sensor response with a high degree of accuracy, where systems using predominantly Ag can be assumed to have a better response in experimental circumstances, compared with Au which shows the opposite trend.

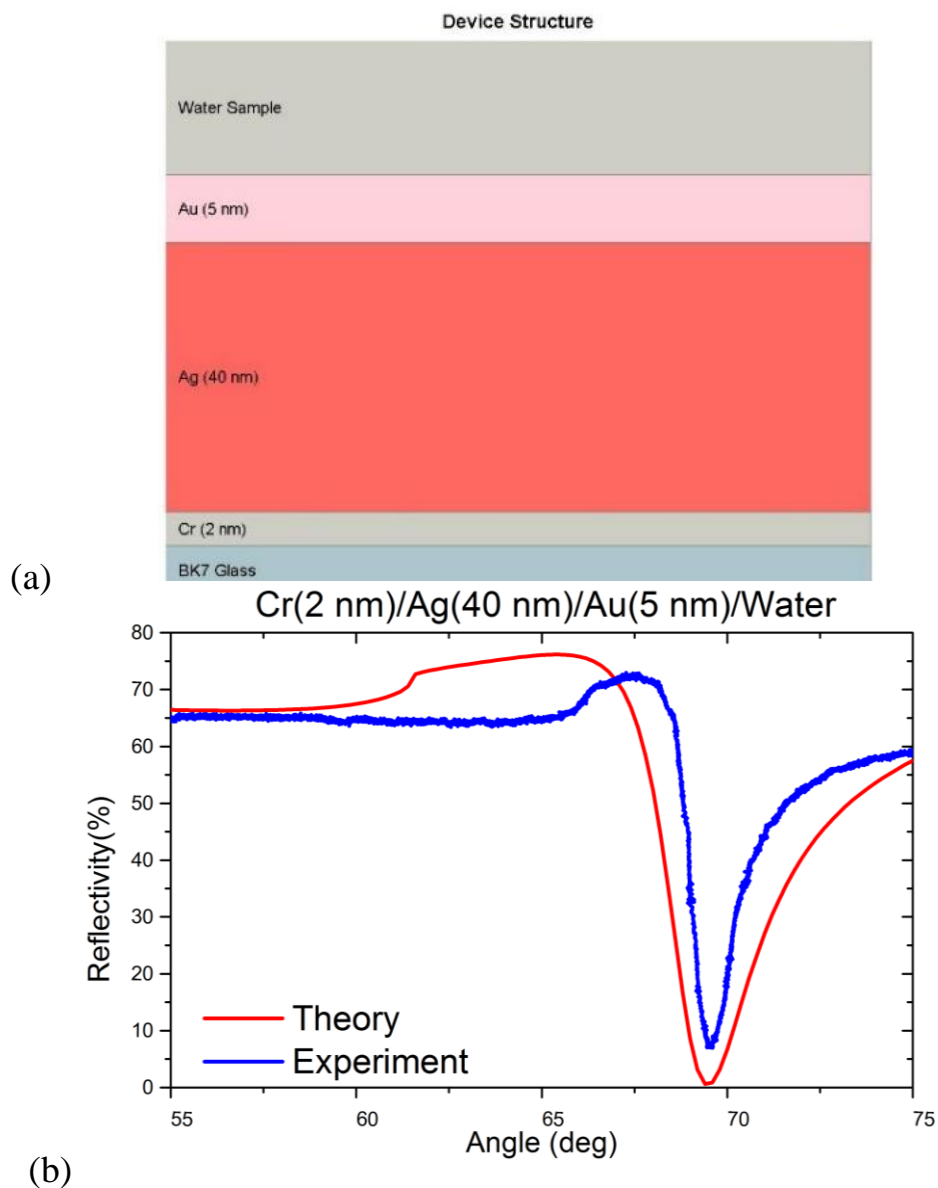


Figure 5.8 : (a) Visual representation of the device structure showing the different layers used for the simulation. The wavelength of the laser is 664 nm. (b) Comparison between experimental (blue) and theoretical (red) results for a Glass/Cr (2 nm)/Ag (40 nm)/Au (5 nm)/H₂O system.

5.4 Optimisation of Interfacial Plasmonic Layers

The SPR layer structure needs to be designed to have the maximum shift in angle for the smallest shift in RIU of the sample and also the smaller the FWHM, then the more accurate the measurement will be. To achieve this for the chosen system, the model outlined in Chapter 3 is used and by verifying the materials and layer thickness we are able to optimise the interfacial layers for the best SPR response.

Au is the plasmonic layer of choice in most situations, the reason behind this is that Au is chemically stable, whereas Ag is quite reactive, forming AgO_2 which degrades the SPR signal and is observed as a widening of the reflectivity response curve. Fig. 5.9a shows the SPR response for different Au Layer thicknesses in a Glass/Cr (2 nm)/Ag (40 nm)/Au(x nm)/Water, as shown in the device structure in Fig. 5.9b. In this case, the best thickness of the Au is determined by the lowest ATR (%) for the peak and the FWHM. Hence, 5nm of Au on-top of the Ag was chosen as optimum.

Ag is known to exhibit high sensitivity in SPR systems, this is because it has a much smaller FWHM compared with Au. Fig. 5.10a shows a Glass (BK7)/Cr (2 nm)/Ag(x nm) system where the thicker the Ag layer, the narrower the SPR peak is (FWHM shown in Fig. 5.10f). However, as the layer increases in thickness (>50 nm) more of the signal is absorbed by the layers lowering the ATR. The point at which the ATR change is greatest and the FWHM is the lowest is the optimum layer thickness for a system of this type. Pure Ag layers for SPR systems have been shown to not be very stable and can oxidise (Szunerits et al., 2008), for this reason a capping layer should be used to protect the layer whilst keeping the desirable characteristics.

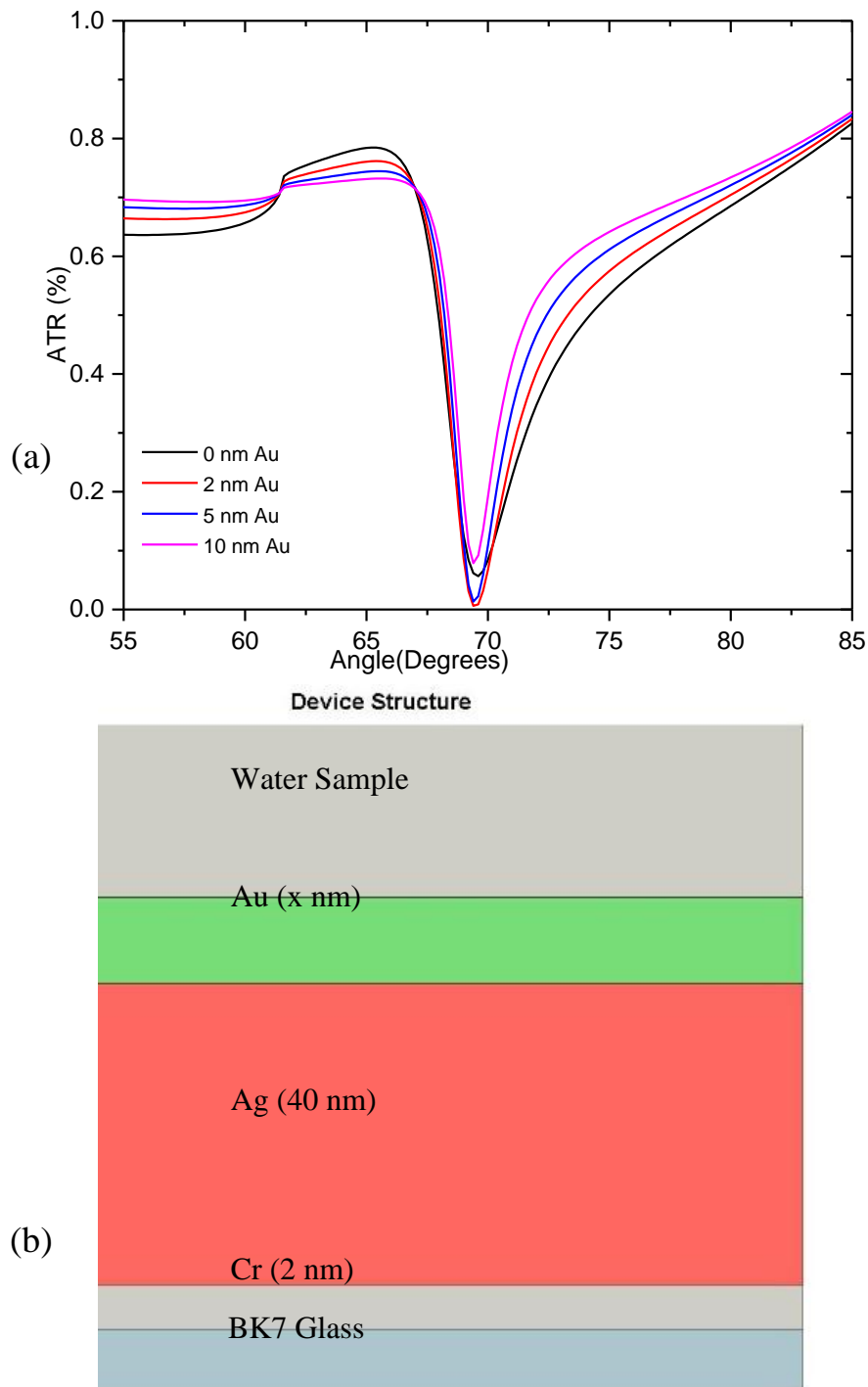


Figure 5.9 : (a) Simulated ATR of a Glass/Cr (2 nm)/Ag (40 nm)/Au (x nm)/H₂O device for the layer thicknesses (0, 2, 5 and 10 nm) at a wavelength of 664 nm. (b) Corresponding device structure showing the different layers.

Fig. 5.10b shown the changes in the SPR peak when a 5 nm Au layer was included on top of the Ag layer at different thicknesses. In this case it has improved the response when compared to just having the Ag layer (FWHM in Fig. 5.10f). It can also be seen in Fig. 5.10b that the introduction of the Au has

changed the resonant angle and the ATR for the different thicknesses and now the optimum thickness of the Ag is different. Further to this, Graphene has been shown to further increase the response due to the dissociated electrons on the surface aiding the plasmon interactions at the interface.

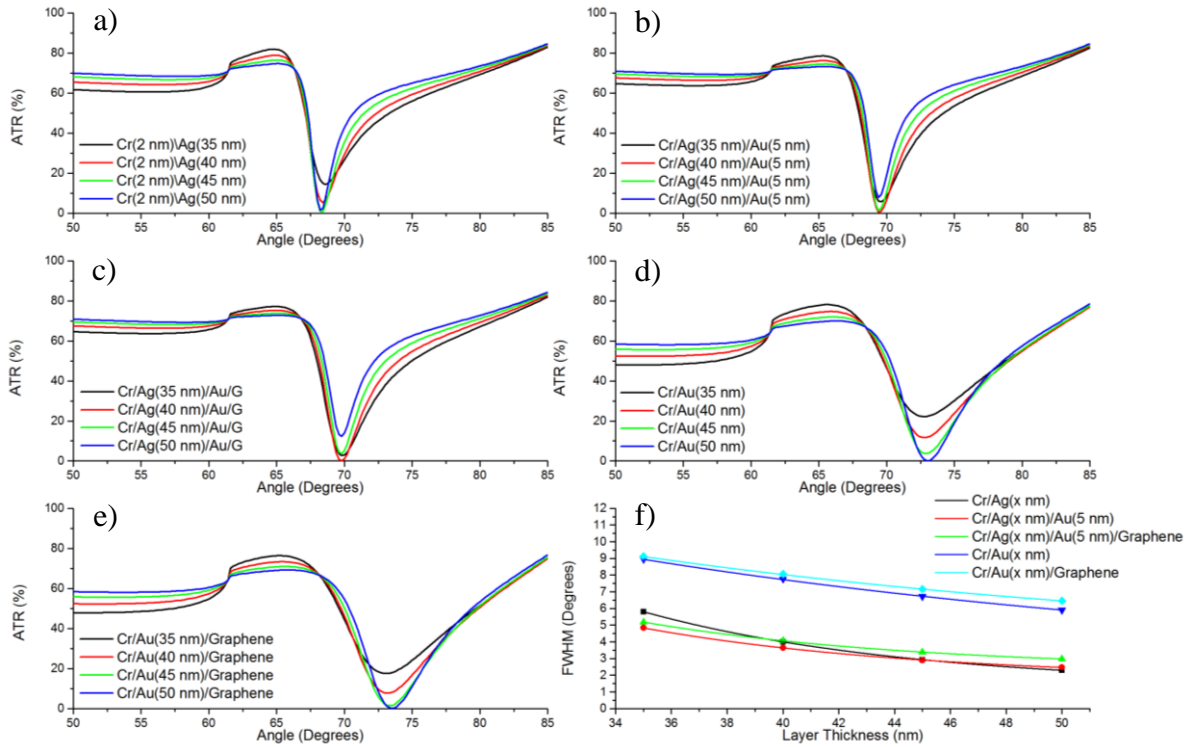


Figure 5.10: ATR response over angle for (a) Glass/Cr(2 nm)/Ag(x nm)/H₂O, (b) Glass/Cr(2 nm)/Ag(x nm)/Au(5 nm)/H₂O, (c) Glass/Cr(2 nm)/Ag(x nm)/Au(5 nm)/Single Layered Graphene/H₂O, (d) Glass/Cr(2 nm)/Au(x nm)/H₂O, (e) Glass/Cr(2 nm)/Au(x nm)/Single Layered Graphene/H₂O, (f) is the FWHM from (a-e) over layer thickness calculated using the Gaussian approximation mentioned in Section 5.3.

Fig. 5.10c shows the same device with a single layer of graphene incorporated which slightly increases the FWHM (Fig. 5.10f) compared with the Ag capped with gold, but with an Ag layer thickness of 40 nm the FWHM, ATR response and Angle are optimum for the SPR system. Now we will look at how the number of Graphene layers affects the SPR response and how the system can be optimised further.

5.5 Optimisation of Graphene layers

Firstly, graphene does not significantly affect the sharpness of the SPR response. Secondly, by determining the thickness of the plasmonic layer that produces the minimum reflectivity without graphene which was 50 nm, with graphene it was reduced to 40 nm. This is expected to increase the SPR sensitivity. The number of layers of graphene was also varied and it was shown that changing from zero layers to seven layers was also influential on the SPR response. The phase response was shown to be sensitive to the number of graphene layers and to be a linear function of the SPR minimum, as the refractive index was varied from 1.333 to 1.336 that is a 0.1 % change.

One thing to note here is the increase of the FWHM from 5.8 to 8.08 degrees for increasing number of layers from 0 to 7, similarly for Ti the FWHM goes from 4.84 to 7.65 deg. It has higher sensitivity than using Cr. The changes here can be attributed to the extinction coefficient of Ti compared with Cr where $k = 4.27$ and $k = 3.85$, respectively (Johnson and Christy, 1974).

Fig. 5.11d shows an increase in the FWHM as the number of graphene layers increases, therefore the less layers the better the resolution of the scan would be. The main difference between the Cr and Ti adhesion layers is the change in the FWHM and the ATR at the SPR angle which can be put down to optimal optical characteristics, where Ti would be the preferred option. However, due to the instability and oxidation of Ti to TiO_2 , Cr will be used.

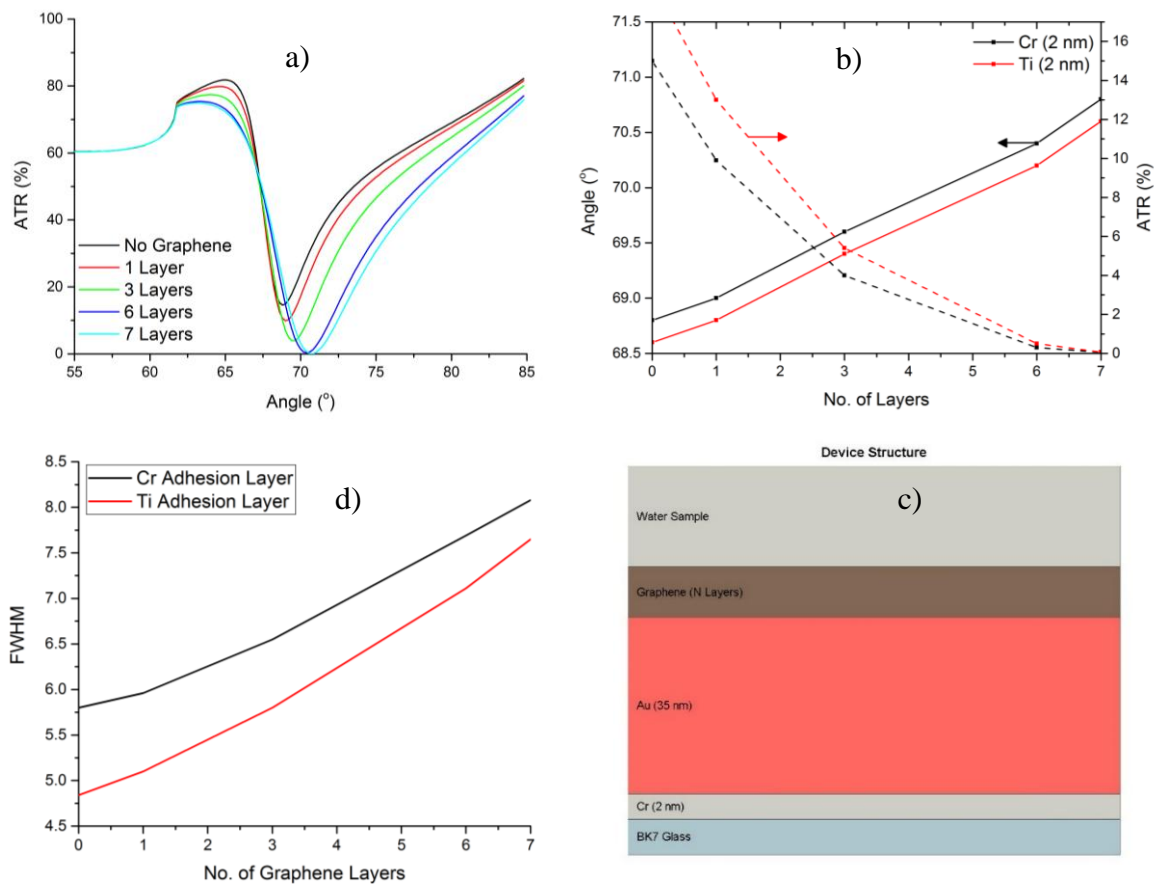


Figure 5.11: (a) Simulation results showing the ATR over angle for different number of graphene layers, (b) (dashed lines) show the Minimum ATR at the resonant angle, solid lines are the resonant angle position, (c) layer structure of BK7 Glass/Cr/Au/Graphene/Sample (d) the FWHM change for the number of Graphene layers and.

5.6 Final Structure

As shown in Section 5.4 Ag shows a much smaller FWHM than gold, but as was mentioned in this section. Ag is not as stable as Au for SPR surface chemical applications, for this reason we opted to use a thin layer of Au on top of Ag which keeps the surface chemistry of Au but allows for better resolution coming from the narrowing of SPR peak from the silver. The lowest ATR recorded from the simulation was obtained when the Au layer was 5nm on-top of a 40 nm Ag film.

It is also apparent that by introducing Graphene into the system we can increase the sensitivity of the sensor, whilst also achieving some desirable qualities such as

improved stability of the surface (reduces chemical changes on the surface of the metals). This is beneficial in realising a re-usable system with a longer usable lifetime; as without the Gr layer the films, especially Ag, will degrade and change their surface chemical properties and hence the refractive index which is not ideal for the system.

A 2 nm layer of Cr has been used as an adhesive layer between the silver and the BK7 substrate; this ensures that the silver is more strongly bound to the glass without much compromise of the performance of the sensor. Hence the final structure is shown in Fig. 5.12, where one-layer of Graphene has been introduced as a capping layer on-top of the 5 nm Au layer.

Device Structure

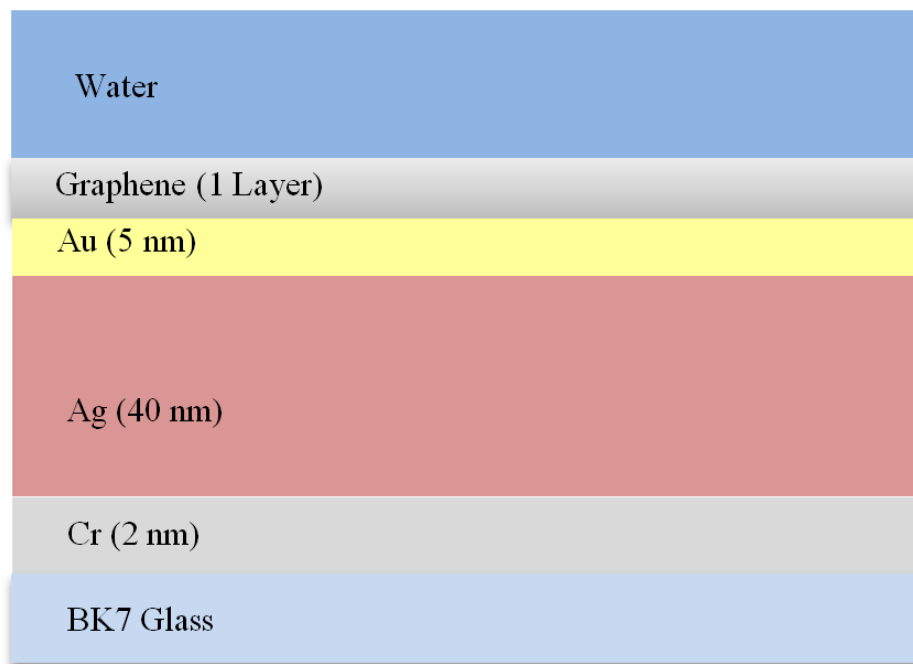


Figure 5.12: Schematic representation of the final system providing with the optimum sensitivity to chemical stability.

5.7 Summary

In this Chapter we have given an introduction of why we would want to introduce Graphene into the system, stating that it protects the metallic layers, whilst improving the SPR response at the same time. We then looked at the optimisation of each of the layers (Section 5.3 to Section 5.5), before giving a description of the optimised system (Section 5.6) used in the next chapter.

CHAPTER 6

6.1 Detection of Silver Nanoparticles and Silver Nitrate using the SPR System

In this chapter we will target the use of the Surface Plasmon Resonance (SPR) bio-sensor for the detection of Silver nanoparticles (Ag NPs) in water and other saline solutions such as Calcium Chloride (CaCl_2) and Sodium Chloride (NaCl). We will also look at the differences in the response of Silver Nitrate (AgNO_3) and Ag NPs to show that we can distinguish between them.

6.2 Methods

All glassware is acid washed prior to use in nitric acid, then triple rinsed with deionised water before being allowed to air dry. The Ag NPs were processed from nano-powder where all weight measurements were taken using a 4 decimal place digital scale.

The Ag NP solution was made up using ultrapure water (ELGA), where 62.5 mg of powder was dissolved into 500 mL of water giving a mass concentration of 125 mg L^{-1} . The solution was sonicated using an ultrasonic bath at 35 kHz for 6 hours (Federici *et al.*, 2007). To obtain smaller concentrations the solution was diluted further and re-sonicated to ensure the NPs are dispersed.

In order to obtain the same weight concentration of Ag in the solution for AgNO₃ as Ag NPs a weight conversion ratio of 1.5748 which relates to the atomic masses of both was used. Hence with the same mass concentration of Ag we obtain 196.8 mg L⁻¹ for AgNO₃.

The NPs in saline solutions were made up into concentrations of 1.1 mM and 0.11 mM using ultrapure water. The nanoparticle solutions, mentioned earlier, were then added to obtain 10 mM NaCl, or CaCl₂ with a 10 mg L⁻¹ mass concentration of Ag in both NP and AgNO₃ form. Humic acid was also used, where the concentrations were made to be the same.

6.3 Analysis of Silver Nanoparticles

Nano Tracking Analysis (NTA) is a variation of Dynamic Light Scattering (DLS) which can provide useful information about nano-particulates such as the size distribution, concentration and information about aggregation. The method is based on tracking individual particles and using the Stokes-Einstein diffusion (D_t) (Eq. 6.1) to calculate the effective diameter of the particles.

$$D_t = \frac{Tk_B}{2\pi\eta d} = \frac{(x,y)^2}{4} \quad (6.1)$$

The drift constant (Eq. 6.1) requires the viscosity (η) and the temperature (T) to calculate the diameter (d), where k_B is Boltzmann's constant. The NTA system obtains the diffusion by tracking the Brownian motion of the particles individually, where the motion is analysed by video unlike the DLS technique.

Fig. 6.1a shows that the average particle size is 139 ± 67 nm. Morphological characteristics such as Ag NP shape and size were analysed using Transmission Electron Microscopy (TEM) JEM-1400 (JEOL).

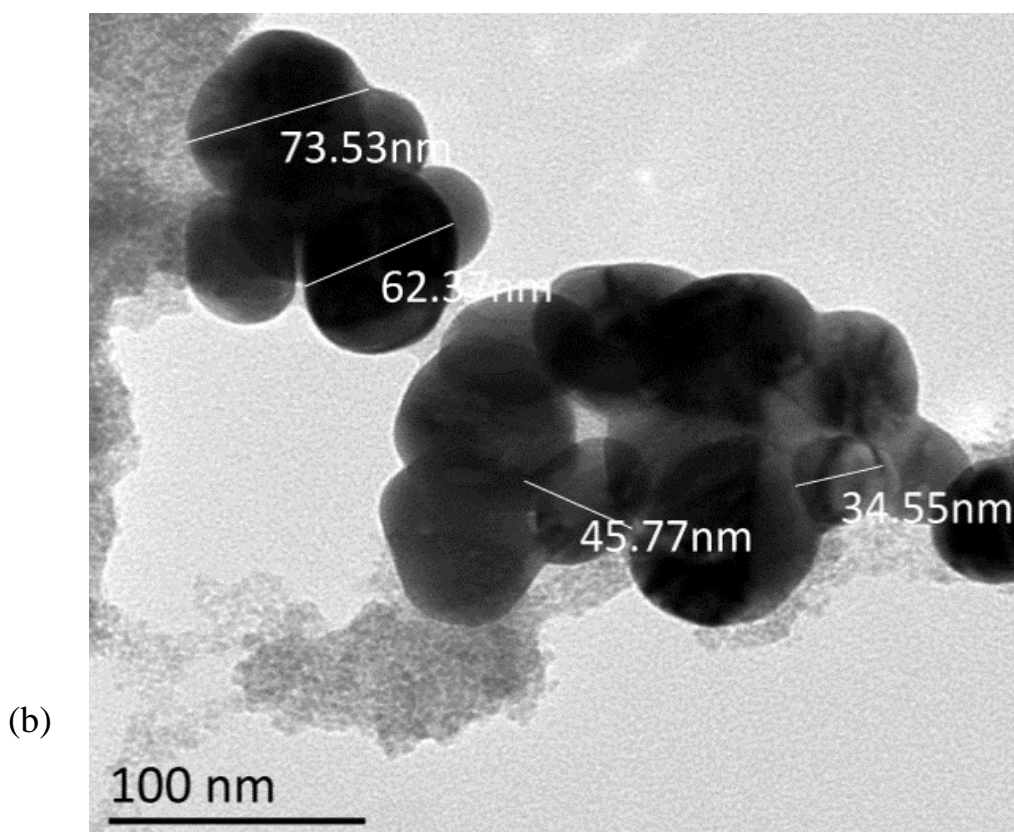
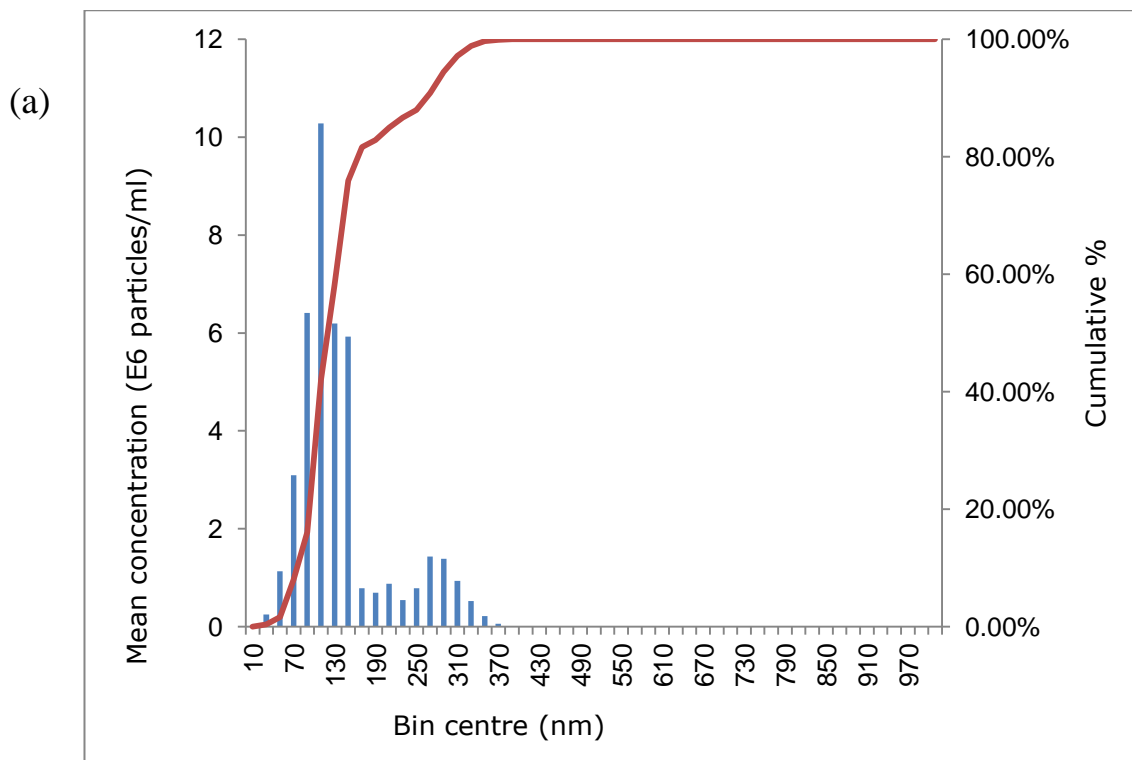


Figure 6.1: (a) The nanosight graph shows the particle distribution of the Ag NPs in 1 mg l⁻¹ Milli-Q water solution. NanoSight tracking results showing particle / cluster size distribution for 1 mg l⁻¹ solution of Sigma Aldrich < 100 nm Ag NPs.. (b) Transmission electron microscope (TEM) image of the Ag nanoparticles, showing residue of PVP used as a stabilising agent during the reduction process. Transmission electron microscopy example image of Ag NPs in 100 mg l⁻¹ Milli-Q water solution.

Gatan Microscopy Suite Software (Statgraphics Centurion XVI.I) was used to analyse images obtained from TEM. Prior to being subjected to TEM analysis, a 100 mgL^{-1} suspension of Ag NPs was prepared in Milli-Q water and dried over Formvar/Carbon Cu-grids film. The result is illustrated in Figure 6.1b. TEM was followed by nanoparticle tracking analysis (NTA) which was carried out for utilizing Ag NPs to determine the particle size distribution. This supports the argument that this method includes all of the aggregates as whole particles, whereas on the TEM image shown in Fig. 6.1b shows that the particulates are made up of smaller particles ($\sim 30 - 70 \text{ nm}$). The average diameter of the nanoparticles is much smaller than that found using the NTA method (Fig. 6.1(a)). This is mostly due to the nanoparticles aggregating into clusters.

6.4 Effective Medium Approximation

The most commonly used method for approximating the optical changes in a mixture of two, or more, materials is to use an Effective Medium Approximation (EMA), such as, the Maxwell-Garnett relation. The predominant reason for the consistent use of these theories is that it requires much less computing resources than other methods, for example, the discrete dipole approximation, or using a Finite Difference Time Domain (FDTD) based method (Battie et al., 2014). In this work, we require a way of accurately predicting the change in optical properties with the inclusion of Ag NPs and AgNO_3 in water; for this reason we used the Bruggeman's EMA.

We will first make the assumption that the Ag NPs are mono-dispersed in the solution based on the average radius from Section 6.2. The second assumption made is that the Ag NPs are homogeneous and spherical and that we will be only using small concentrations. The effective medium comes from applying boundary

conditions to Maxwell relationship between the electric field (\mathbf{E}) and the polarisation (\mathbf{P}), shown in Eq. 6.2 (Niklasson et al., 1981).

$$\mathbf{P} = N\varepsilon_m\alpha\mathbf{E} \quad (6.2)$$

Where N is the number density per m^3 , ε_m is the permittivity of the surrounding media and finally α is the polarizability of the NPs. The polarizability, using specific boundary conditions for an arbitrary sphere, is shown in Eq. 6.3, where r and ε_i are the radius and permittivity of the NPs respectively.

$$\alpha = 4\pi r^3 \left(\frac{\varepsilon_i - \varepsilon_m}{\varepsilon_i + 2\varepsilon_m} \right) \quad (6.3)$$

Using Eq. 6.2 and Eq. 6.3 we can obtain the Maxwell-Garnett formalisation for approximating the effective permittivity (ε_{eff}) of the bulk material which is shown in Eq. 6.4:

$$\left(\frac{\varepsilon_{eff} - \varepsilon_m}{\varepsilon_{eff} + 2\varepsilon_m} \right) = f_i \left(\frac{\varepsilon_i - \varepsilon_m}{\varepsilon_i + 2\varepsilon_m} \right) \quad (6.4)$$

Where f_i is the volume fraction of NPs in the solution, the derivation for this is shown in more detail in Appendix F and has been checked against the literature (Niklasson et al., 1981, Khardani et al., 2007). An extension to the Maxwell-Garnett formalisation, namely the Bruggeman EMA, was developed, that can work with one or more materials in the same fashion. The formal of the general equation is very similar and is shown in Eq. 6.5, where f_a the volume fraction of the first inclusion is included material, f_b is the volume fraction of the second inclusion and $\varepsilon_{a,b}$ are the permittivity's associated with the volume fractions. Following the conservation of Energy laws, this relationship holds true.

$$(1 - f_a - f_b) \left(\frac{\varepsilon_m - \varepsilon_{eff}}{\varepsilon_m + 2\varepsilon_{eff}} \right) + f_a \left(\frac{\varepsilon_a - \varepsilon_{eff}}{\varepsilon_a + 2\varepsilon_{eff}} \right) + f_b \left(\frac{\varepsilon_b - \varepsilon_{eff}}{\varepsilon_b + 2\varepsilon_{eff}} \right) = 0 \quad (6.5)$$

This enables us to approximate the shift of the refractive index with the inclusion of both AgNO₃ and Ag NPs. However, there are some inaccuracies relating to the energy that should be noted. Battie *et al.* (Battie *et al.*, 2014) have shown that for both EMAs that above 2.6 eV they start to become inaccurate. Niklasson *et al.* (Niklasson *et al.*, 1981) also showed that for high volume fractions (> 0.7) both theories are inaccurate, where both are good approximations below volume fractions of 0.3 (Homes *et al.*, 2012, Niklasson *et al.*, 1981). They also showed that for nanoparticle size radii of < 5 nm, where the band structure starts to fall down and other quantum based methods should be used for more accurate results (Niklasson *et al.*, 1981).

6.5 Simulation of different concentrations of nanoparticles

Using the Bruggeman's EMA we have approximated the change in refractive index for different volume fractions of Ag NPs in water. Fig. 6.2a shows the results of the model, the solid line represents the ATR and the dashed lines represent the change in phase over angle, of the system with varying nanoparticle volume concentrations. Fig. 6.2b shows the change in resonance which can be found by taking the angle when the change in phase is at a minimum. It shows us that the change in refractive index with changing nanoparticle concentrations is linear, from this we can work out the sensitivity of the system.

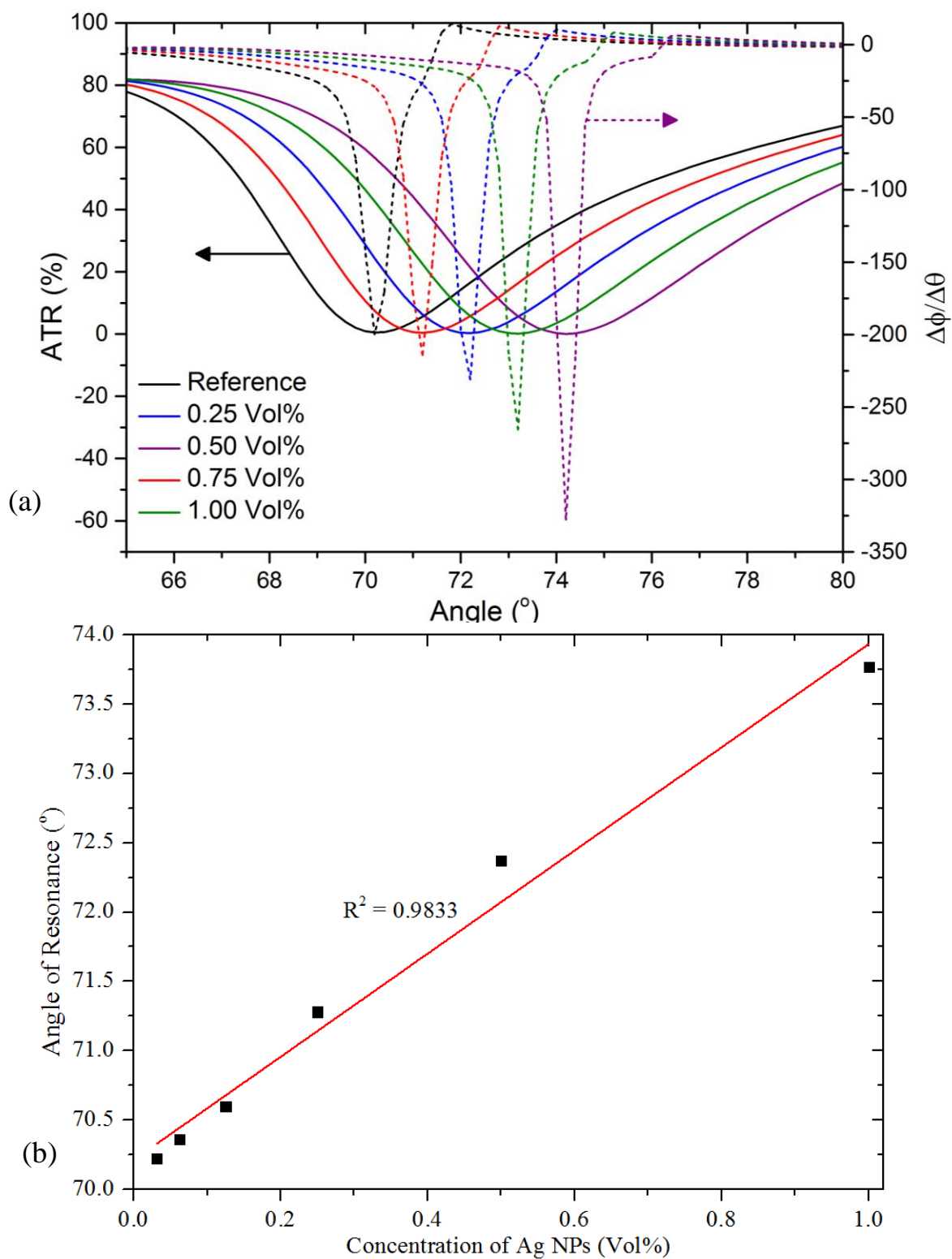


Figure 6.2: (a) The difference in the phase over angle ($\Delta\Phi/\Delta\theta$) overlaid with the ATR for each of the 4 different concentrations, showing a linear shift over angle. The minima of the difference in the phase over angle can be used for a better determination of the resonant angle compared with the ATR. (b) Linearity of the change in resonant angle compared to nanoparticle concentrations. The Ag NP size used in this simulation was 35 nm. 1 mgL^{-1} of silver relates to 9.54×10^{-5} volume fraction or ~ 0.01 Vol %. 0.6% for 62.5 mgL^{-1} ,

A function for this system for the shift in resonant angle for concentration can be made into a formula which is shown in Eq. 6.6

$$\Delta\tilde{n}(f) = \sqrt{|\varepsilon_m - \varepsilon_{eff}(f)|} \quad (6.6)$$

Where f is the volume fraction of Ag NPs to water. This has provided a good starting point for what to expect during the experiments, giving the predicted change in resonant angle for concentrations. To verify that this is an accurate determination of the system, experimentally obtained ATR for different concentrations of Ag NPs in water were compared with the simulation. The system, discussed in Section 5.4, is made up of BK7 Glass/Cr (2 nm)/Ag (40 nm)/Graphene (0.34 nm). Then the system was run with air (Fig. 6.3(a)) which showed the resonant angle to be 44.4° , where the experimentally obtained resonant angle agrees completely with the simulation. Then the experimental ATR for 250 mg L^{-1} of Ag NPs in water (2.4 Vol%) (Fig.6.3b) was obtained, showing good agreement between the experiment and simulation. However, it can be clearly seen in Fig. 6.3b that there is a slight shift of the resonant angle by approximately $+0.4^\circ$ which can be put down to a higher concentration of nanoparticles sitting at the surface compared with the averaged concentration within the solution. By this assumption, over time the nanoparticles settling on the surface will cause the resonant angle to shift further at a constant rate.

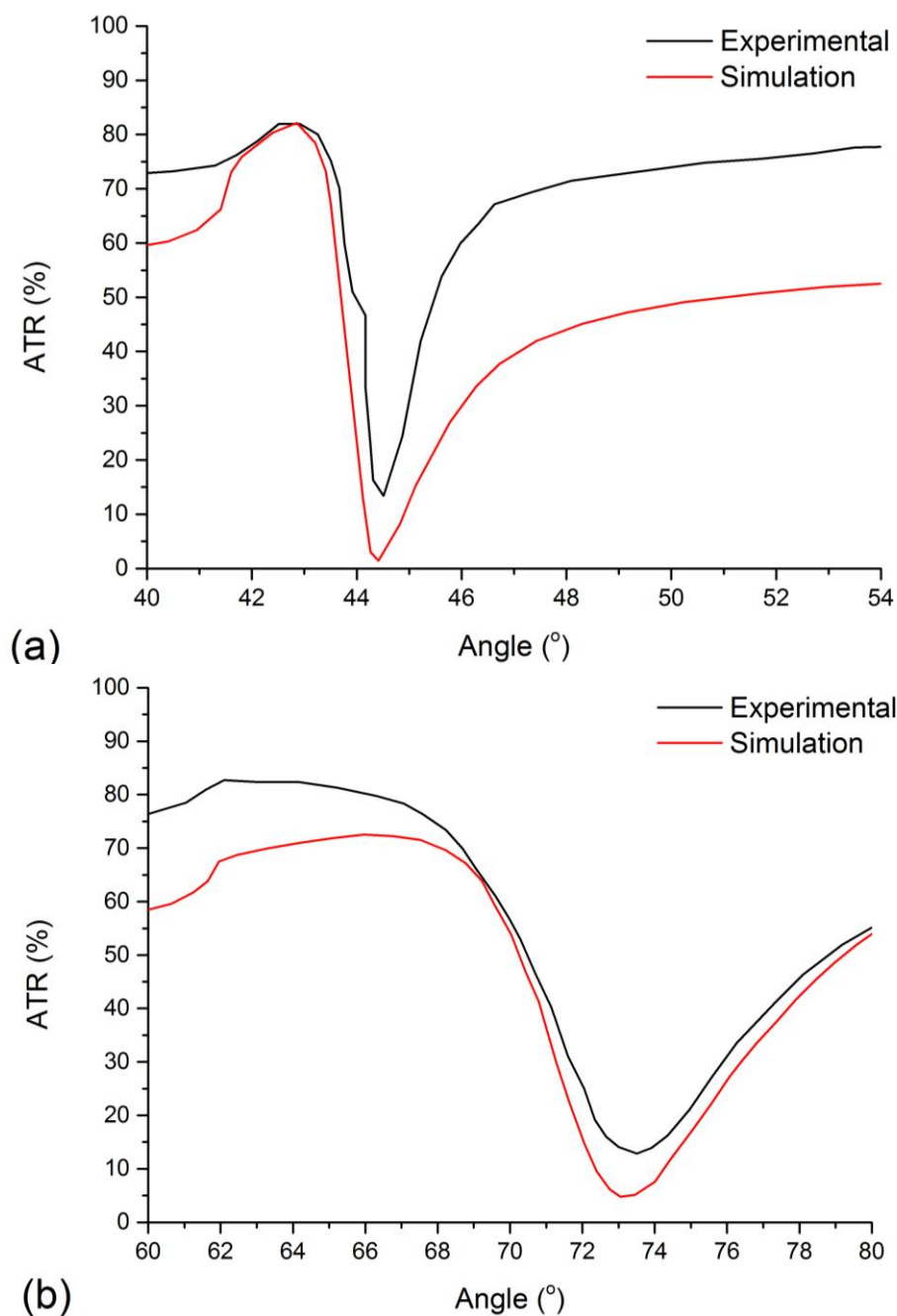


Figure 6.3: SPR - theoretical and experimental results for (a) air and (b) water - with 250 mg L^{-1} (2.4Vol %) of Ag NPs.

Now we have shown that we can accurately determine the resonant angle for Ag NPs in water, by showing experimental simulation for the same concentrations, we will now look at the detection of NPs in complex mediums.

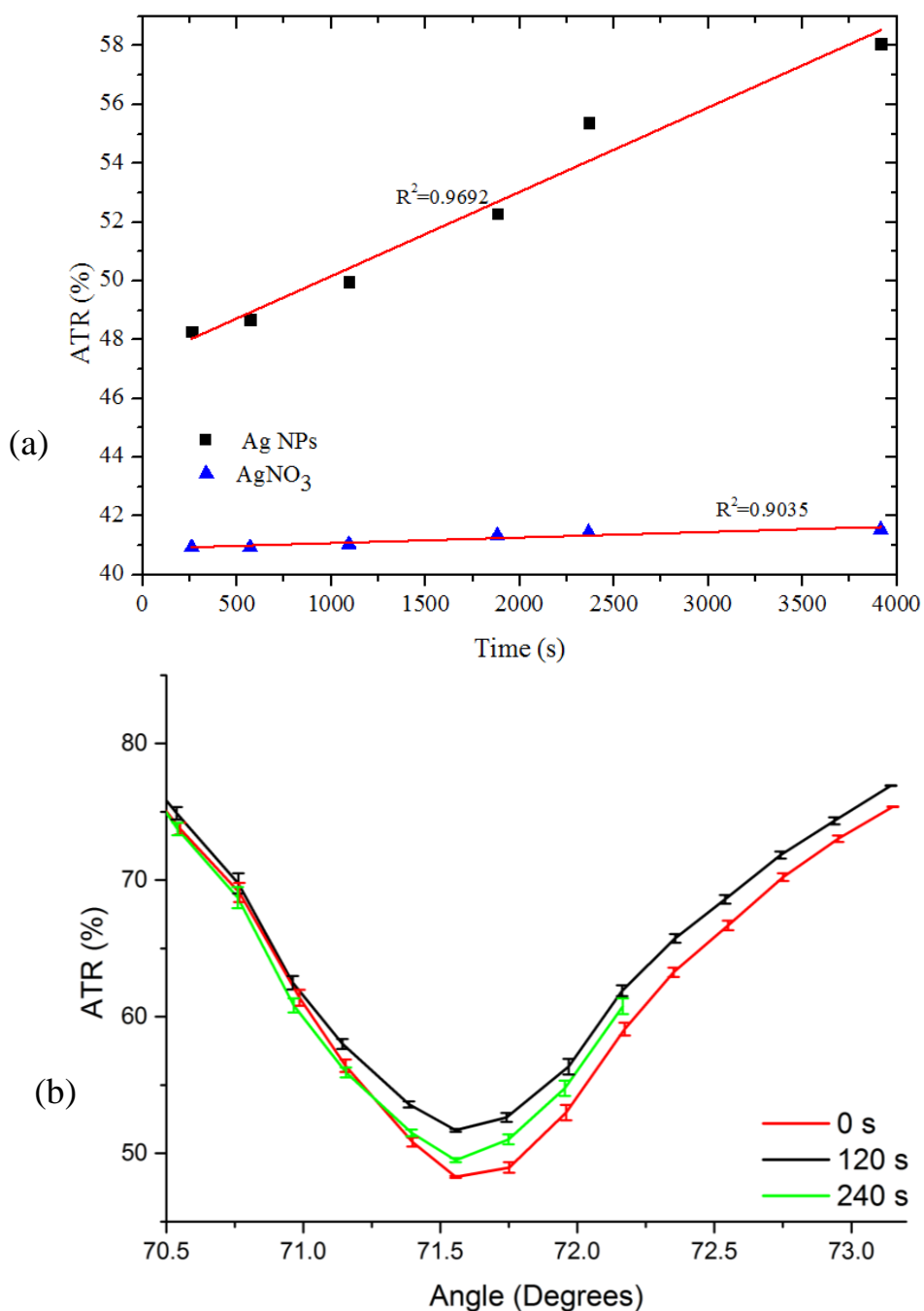


Figure 6.4: (a) The change in ATR over time given for AgNO₃ and Ag NPs. (b) scans over angle at time = 0s, 120s and 240s for Ag NPs in CaCl₂.

Fig. 6.4a shows the changes in the ATR over time, where it has been fit using a straight line showing a linear dependence with time. The ATR of the Ag NP sample increases significantly over time compared with the AgNO₃ sample. A possible reason for this is the AgNO₃ will stay completely suspended in solution, whereas the NPs will, over time, settle on the surface depending on the

concentration and will eventually saturate. This also suggests that over time we would be able to accurately differentiate the NPs from AgNO_3 and other complex solutions, such as CaCl_2 . Fig. 6.4b shows the changes in the ATR over angle for three different times of AgNPs in CaCl_2 which shows a decrease in the resonant angle over time and also a decrease in the FWHM from approximately 1.4 degrees to 1.3 after 120s.

The result in Fig. 6.4a is fundamental in quantifying the amounts of silver within complex media, where the slope of the curve could give information such as settling rates on the surface of the SPR sensor and hence a better quantification of the concentration of Ag NPs.

6.6 Experimental and Simulation of Ag NPs in complex mediums

It is also possible to detect other forms of Ag, for example, AgNO_3 . In this experiment we used the same concentration of Ag in the form of NPs and AgNO_3 to see if we are able to differentiate between the two. Fig. 6.4 shows the experimental and simulation results for 62.5 mg L^{-1} (2.4 Vol %) of Ag in both forms. It shows that the resonant peak from the simulation agrees with the experimental, however there is quite a distinct difference in the full-width half-maxima (FWHM) of the resonant peaks. The NPs shift the resonant peak further than the AgNO_3 does compared to Water. It is also apparent that the FWHM of the SPR curve changes with the inclusion of Ag. The FWHM of the Water sample is approximately 1.19 degrees and decreases with the inclusion of AgNO_3 to 1.08 degrees and then decreases further to 0.9 degrees for the Ag NP sample, figure 6.5(a).

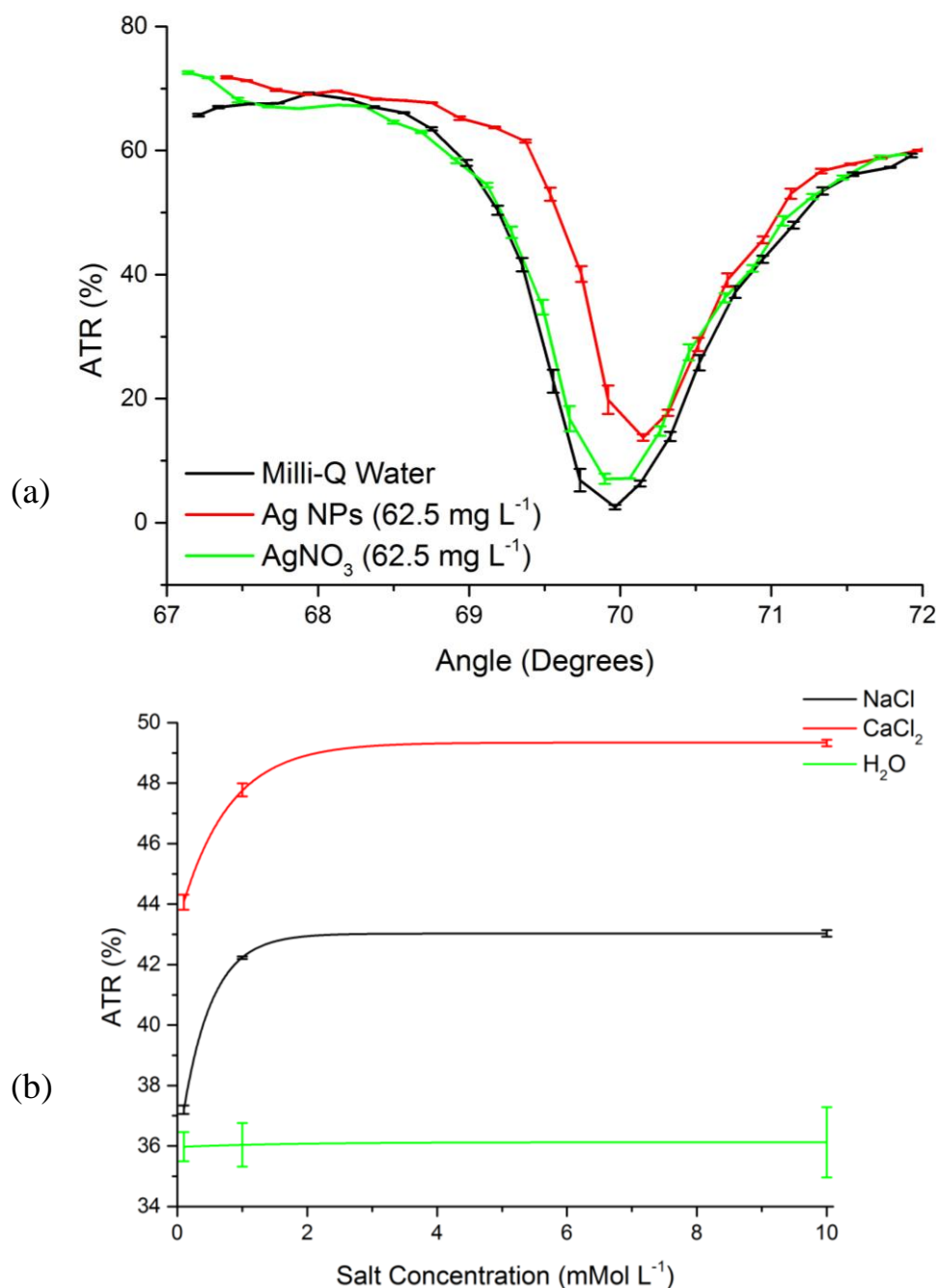


Figure 6.5: (a) ATR change between pure water, AgNO₃ and Ag NPs (62.5 mg l⁻¹), (b) changes in salt concentration with nanoparticles in.

To look at the changes for the concentration of nanoparticles in different, complex mediums, we chose to experiment with saline solutions. The saline solutions would be one of many typical media that you would find in a natural water. Concentrations of 0.1 mM, 1 mM and 10 mM of Ag NPs were used in the experiment. The complex media used in this experiment were Sodium Chloride (NaCl) and Calcium Chloride (CaCl₂) and referenced against water. Three

different measurements were taken for each concentration in each solution. The average and standard deviation of these measurements are shown in Fig. 6.5(b).

Fig. 6.6a shows the intensity of the ATR at the resonant angle. The standard deviation provides some interesting information; for water the error in measurement of the resonant angle is very small, however, the error shown in the Intensity is significant. Fig. 6.6b shows the average resonant angle over three independent measurements, the red bars in the graph represent the standard deviation between the measurements. NaCl and CaCl₂ show much more consistent results over the three measurements, in addition the changes with concentration is shown to be more linear for the saline solutions than water, especially in the changes in the resonant angle.

Another solution used which can be seen in Fig. 6.6, was Humic acid and then the detection of AgNO₃. Because the refractive index of Humic acid is higher than that of AgNO₃, there is a negative change in the resonant angle when it is introduced.

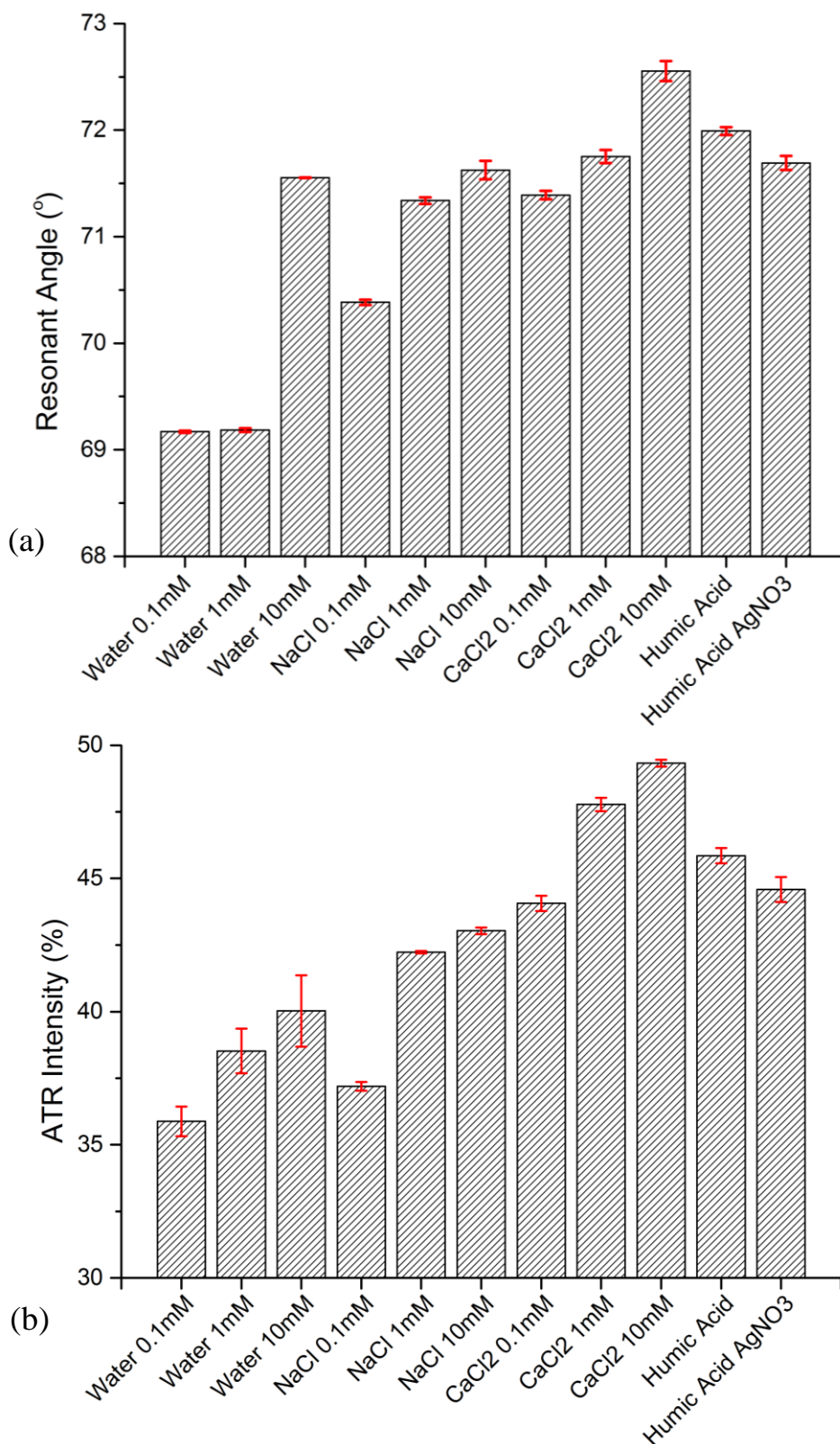


Figure 6.6: The detection of different concentrations of <Size nm> Ag NPs in water and other different saline solutions, Sodium Chloride (NaCl), Calcium Chloride (CaCl₂) and finally the change of Humic Acid with and without Silver Nitrate (AgNO₃). (a) Average resonant angle of each concentration, (b) Average SPR peak intensity, the errors over three measurements are shown as the standard deviation (Red).

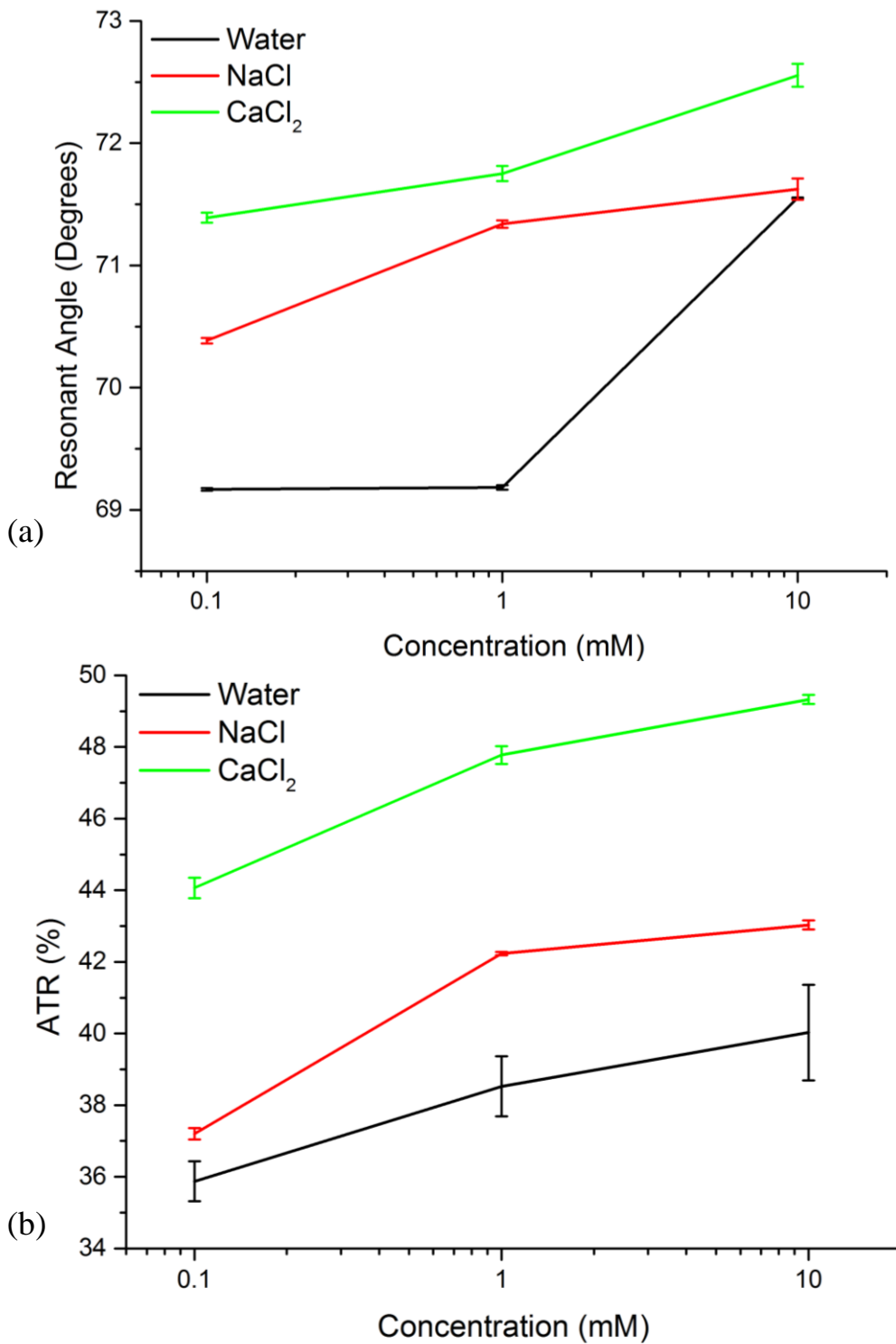


Figure 6.7: change in (a) resonant angle and (b) ATR at the resonant angle over different concentrations of Ag NPs in different complex media (Water, NaCl and CaCl₂).

Fig. 6.7(a) shows the change in resonant angle with different concentrations; unlike the intensity, the saline solutions are shown to exhibit a much more linear regression compared with water. Fig. 6.7(b) shows the change in the intensity over concentration, the error bars are the standard deviation over three

measurements. Both water and CaCl_2 show almost linear increase in the intensity over the different concentrations, whereas NaCl shows a much lower change in the intensity at larger concentrations.

It is also apparent that the error between measurements for water, in terms of the intensity, is much greater than for the other complex solutions.

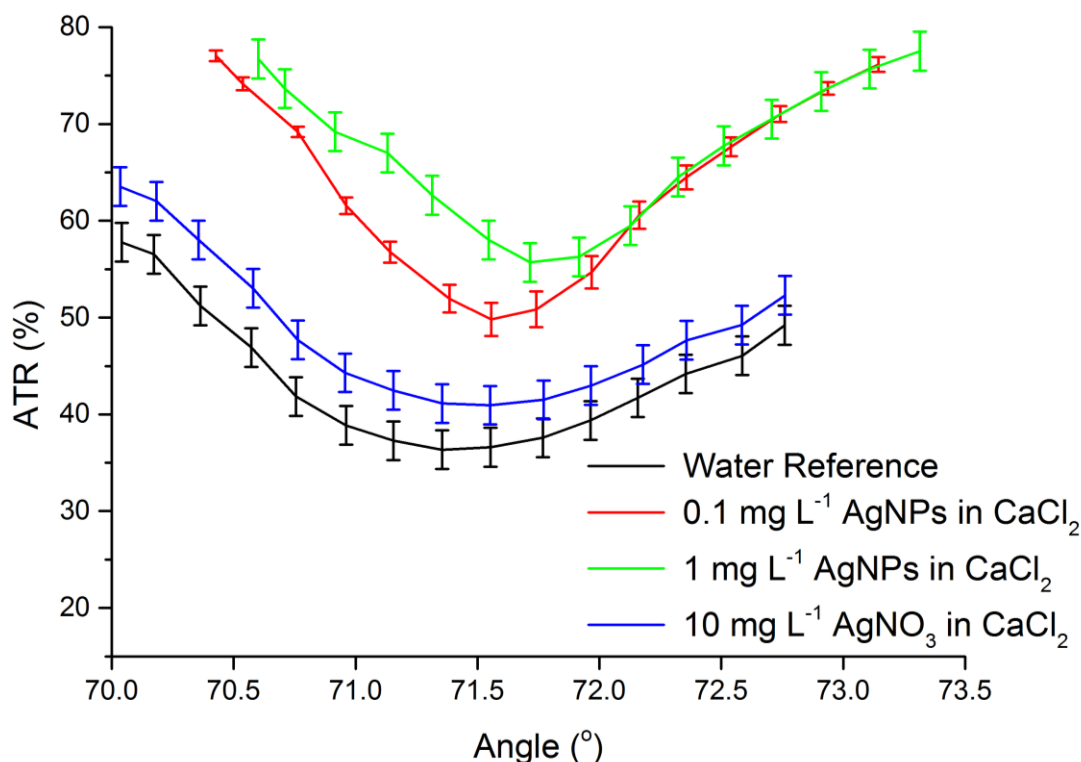


Figure 6.8: Different concentrations of Ag NPs in CaCl_2 (Red and Green), showing increase in both angle and ATR at the resonant angle. Also this is compared against 10 mg L^{-1} of AgNO_3 .

This shows that AgNO_3 does not affect the resonant angle significantly enough to be able to measure smaller concentrations. To do this, the system would need to be re-designed with this in mind. However for Ag NPs there is quite a large, and linear change in the resonant angle with increasing concentrations. This suggests that the designed system is able to accurately determine different concentrations of the Ag NPs in water and other complex solutions which enables the detection of Ag NPs in natural water samples as specified in the aims and objectives of this

thesis. (0.00095 Vol%) (0.0095 Vol%) Ag NPs to H₂O and (0.0023 Vol% AgNO₃ to H₂O).

The limit of NP concentration that can be sensed is down to the FWHM of the resonance peak; it becomes more difficult to determine the resonant angle the smaller the concentration. Hence, the system would also need to be redesigned if the requirement for measuring smaller, or larger, concentrations of Ag NPs.

6.7 Summary

In this chapter we showed that it is possible to detect small concentrations of Ag NPs in water and other saline solutions; namely CaCl₂, AgNO₃ and NaCl. We also looked at the changes with Humic acid as an additive, showing similar results to the saline solutions. It was apparent that it is still possible to identify small concentrations of Ag NPs regardless of the complex surrounding media and hence working towards the quantification of the concentration.

CHAPTER 7

7.1 Conclusions and Future Work

In this chapter we will summarise the results obtained in this research on the development of the Surface Plasmon Resonance (SPR) based bio-sensor. Then some suggestions for future work have been made, specifically targeting the further development of the system in terms of improved sensitivity and accuracy.

7.2 Conclusions

The goal of this work was to predict theoretically the SPR conditions in a multi-layered system for the detection of Silver Nanoparticles (Ag NPs) in complex media, then design and construct the complete SPR system. The aim was to use the theoretically obtained results to optimise the system in terms of the detectability of Ag, this was achieved by verifying the theoretically obtained results with experimentally obtained data from the designed system. The system needed to be automated, calculating the Attenuated Total Reflection (ATR) over a range of angle from a solution based sample which was achieved with good agreement between experimental and modelling results.

Chapter 1 outlined the problem of Ag NPs in the natural environment, where it is of growing concern and many people are trying to detect very small concentrations. We outlined the need of such system to assess and quantify the existence of particles in clean water supplies.

An in depth study of the literature (Chapter 2) determined that SPR based biosensors could be used to achieve the goal of sensing NPs in an aquatic system, where we described the different configurations that are commonly used to achieve SPR conditions, branching into the principles of the chosen system giving sufficient knowledge required to understand the optical mechanisms of the system.

From the literature and theory we were able to construct a mathematical model to describe the resonant conditions based on angular interrogation techniques, where the angle is changed and the ATR is monitored; when there is a local minima in the ATR, this means that the SPR conditions have been satisfied. As the complex refractive index of the sample changes, the SPR conditions change. This allows us to determine the refractive index change relative to a pure water sample with no contaminants. We show how the experimental results compare to the mathematical model, showing good agreement between the two, allowing us to use the model to optimise the multi-layered system for the specific application.

Chapter 4 covers the experimental techniques used throughout the work and a detailed description of the designed system; including the mechanical, electrical and software aspects.

Linking Chapter 3 with Chapter 4, we were able to use the mathematical model to optimise the materials and layer thicknesses, in the desired system and introduce Graphene (Gr) as a capping layer (shown in Chapter 5). Gr has been shown to improve the SPR response of many sensor based affinity sensors and was chosen to increase the sensitivity of the system, whilst protecting the dielectric-metal interface. We showed that the optimum sensing system for this specific application was BK7 Glass substrate/Cr (2 nm)/Ag (40 nm)/Au (5 nm)/Graphene (0.34 nm).

This model was verified experimentally using different samples in Chapter 6. Ag NPs in small concentrations were introduced into water and other saline solutions which showed that the concentration of Ag NPs can be quantified regardless of the complex media it is in. We also showed that if we also introduced Silver Nitrate (AgNO_3) with Ag NPs in the system, we were able to distinguish between the two, assuming that the concentration of AgNO_3 in the system is known.

During this study, the SPR sensor was employed to study refractive indices of liquid samples and commercial applicability. We show that the system can also be used for the analysis of chemical and biochemical samples *in situ*.

7.3 Future Work

The original goal for detecting Ag NPs in an aqueous solution has been realised. However, there are some aspects that could further improve the system. Firstly, the experimental set-up has the ability to probe the ATR from the angle. By measuring the phase of the polarised light would allow for the monitoring of *phase* change through the system. We showed in Chapter 6 that by using the unique multilayered system it is possible to more accurately determine the SPR peak from different samples as compared with the ATR spectra. This has a narrower peak (small Full-Width Half-Maxima). By improving the position sensor of the laser and detector of the experimental system higher position sensor resolution will be achieved. Using an optical Encoder is one option which has been started and tested on the system, figure 7.1a.

7.3.1 Encoder Mounting

The holders for the encoder is designed using Solidworks and Sketch Up software and build it using aluminium metal. Then, it has been integrated into the

experimental setup to be used as holders for the encoder. The movement of encoder shaft proportional to the motion of the laser and detector is brought about by two connecting rods on each end which are fixed directly to the encoder knob on one end. The other end of the connecting rod is attached to the shaft of the laser and detector to obtain a proportional movement of encoder shaft according to the angle of laser and detector.

For the two-dimensional movement between both the connecting rods a pair of ball bearings are used with a shaft between them, to obtain a smooth movement between them as both the connecting rods move. Two ballbearings are used within the holes of the connecting rods, connected by a shaft for a continuous two-dimensional movement, figure 7.1b.

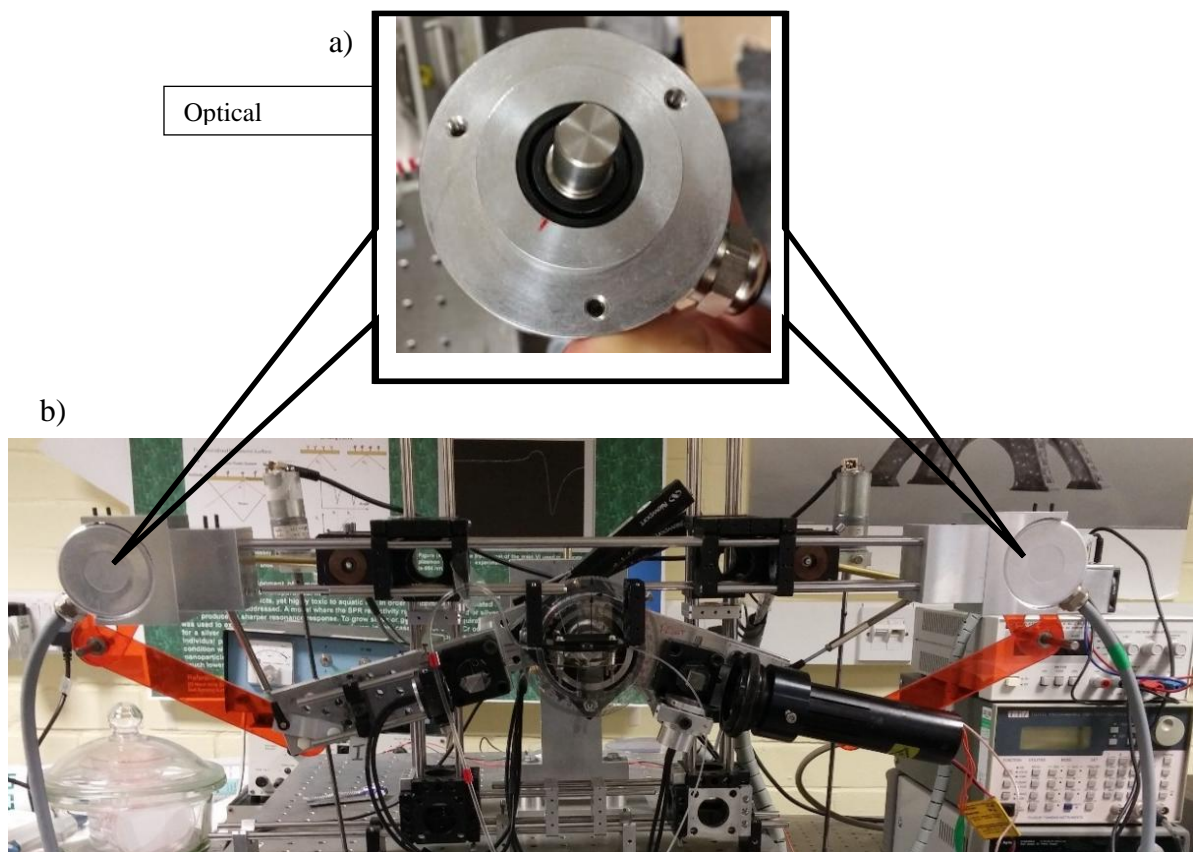


Figure 7.1: a) Optical Encoder. b)The entire experimental setup with the left and right encoders mounted is shown in the figure. Encoders are more efficient and have a higher accuracy compared to potentiometers. Hence, the output obtained with the encoders would be more sensitive than using potentiometers.

7.3.2 Improving Controlling LabVIEW program

In almost all commercial SPR based biosensors the real time reaction would be under consideration. i.e. antibody antigen interaction. This could be achieved alongside the ATR by improving the controlling program to a level which allows the user to run the system and find the position of the minimum spectrum then record a data while introducing the antigen antibody to the system, figure 7.2. Using the binding reaction of an antibody to an antigen and subsequently the detailed binding of an antibody to its antigen is accomplished. The desirable antigen based antibodies are immobilized onto the sensor surface and antibodies are then bound by introducing the antigens.

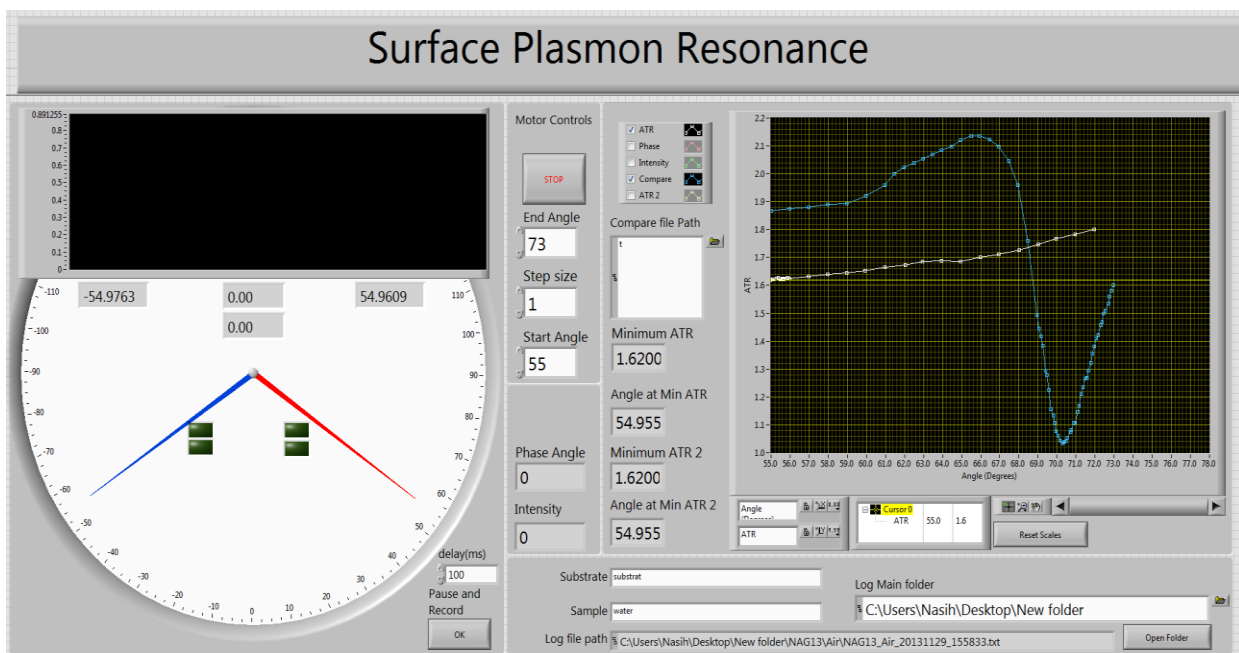


Figure 7.2: Improved LabVIEW program which allows run the system and record the data while introducing the different testing samples to the system.

Complete Bibliography

- F. S. L. A. C. R. T. 2008. OPTICAL BIOSENSORS: TODAY AND TOMORROW, Washington DC, USA, Center for Bio/Molecular Science & Engineering.
- ABDULHALIM, I., ZOUROB, M. & LAKHTAKIA, A. 2008. Surface Plasmon Resonance for Biosensing: A Mini-Review. *Electromagnetics*, 28, 214-242.
- ADEGBOYEGA, N., SHARMA, V. K., SISKOVA, K., ZBORIL, R., SOHN, M. L., SCHULTZ, B. J. & BANERJEE, S. 2012. Interactions of Aqueous Ag⁺ with Fulvic Acids: Mechanisms of Silver Nanoparticle Formation and Investigation of Stability. *Environmental science & technology*.
- AKIMOTO, T., SASAKI, S., IKEBUKURO, K. & KARUBE, I. 1999. Refractive-index and thickness sensitivity in surface plasmon resonance spectroscopy. *Applied optics*, 38, 4058-4064.
- ALLEYNE, C. J., KIRK, A. G., MCPHEDRAN, R. C., NICOROVICI, N.-A. P. & MAYSTRE, D. 2007. Enhanced SPR sensitivity using periodic metallic structures. *Optics express*, 15, 8163-8169.
- AMINE, A., MOHAMMADI, H., BOURAIS, I. & PALLESCHI, G. 2006. Enzyme inhibition-based biosensors for food safety and environmental monitoring. *Biosensors & bioelectronics*, 21, 1405.
- ANDERSSON, O. 2008. Imaging surface plasmon resonance. doctora, Linköping University.
- ANDREW D. MAYNARD, D. Y. H. P. 2007. Nanotechnology and Occupational Health, USA, Reprinted from the Journal of Nanoparticle Research.
- ANKER, J. N., HALL, W. P., LYANDRES, O., SHAH, N. C., ZHAO, J. & VAN DUYN, R. P. 2008. Biosensing with plasmonic nanosensors. *Nature materials*, 7, 442-453.
- ANTONIETTA M GATTI, S. M. 2008. NANOPATHOLOGY THE HEALTH IMPACT OF NANOPARTICLES.
- ASHARANI, P., LOW KAH MUN, G., HANDE, M. P. & VALIYAVEETIL, S. 2008. Cytotoxicity and genotoxicity of silver nanoparticles in human cells. *ACS nano*, 3, 279-290.
- BABAAHMADI, V., GHANBARAJJEH, M., TOLIYAT, T. & MONTAZER, M. 2011. Photochemical reduction of silver nitrate to nano silver using stannous chloride, CTAB and daylight irradiation.
- BAE, S., KIM, H., LEE, Y., XU, X., PARK, J.-S., ZHENG, Y., BALAKRISHNAN, J., LEI, T., KIM, H. R. & SONG, Y. I. 2010. Roll-to-roll

- production of 30-inch graphene films for transparent electrodes. *Nature nanotechnology*, 5, 574-578.
- BAEZA-SQUIBAN, A., BOLAND, S., HUSSAIN, S. & MARANO, F. 2011. Health Effects of Nanoparticles. General, Applied and Systems Toxicology.
- BAKALOVA, R., OHBA, H., ZHELEV, Z., ISHIKAWA, M. & BABA, Y. 2004. Quantum dots as photosensitizers? *Nature biotechnology*, 22, 1360-1361.
- BAND, Y. B. 2010. *Light and Matter*, John Wiley & Sons, Ltd.
- BARNES, W. L., DEREUX, A. & EBBESEN, T. W. 2003. Surface plasmon subwavelength optics. *Nature*, 424, 824-830.
- BATHAE KUMARESH, P. 2007. OPTIMIZATION OF A DUAL-MODE SURFACE PLASMON RESONANCE SENSOR.
- BATTIE, Y., EN NACIRI, A., CHAMORRO, W. & HORWAT, D. 2014. Generalized effective medium theory to extract the optical properties of two-dimensional nonspherical metallic nanoparticle layers. *The Journal of Physical Chemistry C*, 118, 4899-4905.
- BEDFORD, E. E., SPADAVECCHIA, J., PRADIER, C. M. & GU, F. X. 2012. Surface Plasmon Resonance Biosensors Incorporating Gold Nanoparticles. *Macromolecular bioscience*.
- BENJAMIN, P. & WEAVER, C. The adhesion of evaporated metal films on glass. *Proceedings of the Royal Society of London A: Mathematical, Physical and Engineering Sciences*, 1961. The Royal Society, 516-531.
- BESINIS, A., DE PERALTA, T. & HANDY, R. D. 2014. The antibacterial effects of silver, titanium dioxide and silica dioxide nanoparticles compared to the dental disinfectant chlorhexidine on *Streptococcus mutans* using a suite of bioassays. *Nanotoxicology*, 8, 1-16.
- BESINIS, A., DE PERALTA, T. & HANDY, R. D. 2014. Inhibition of biofilm formation and antibacterial properties of a silver nano-coating on human dentine. *Nanotoxicology*, 8, 745-754.
- BHUSHAN, B. 2010. *Springer handbook of nanotechnology*, Springer.
- BINGHAM, J. M., ANKER, J. N., KRENO, L. E. & VAN DUYNE, R. P. 2010. Gas sensing with high-resolution localized surface plasmon resonance spectroscopy. *Journal of the American Chemical Society*, 132, 17358-17359.
- BINNS, C. 2010. *Introduction to nanoscience and nanotechnology*, Wiley.
- BOOZER, C., KIM, G., CONG, S., GUAN, H. W. & LONDERGAN, T. 2006. Looking towards label-free biomolecular interaction analysis in a high-throughput format: a review of new surface plasmon resonance technologies. *Current opinion in biotechnology*, 17, 400-405.
- BORISOV, S. M. & WOLFBEIS, O. S. 2008. Optical biosensors. *Chemical reviews*, 108, 423-461.
- BORN, M. & WOLF, E. 1999. *Principles of optics: electromagnetic theory of propagation, interference and diffraction of light*, CUP Archive.
- BOUWMEESTER, H., DEKKERS, S., NOORDAM, M. Y., HAGENS, W. I., BULDER, A. S., DE HEER, C., TEN VOORDE, S. E., WIJNHOFEN, S. W., MARVIN, H. J. & SIPS, A. J. 2009. Review of health safety aspects of

- nanotechnologies in food production. *Regulatory toxicology and pharmacology*, 53, 52-62.
- BRADFORD, A., HANDY, R. D., READMAN, J. W., ATFIELD, A. & MÜHLING, M. 2009. Impact of silver nanoparticle contamination on the genetic diversity of natural bacterial assemblages in estuarine sediments. *Environmental science & technology*, 43, 4530-4536.
- BRECHT, A. & GAUGLITZ, G. 1995. Optical probes and transducers. *Biosensors and Bioelectronics*, 10, 923-936.
- BRULS, D., EVERS, T., KAHLMAN, J., VAN LANKVELT, P., OVSYANKO, M., PELSSERS, E., SCHLEIPEN, J., DE THEIJE, F., VERSCHUREN, C. & VAN DER WIJK, T. 2009. Rapid integrated biosensor for multiplexed immunoassays based on actuated magnetic nanoparticles. *Lab Chip*, 9, 3504-3510.
- BRUNA, M. & BORINI, S. 2009. Optical constants of graphene layers in the visible range. *Applied Physics Letters*, 94, 031901-031901-3.
- BRUUS, H. 2004. Introduction to nanotechnology, Department of Micro and Nanotechnology, Technical University of Denmark.
- BRYAN-BROWN, G., YANG, F., BRADBERRY, G. & SAMBLES, J. 1991. Prism and grating coupling to long-range coupled-surface exciton-polaritons. *JOSA B*, 8, 765-769.
- BUNSHAH, R. F. 2001. Handbook of hard coatings.
- BUZEA, C., PACHECO, I. I. & ROBBIE, K. 2007. Nanomaterials and nanoparticles: sources and toxicity. *Biointerphases*, 2.
- BUZEA, C. & ROBBIE, K. 2005. State of the art in thin film thickness and deposition rate monitoring sensors. *Reports on Progress in Physics*, 68, 385.
- BYSTRZEJEWSKA-PIOTROWSKA, G., GOLIMOWSKI, J. & URBAN, P. L. 2009. Nanoparticles: their potential toxicity, waste and environmental management. *Waste Management*, 29, 2587-2595.
- CAMPAGNOLO, C., MEYERS, K. J., RYAN, T., ATKINSON, R. C., CHEN, Y.-T., SCANLAN, M. J., RITTER, G., OLD, L. J. & BATT, C. A. 2004. Real-Time, label-free monitoring of tumor antigen and serum antibody interactions. *Journal of biochemical and biophysical methods*, 61, 283-298.
- CHAN, W. C. W. 2007. Bio-applications of Nanoparticles, Springer.
- CHARLIER, J.-C., EKLUND, P., ZHU, J. & FERRARI, A. 2008. Electron and phonon properties of graphene: their relationship with carbon nanotubes. *Carbon nanotubes*. Springer.
- CHAUDHRY, Q., CASTLE, L. & WATKINS, R. 2010. Nanotechnologies in food, Royal Society of Chemistry.
- CHAUDHRY, Q., SCOTTER, M., BLACKBURN, J., ROSS, B., BOXALL, A., CASTLE, L., AITKEN, R. & WATKINS, R. 2008. Applications and implications of nanotechnologies for the food sector. *Food additives and contaminants*, 25, 241-258.
- CHEN, F. F. & CHANG, J. P. 2012. Lecture notes on principles of plasma processing, Springer Science & Business Media.

- CHEN, S.-J., SU, Y.-D., HSIU, F.-M., TSOU, C.-Y. & CHEN, Y.-K. 2005. Surface plasmon resonance phase-shift interferometry: real-time DNA microarray hybridization analysis. *Journal of Biomedical Optics*, 10, 034005-0340056.
- CHEN, W. & CHEN, J. 1980. Surface plasma wave study of submonolayer Cs and CsO covered Ag surfaces. *Surface science*, 91, 601-617.
- CHEN, W. & CHEN, J. 1981. Use of surface plasma waves for determination of the thickness and optical constants of thin metallic films. *JOSA*, 71, 189-191.
- CHEN, Y. & MING, H. 2012. Review of surface plasmon resonance and localized surface plasmon resonance sensor. *Photonic Sensors*, 2, 37-49.
- CHIEN, F. C. & CHEN, S. J. 2004. A sensitivity comparison of optical biosensors based on four different surface plasmon resonance modes. *Biosensors and Bioelectronics*, 20, 633-642.
- CHIN, C. W. S. 2011. Localized Surface Plasmon Resonance with the use of Silver and Titanium Oxide Nanostructures.
- CHOI, S. H. & BYUN, K. M. 2010. Investigation on an application of silver substrates for sensitive surface plasmon resonance imaging detection. *JOSA A*, 27, 2229-2236.
- CHOI, S. H., KIM, Y. L. & BYUN, K. M. 2011. Graphene-on-silver substrates for sensitive surface plasmon resonance imaging biosensors. *Optics express*, 19, 458-466.
- CHRISTINA BOOZER, G. K., SHUXIN CONG, HANNWEN GUAN, TIMOTHY LONDERGAN 2006. Looking towards label-free biomolecular interaction analysis in a high-throughput format: a review of new surface plasmon resonance technologies. *sciencedirect*, Volume 17, Issue 4, August 2006, Pages 400-405.
- CLARK JR, L. C. & LYONS, C. 2009. Electrode systems for continuous monitoring in cardiovascular surgery. *Annals of the New York Academy of Sciences*, 102, 29-45.
- COOPER, J. & CASS, T. 2004. *Biosensors*, Oxford University Press, USA.
- COOPER, M. A. 2009. *Label-free biosensors. Techniques and applications*. University of Cambridge.
- DAGHESTANI, H. N. & DAY, B. W. 2010. Theory and applications of surface plasmon resonance, resonant mirror, resonant waveguide grating and dual polarisation interferometry biosensors. *Sensors*, 10, 9630-9646.
- DAS, M., HOHERTZ, D., NIRWAN, R., BROLO, A. G., KAVANAGH, K. L. & GORDON, R. 2011. Improved Performance of Nanohole Surface Plasmon Resonance Sensors by the Integrated Response Method. *IEEE Photonics Journal*, 3, 441-449.
- DAVUT IBRAHIM MAHCICEK, B. E. M. E. Z. 2008. Sensitivity Investigation of Au Dot Arrays for Localized Surface Plasmon Resonance Based Biosensor Semester Project.
- DE BRUIJN, H. E., KOOYMAN, R. P. H. & GREVE, J. 1992. Choice of metal and wavelength for surface-plasmon resonance sensors: some considerations. *Applied optics*, 31, 440_1-442.

- DEKKERS, S., BOUWMEESTER, H., BOS, P. M., PETERS, R. J., RIETVELD, A. G. & OOMEN, A. G. 2013. Knowledge gaps in risk assessment of nanosilica in food: evaluation of the dissolution and toxicity of different forms of silica. *Nanotoxicology*, 7, 367-377.
- DENKOV, N., VELEV, O., KRALCHEVSKI, P., IVANOV, I., YOSHIMURA, H. & NAGAYAMA, K. 1992. Mechanism of formation of two-dimensional crystals from latex particles on substrates. *Langmuir*, 8, 3183-3190.
- DÍAZ-GONZÁLEZ, M., GONZÁLEZ-GARCÍA, M. B. & COSTA-GARCÍA, A. 2005. Recent advances in electrochemical enzyme immunoassays. *Electroanalysis*, 17, 1901-1918.
- DOSTÁLEK, J., HOMOLA, J. & MILER, M. 2005. Rich information format surface plasmon resonance biosensor based on array of diffraction gratings. *Sensors and Actuators B: Chemical*, 107, 154-161.
- DREZET, A., HOHENAU, A., KRENN, J. R., BRUN, M. & HUANT, S. 2007. Surface plasmon mediated near-field imaging and optical addressing in nanoscience. *Micron*, 38, 427-437.
- DU, B. A., LI, Z. P. & LIU, C. H. 2006. One-step homogeneous detection of DNA hybridization with gold nanoparticle probes by using a linear light-scattering technique. *Angewandte Chemie International Edition*, 45, 8022-8025.
- DUNCAN, T. V. 2011. Applications of nanotechnology in food packaging and food safety: barrier materials, antimicrobials and sensors. *Journal of colloid and interface science*, 363, 1-24.
- DUROU, C., GIRAUDOU, J.-C. & MOUTOU, C. 1973. Refractive indexes of aqueous solutions of copper (II) sulfate, zinc sulfate, silver nitrate, potassium chloride and sulfuric acid for helium-neon laser light at $\theta = 25^{\circ}$. *Journal of Chemical and Engineering Data*, 18, 289-290.
- EARP JR, R. L. 1998. Multiwavelength Surface Plasmon Resonance Sensor Designs for Chemical and Biochemical Detection.
- ECHTERMAYER, T., BRITNELL, L., JASNOS, P., LOMBARDO, A., GORBACHEV, R., GRIGORENKO, A., GEIM, A., FERRARI, A. & NOVOSELOV, K. 2011. Strong plasmonic enhancement of photovoltage in graphene. *Nature communications*, 2, 458.
- EI-BADAWY, A., FELDHAKE, D. & VENKATAPATHY, R. 2010. State of the Science Literature Review: Everything Nanosilver and More. Scientific, Technical, Research, Engineering and Modelling Support Final Report, United States Environmental Protection Agency.
- EKGASIT, S., THAMMACHAROEN, C. & KNOLL, W. 2004. Surface plasmon resonance spectroscopy based on evanescent field treatment. *Analytical chemistry*, 76, 561-568.
- ENOCH, S. & BONOD, N. 2012. Plasmonics: from basics to advanced topics.
- ESTEVEZ, M.-C., OTTE, M. A., SEPULVEDA, B. & LECHUGA, L. M. 2014. Trends and challenges of refractometric nanoplasmonic biosensors: A review. *Analytica chimica acta*, 806, 55-73.

EUROPE, F. A. W. 2013. Unseen Hazards From Nanotechnology to Nanotoxicity. EXPERIMENT 2012. surface plasmon resonance in a Thin Metal Film. laboratory.

FABIEN REMY-MARTINA, C., MARVEN EL OSTAB, GERALDINE LUCCHIB, RABAH ZEGGARIA, THERESE LEBLOISA, SOPHIE BELLONC, PATRICK DUCOROYB, WILFRID BOIREAU. 2012. Automated cancer marker characterization in human plasma using Surface Plasmon Resonance in Array combined with Mass Spectrometry (SUPRA-MS).

FAN, X., WHITE, I. M., SHOPOVA, S. I., ZHU, H., SUTER, J. D. & SUN, Y. 2008. Sensitive optical biosensors for unlabeled targets: A review. *Analytica chimica acta*, 620, 8-26.

FANO, U. 1941. The theory of anomalous diffraction gratings and of quasi-stationary waves on metallic surfaces (Sommerfeld's waves). *JOSA*, 31, 213-222.

FEDERICI, G., SHAW, B. J. & HANDY, R. D. 2007. Toxicity of titanium dioxide nanoparticles to rainbow trout (*Oncorhynchus mykiss*): Gill injury, oxidative stress and other physiological effects. *Aquatic Toxicology*, 84, 415-430.

FEHRENBACHER, M., WINNERL, S., SCHNEIDER, H., DÖRING, J., KEHR, S. C., ENG, L. M., HUO, Y., SCHMIDT, O. G., YAO, K. & LIU, Y. 2015. Plasmonic Superlensing in Doped GaAs. *Nano letters*.

FEN, Y. W., YUNUS, W. M. M. & YUSOF, N. A. 2011. Detection of mercury and copper ions using surface plasmon resonance optical sensor. *Sensors and Materials*, 23, 325-334.

FENGJUN, Z., KEHUA, Z., FAZHI, X., JIN, L., HONGFEI, D., WEI, Z. & ZEDA, M. 2013. Surface plasmon resonance induced reduction of high quality Ag/graphene composite at water/toluene phase for reduction of H₂O₂.

FERRARI, A. C. 2007. Raman spectroscopy of graphene and graphite: disorder, electron-phonon coupling, doping and nonadiabatic effects. *Solid state communications*, 143, 47-57.

FERRARI, A. C. & BASKO, D. M. 2013. Raman spectroscopy as a versatile tool for studying the properties of graphene. *Nature nanotechnology*, 8, 235-246.

FEYNMAN, R. P. 1960. There's plenty of room at the bottom. *Engineering and Science*, 23, 22-36.

FONTANA, E. 2004. Theoretical and experimental study of the surface plasmon resonance effect on a recordable compact disk. *Applied optics*, 43, 79-87.

FRANZOI, A. C., VIEIRA, I. C., DUPONT, J., SCHEEREN, C. W. & DE OLIVEIRA, L. F. 2009. Biosensor for luteolin based on silver or gold nanoparticles in ionic liquid and laccase immobilized in chitosan modified with cyanuric chloride. *Analyst*, 134, 2320-2328.

FRATZKE, S. B. 2010. Integration of microfluidics with surface plasmon resonance. California Polytechnic State University.

FRUK, L., KUHLMANN, J. & NIEMEYER, C. M. 2009. Analysis of heme-reconstitution of apoenzymes by means of surface plasmon resonance. *Chem. Commun.*, 230-232.

FUJII, E., KOIKE, T., NAKAMURA, K., SASAKI, S.-I., KURIHARA, K., CITTERIO, D., IWASAKI, Y., NIWA, O. & SUZUKI, K. 2002. Application of

an absorption-based surface plasmon resonance principle to the development of SPR ammonium ion and enzyme sensors. *Analytical chemistry*, 74, 6106-6110.

FUJIMURA, T., EDAMATSU, K., ITOH, T., SHIMADA, R., IMADA, A., KODA, T., CHIBA, N., MURAMATSU, H. & ATAKA, T. 1997. Scanning near-field optical images of ordered polystyrene particle layers in transmission and luminescence excitation modes. *Optics letters*, 22, 489-491.

GAO, C., LU, Z., LIU, Y., ZHANG, Q., CHI, M., CHENG, Q. & YIN, Y. 2012. Highly stable silver nanoplates for surface plasmon resonance biosensing. *Angewandte Chemie International Edition*, 51, 5629-5633.

GAO, S., KOSHIZAKI, N., TOKUHISA, H., KOYAMA, E., SASAKI, T., KIM, J. K., RYU, J., KIM, D. S. & SHIMIZU, Y. 2010. Highly stable Au nanoparticles with tunable spacing and their potential application in surface plasmon resonance biosensors. *Advanced Functional Materials*, 20, 78-86.

GARCIA, M. 2011. Surface plasmons in metallic nanoparticles: fundamentals and applications. *Journal of Physics D: Applied Physics*, 44, 283001.

GEIM, A. K. & NOVOSELOV, K. S. 2007. The rise of graphene. *Nature materials*, 6, 183-191.

GLOCKER, D. A. 1993. Influence of the plasma on substrate heating during low-frequency reactive sputtering of AlN. *Journal of Vacuum Science & Technology A*, 11, 2989-2993.

GOBI, K. V., SATO, Y. & MIZUTANI, F. 2001. Mediatorless Superoxide Dismutase Sensors Using Cytochrome c-Modified Electrodes: Xanthine Oxidase Incorporated Polyion Complex Membrane for Enhanced Activity and In Vivo Analysis. *Electroanalysis*, 13, 397-403.

GONZÁLEZ, A., NOGUEZ, C. & BARNARD, A. 2012. Map of the Structural and Optical Properties of Gold Nanoparticles at Thermal Equilibrium. *The Journal of Physical Chemistry C*, 116, 14170-14175.

GORTON, L. 2005. *Biosensors and modern biospecific analytical techniques*, Elsevier.

GREENLEY, M. 2012. *Design, Characterization and Evaluation of a Surface Plasmon Resonance Sensor*. Duke University.

GRIEGER, K. D., LAURENT, A., MISELJIC, M., CHRISTENSEN, F., BAUN, A. & OLSEN, S. I. 2012. Analysis of current research addressing complementary use of life-cycle assessment and risk assessment for engineered nanomaterials: have lessons been learned from previous experience with chemicals? *Journal of Nanoparticle Research*, 14, 1-23.

GRIGORENKO, A., POLINI, M. & NOVOSELOV, K. 2012. Graphene plasmonics. *Nature photonics*, 6, 749-758.

GROBE, A., RENN, O. & JAEGER, A. 2008. *Risk Governance of Nanotechnology Applications in Food and Cosmetics*. International Risk Governance Council, Geneva www.irgc.org/IMG/pdf/IRGC_Report_FINAL_For_Web.pdf.

GUBIN, S. P., KOKSHAROV, Y. A., KHOMUTOV, G. & YURKOV, G. Y. 2005. Magnetic nanoparticles: preparation, structure and properties. *Russian Chemical Reviews*, 74, 489.

- GUO, X. 2012. Surface plasmon resonance based biosensor technique: A review. *Journal of Biophotonics*.
- GWINN, M. R. & VALLYATHAN, V. 2006. Nanoparticles: health effects—pros and cons [Online]. Available: <http://www.ncbi.nlm.nih.gov/pmc/articles/PMC1764161/> [Accessed 12 1 2015].
- GWON, H. R. & LEE, S. H. 2010. Spectral and angular responses of surface plasmon resonance based on the Kretschmann prism configuration. *Materials transactions*, 51, 1150-1155.
- HACKENBERG, S., SCHERZED, A., KESSLER, M., HUMMEL, S., TECHNAU, A., FROELICH, K., GINZKEY, C., KOEHLER, C., HAGEN, R. & KLEINSASSER, N. 2011. Silver nanoparticles: evaluation of DNA damage, toxicity and functional impairment in human mesenchymal stem cells. *Toxicology letters*, 201, 27-33.
- HAES, A. J. & VAN DUYN, R. P. 2002. A nanoscale optical biosensor: sensitivity and selectivity of an approach based on the localized surface plasmon resonance spectroscopy of triangular silver nanoparticles. *Journal of the American Chemical Society*, 124, 10596-10604.
- HANNING, A., ROERAADE, J., DELROW, J. J. & JORGENSON, R. C. 1999. Enhanced sensitivity of wavelength modulated surface plasmon resonance devices using dispersion from a dye solution. *Sensors and Actuators B: Chemical*, 54, 25-36.
- HANSEN, P. S. 2006. Monoclonal antibody-based Surface Plasmon Resonance sensors for pathogen detection.
- HARTSTEIN, A., KIRTLEY, J. & TSANG, J. 1980. Enhancement of the infrared absorption from molecular monolayers with thin metal overlayers. *Physical Review Letters*, 45, 201-204.
- HASSAN, A., NABOK, A., RAY, A., LUCKE, A., SMITH, K., STIRLING, C. & DAVIS, F. 1999. Thin films of calix-4-resorcinarene deposited by spin coating and Langmuir–Blodgett techniques: determination of film parameters by surface plasmon resonance. *Materials Science and Engineering: C*, 8, 251-255.
- HEIDEMAN, R., KOOYMAN, R. & GREVE, J. 1991. Development of an optical waveguide interferometric immunosensor. *Sensors and Actuators B: Chemical*, 4, 297-299.
- HEITMANN, D. 2001. Radiative decay of surface plasmons excited by fast electrons on periodically modulated silver surfaces. *Journal of Physics C: Solid State Physics*, 10, 397.
- HEROLD, A. R. A. K. E. 2009. *Biosensors and Biodetection*, FDA Center for Devices and Radiological Health, Silver Spring, MD, USA, Humana Press, a part of Springer Science+Business Media, LLC 2009.
- HIBBINS, A. P., SAMBLES, J. R. & LAWRENCE, C. R. 1998. Surface plasmon-polariton study of the optical dielectric function of titanium nitride. *journal of modern optics*, 45, 2051-2062.
- HO, H. P., WU, S. Y., LAW, W. C. & CHINLON, L. Application of differential phase detection for sensitivity improvement in surface plasmon resonance sensors. *Biophotonics*, 2004. APBP 2004. The Second Asian and Pacific Rim Symposium on, 14-17 Dec. 2004 2004. 221-222.

- HODNIK, V. & ANDERLUH, G. 2009. Toxin detection by surface plasmon resonance. *Sensors*, 9, 1339-1354.
- HOMES, C., XU, Z., WEN, J. & GU, G. 2012. Effective medium approximation and the complex optical properties of the inhomogeneous superconductor $K_{0.8}Fe_{2-y}Se_2$. *Physical Review B*, 86, 144530.
- HOMOLA, J. 2003. Present and future of surface plasmon resonance biosensors. *Analytical and bioanalytical chemistry*, 377, 528-539.
- HOMOLA, J. 2006. *Surface plasmon resonance based sensors*, Springer.
- HOMOLA, J. 2008. Surface plasmon resonance sensors for detection of chemical and biological species. *Chemical reviews*, 108, 462-493.
- HOMOLA, J., KOUDELA, I. & YEE, S. S. 1999. Surface plasmon resonance sensors based on diffraction gratings and prism couplers: sensitivity comparison. *Sensors and Actuators B: Chemical*, 54, 16-24.
- HOMOLA, J., VAISOCHEROVÁ, H., DOSTÁLEK, J. & PILIARIK, M. 2005. Multi-analyte surface plasmon resonance biosensing. *Methods*, 37, 26-36.
- HOMOLA, J., YEE, S. S. & GAUGLITZ, G. 1999. Surface plasmon resonance sensors: review. *Sensors and Actuators B: Chemical*, 54, 3-15.
- HOOGVLIET, J. & VAN BENNEKOM, W. 2001. Gold thin-film electrodes: an EQCM study of the influence of chromium and titanium adhesion layers on the response. *Electrochimica acta*, 47, 599-611.
- HOOPER, I., SAMBLES, J., PITTER, M. & SOMEKH, M. 2006. Phase sensitive array detection with polarisation modulated differential sensing. *Sensors and Actuators B: Chemical*, 119, 651-655.
- HOSOKAWA, M., NOGI, K., NAITO, M. & YOKOYAMA, T. 2007. *Nanoparticle technology handbook*, Elsevier Science.
- HUANG, Y., HO, H., WU, S. & KONG, S. 2011. Detecting Phase Shifts in Surface Plasmon Resonance: A Review. *Advances in Optical Technologies*, 2012.
- HUBER, A., DEMARTIS, S. & NERI, D. 1999. The use of biosensor technology for the engineering of antibodies and enzymes. *Journal of Molecular Recognition*, 12, 198-216.
- HUTTER, E., FENDLER, J. & ROY, D. 2001. Surface plasmon resonance studies of gold and silver nanoparticles linked to gold and silver substrates by 2-aminoethanethiol and 1, 6-hexanedithiol. *The Journal of Physical Chemistry B*, 105, 11159-11168.
- INITIATIVE, N. N. 2012. NNI [Online]. Available: <http://www.nano.gov/nanotech-101/what/definition> [Accessed 17 3 2015].
- ISSA, B., OBAIDAT, I. M., ALBISS, B. A. & HAIK, Y. 2013. Magnetic nanoparticles: surface effects and properties related to biomedicine applications. *International journal of molecular sciences*, 14, 21266-21305.
- IWATA, T. & MAEDA, S. 2007. Simulation of an absorption-based surface-plasmon resonance sensor by means of ellipsometry. *Applied optics*, 46, 1575-1582.

- JAIN, P. K., HUANG, X., EL-SAYED, I. H. & EL-SAYED, M. A. 2007. Review of some interesting surface plasmon resonance-enhanced properties of noble metal nanoparticles and their applications to biosystems. *Plasmonics*, 2, 107-118.
- JAIN, P. K., HUANG, X., EL-SAYED, I. H. & EL-SAYED, M. A. 2008. Noble metals on the nanoscale: optical and photothermal properties and some applications in imaging, sensing, biology and medicine. *Accounts of Chemical Research*, 41, 1578-1586.
- JANG, D., LIM, D., CHAE, G.-H. & YOO, J. 2014. A novel algorithm based on the coefficient of determination of linear regression fitting to automatically find the optimum angle for miniaturized surface plasmon resonance measurement. *Sensors and Actuators B: Chemical*, 199, 488-492.
- JHA, R. & SHARMA, A. K. 2009. High-performance sensor based on surface plasmon resonance with chalcogenide prism and aluminum for detection in infrared. *Optics letters*, 34, 749-751.
- JOHNSON, P. & CHRISTY, R. 1974. Optical constants of transition metals: Ti, v, cr, mn, fe, co, ni and pd. *Physical Review B*, 9, 5056.
- JORGENSEN, R. & YEE, S. 1993. A fiber-optic chemical sensor based on surface plasmon resonance. *Sensors and Actuators B: Chemical*, 12, 213-220.
- JUSTIN PEATROSS, M. 2011. *Physics of Light and Optics*.
- KABASHIN, A. V., PATSKOVSKY, S. & GRIGORENKO, A. N. 2009. Phase and amplitude sensitivities in surface plasmon resonance bio and chemical sensing. *Optics express*, 17, 21191-21204.
- KANO, H. & KAWATA, S. 1994. Surface-plasmon sensor for absorption-sensitivity enhancement. *Applied optics*, 33, 5166-5170.
- KARAKOTI, A., HENCH, L. & SEAL, S. 2006. The potential toxicity of nanomaterials—the role of surfaces. *Jom*, 58, 77-82.
- KARLSSON, R. 2004. SPR for molecular interaction analysis: a review of emerging application areas. *Journal of Molecular Recognition*, 17, 151-161.
- KARLSSON, R. & FÄLT, A. 1997. Experimental design for kinetic analysis of protein-protein interactions with surface plasmon resonance biosensors. *Journal of immunological methods*, 200, 121-133.
- KAWAKAMI, S., KAWASHIMA, T. & SATO, T. 1999. Mechanism of shape formation of three-dimensional periodic nanostructures by bias sputtering. *Applied physics letters*, 74, 463-465.
- KELLY, K. L., CORONADO, E., ZHAO, L. L. & SCHATZ, G. C. 2003. The optical properties of metal nanoparticles: the influence of size, shape and dielectric environment. *The Journal of Physical Chemistry B*, 107, 668-677.
- KHARDANI, M., BOUAÏCHA, M. & BESSAÏS, B. 2007. Bruggeman effective medium approach for modelling optical properties of porous silicon: comparison with experiment. *physica status solidi (c)*, 4, 1986-1990.
- KIHM, K., CHEON, S., PARK, J., KIM, H., LEE, J., KIM, I. & YI, H. 2012. Surface plasmon resonance (SPR) reflectance imaging: Far-field recognition of near-field phenomena. *Optics and Lasers in Engineering*.
- KIM, J. S., KUK, E., YU, K. N., KIM, J.-H., PARK, S. J., LEE, H. J., KIM, S. H., PARK, Y. K., PARK, Y. H. & HWANG, C.-Y. 2007. Antimicrobial effects of

- silver nanoparticles. *Nanomedicine: Nanotechnology, Biology and Medicine*, 3, 95-101.
- KLAINÉ, S. J., KOELMANS, A. A., HORNE, N., CARLEY, S., HANDY, R. D., KAPUSTKA, L., NOWACK, B. & VON DER KAMMER, F. 2012. Paradigms to assess the environmental impact of manufactured nanomaterials. *Environmental Toxicology and Chemistry*, 31, 3-14.
- KODADEK, T. 2001. Protein microarrays: prospects and problems. *Chemistry & biology*, 8, 105-115.
- KOGELNIK, H. 1969. Coupled wave theory for thick hologram gratings. *Bell System Technical Journal*, 48, 2909-2947.
- KOLOMENSKII, A. A., GERSHON, P. D. & SCHUESSLER, H. A. 2000. Surface-plasmon resonance spectrometry and characterization of absorbing liquids. *Applied optics*, 39, 3314-3320.
- KOTSEV, S., DUSHKIN, C., ILEV, I. & NAGAYAMA, K. 2003. Refractive index of transparent nanoparticle films measured by surface plasmon microscopy. *Colloid and Polymer Science*, 281, 343-352.
- KRALCHEVSKY, P. & NAGAYAMA, K. 2001. Particles at fluid interfaces and membranes: attachment of colloid particles and proteins to interfaces and formation of two-dimensional arrays, Elsevier.
- KRAVETS, V., SCHEDIN, F., JALIL, R., BRITNELL, L., GORBACHEV, R., ANSELL, D., THACKRAY, B., NOVOSELOV, K., GEIM, A. & KABASHIN, A. 2013. Singular phase nano-optics in plasmonic metamaterials for label-free single-molecule detection. *Nature materials*, 12, 304-309.
- KRENO, L. E., HUPP, J. T. & VAN DUYNÉ, R. P. 2010. Metal-organic framework thin film for enhanced localized surface plasmon resonance gas sensing. *Analytical chemistry*, 82, 8042-8046.
- KRETSCHMANN, E. 1971. Die bestimmung optischer konstanten von metallen durch anregung von oberflächenplasmaschwingungen. *Zeitschrift für Physik A Hadrons and Nuclei*, 241, 313-324.
- KRETSCHMANN, E. 1972. Decay of non radiative surface plasmons into light on rough silver films. Comparison of experimental and theoretical results. *Optics Communications*, 6, 185-187.
- KRETSCHMANN, E. & RAETHER, H. 1968. Radiative decay of non radiative surface plasmons excited by light. *Zeitschrift Fuer Naturforschung, Teil A*, 23, 2135.
- KRISHNA PODAGATLAPALLI, G., HAMAD, S., TEWARI, S. P., SREEDHAR, S., PRASAD, M. D. & VENUGOPAL RAO, S. 2013. Silver nano-entities through ultrafast double ablation in aqueous media for surface enhanced Raman scattering and photonics applications. *Journal of Applied Physics*, 113, 073106-073106-14.
- KRISHNAMOORTHY, G. 2010. Lab-on-a-chip surface plasmon resonance biosensor for multiplex bioassays.
- KRIZKOVA, S., HUSKA, D., BEKLOVA, M., HUBALEK, J., ADAM, V., TRNKOVA, L. & KIZEK, R. 2010. Protein-based electrochemical biosensor for detection of silver (I) ions. *Environmental Toxicology and Chemistry*, 29, 492-496.

- KURIHARA, K., NAKAMURA, K., HIRAYAMA, E. & SUZUKI, K. 2002. An absorption-based surface plasmon resonance sensor applied to sodium ion sensing based on an ion-selective optode membrane. *Analytical chemistry*, 74, 6323-6333.
- KURIHARA, K. & SUZUKI, K. 2002. Theoretical understanding of an absorption-based surface plasmon resonance sensor based on Kretschmann's theory. *Analytical chemistry*, 74, 696-701.
- KWON, M. J., LEE, J., WARK, A. W. & LEE, H. J. 2012. Nanoparticle-enhanced surface plasmon resonance detection of proteins at attomolar concentrations: comparing different nanoparticle shapes and sizes. *Analytical chemistry*, 84, 1702-1707.
- KYO, M., USUI-AOKI, K. & KOGA, H. 2005. Label-free detection of proteins in crude cell lysate with antibody arrays by a surface plasmon resonance imaging technique. *Analytical chemistry*, 77, 7115-7121.
- LAHAV, A., AUSLENDER, M. & ABDULHALIM, I. 2008. Sensitivity enhancement of guided-wave surface-plasmon resonance sensors. *Optics letters*, 33, 2539-2541.
- LASSEN, B. & MALMSTEN, M. 1997. Competitive protein adsorption at plasma polymer surfaces. *Journal of colloid and interface science*, 186, 9-16.
- LAW, W.-C., YONG, K.-T., BAEV, A., HU, R. & PRASAD, P. N. 2009. Nanoparticle enhanced surface plasmon resonance biosensing: application of gold nanorods. *Optics express*, 17, 19041-19046.
- LAZAROV, G. S., DENKOV, N. D., VELEV, O. D., KRALCHEVSKY, P. A. & NAGAYAMA, K. 1994. Formation of two-dimensional structures from colloidal particles on fluorinated oil substrate. *J. Chem. Soc., Faraday Trans.*, 90, 2077-2083.
- LE PERSON, J., COLAS, F., COMPERE, C., LEHAITRE, M., ANNE, M. L., BOUSSARD-PLÉDEL, C., BUREAU, B., ADAM, J. L., DEPUTIER, S. & GUILLOUX-VIRY, M. 2008. Surface plasmon resonance in chalcogenide glass-based optical system. *Sensors and Actuators B: Chemical*, 130, 771-776.
- LEE, J. L. 2009. Better living through plasmonics: Mixing light with nanotechnology could help treat cancer and build faster computers. *Science News*, 176, 26-29.
- LEE*2, H. R. G. A. S. H. 2010. Spectral and Angular Responses of Surface Plasmon Resonance Based on the Kretschmann Prism Configuratio. *Materials Transactions*, 51, 6.
- LEROY, F., ROUSSEAU, A., PAYAN, S., DOGHECHE, E., JENKINS, D., DECOSTER, D. & MAGLIONE, M. 2013. Guided-wave electro-optic characterization of BaTiO₃ thin films using the prism coupling technique. *Optics Letters*, 38, 1037-1039.
- LI, B., PAN, G., AWAN, S. A. & AVENT, N. 2014. Techniques for Production of Large Area Graphene for Electronic and Sensor Device Applications. *Graphene and 2D Materials*, 1.
- LI, B., PAN, G., JAMIL, N. Y., AL TAAN, L., AWAN, S. & AVENT, N. 2015. Shielding technique for deposition of Au electrical contacts on graphene by sputtering. *Journal of Vacuum Science & Technology A*, 33, 030601.

- LI, X., CAI, W., AN, J., KIM, S., NAH, J., YANG, D., PINER, R., VELAMAKANNI, A., JUNG, I. & TUTUC, E. 2009. Large-area synthesis of high-quality and uniform graphene films on copper foils. *Science*, 324, 1312-1314.
- LIDE, D. R. 2010. *CRC handbook of chemistry and physics*, CRC press Boca Raton, FL.
- LIEDBERG, B., NYLANDER, C. & LUNDSTRÖM, I. 1995. Biosensing with surface plasmon resonance--how it all started. *Biosensors and Bioelectronics*, 10, i-ix.
- LIEDBERG, B., NYLANDER, C. & LUNSTRÖM, I. 1983. Surface plasmon resonance for gas detection and biosensing. *Sensors and Actuators*, 4, 299-304.
- LIGLER, F. S. & TAITT, C. A. R. 2002. *Optical biosensors: present and future*, Gulf Professional Publishing.
- LIGLER, F. S. & TAITT, C. R. 2008. *Optical biosensors: today and tomorrow*, Elsevier Science.
- LIN, Y. C. 2014. A fiber-optic alcohol sensor based on surface plasmon resonance. *Microwave and Optical Technology Letters*, 56, 766-769.
- LISMONT, M. & DREESEN, L. 2012. Comparative study of Ag and Au nanoparticles biosensors based on surface plasmon resonance phenomenon. *Materials Science and Engineering: C*.
- LIU, G. L., YIN, Y., KUNCHAKARRA, S., MUKHERJEE, B., GERION, D., JETT, S. D., BEAR, D. G., GRAY, J. W., ALIVISATOS, A. P. & LEE, L. P. 2006. A nanoplasmonic molecular ruler for measuring nuclease activity and DNA footprinting. *Nature nanotechnology*, 1, 47-52.
- LIU, Q., QI, Z. M., ZHANG, Z. & LU, D. F. Theoretical and experimental investigation of ultrahigh sensitivity of wavelength-interrogated infrared surface plasmon resonance sensors. 2011. *IEEE*, 2126-2129.
- LIU, Q. & WANG, P. 2009. *Cell-based biosensors: principles and applications*, Artech House.
- LIU, Q., WU, C., CAI, H., HU, N., ZHOU, J. & WANG, P. 2014. Cell-based biosensors and their application in biomedicine. *Chemical reviews*, 114, 6423-6461.
- LOCKETT, M. R., WEIBEL, S. C., PHILLIPS, M. F., SHORTREED, M. R., SUN, B., CORN, R. M., HAMERS, R. J., CERRINA, F. & SMITH, L. M. 2008. Carbon-on-metal films for surface plasmon resonance detection of DNA arrays. *Journal of the American Chemical Society*, 130, 8611-8613.
- LOK, C.-N., HO, C.-M., CHEN, R., HE, Q.-Y., YU, W.-Y., SUN, H., TAM, P. K.-H., CHIU, J.-F. & CHE, C.-M. 2007. Silver nanoparticles: partial oxidation and antibacterial activities. *JBIC Journal of Biological Inorganic Chemistry*, 12, 527-534.
- LUNDSTRÖM, I. 2014. From a Laboratory Exercise for Students to a Pioneering Biosensing Technology. *Plasmonics*, 9, 741-751.
- LUPPA, P. B., SOKOLL, L. J. & CHAN, D. W. 2001. Immunosensors—principles and applications to clinical chemistry. *Clinica Chimica Acta*, 314, 1-26.

- LYKLEMA, J. 2005. *Fundamentals of interface and colloid science: soft colloids*, Academic press.
- LYON, L. A., MUSICK, M. D. & NATAN, M. J. 1998. Colloidal Au-enhanced surface plasmon resonance immunosensing. *Analytical chemistry*, 70, 5177-5183.
- MAALOULI, N., GOUGET-LAEMMEL, A. C., PINCHEMEL, B., BOUAZAOU, M., CHAZALVIEL, J.-N., OZANAM, F. O., YANG, Y., BURKHARD, P., BOUKHERROUB, R. & SZUNERITS, S. 2011. Development of a metal-chelated plasmonic interface for the linking of his-peptides with a droplet-based surface plasmon resonance read-off scheme. *Langmuir*, 27, 5498-5505.
- MAENOSONO, S., DUSHKIN, C. D., SAITA, S. & YAMAGUCHI, Y. 2000. Optical memory media based on excitation-time dependent luminescence from a thin film of semiconductor nanocrystals. *Japanese Journal of Applied Physics*, 39, 4006.
- MAHARANA, P. K. & JHA, R. 2012. Chalcogenide prism and graphene multilayer based surface plasmon resonance affinity biosensor for high performance. *Sensors and Actuators B: Chemical*.
- MAHARANA, P. K., SRIVASTAVA, T. & JHA, R. 2014. On the Performance of Highly Sensitive and Accurate Graphene-on-Aluminum and Silicon-Based SPR Biosensor for Visible and Near Infrared. *Plasmonics*, 9, 1113-1120.
- MAIER, S. A. 2007. *Plasmonics: fundamentals and applications*, Springer.
- MANERA, M., SPADAVECCHIA, J., LEONE, A., QUARANTA, F., RELLA, R., DELL'ATTI, D., MINUNNI, M., MASCINI, M. & SICILIANO, P. 2008. Surface plasmon resonance imaging technique for nucleic acid detection. *Sensors and Actuators B: Chemical*, 130, 82-87.
- MANNELLI, I., COURTOIS, V., LECARUYER, P., ROGER, G., MILLOT, M.-C., GOOSSENS, M. & CANVA, M. 2006. Surface plasmon resonance imaging (SPRI) system and real-time monitoring of DNA biochip for human genetic mutation diagnosis of DNA amplified samples. *Sensors and Actuators B: Chemical*, 119, 583-591.
- MAPPS, D., CHANDRASEKHAR, R., GRADY, K., CAMBRIDGE, J. & DOOLE, R. 1997. Magnetic properties of NdFeB thin films on platinum underlayers. *Magnetics, IEEE Transactions on*, 33, 3007-3009.
- MARAMBIO-JONES, C. & HOEK, E. M. 2010. A review of the antibacterial effects of silver nanomaterials and potential implications for human health and the environment. *Journal of Nanoparticle Research*, 12, 1531-1551.
- MARIJNISSEN, J. & GRADON, L. 2009. *Nanoparticles in medicine and environment: inhalation and health effects*, Springer.
- MARIN, A., COJOCARIU, C., CONSTANTIN, D. & ANDREI, O. C. 2011. **BIOSENSORS BASED ON SURFACE PLASMON RESONANCE PHENOMENON: A THEORETICAL REVIEW.**
- MARKS, R. S. 2007. *Handbook of biosensors and biochips*.
- MARUSOV, G. P., SWEATT, A. J., PIETROSIMONE, K., BENSON, D. R., GEARY, S. J., SILBART, L. K., CHALLA, S., LAGOY, J., LAWRENCE, D. A. & LYNES, M. 2011. A Microarray Biosensor for Multiplexed Detection of

- Microbes Using Grating-Coupled Surface Plasmon Resonance Imaging. Environmental science & technology.
- MATCHESWALA, A. M. 2010. Gold nanospheres and gold nanorods as localized surface plasmon resonance sensors.
- MATHEMATICS 2012. calculation and equations. llll, 000.
- MATSUBARA, K., KAWATA, S. & MINAMI, S. 1988. A compact surface plasmon resonance sensor for measurement of water in process. Applied spectroscopy, 42, 1375-1379.
- MATSUBARA, K., KAWATA, S. & MINAMI, S. 1988. Optical chemical sensor based on surface plasmon measurement. Applied optics, 27, 1160-1163.
- MATTOX, D. M. 2010. Handbook of physical vapor deposition (PVD) processing, William Andrew.
- MAYNARD, A. D. & PUI, D. Y. H. 2007. Nanotechnology and occupational health, Springer.
- MILLER, J. C. 2005. The handbook of nanotechnology: business, policy and intellectual property law, Wiley.
- MILLER, J. C., SERRATO, R., REPRESAS-CARDENAS, J. M. & KUNDAHL, G. 2004. The handbook of nanotechnology: business, policy and intellectual property law, Wiley.
- MINAMI, T. 2008. Present status of transparent conducting oxide thin-film development for indium-tin-oxide (ITO) substitutes. Thin Solid Films, 516, 5822-5828.
- MIYANO, K., ASANO, K. & SHIMOMURA, M. 1991. Adsorption kinetics of water-soluble polymers onto a spread monolayer. Langmuir, 7, 444-445.
- MONZÓN-HERNÁNDEZ, D., VILLATORO, J., TALAVERA, D. & LUNA-MORENO, D. 2004. Optical-fiber surface-plasmon resonance sensor with multiple resonance peaks. Applied optics, 43, 1216-1220.
- MOORE, M. 2006. Do nanoparticles present ecotoxicological risks for the health of the aquatic environment? Environment International, 32, 967-976.
- MOREIRA, C., LIMA, A. & NEFF, H. Influence of temperature effects on sensitivity of surface Plasmon resonance sensors. 2008. IEEE, 170-175.
- MORGAN, H. & TAYLOR, D. M. 1994. Surface plasmon resonance microscopy: Reconstructing a three-dimensional image. Applied physics letters, 64, 1330-1331.
- MORGAN, I. J., HENRY, R. P. & WOOD, C. M. 1997. The mechanism of acute silver nitrate toxicity in freshwater rainbow trout (*Oncorhynchus mykiss*) is inhibition of gill Na^+ and Cl^- transport. Aquatic Toxicology, 38, 145-163.
- MORONES, J. R., ELECHIGUERRA, J. L., CAMACHO, A., HOLT, K., KOURI, J. B., RAMÍREZ, J. T. & YACAMAN, M. J. 2005. The bactericidal effect of silver nanoparticles. Nanotechnology, 16, 2346.
- MORRISON JR, C. F. 1981. Magnetically enhanced sputtering device. Google Patents.
- MULLETT, W. M., LAI, E. P. & YEUNG, J. M. 2000. Surface plasmon resonance-based immunoassays. Methods, 22, 77-91.

- MURPHY, C. J. 2007. Biosensors: Plasmons spring into action. *Nature materials*, 6, 259-260.
- MURRAY, W. A. & BARNES, W. L. 2007. Plasmonic materials. *Advanced materials*, 19, 3771-3782.
- NAIR, R., BLAKE, P., GRIGORENKO, A., NOVOSELOV, K., BOOTH, T., STAUBER, T., PERES, N. & GEIM, A. 2008. Fine structure constant defines visual transparency of graphene. *Science*, 320, 1308-1308.
- NAKKACH, M., LECARUYER, P., BARDIN, F., SAKLY, J., LAKHDAR, Z. B. & CANVA, M. 2008. Absorption and related optical dispersion effects on the spectral response of a surface plasmon resonance sensor. *Applied optics*, 47, 6177-6182.
- NARAOKA, R. & KAJIKAWA, K. 2005. Phase detection of surface plasmon resonance using rotating analyzer method. *Sensors and Actuators B: Chemical*, 107, 952-956.
- NASH, D. & SAMBLES, J. 1996. Surface plasmon-polariton study of the optical dielectric function of silver. *Journal of modern optics*, 43, 81-91.
- NEL, A. E., MÄDLER, L., VELEGOL, D., XIA, T., HOEK, E. M., SOMASUNDARAN, P., KLAESSIG, F., CASTRANOVA, V. & THOMPSON, M. 2009. Understanding biophysicochemical interactions at the nano-bio interface. *Nature materials*, 8, 543-557.
- NELSON, S., JOHNSTON, K. S. & YEE, S. S. 1996. High sensitivity surface plasmon resonance sensor based on phase detection. *Sensors and Actuators B: Chemical*, 35, 187-191.
- NEVES-PETERSEN, M. T., SNABE, T., KLITGAARD, S., DUROUX, M. & PETERSEN, S. B. 2006. Photonic activation of disulfide bridges achieves oriented protein immobilization on biosensor surfaces. *Protein science*, 15, 343-351.
- NICO J. DE MOL, M. J. E. F. 2010. *Surface Plasmon Resonance Methods and Protocols*, Springer Science+Business Media, LLC 2010.
- NIKLASSON, G. A., GRANQVIST, C. & HUNDERI, O. 1981. Effective medium models for the optical properties of inhomogeneous materials. *Applied Optics*, 20, 26-30.
- NISHIKAWA, T., YAMASHITA, H., NAKAMURA, M., HASUI, R., MATSUSHITA, T. & AOYAMA, S. Development of new localized surface plasmon resonance sensor with nanoimprinting technique. 2006. *IEEE*, 262-265.
- NORRIS, D. J., HAN, S. E., BHAN, A., NAGPAL, P., LINDQUIST, N. C. & OH, S.-H. 2009. Replication of patterned thin-film structures for use in plasmonics and metamaterials. *Google Patents*.
- NOUAILHAT, A. 2010. *An Introduction to Nanosciences and Nanotechnology*, Wiley-ISTE.
- NOVOSELOV, K., GEIM, A. K., MOROZOV, S., JIANG, D., ZHANG, Y., DUBONOS, S., GRIGORIEVA, I. & FIRSOV, A. 2004. Electric field effect in atomically thin carbon films. *Science*, 306, 666-669.

- NUNES, A., MAJKRZAK, C. & BERKOWITZ, A. 1983. Polarized neutron study of the magnetization density distribution within a CoFe₂O₄ colloidal particle. *Journal of Magnetism and Magnetic Materials*, 39, 59-63.
- NUSTER, R., PALTAUF, G. & BURGHOLZER, P. 2007. Comparison of surface plasmon resonance devices for acoustic wave detection in liquid. *Optics express*, 15, 6087-6095.
- OLIVEIRA, L. C., MELCHER, E. U. K., THIRSTRUP, C., LIMA, A. M. N., MOREIRA, C. S. & NEFF, H. F. A surface plasmon resonance biosensor for angular and wavelength operation. *Instrumentation and Measurement Technology Conference (I2MTC), 2012 IEEE International*, 13-16 May 2012 2012. 1214-1219.
- OMAR, O., RAY, A., HASSAN, A. & DAVIS, F. 1997. Resorcinol calixarenes (resorcarenes): Langmuir-Blodgett films and optical properties. *Supramolecular Science*, 4, 417-421.
- OTTO, A. 1968. Excitation of nonradiative surface plasma waves in silver by the method of frustrated total reflection. *Zeitschrift für Physik A Hadrons and Nuclei*, 216, 398-410.
- PAL, S., TAK, Y. K. & SONG, J. M. 2007. Does the antibacterial activity of silver nanoparticles depend on the shape of the nanoparticle? A study of the gram-negative bacterium *Escherichia coli*. *Applied and environmental microbiology*, 73, 1712-1720.
- PALIK, E. D. 1998. *Handbook of optical constants of solids*, Academic press.
- PALUMBO, M., NAGEL, J. & PETTY, M. C. 2005. Surface plasmon resonance detection of metal ions: layer-by-layer assembly of polyelectrolyte sensing layers on a multichannel chip. *Sensors Journal, IEEE*, 5, 1159-1164.
- PAN, G., LI, B., HEATH, M., HORSELL, D., WEARS, M. L., AL TAAN, L. & AWAN, S. 2013. Transfer-free growth of graphene on SiO₂ insulator substrate from sputtered carbon and nickel films. *Carbon*, 65, 349-358.
- PENG, W., LIU, Y., FANG, P., LIU, X., GONG, Z., WANG, H. & CHENG, F. 2014. Compact surface plasmon resonance imaging sensing system based on general optoelectronic components. *Optics express*, 22, 6174-6185.
- PETERSON, A. W., HALTER, M., TONA, A. & PLANT, A. L. 2014. High resolution surface plasmon resonance imaging for single cells. *BMC Cell Biology*, 15, 35.
- PETRYAYEVA, E. & KRULL, U. J. 2011. Localized Surface Plasmon Resonance: Nanostructures, Bioassays and Biosensing-A Review. *Analytica chimica acta*.
- PETTERSSON, L. A., ROMAN, L. S. & INGANAS, O. 1999. Modeling photocurrent action spectra of photovoltaic devices based on organic thin films. *Journal of Applied Physics*, 86, 487-496.
- PILIARIK, M., HOMOLA, J., MANÍKOVÁ, Z. & ČTYROKÝ, J. 2003. Surface plasmon resonance sensor based on a single-mode polarisation-maintaining optical fiber. *Sensors and Actuators B: Chemical*, 90, 236-242.
- PIRKLE, A., CHAN, J., VENUGOPAL, A., HINOJOS, D., MAGNUSON, C., MCDONNELL, S., COLOMBO, L., VOGEL, E., RUOFF, R. & WALLACE, R. 2011. The effect of chemical residues on the physical and electrical properties of

- chemical vapor deposited graphene transferred to SiO₂. *Applied Physics Letters*, 99, 122108.
- PITTER, M., GOH, J., SOMEKH, M., HAYES-GILL, B., CLARK, M. & MORGAN, S. 2003. Phase-sensitive CMOS photo-circuit array for modulated thermorefectance measurements. *Electronics Letters*, 39, 1339-1340.
- POCKRAND, I. 1978. Surface plasma oscillations at silver surfaces with thin transparent and absorbing coatings. *Surface science*, 72, 577-588.
- POCKRAND, I., SWALEN, J., GORDON II, J. & PHILPOTT, M. 1978. Surface plasmon spectroscopy of organic monolayer assemblies. *Surface science*, 74, 237-244.
- POLAND, C. A., DUFFIN, R., KINLOCH, I., MAYNARD, A., WALLACE, W. A., SEATON, A., STONE, V., BROWN, S., MACNEE, W. & DONALDSON, K. 2008. Carbon nanotubes introduced into the abdominal cavity of mice show asbestos-like pathogenicity in a pilot study. *Nature nanotechnology*, 3, 423-428.
- POPESCU, A., SAVASTRU, R. & SAVASTRU, D. 2011. Application of vitreous as-s-se chalcogenides as active layer in surface plasmon resonance configuration. *Digest Journal of Nanomaterials and Biostructures*, 6, 1245-1252.
- POPOV, I. A., BOZHENKO, K. V. & BOLDYREV, A. I. 2012. Is graphene aromatic? *Nano Research*, 5, 117-123.
- RAETHER, H. 1988. *Surface Plasmon on Smooth and Rough Surfaces and on Gratings*, Berlin Heidelberg New York London Paris Tokyo, Springer-Verlag.
- RAI, M., YADAV, A. & GADE, A. 2009. Silver nanoparticles as a new generation of antimicrobials. *Biotechnology advances*, 27, 76-83.
- RAMPRASAD, R., ZURCHER, P., PETRAS, M., MILLER, M. & RENAUD, P. 2004. Magnetic properties of metallic ferromagnetic nanoparticle composites. *Journal of Applied Physics*, 96, 519-529.
- RAN, B. & LIPSON, S. 2006. Comparison between sensitivities of phase and intensity detection in surface plasmon resonance. *Optics express*, 14, 5641-5650.
- RASCHKE, G., KOWARIK, S., FRANZL, T., SÖNNICHSEN, C., KLAR, T., FELDMANN, J., NICHTL, A. & KÜRZINGER, K. 2003. Biomolecular recognition based on single gold nanoparticle light scattering. *Nano letters*, 3, 935-938.
- RAY, A., HASSAN, A., SAATCHI, M. & COOK, M. 1997. Surface plasmon resonance studies on Langmuir-Blodgett films of novel octa-substituted metal-free phthalocyanine molecules. *Philosophical Magazine Part B*, 76, 961-971.
- RAYLEIGH, L. 1907. On the dynamical theory of gratings. *Proceedings of the Royal Society of London. Series A, Containing Papers of a Mathematical and Physical Character*, 79, 399-416.
- RAZ, S. R., LEONTARIDOU, M., BREMER, M. G., PETERS, R. & WEIGEL, S. 2012. Development of surface plasmon resonance-based sensor for detection of silver nanoparticles in food and the environment. *Analytical and bioanalytical chemistry*, 403, 2843-2850.
- RAZA, S., YAN, W., STENGER, N., WUBS, M. & MORTENSEN, N. A. 2013. Blueshift of the surface plasmon resonance in silver nanoparticles: substrate effects. *Optics express*, 21, 27344-27355.

- REGATOS, D., FARIÑA, D., CALLE, A., CEBOLLADA, A., SEPÚLVEDA, B., ARMELLES, G. & LECHUGA, L. M. 2010. Au/Fe/Au multilayer transducers for magneto-optic surface plasmon resonance sensing. *Journal of Applied Physics*, 108, 054502.
- RENGER, J. 2006. Excitation, interaction and scattering of localized and propagating surface polaritons. *Saechsische Landesbibliothek-Staats-und Universitaetsbibliothek Dresden*.
- RHYKERD JR, C., CUSHMAN, J. H. & LOW, P. 1991. Application of multiple-angle-of-incidence ellipsometry to the study of thin fluid films adsorbed on surfaces. *Langmuir*, 7, 2219-2229.
- RISKIN, M., TEL-VERED, R., FRASCONI, M., YAVO, N. & WILLNER, I. 2010. Stereoselective and Chiroselective Surface Plasmon Resonance (SPR) Analysis of Amino Acids by Molecularly Imprinted Au-Nanoparticle Composites. *Chemistry-A European Journal*, 16, 7114-7120.
- RITCHIE, R. 1957. Plasma losses by fast electrons in thin films. *Physical Review*, 106, 874.
- RODRIGUEZ-MOZAZ, S., DE ALDA, M. J. L. & BARCELÓ, D. 2006. Biosensors as useful tools for environmental analysis and monitoring. *Analytical and bioanalytical chemistry*, 386, 1025-1041.
- RODUNER, E. 2006. Size matters: why nanomaterials are different. *Chem. Soc. Rev.*, 35, 583-592.
- ROH, S., CHUNG, T. & LEE, B. 2011. Overview of the characteristics of micro- and nano-structured surface plasmon resonance sensors. *Sensors*, 11, 1565-1588.
- ROHDE, F. & PORCAR, R. A localized surface plasmon sensor for early cancer detection. *BioPhotonics, 2011 International Workshop on, 8-10 June 2011* 2011. 1-3.
- ROMAN, L. 2004. Piezoelectric thin films for Bulk Acoustic Wave resonator applications: From processing to microwave filters. *ÉCOLE POLYTECHNIQUE FÉDÉRALE DE LAUSANNE*.
- ROTELLO, V. M. 2004. *Nanoparticles: building blocks for nanotechnology*, Springer.
- SALAH, N. H., JENKINS, D. & HANDY, R. 2014. Graphene and its Influence in the Improvement of Surface Plasmon Resonance (SPR) Based Sensors: a Review.
- SALAH, N. H., JENKINS, D., PANINA, L., HANDY, R., PAN, G. & AWAN, S. 2012. Self-sensing surface plasmon resonance for the detection of metallic nanoparticles.
- SALAZAR, A., CAMACHO-LEÓN, S., ROSSETTO, O. & MARTÍNEZ-CHAPA, S. Electromagnetic modeling of surface plasmon resonance with Kretschmann configuration for biosensing applications in a CMOS-compatible interface. *SPIE OPTO, 2013. International Society for Optics and Photonics*, 86190V-86190V-8.
- SALIHOGU, O., BALCI, S. & KOCABAS, C. 2012. Plasmon-polaritons on graphene-metal surface and their use in biosensors. *Applied Physics Letters*, 100, 213110-213110-5.

- SAMBLES, J., BRADBURY, G. & YANG, F. 1991. Optical excitation of surface plasmons: an introduction. *Contemporary physics*, 32, 173-183.
- SASSOLAS, A., LECA-BOUVIER, B. D. & BLUM, L. J. 2008. DNA biosensors and microarrays. *Chemical reviews*, 108, 109-139.
- SATTLER, K. D., SATTLER, K. D., SATTLER, K. D. & PHYSICIST, F. 2010. *Handbook of nanophysics*, CRC press.
- SCHOLARS, W. W. I. C. F. 2015. Nanotechnology consumer product inventory [Online]. Available: <http://www.nanotech-project.org> [Accessed 25 5 2015].
- SCHUCK, P. 1997. Use of surface plasmon resonance to probe the equilibrium and dynamic aspects of interactions between biological macromolecules 1. *Annual review of biophysics and biomolecular structure*, 26, 541-566.
- SHAHVERDI, A. R., FAKHIMI, A., SHAHVERDI, H. R. & MINAIAN, S. 2007. Synthesis and effect of silver nanoparticles on the antibacterial activity of different antibiotics against *Staphylococcus aureus* and *Escherichia coli*. *Nanomedicine: Nanotechnology, Biology and Medicine*, 3, 168-171.
- SHALAEV, V. M. & KAWATA, S. 2007. *Nanophotonics with surface plasmons*, Elsevier Science.
- SHANKARAN, D. R., GOBI, K. V. & MIURA, N. 2007. Recent advancements in surface plasmon resonance immunosensors for detection of small molecules of biomedical, food and environmental interest. *Sensors and Actuators B: Chemical*, 121, 158-177.
- SHARMA, A. K. & GUPTA, B. 2004. Absorption-based fiber optic surface plasmon resonance sensor: a theoretical evaluation. *Sensors and Actuators B: Chemical*, 100, 423-431.
- SHARMA, A. K. & GUPTA, B. 2007. Fibre optic sensor based on long-range surface plasmon resonance: a theoretical analysis. *Journal of Optics A: Pure and Applied Optics*, 9, 682.
- SHAW, B. J. & HANDY, R. D. 2011. Physiological effects of nanoparticles on fish: a comparison of nanometals versus metal ions. *Environment International*, 37, 1083-1097.
- SHINN-FWU, W., YANG, W., AN-LI, L., FU-HSI, K. & SHYH-RONG, L. Design of a small-displacement sensing system based on the surface plasmon resonance technology in heterodyne interferometry. *Instrumentation and Measurement Technology Conference (I2MTC), 2012 IEEE International*, 13-16 May 2012 2012. 1391-1394.
- SHRIVASTAVA, S., BERA, T., ROY, A., SINGH, G., RAMACHANDRARAO, P. & DASH, D. 2007. Characterization of enhanced antibacterial effects of novel silver nanoparticles. *Nanotechnology*, 18, 225103.
- SOMMERS, D. R. 2004. Design and verification of a surface plasmon resonance biosensor.
- SONG, B., LI, D., QI, W., ELSTNER, M., FAN, C. & FANG, H. 2010. Graphene on Au (111): A Highly Conductive Material with Excellent Adsorption Properties for High-Resolution Bio/Nanodetection and Identification. *ChemPhysChem*, 11, 585-589.

- SÖNNICHSEN, C., REINHARD, B. M., LIPHARDT, J. & ALIVISATOS, A. P. 2005. A molecular ruler based on plasmon coupling of single gold and silver nanoparticles. *Nature biotechnology*, 23, 741-745.
- SOVOVÁ, T., BOYLE, D., SLOMAN, K. A., VANEGAS PÉREZ, C. & HANDY, R. D. 2014. Impaired behavioural response to alarm substance in rainbow trout exposed to copper nanoparticles. *Aquatic Toxicology*, 152, 195-204.
- STERN, E. & FERRELL, R. 1960. Surface plasma oscillations of a degenerate electron gas. *Physical Review*, 120, 130.
- STEWART, C., HOOPER, I. & SAMBLES, J. 2008. Surface plasmon differential ellipsometry of aqueous solutions for bio-chemical sensing. *Journal of Physics D: Applied Physics*, 41, 105408.
- STOLZ, A., CONSIDINE, L., FACI, S., DOGHECHE, E., TRIPON-CANSELIET, C., LOISEAUX, B., PAVLIDIS, D., DECOSTER, D. & CHAZELAS, J. 2012. Gallium-nitride-based plasmonic multilayer operating at 1.55 μm . *Optics Letters*, 37, 3039-3041.
- STOYANOV, J. V., MAGNANI, D. & SOLIOZ, M. 2003. Measurement of cytoplasmic copper, silver and gold with a lux biosensor shows copper and silver, but not gold, efflux by the CopA ATPase of *Escherichia coli*. *FEBS letters*, 546, 391-394.
- SULLIVAN, B. T., CLARKE, G. A., AKIYAMA, T., OSBORNE, N., RANGER, M., DOBROWOLSKI, J., HOWE, L., MATSUMOTO, A., SONG, Y. & KIKUCHI, K. 2000. High-rate automated deposition system for the manufacture of complex multilayer coatings. *Applied optics*, 39, 157-167.
- SULLIVAN, B. T. & DOBROWOLSKI, J. 1993. Deposition error compensation for optical multilayer coatings. II. Experimental results—sputtering system. *Applied optics*, 32, 2351-2360.
- SUN, S., MURRAY, C., WELLER, D., FOLKS, L. & MOSER, A. 2000. Monodisperse FePt nanoparticles and ferromagnetic FePt nanocrystal superlattices. *Science*, 287, 1989-1992.
- SWALEN, J., GORDON II, J., PHILPOTT, M., BRILLANTE, A., POCKRAND, I. & SANTO, R. 1980. Plasmon surface polariton dispersion by direct optical observation. *American Journal of Physics*, 48, 669.
- SZUNERITS, S., CASTEL, X. & BOUKHERROUB, R. 2008. Surface plasmon resonance investigation of silver and gold films coated with thin indium tin oxide layers: Influence on stability and sensitivity. *The Journal of Physical Chemistry C*, 112, 15813-15817.
- SZUNERITS, S., MAALLOULI, N., WIJAYA, E., VILCOT, J.-P. & BOUKHERROUB, R. 2013. Recent advances in the development of graphene-based surface plasmon resonance (SPR) interfaces. *Analytical and bioanalytical chemistry*, 405, 1435-1443.
- TANIOUS, F. A., NGUYEN, B. & WILSON, W. D. 2008. Biosensor-Surface Plasmon Resonance Methods for Quantitative Analysis of Biomolecular Interactions. *Methods in cell biology*.
- TIEDE, K., BOXALL, A. B., TEAR, S. P., LEWIS, J., DAVID, H. & HASSELLÖV, M. 2008. Detection and characterization of engineered

- nanoparticles in food and the environment. *Food Additives and Contaminants*, 25, 795-821.
- TOMASZEWSKA, E., SOLIWODA, K., KADZIOLA, K., TKACZ-SZCZESNA, B., CELICHOWSKI, G., CICHOMSKI, M., SZMAJA, W. & GROBELNY, J. 2013. Detection limits of DLS and UV-Vis spectroscopy in characterization of polydisperse nanoparticles colloids. *Journal of Nanomaterials*, 2013, 60.
- TORRERI, P., CECCARINI, M., MACIOCE, P. & PETRUCCI, T. C. 2005. Biomolecular interactions by surface plasmon resonance technology. *Ann Ist Super Sanità*, 41, 437-441.
- TRÜGLER, A. & HOHENESTER, U. 2011. Optical properties of metallic nanoparticles. Doctoral thesis at the Karl-Franzens University Graz.
- TUDOS, R. B. M. S. A. A. J. 2008. Handbook of Surface PLasmon Resonance.
- TUNG, Y. C. & KUO, W. K. A High Sensitivity Surface Plasmon Resonance Configuration based on the Phase Retardation Detection. 2007. *IEEE*, 135-136.
- TURCHENIUK, K., HAGE, C.-H., SPADAVECCHIA, J., SERRANO, A. Y., LARROULET, I., PESQUERA, A., ZURUTUZA, A., PISFIL, M. G., HÉLIOT, L. & BOUKAERT, J. 2015. Plasmonic photothermal destruction of uropathogenic *E. coli* with reduced graphene oxide and core/shell nanocomposites of gold nanorods/reduced graphene oxide. *Journal of Materials Chemistry B*, 3, 375-386.
- ULRICH, C. ANDERSSON, O., NYHOLM, L. & BJÖREFORS, F. 2008. Formation of molecular gradients on bipolar electrodes. *Angewandte Chemie International Edition*, 47, 3034-3036.
- VAN BLAADEREN, A., RUEL, R. & WILTZIUS, P. 1997. Template-directed colloidal crystallization. *Nature*, 385, 321-324.
- VAN DELDEN, C., LENS, J., KOOYMAN, R., ENGBERS, G. & FEIJEN, J. 1997. Heparinization of gas plasma-modified polystyrene surfaces and the interactions of these surfaces with proteins studied with surface plasmon resonance. *Biomaterials*, 18, 845-852.
- VARADAN, V. K., CHEN, L. & XIE, J. 2008. Design and Applications of Magnetic Nanomaterials, Nanosensors and Nanosystems, Wiley Online Library.
- VASIC, B., ISIC, G. & GAJIC, R. 2013. Localized surface plasmon resonances in graphene ribbon arrays for sensing of dielectric environment at infrared frequencies. *Journal of Applied Physics*, 113, 013110-013110-7.
- VASILACHE, V., POPA, C., FILOTE, C., CRETU, M. A. & BENTA, M. 2011. NANOPARTICLES APPLICATIONS FOR IMPROVING THE FOOD SAFETY AND FOOD PROCESSING. 7th international conference on material Science and Engineering. BRAMAT 2011.
- VENKATRAM, N., RAO, D. N. & AKUNDI, M. 2005. Nonlinear absorption, scattering and optical limiting studies of CdS nanoparticles. *Optics express*, 13, 867-872.
- VERHAGEN, E. 2009. Subwavelength light confinement with surface plasmon polaritons.
- VERMA, R., GUPTA, B. D. & JHA, R. 2011. Sensitivity enhancement of a surface plasmon resonance based biomolecules sensor using graphene and silicon layers. *Sensors and Actuators B: Chemical*, 160, 623-631.

- VOGT, K., KOHL, P., CARTER, W., BELL, R. & BOTTOMLEY, L. 1994. Characterization of thin titanium oxide adhesion layers on gold: resistivity, morphology and composition. *Surface science*, 301, 203-213.
- VOLLMER, F. & ARNOLD, S. 2008. Whispering-gallery-mode biosensing: label-free detection down to single molecules. *Nature methods*, 5, 591-596.
- VOLOSHINA, E. & DEDKOV, Y. 2012. Graphene on metallic surfaces: problems and perspectives. *Physical Chemistry Chemical Physics*, 14, 13502-13514.
- WANG, C., HO, H.-P. & SHUM, P. 2012. High performance spectral-phase surface plasmon resonance biosensors based on single-and double-layer schemes. *Optics Communications*.
- WANG, J. 2005. Nanomaterial-based electrochemical biosensors. *Analyst*, 130, 421-426.
- WANG, S., BOUSSAAD, S. & TAO, N. 2001. Surface plasmon resonance enhanced optical absorption spectroscopy for studying molecular adsorbates. *Review of scientific instruments*, 72, 3055-3060.
- WANG, S. F., KAO, F. H., LIU, A. L., CHIU, J. S., LAI, W., HSIEH, M. F. & CHUNG, H. C. 2011. New Type Small-Angle Sensor Based on the Surface Plasmon Resonance Technology in Heterodyne Interferometry.
- WANG, S. F., LIN, C. J., HSU, C. L., TSAI, H. S. & LIU, C. Y. New type small-angle sensor based on the surface plasmon resonance technology. 2009. *IEEE*, 563-565.
- WANG, X., HANSON, J. C., LIU, G., RODRIGUEZ, J. A., IGLESIAS-JUEZ, A. & FERNÁNDEZ-GARCÍA, M. 2004. The behavior of mixed-metal oxides: physical and chemical properties of bulk $Ce_{1-x}Tb_xO_2$ and nanoparticles of $Ce_{1-x}Tb_xO_y$. *The Journal of chemical physics*, 121, 5434-5444.
- WANG, X., ZHAN, S., HUANG, Z. & HONG, X. 2013. REVIEW: ADVANCES AND APPLICATIONS OF SURFACE PLASMON RESONANCE BIOSENSING INSTRUMENTATION. *Instrumentation Science & Technology*, 41, 574-607.
- WATSON, H. J., SIMON, H.J., MITCHELL, D.E. 1975. Surface plasmons in silver films—a novel undergraduate experiment. *Am. J. Phys.* Vol. 43, No. 7, 1975.
- WEBSTER, T. J. 2008. *Safety of Nanoparticles: From Manufacturing to medical applications*, Springer.
- WEISS, M. N., SRIVASTAVA, R., GROGER, H., LO, P. & LUO, S. F. 1996. A theoretical investigation of environmental monitoring using surface plasmon resonance waveguide sensors. *Sensors and Actuators A: Physical*, 51, 211-217.
- WILLETS, K. A. & VAN DUYNE, R. P. 2007. Localized surface plasmon resonance spectroscopy and sensing. *Annu. Rev. Phys. Chem.*, 58, 267-297.
- WINTTERLIN, J. & BOCQUET, M.-L. 2009. Graphene on metal surfaces. *Surface science*, 603, 1841-1852.
- WOOD, R. 1912. XXVII. Diffraction gratings with controlled groove form and abnormal distribution of intensity. *The London, Edinburgh and Dublin Philosophical Magazine and Journal of Science*, 23, 310-317.

- WOOD, R. W. 1902. On a remarkable case of uneven distribution of light in a diffraction grating spectrum. *Proceedings of the Physical Society of London*, 18, 269.
- WU, L., CHU, H., KOH, W. & LI, E. 2010. Highly sensitive graphene biosensors based on surface plasmon resonance. *Optics express*, 18, 14395-14400.
- WU, L. P., LI, Y. F., HUANG, C. Z. & ZHANG, Q. 2006. Visual detection of Sudan dyes based on the plasmon resonance light scattering signals of silver nanoparticles. *Analytical chemistry*, 78, 5570-5577.
- XAVIER, P. L., CHAUDHARI, K., BAKSI, A. & PRADEEP, T. 2012. Protein-protected luminescent noble metal quantum clusters: an emerging trend in atomic cluster nanoscience. *Nano Reviews*, 3, 14767_1-14767_16.
- XIA, T., LI, N. & NEL, A. E. 2009. Potential health impact of nanoparticles. *Annual review of public health*, 30, 137-150.
- XIAO, F., LI, G., ALAMEH, K. & XU, A. 2012. Fabry–Pérot-based surface plasmon resonance sensors. *Optics Letters*, 37, 4582-4584.
- XING, F., LIU, Z. B., DENG, Z. C., KONG, X. T., YAN, X. Q., CHEN, X. D., YE, Q., ZHANG, C. P., CHEN, Y. S. & TIAN, J. G. 2012. Sensitive real-time monitoring of refractive indexes using a novel graphene-based optical sensor. *Scientific Reports*, 2.
- XIU, Z.-M., ZHANG, Q.-B., PUPPALA, H. L., COLVIN, V. L. & ALVAREZ, P. J. 2012. Negligible particle-specific antibacterial activity of silver nanoparticles. *Nano letters*, 12, 4271-4275.
- XUE-FENG, L. & LI, H. A universal model of surface plasmon resonance characteristics for isotropic multilayer films. 2010. *IEEE*, 263-266.
- YAN, H., LAI-XU, G., SONG-QUAN, L., WEN-LING, S. & HONG-AN, Y. 2011. Research on surface plasmon resonance sensor based on wavelength modulation by using theoretical simulation resonance sensor based on wavelength modulation by using theoretical simulation. 83-86.
- YAN, H., LAI-XU, G., WEN-LING, S., SONG-QUAN, L. & HONG-AN, Y. Realization of surface plasmon resonance sensor based on wavelength modulation by using 50nm broadband light source. 2010. *IEEE*, 182-185.
- YAN, Z., HU, T., GUO, W., DENG, A. & DI, J. 2014. A label-free immunosensor for determination of salbutamol based on localized surface plasmon resonance biosensing. *Bioprocess and biosystems engineering*, 37, 651-657.
- YAO, Y., YI, B., XIAO, J. & LI, Z. H. Surface plasmon resonance biosensors and its application. 2007. *IEEE*, 1043-1046.
- YE, Q., WANG, J., LIU, Z., DENG, Z. C., KONG, X. T., XING, F., CHEN, X. D., ZHOU, W. Y., ZHANG, C. P. & TIAN, J. G. 2013. Polarisation-dependent optical absorption of graphene under total internal reflection. *Applied Physics Letters*, 102, 021912-021912-4.
- YIH, J. N., CHIU, K. C., CHOU, S. Y., LIN, C. M., LAN, Y. S., CHEN, S. J. & CHENG, N. J. Surface plasmon resonance biosensor based on grating disc with circular fluidic channel. 2011. *IEEE*, 571-574.

- YIN, L. & FANG, N. X. 2009. Enhanced surface photon drag on plasmonic metamaterials: a fizeau-doppler shift study. Arxiv preprint arXiv:0907.1712.
- YOSHIMURA, H., MATSUMOTO, M., ENDO, S. & NAGAYAMA, K. 1990. Two-dimensional crystallization of proteins on mercury. *Ultramicroscopy*, 32, 265-274.
- YUAN, X., ONG, B., TAN, Y., ZHANG, D., IRAWAN, R. & TJIN, S. 2006. Sensitivity–stability-optimized surface plasmon resonance sensing with double metal layers. *Journal of Optics A: Pure and Applied Optics*, 8, 959.
- YUSMAWATI, W., CHUAH, H. & MAHMOOD, M. 2007. Optical properties and sugar content determination of commercial carbonated drinks using surface plasmon resonance. *American Journal of Applied Sciences*, 4, 1.
- ZAGORODKO, O., SPADAVECCHIA, J., YANGUAS, A., LARROULET, I., PESQUERA, A., ZURUTUZA, A., BOUKHERROUB, R. & SZUNERITS, S. 2014. Highly sensitive detection of DNA hybridization on commercialized graphene coated surface plasmon resonance interfaces. *Analytical chemistry*.
- ZENG, J., LIANG, D. & CAO, Z. Applications of optical fiber SPR sensor for measuring of temperature and concentration of liquids. Bruges, Belgium-Deadline Past, 2005. *International Society for Optics and Photonics*, 667-670.
- ZENG, S., BAILLARGEAT, D., HO, H.-P. & YONG, K.-T. 2014. Nanomaterials enhanced surface plasmon resonance for biological and chemical sensing applications. *Chem. Soc. Rev.*, 43(10), 3426-52.
- ZENG, S., YU, X., LAW, W.-C., ZHANG, Y., HU, R., DINH, X.-Q., HO, H.-P. & YONG, K.-T. 2012. Size dependence of Au NP-enhanced surface plasmon resonance based on differential phase measurement. *Sensors and Actuators B: Chemical*, 176, 1128-1133.
- ZHANG, H., BOUSSAAD, S. & TAO, N. 2003. High-performance differential surface plasmon resonance sensor using quadrant cell photodetector. *Review of scientific instruments*, 74, 150-153.
- ZHANG, J., ZHANG, L. & XU, W. 2012. Surface plasmon polaritons: physics and applications. *Journal of Physics D: Applied Physics*, 45, 113001.
- ZHANG, Y. 2013. Study of an absorption-based surface plasmon resonance sensor in detecting the real part of refractive index. *Optical Engineering*, 52, 014405-014405.
- ZHU, S., DU, C. & FU, Y. 2009. Localized surface plasmon resonance-based hybrid Au–Ag nanoparticles for detection of *Staphylococcus aureus* enterotoxin B. *Optical Materials*, 31, 1608-1613.
- ZHU, Y., MURALI, S., CAI, W., LI, X., SUK, J. W., POTTS, J. R. & RUOFF, R. S. 2010. Graphene and graphene oxide: synthesis, properties and applications. *Advanced materials*, 22, 3906-3924.
- ZOUROB, M., ELWARY, S., FAN, X., MOHR, S. & GODDARD, N. J. 2009. Label-free detection with the resonant mirror biosensor. *Biosensors and Biodetection*. Springer.
- ZOUROB, M., MOHR, S., BROWN, B. J. T., FIELDEN, P. R., MCDONNELL, M. B. & GODDARD, N. J. 2005. Bacteria detection using disposable optical leaky waveguide sensors. *Biosensors and Bioelectronics*, 21, 293-302.

Appendix A

Transfer Matrix Method Derivation

Here we will show the derivation of the transfer matrix (M) which was shown in the Thesis. This can be derived by applying specific boundary conditions to Maxwell's equations.

A.1 Obtaining Maxwell's wave equations

Maxwell's equations are usually used as the starting point for Fresnel's equations for complex reflection and transmission. The reflected intensity can then be found from these coefficients. Therefore we start with Maxwell's equations for electrostatics (Eq. A.1a-A.1d).

$$\nabla \times \mathbf{H} = \mathbf{J} + \frac{\partial}{\partial t} \mathbf{D} \quad (\text{A. 1a})$$

$$\nabla \times \mathbf{E} = -\frac{\partial}{\partial t} \mathbf{B} \quad (\text{A. 1b})$$

$$\nabla \cdot \mathbf{D} = \rho \quad (\text{A. 1c})$$

$$\nabla \cdot \mathbf{B} = 0 \quad (\text{A. 1d})$$

Eq. A.1a comes from Ampere's circuit laws, where he describes the magnetic field associated with a current which Maxwell later adapted to include the displacement current (Maxwell, 1861, Philosophical Magazine). In the equation, \mathbf{H} is the magnetic field vector, \mathbf{D} is the electric displacement field and \mathbf{J} is the free current density which for dielectric materials is equal to zero. Hence, Eq. A.1a becomes:

$$\nabla \times \mathbf{H} = \frac{\partial}{\partial t} \mathbf{D} \quad (\text{A. 2})$$

Eq. A.1b is a generalisation of Faraday's law, more commonly termed the Maxwell-Faraday equation, where \mathbf{E} is the electric field vector and \mathbf{B} is the magnetic displacement field. The equation describes the relationship between the magnetic and electric field components. Eq. A.1c and Eq. A.1d come from Gauss' laws, where Eq. A.1c relates the divergence of the electric field vector to the free charge density of the material. The free charge density, like the free current density and therefore is equal to zero ($\nabla \cdot \mathbf{D} = 0$). Eq. A.1d comes from Gauss's law on magnetism, where it states that no magnetic monopoles can exist within the system.

The materials are assumed to be homogenous and isotropic and hence the electrical displacement field vector can be related to the electric field vector by the permittivity of the material (ϵ) which is shown in Eq. 3a. A similar relationship between the magnetic field and magnetic displacement field can be described using the permeability of the material (μ) which is shown in Eq. A.3b.

$$\mathbf{D} = \epsilon \mathbf{E} \quad (\text{A. 3a})$$

$$\mathbf{B} = \mu \mathbf{H} \quad (\text{A. 3b})$$

Where $\epsilon = \epsilon_0 \epsilon_r$ and $\mu = \mu_0 \mu_r$. μ_0 is the permeability of free space which is $4\pi \cdot 10^{-7} \text{ V} \cdot \text{s}/(\text{A} \cdot \text{m})$, ϵ_0 is the permittivity of free space which is approximately $8.854 \cdot 10^{-12} \text{ F/m}$. ϵ_r and μ_r are the material relative permittivity and permeability respectfully. By using the relationships in Eq. A. 3a and Eq. A. 3b, Eq. A. 1b and Eq. A. 2 can be re-written in terms of the electric and magnetic field vectors.

$$\nabla \times \mathbf{H} = \epsilon \frac{\partial}{\partial t} \mathbf{E} \quad (\text{A. 4a})$$

$$\nabla \times \mathbf{E} = -\mu \frac{\partial}{\partial t} \mathbf{H} \quad (\text{A. 4b})$$

Taking the curl of Eq. A. 4a and 4b we obtain:

$$\nabla \times (\nabla \times \mathbf{H}) = \varepsilon \frac{\partial}{\partial t} (\nabla \times \mathbf{E}) \quad (\text{A. 5a})$$

$$\nabla \times (\nabla \times \mathbf{E}) = -\mu \frac{\partial}{\partial t} (\nabla \times \mathbf{H}) \quad (\text{A. 5b})$$

By using the curl identity $\nabla \times (\nabla \times x) = \nabla(\nabla \cdot x) - \nabla^2 x$ and substituting Eq. A. 4a and Eq. A. 1c into Eq. A. 5b and Eq. A. 4b and Eq. A. 1d into Eq. A. 5a, we can obtain the wave equation in standard form as shown in Eq. A. 6. Where $c = 1/\sqrt{\mu_0 \varepsilon_0}$.

$$\frac{\partial^2}{\partial t^2} \mathbf{E} - \frac{c^2}{\mu_r \varepsilon_r} \nabla^2 \mathbf{E} = 0 \quad (\text{A. 5b})$$

$$\frac{\partial^2}{\partial t^2} \mathbf{H} - \frac{c^2}{\mu_r \varepsilon_r} \nabla^2 \mathbf{H} = 0 \quad (\text{A. 5b})$$

In the case of non-magnetic materials, $\mu_r = 1$, the equation can be adapted to be anisotropic, where the permittivity changes over space, this can be described with the use of a tensor for the relative permittivity which we will denote as $\hat{\boldsymbol{\varepsilon}}$.

For time-varying waves the electric field can be described as shown in Eq. A. 6, where

$$\mathbf{E}(\mathbf{r}, t) = \mathbf{E}_0 e^{-i(\omega t - \mathbf{k} \cdot \mathbf{r})} \quad (\text{A. 6})$$

A.2 Obtaining Fresnel's equations from boundary applied Maxwell equations

At the boundary between two materials, two things happen, some of the light is refracted into the device at an angle proportional to the difference between two materials. And also there is reflection from the boundary, dependant again on the difference between two materials. For this reason we should set some boundary conditions and obtain Fresnel's transmission and reflection coefficients.

For TE waves, at the boundary we have a unit directional vector (\mathbf{s}) for each of the waves for incident, transmission and reflection. In the x-z plane we can state that each of the vectors can be described as:

$$\mathbf{s}_i = [0 \quad \sin(\theta_i) \quad \cos(\theta_i)]$$

$$\mathbf{s}_r = [0 \quad \sin(\theta_r) \quad \cos(\theta_r)]$$

$$\mathbf{s}_t = [0 \quad \sin(\theta_t) \quad \cos(\theta_t)]$$

$$\sin(\theta_r) = \sin(\theta_i), \quad \cos(\theta_r) = -\cos(\theta_i)$$

Where the directional vector (\mathbf{r}) is:

$$\mathbf{r} = \begin{bmatrix} x \\ y \\ z \end{bmatrix}$$

So each of the propagating waves can be described as $\mathbf{r} \cdot \mathbf{s} = \xi$, $r(x,y,z)$ and $s(s_x, s_y, s_z)$:

$$\frac{d}{dx} = s_x \frac{d}{d\xi}, \quad \frac{d}{dy} = s_y \frac{d}{d\xi}, \quad \frac{d}{dz} = s_z \frac{d}{d\xi}$$

So the function = $V(\mathbf{r} \cdot \mathbf{s}, t)$ and $\nabla^2 V = \frac{d^2}{d\xi^2} V$. The propagation constant in each of the medium will be denoted as V_1 and V_2 .

If the relations are expanded we obtain with z as the direction of propagation is:

$$\frac{xs_x^i + ys_y^i}{V_1}, \quad \frac{xs_x^r + ys_y^r}{V_1}, \quad \frac{xs_x^t + ys_y^t}{V_2}$$

In the z-x plane of incidence this then becomes:

$$\frac{s_x^i}{V_1} = \frac{s_x^r}{V_1} = \frac{s_x^t}{V_2}$$

$$\frac{\sin(\theta_i)}{V_1} = \frac{\sin(\theta_r)}{V_1} = \frac{\sin(\theta_t)}{V_2}$$

$$\sin(\theta_i) = \sin(\theta_r)$$

$$\cos(\theta_i) = -\cos(\theta_r)$$

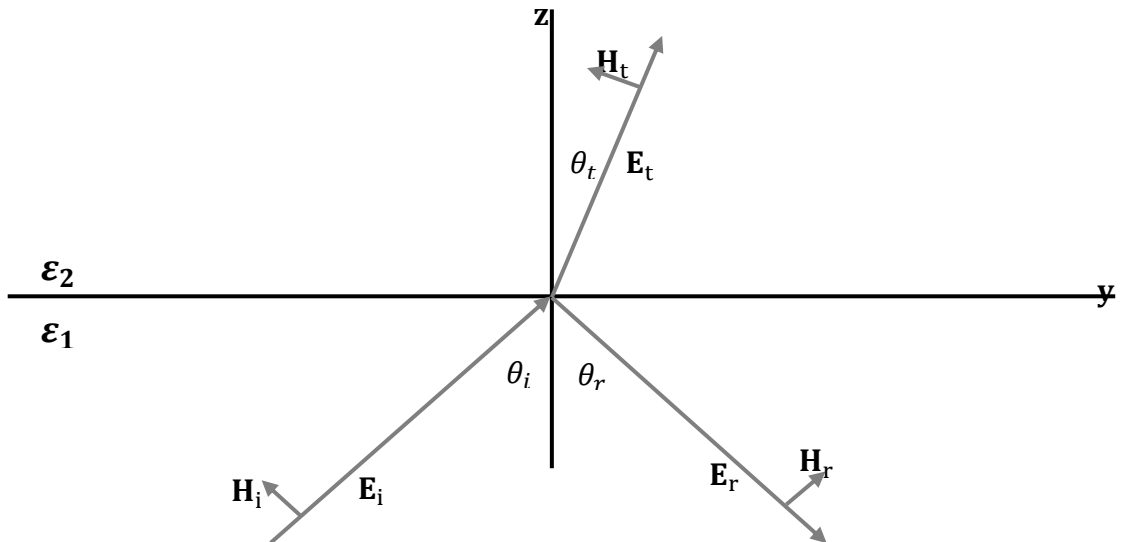


Figure A.1 Shows the electric and magnetic field vectors in the (y, z) plane, the subscripts j, r and t, relate to incident, reflected and transmitted vectors. ϵ_1 is the permittivity of the first material and ϵ_2 is the permittivity of the second material, the line between the two symbolises the boundary between the two materials.

A series of equations at the boundary can be found, where the waves are in the form:

$$U = U_0 e^{-i\omega\left(t - \sqrt{\frac{\epsilon\mu}{c}} \mathbf{r} \cdot \mathbf{s}\right)}$$

We can denote from previous equations:

$$\tau_i = \omega \left(t - \frac{x \sin(\theta_i) + z \sin(\theta_i)}{v_1} \right)$$

$$\tau_r = \omega \left(t - \frac{x \sin(\theta_r) + z \sin(\theta_r)}{v_1} \right)$$

$$\tau_t = \omega \left(t - \frac{x \sin(\theta_t) + z \sin(\theta_t)}{v_2} \right)$$

Where $v_1 = \frac{c}{\sqrt{\epsilon_1}}$, $v_2 = \frac{c}{\sqrt{\epsilon_2}}$.

E_x, E_y and E_z can be described by an currently unknown amplitude for each transmitted (T), reflected (R) and incident (A) and also a subscript to determine parallel or transverse field to the plane of origin...

$$E_x^i = -A_{||} \cos(\theta_i) e^{-i\tau_i}$$

$$E_y^i = A_{\perp} e^{-i\tau_i}$$

$$E_z^i = A_{||} \sin(\theta_i) e^{-i\tau_i}$$

$$E_x^r = -R_{||} \cos(\theta_r) e^{-i\tau_r}$$

$$E_y^r = R_{\perp} e^{-i\tau_r}$$

$$E_z^r = R_{||} \sin(\theta_r) e^{-i\tau_r}$$

$$E_x^t = -T_{||} \cos(\theta_t) e^{-i\tau_t}$$

$$E_y^t = T_{\perp} e^{-i\tau_t}$$

$$E_z^t = T_{||} \sin(\theta_t) e^{-i\tau_t}$$

From the relationship:

$$\sin(\theta_i) = \sin(\theta_r)$$

$$\cos(\theta_i) = -\cos(\theta_r)$$

And also

$$\mathbf{H} = \sqrt{\varepsilon}(\mathbf{s} \times \mathbf{E})$$

We can state the following relationships:

$$\cos(\theta_i) (A_{\parallel} - R_{\parallel}) = \cos(\theta_t)(T_{\parallel})$$

$$\sqrt{\varepsilon_1}(A_{\parallel} + R_{\parallel}) = \sqrt{\varepsilon_2}(T_{\parallel})$$

$$A_{\perp} + R_{\perp} = T_{\perp}$$

$$\sqrt{\varepsilon_1} \cos(\theta_i) (A_{\perp} + R_{\perp}) = \sqrt{\varepsilon_2} \cos(\theta_t) (T_{\perp})$$

Using simultaneous equations is it possible to obtain an equation for the transmission of the incident energy which for this is:

$$T_{\parallel} = \frac{2\sqrt{\varepsilon_1} \cos(\theta_i)}{\sqrt{\varepsilon_1} \cos(\theta_t) + \sqrt{\varepsilon_2} \cos(\theta_i)} A_{\parallel}$$

A.3 Transfer Matrix Method from Maxwell's partial differential equations

From the Maxwell equation:

$$\nabla \times \mathbf{H} = \varepsilon\mu \frac{d}{dt} \mathbf{E}$$

If \mathbf{E} is in the form: $E = E_0 e^{-i\omega t}$, then:

$$\frac{\varepsilon}{c} \frac{d}{dt} \mathbf{E} = -ik_0 \varepsilon\mu \mathbf{E}(r, t)$$

Taking the curl of the Magnetic field we obtain:

$$\frac{d}{dy} H_z - \frac{d}{dz} H_y + i\omega\varepsilon\mu E_x$$

$$\frac{d}{dz} H_x - \frac{d}{dx} H_z + i\omega\varepsilon\mu E_y$$

$$\frac{d}{dx}H_y - \frac{d}{dy}H_x + i\omega\varepsilon\mu E_z$$

And the curl of the electric field which:

$$\nabla \times \mathbf{E} = -\mu \frac{d}{dt} \mathbf{H}$$

$$-\mu \frac{d}{dt} \mathbf{H} = i\omega\mu \mathbf{H}(r, t)$$

Therefore:

$$\frac{d}{dy}E_z - \frac{d}{dz}E_y - i\omega\mu H_x$$

$$\frac{d}{dz}E_x - \frac{d}{dx}E_z - i\omega\mu H_y$$

$$\frac{d}{dx}E_y - \frac{d}{dy}E_x - i\omega\mu H_z$$

In TE mode in the z-x plane:

$$E_y = E_z = 0$$

Therefore the full set of 6 equations become:

$$\frac{d}{dy}H_z - \frac{d}{dz}H_y + i\omega\varepsilon\mu E_x = 0$$

$$\frac{d}{dz}H_x - \frac{d}{dx}H_z = 0$$

$$\frac{d}{dx}H_y - \frac{d}{dy}H_x = 0$$

$$-i\omega\mu H_x = 0$$

$$\frac{d}{dz}E_x - i\omega\mu H_y = 0$$

$$\frac{d}{dy}E_x + i\omega\mu H_z = 0$$

Rearranging the last two equations we can get H_y and H_z , as a function of E_x

which we can use to substitute into the first equation:

$$H_y = -\frac{i}{\omega\mu} \frac{d}{dz} E_x$$

$$H_z = \frac{i}{\omega\mu} \frac{d}{dy} E_x$$

$$\frac{d}{dy} H_z - \frac{d}{dz} H_y + i\omega\varepsilon\mu E_x = \frac{i}{\omega\mu} \frac{d^2}{dy^2} E_x + \frac{i}{\omega\mu} \frac{d^2}{dz^2} E_x + i\omega\varepsilon\mu E_x = 0$$

$$\frac{d^2}{dy^2} E_x + \frac{d^2}{dz^2} E_x + n^2 k_0^2 E_x = 0$$

$$E_x(y, z) = Y(y)U(z)$$

If we substitute in this we get:

$$U(z) \frac{d^2}{dy^2} Y(y) + Y(y) \frac{d^2}{dz^2} U(z) + n^2 k_0^2 Y(y)U(z) = 0$$

$$\frac{1}{Y(y)} \frac{d^2}{dy^2} Y(y) = -\frac{1}{U(z)} \frac{d^2}{dz^2} U(z) - n^2 k_0^2$$

Now we need to use partial differential equations substitution method to solve this equation, in this example, like Born and Wolf, we will use a constant:

$$\frac{1}{Y(y)} \frac{d^2}{dy^2} Y(y) = -Q^2$$

Where:

$$Q^2 U(z) = \frac{d^2}{dz^2} U(z) + n^2 k_0^2 U(z)$$

For convenience $Q^2 = k_0^2 \alpha^2$

For the partial Y system to balance it must be equal to $k_0^2 \alpha^2$:

$$\frac{1}{Y(y)} \frac{d^2}{dy^2} Y(y) = -k_0^2 \alpha^2$$

From e^{iXy} , we can calculate X needs to be $k_0\alpha$, therefore we can specify that:

$$Y(z) = e^{ik_0\alpha y}$$

Putting this back into the original equation for E_x :

$$E_x(y, z, t) = U(z)e^{-i(\omega t - k_0\alpha y)}$$

Form the earlier equations for H_y and H_z , we can obtain the following equations:

$$H_y = -i \frac{c}{\omega\mu} \frac{d}{dz} E_x$$

As shown above we now have a partial representation for E_x , so this becomes:

$$H_y = -i \frac{c}{\omega\mu} e^{i(k_0\alpha y - \omega t)} \cdot \frac{d}{dz} U(z)$$

Which we will now present as

$$H_y = V(z)e^{i(k_0\alpha y - \omega t)}$$

The same applies for H_z :

$$H_z = -i \frac{c}{\omega\mu} \frac{d}{dy} E_x$$

$$H_z = -\frac{k_0\alpha c}{\omega} e^{i(k_0\alpha y - \omega t)} U(z)$$

Which we will denote as:

$$H_z = W(z)e^{i(k_0\alpha y - \omega t)}$$

If we substitute this back into the first equations:

$$\frac{d}{dy} H_z - \frac{d}{dz} H_y + i\omega\epsilon\mu E_x = \left[ik_0\alpha \frac{d}{dy} W(z) - \frac{d}{dz} V(z) + i\epsilon k_0 U(z) \right] e^{i(k_0\alpha y - \omega t)}$$

We can then draw some relationships:

$$\frac{d}{dz}V(z) = ik_0[\alpha W(z) + \varepsilon U(z)]$$

$$\frac{d^2}{dz^2}U(z) = ik_0\mu V(z)$$

$$\alpha U(z) + \mu W(z) = 0$$

Therefore:

$$-\frac{\alpha}{\mu}U(z) = W(z)$$

Substituting this into earlier equation:

$$\frac{d}{dz}V(z) = ik_0\left[-\frac{\alpha^2}{\mu}U(z) + \varepsilon U(z)\right] = ik_0[\varepsilon\mu - \alpha^2]U(z)$$

Given this, we can state:

$$\frac{d}{dz}U(z_1) = ik_0\mu V(z_1)$$

$$\frac{d}{dz}V(z_1) = ik_0[\varepsilon\mu - \alpha^2]U(z_1)$$

$$\frac{d}{dz}U(z_2) = ik_0\mu V(z_2)$$

$$\frac{d}{dz}V(z_2) = ik_0[\varepsilon\mu - \alpha^2]U(z_2)$$

The following relationships must be true:

$$V_1U_2' - U_1V_2' = 0$$

$$U_1V_2' - V_1U_2' = 0$$

Therefore

$$\frac{d}{dz}(U_1V_2 - U_2V_1) = 0$$

Using this relationship we can form a matrix such that the determinant of the matrix is $U_1V_2 - V_1U_2$, we will call the matrix D:

$$D = \begin{bmatrix} U_1 & V_1 \\ U_2 & V_2 \end{bmatrix}$$

$$|D| = \det(D) = U_1V_2 - V_1U_2 = 1$$

We will denote the system for convenience as:

$$U_1 = f(z), \quad U_2 = F(z), \quad V_1 = g(z), \quad V_2 = G(z)$$

Where $f(0) = G(0) = 0$ and $F(0) = g(0) = 1$;

From the equations for each of both U and V, we need the equations:

$$U(z) = F(z)U_0 + f(z)V_0$$

$$V(z) = G(z)U_0 + g(z)V_0$$

This means that we rely on the initial values at $z=0$ and hence the matrix becomes:

$$\begin{bmatrix} U(z) \\ V(z) \end{bmatrix} = \begin{bmatrix} F(z) & f(z) \\ G(z) & g(z) \end{bmatrix} \cdot \begin{bmatrix} U_0 \\ V_0 \end{bmatrix}$$

$$N = \begin{bmatrix} F(z) & f(z) \\ G(z) & g(z) \end{bmatrix}, \quad Q_0 = \begin{bmatrix} U_0 \\ V_0 \end{bmatrix}$$

$$Q = NQ_0$$

Where the determinant of N must be equal to 1 according to the relationship shown in equation above.

The transfer matrix is categorically defines as $M = N^{-1}$, $Q_0 = N^{-1}Q$:

$$M(z) = \begin{bmatrix} g(z) & -f(z) \\ -G(z) & F(z) \end{bmatrix}$$

$M(z)$ related the x and y components of the electric field to the plane $z=0$ or initial ambient conditions. The determinant which equals 1, can be used to check the results as it is directly related to the conservation of energy, where it must always be equal.

In the case of homogeneous and isotropic, non-magnetic ($\mu = 1$) media, $\alpha = n_j \sin(\theta_j)$ and hence the differential equations can be solved from:

$$\frac{d^2}{dz^2} U(z) + k_0^2 \cos^2(\theta) \epsilon U(z) = 0$$

$$\frac{d^2}{dz^2} V(z) + k_0^2 \cos^2(\theta) \epsilon U(z) = 0$$

We know that $U(z)$ and $V(z)$ follow the same $e^{ik_0 n \cos(\theta) z}$, we can solve this by using Euler's rule and solving for the general solution to second order differential equations we obtain:

$$U(z) = A \cos(k_0 n \cos(\theta) z) + B \sin(k_0 n \cos(\theta) z)$$

Because $V(z)$ relates $U(z)$ to the magnetic component H_z , we can use the constructive relations:

$$V(z) = -i \sqrt{\frac{\epsilon}{\mu}} \cos(\theta) [B \cos(k_0 n \cos(\theta) z) - A \sin(k_0 n \cos(\theta) z)]$$

By using the boundary conditions earlier we can obtain a set of equations:

$$f(z) = i \frac{1}{\cos(\theta)} \sqrt{\frac{\mu}{\epsilon}} \sin(k_0 n \cos(\theta) z)$$

$$g(z) = \cos(k_0 n \cos(\theta) z)$$

$$F(z) = \cos(k_0 n \cos(\theta) z)$$

$$G(z) = i \cos(\theta) \sqrt{\frac{\epsilon}{\mu}} \sin(k_0 n \cos(\theta) z)$$

We will define $p = \sqrt{\frac{\epsilon}{\mu}} \cos(\theta)$, so the transfer matrix, M , becomes:

$$M(z) = \begin{bmatrix} \cos(k_0 n \cos(\theta) z) & -i \frac{1}{p} \sin(k_0 n \cos(\theta) z) \\ -i p \sin(k_0 n \cos(\theta) z) & \cos(k_0 n \cos(\theta) z) \end{bmatrix}$$

Due to the relationship between the transverse magnetic and transverse electric modes we can re-write $M(z)$ for TM by replacing p with q , where:

$$q = \sqrt{\frac{\mu}{\epsilon}} \cos(\theta)$$

$$M(z) = \begin{bmatrix} \cos(k_0 n \cos(\theta) z) & -i \frac{1}{q} \sin(k_0 n \cos(\theta) z) \\ -i q \sin(k_0 n \cos(\theta) z) & \cos(k_0 n \cos(\theta) z) \end{bmatrix}$$

If we define $\beta_j = k_0 n_j \cos(\theta_j)$ and $z = h_j$, then we obtain the same solution as in the chapter.

$$\hat{M}_j = \begin{pmatrix} \cos(\beta_j h_j) & \frac{i}{p_j} \sin(\beta_j h_j) \\ ip_i \sin(\beta_j h_j) & \cos(\beta_j h_j) \end{pmatrix}$$

Appendix B: SolidWork Design

89
 $\phi 50$

SECTION A-A
 SECTION B-B

SECTION C-C

$\phi 59$
 $\phi 50$
 4.500

3.850
 3.850
 $\phi 50$
 27
 12.700
 7.800
 $\phi 50.700$
 $\phi 59$
 7.100
 1.300

UNLESS OTHERWISE SPECIFIED: DIMENSIONS ARE IN MILLIMETERS SURFACE FINISH: TOLERANCES: LINEAR ANGULAR		FINISH	DIM'S AND BREAK SHARP EDGES		DO NOT SCALE DRAWING	REVISION
NAME	SIGNATURE	DATE			FILE:	
DRAWN Nash					base part	
CHECKED					DWG NO.	009
APPROVED						A3
MFG					SCALE: 1:1	SHEET 1 OF 1
S.A.						

**SolidWorks Student Edition.
For Academic Use Only.**

$\phi 60$
 $\phi 50$
 90

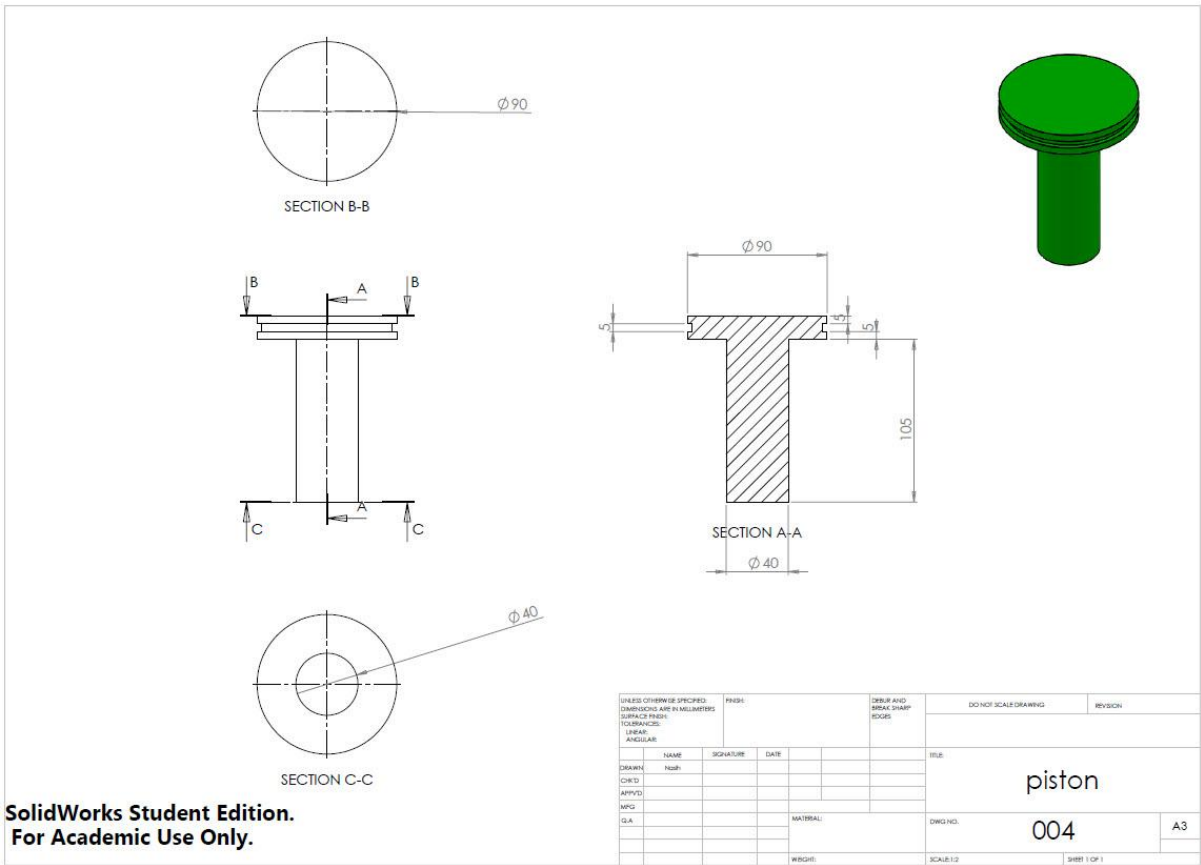
5
 10
 30
 90

TRUE R2.500

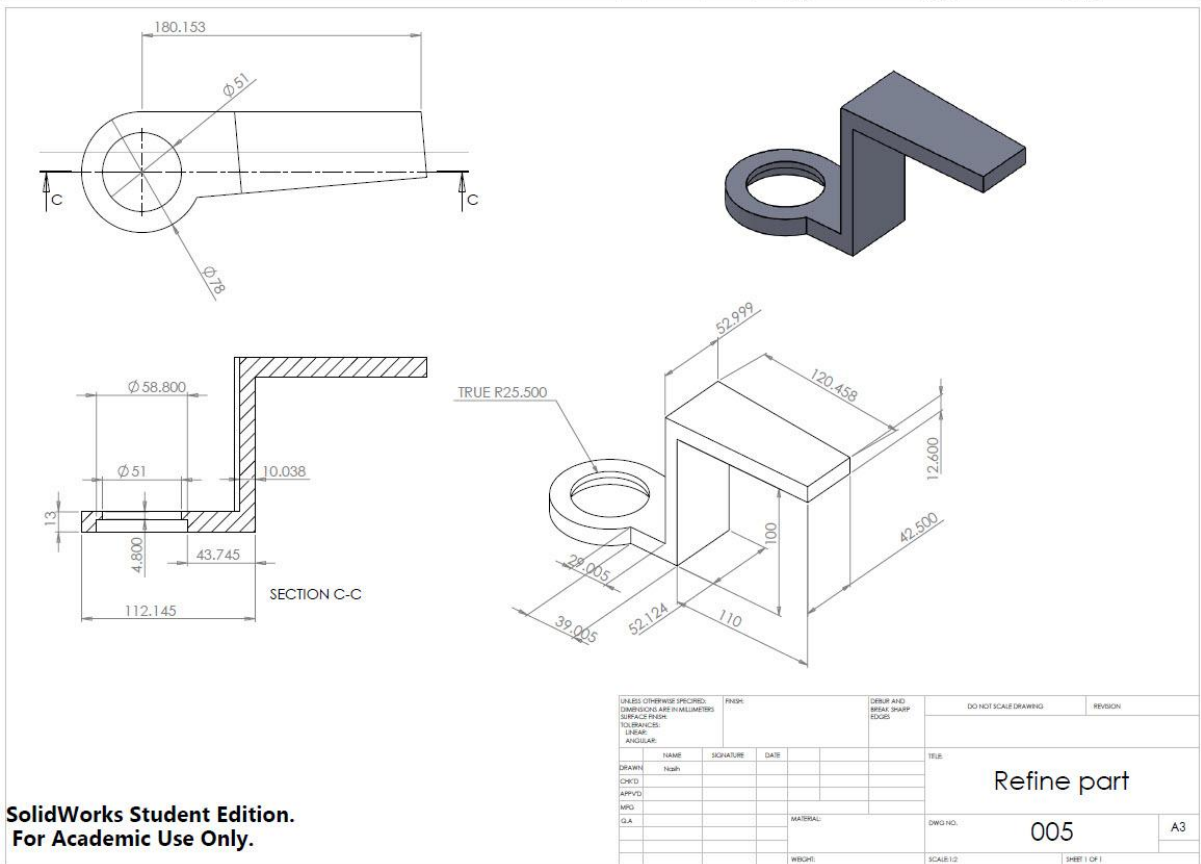
10
 90

UNLESS OTHERWISE SPECIFIED: DIMENSIONS ARE IN MILLIMETERS SURFACE FINISH: TOLERANCES: LINEAR ANGULAR		FINISH	DIM'S AND BREAK SHARP EDGES		DO NOT SCALE DRAWING	REVISION
NAME	SIGNATURE	DATE			FILE:	
DRAWN Nash					base part double	
CHECKED					DWG NO.	008
APPROVED						A3
MFG					SCALE: 1:1	SHEET 1 OF 1
S.A.						

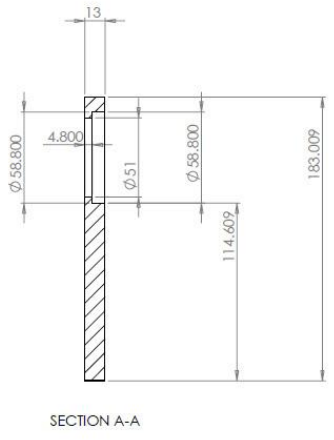
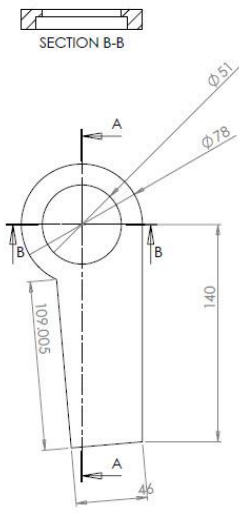
**SolidWorks Student Edition.
For Academic Use Only.**



SolidWorks Student Edition.
For Academic Use Only.

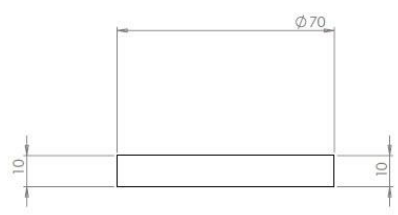
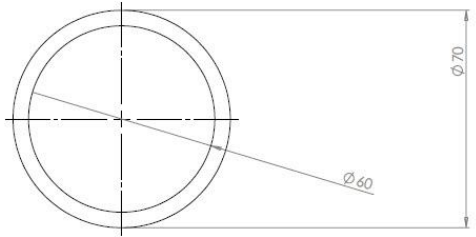


SolidWorks Student Edition.
For Academic Use Only.



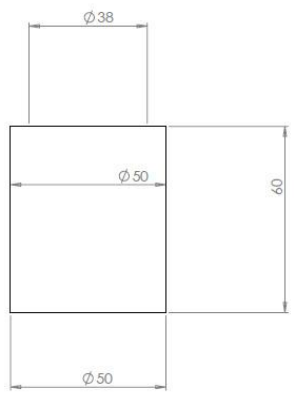
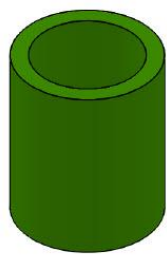
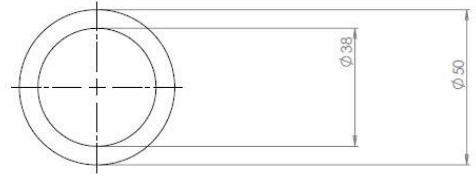
UNLESS OTHERWISE SPECIFIED: DIMENSIONS ARE IN MILLIMETERS SURFACE FINISH: TOLERANCES: LINEAR: ANGULAR:		FINISH:	DIMENSIONS AND BREAK SHARP EDGES		DO NOT SCALE DRAWING	REVISION
DRAWN	NAME	SIGNATURE	DATE		TITLE: Refine part top	
CHKD	NAME					
APPROV						
MFG						
G.A.				MATERIAL:	DWG NO. 003	A3
				WEIGHT:	SCALE: 1:2	SHEET 1 OF 1

SolidWorks Student Edition.
For Academic Use Only.



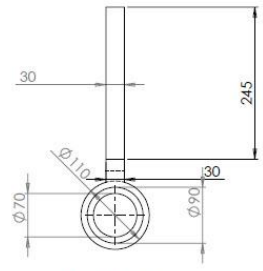
UNLESS OTHERWISE SPECIFIED: DIMENSIONS ARE IN MILLIMETERS SURFACE FINISH: TOLERANCES: LINEAR: ANGULAR:		FINISH:	DIMENSIONS AND BREAK SHARP EDGES		DO NOT SCALE DRAWING	REVISION
DRAWN	NAME	SIGNATURE	DATE		TITLE: rings	
CHKD	NAME					
APPROV						
MFG						
G.A.				MATERIAL:	DWG NO. 007	A3
				WEIGHT:	SCALE: 1:1	SHEET 1 OF 1

SolidWorks Student Edition.
For Academic Use Only.

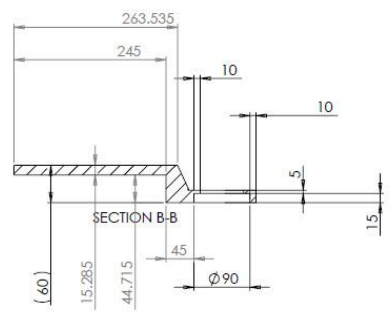
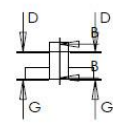


UNLESS OTHERWISE SPECIFIED DIMENSIONS ARE IN MILLIMETERS SURFACE FINISH: TO DIMENSIONS: LINEAR: ANGULAR:				FINISH:	DRILL AND BREAK SHARP EDGES:	DO NOT SCALE DRAWING	REVISION
DRAWN	NAME	SIGNATURE	DATE			TITLE: spacer	
CHK'D	NO.:					DWG. NO. 006	A3
APP'D:						SCALE: 1:1	SHEET 1 OF 1
WFG:							
G.A.							

SolidWorks Student Edition.
For Academic Use Only.



SECTION G-G



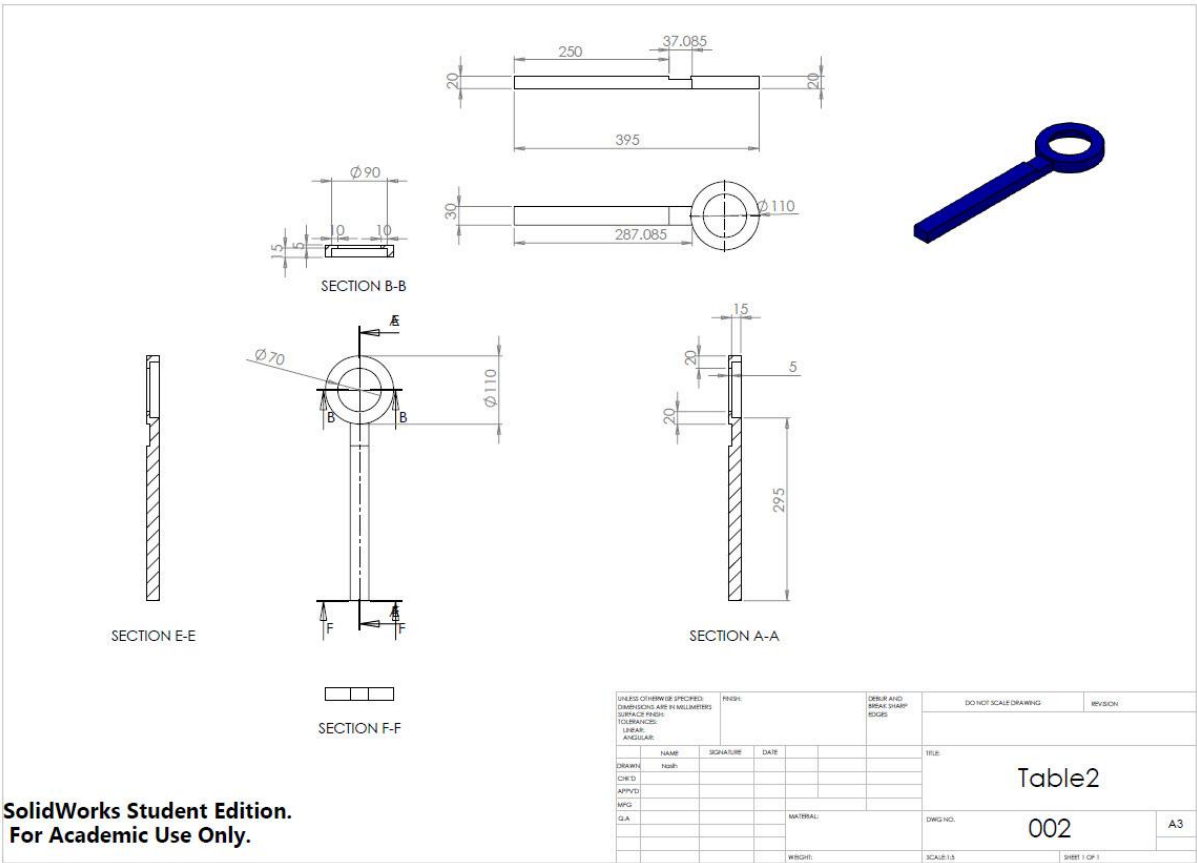
SECTION B-B



SECTION D-D

UNLESS OTHERWISE SPECIFIED DIMENSIONS ARE IN MILLIMETERS SURFACE FINISH: TO DIMENSIONS: LINEAR: ANGULAR:				FINISH:	DRILL AND BREAK SHARP EDGES:	DO NOT SCALE DRAWING	REVISION
DRAWN	NAME	SIGNATURE	DATE			TITLE: Table1	
CHK'D	NO.:					DWG. NO. 001	A3
APP'D:						SCALE: 1:1	SHEET 1 OF 1
WFG:							
G.A.							

SolidWorks Student Edition.
For Academic Use Only.

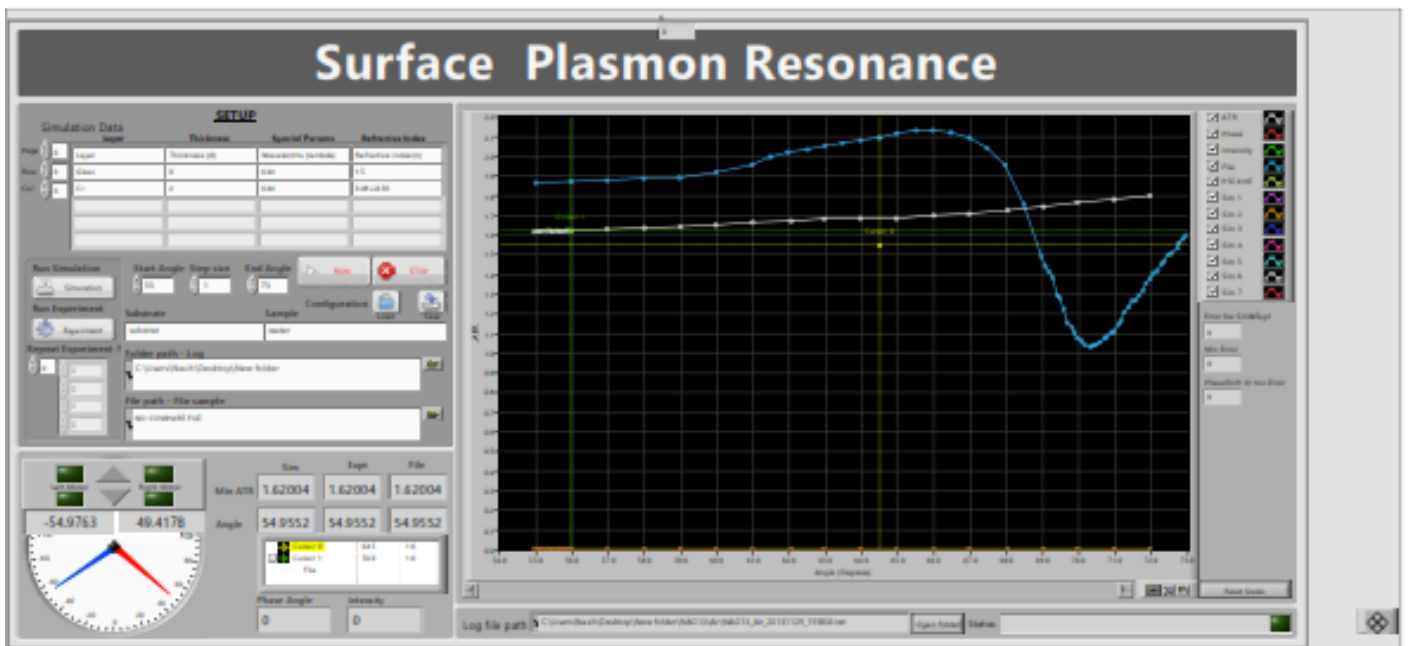


SolidWorks Student Edition.
For Academic Use Only.

Appendix C: LabVIEW Programming - SPR System



Main VI v4.vi



- Start Angle
- Step size
- End Angle
- Folder path - Log
- File path - File sample
- Substrate
- Sample
- Open Folder
- Global Stop
- Reset
- Run Simulation
- Run Experiment
- Repeat Experiment ?
- Numeric
- RUN



[abc] Simulation Data
 This is when simulation data is entered.
 Pages: Different samples
 Rows: Different substrates in order
 Cols: Layer name, Thickness d (nano meters), Special params, Refractive Index (eta)
 SPECIAL PARAMS:
 1st row - Wavelength in nm
 last row - Concentration milli-mole (mM)

[abc] String

[TF] Load

[TF] Save

[FDBL] Minimum ATR Expt

[FDBL] Angle at Min ATR Expt

[Log] Log file path

[FDBL] Phase Angle

[FDBL] Intensity

[G] Display Graph

[FDBL] Angle at Min ATR Compare

[FDBL] Minimum ATR Compare

[FDBL] Angle at Min ATR Sim

[FDBL] Minimum ATR Sim

[G] Gauge

[TF] RU

[TF] LU

[TF] LD

[TF] RD

[abc] Status

[G] Cluster

[FDBL] ATR Sim
[FDBL] >Left M> out

[FDBL] ATR Expt
[FDBL] >Left M> out

[FDBL] ATR Comp
[FDBL] >Left M> out

[FDBL] Angle
[FDBL] >Left M> out

[FDBL] Current




 Phase
 >Left M> out


 Intensity
 >Left M> out

 Start Angle


 Step size


 End Angle

 State

 Simulation Data


 String

 Run Sim

 Run Expt

 Comp file Path

 Log Folder Path

 Repeat Experiment ?

 Numeric

 error

error in can accept error information wired from VIs previously called. Use this information to decide if any functionality should be bypassed in the event of errors from other VIs.

Right-click the error in control on the front panel and select Explain Error or Explain Warning from the shortcut menu for more information about the error.

 status

status is TRUE (X) if an error occurred or FALSE (checkmark) to indicate a warning or that no error occurred.

Right-click the error in control on the front panel and select Explain Error or Explain Warning from the shortcut menu for more information about the error.

 code

code is the error or warning code.

Right-click the error in control on the front panel and select Explain Error or Explain Warning from the shortcut menu for more information about the error.

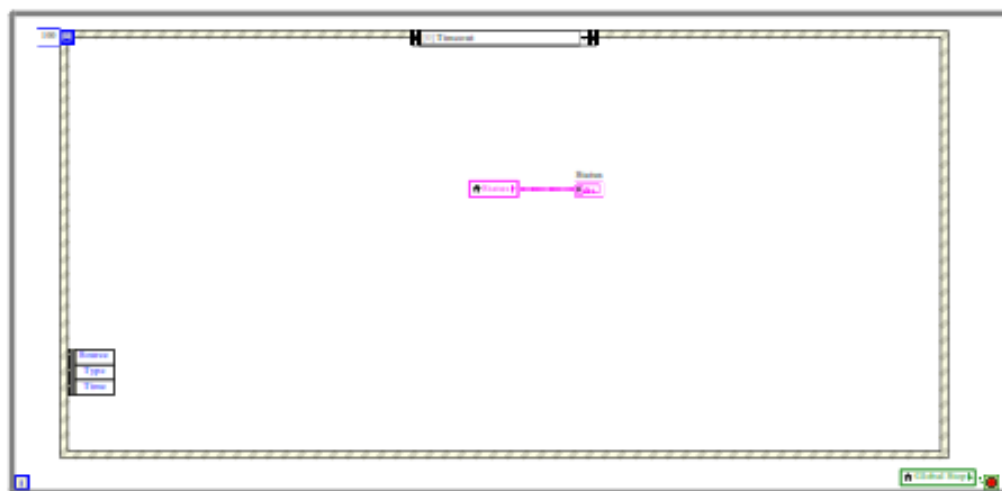
 source

source describes the origin of the error or warning.

Right-click the error in control on the front panel and select Explain Error or Explain Warning from the shortcut menu for more information about the error.



Fabc Substrate
Fabc Sample
Fabc Display Graph
Fabc
F0BL Y
F0BL
F0BL Y
F0BL
F0BL Angle File
F0BL >Left M> out
TF Heart Beat
F0BL Error bw Sim&Expt
F0BL Min Error
F0BL PhaseShift @ min Error
F0BL K

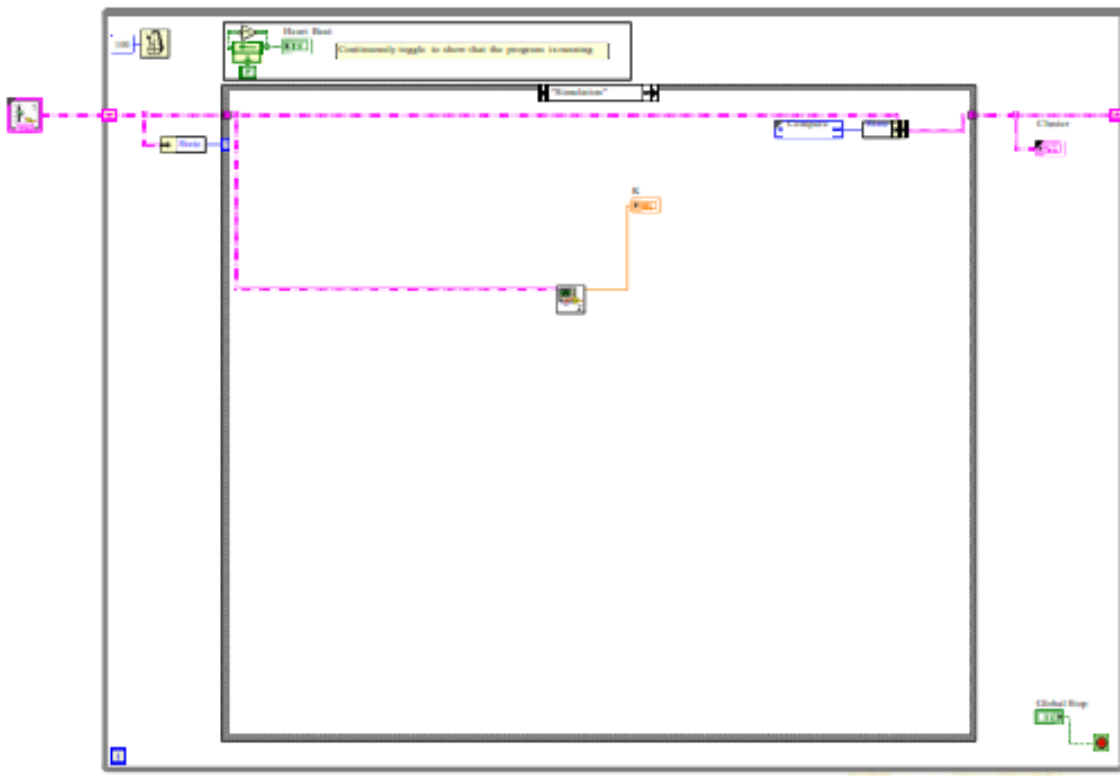


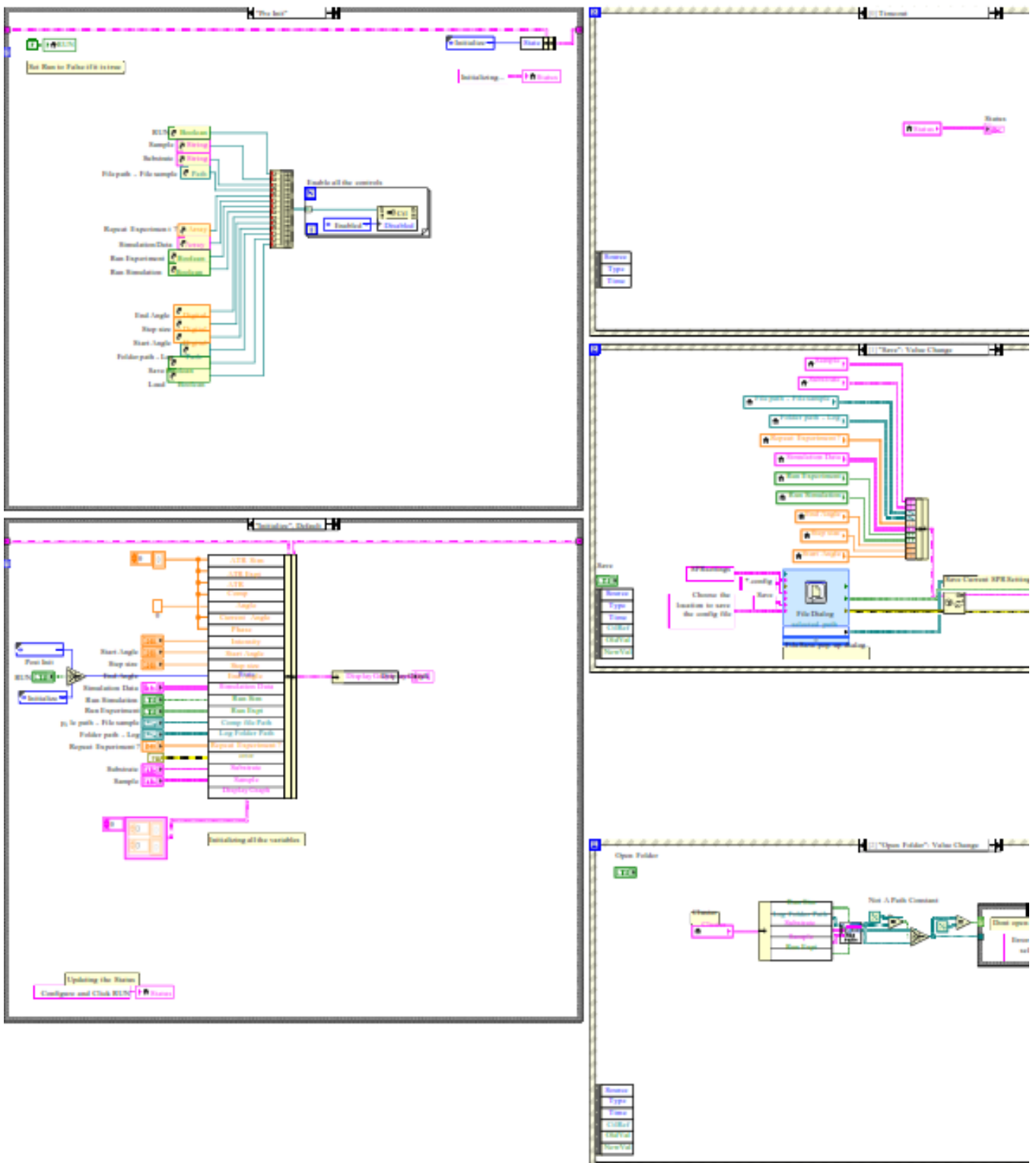
- Maximum ATK
- Maximum ATK
- BT
- Angle at Min.ATK
- Angle at Min.ATK
- LD
- LD

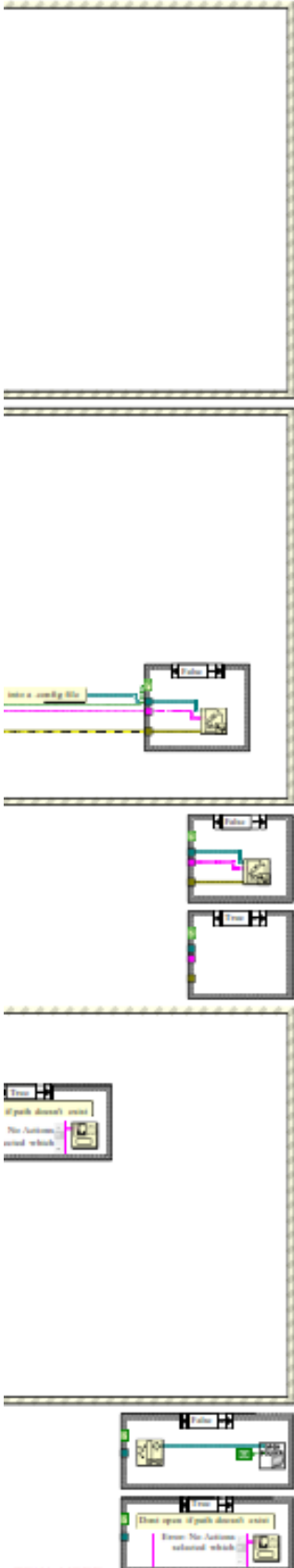
- Reset

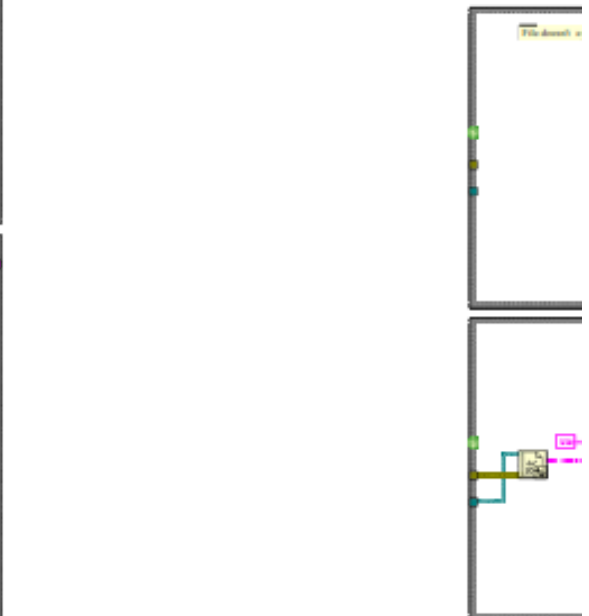
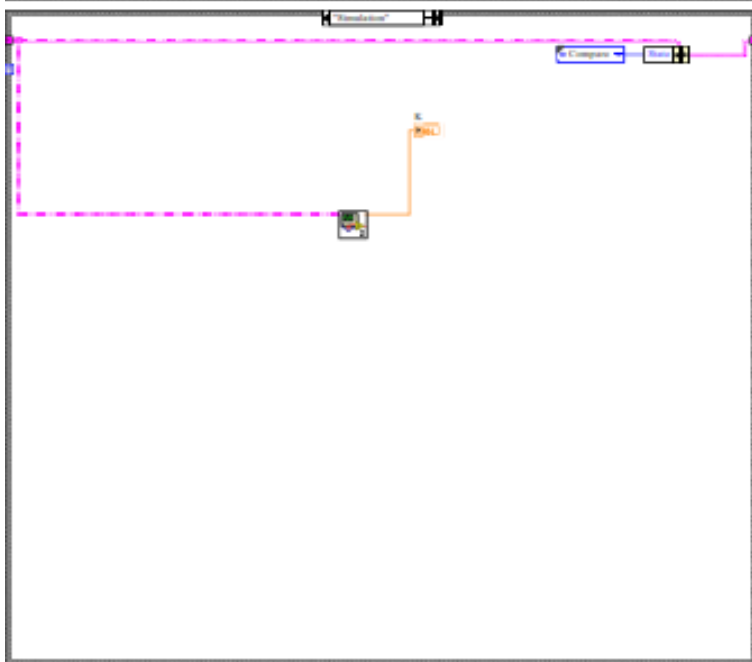
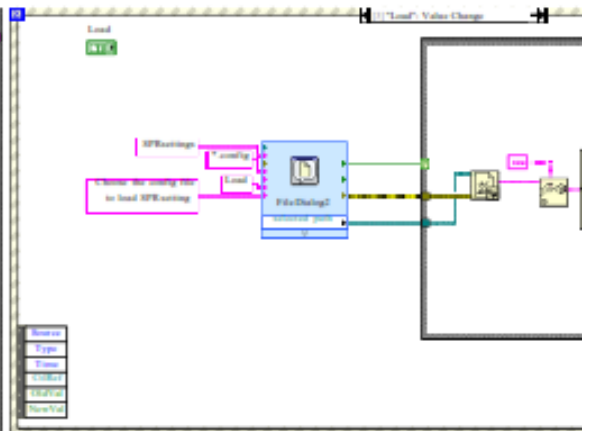
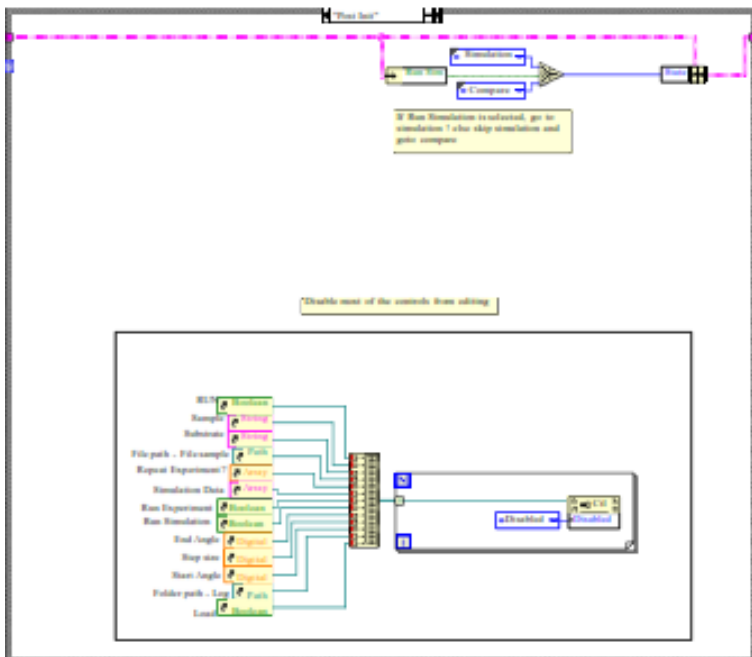
- Log file path

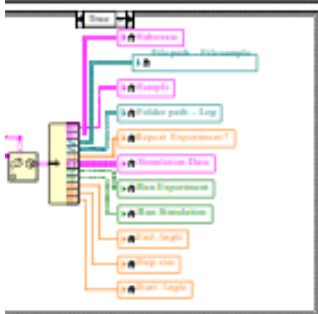
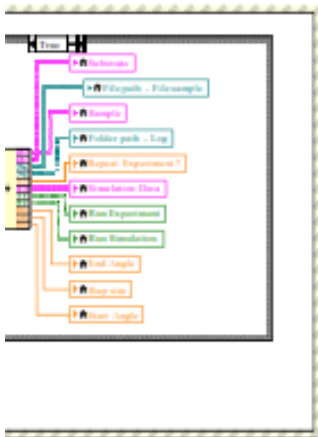
- Phase Angle
- Intensity
- Error for RoadEdge
- Min Error
- PhaseShift (2) min Error

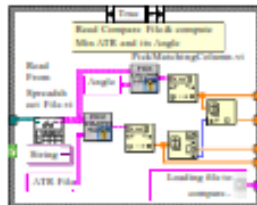
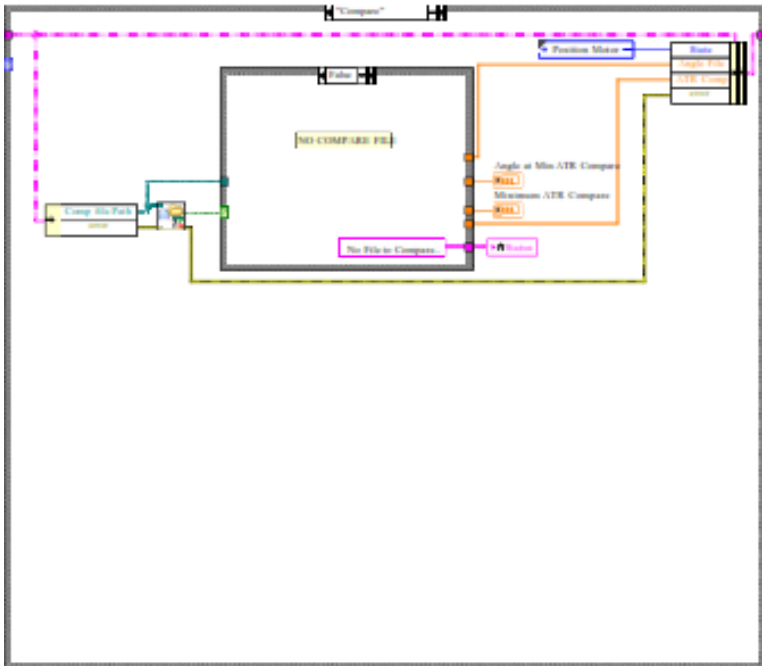


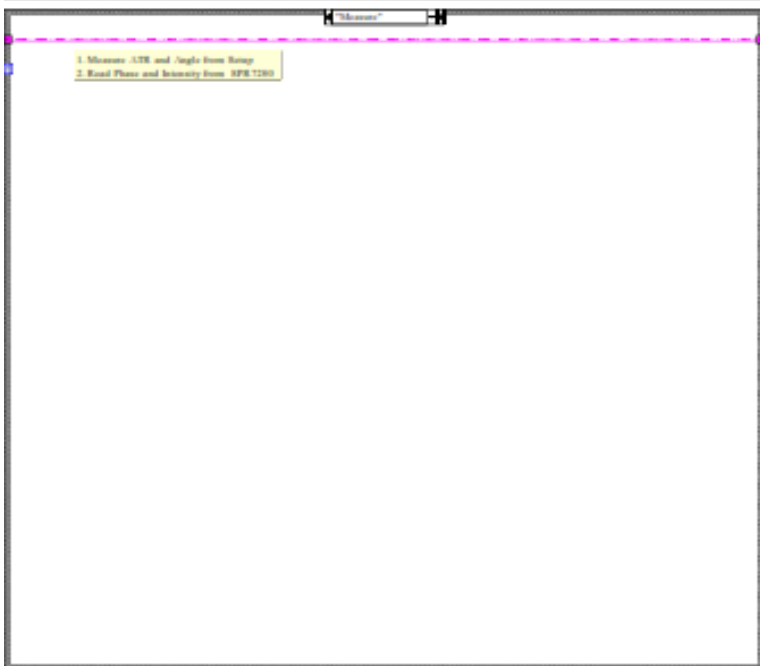
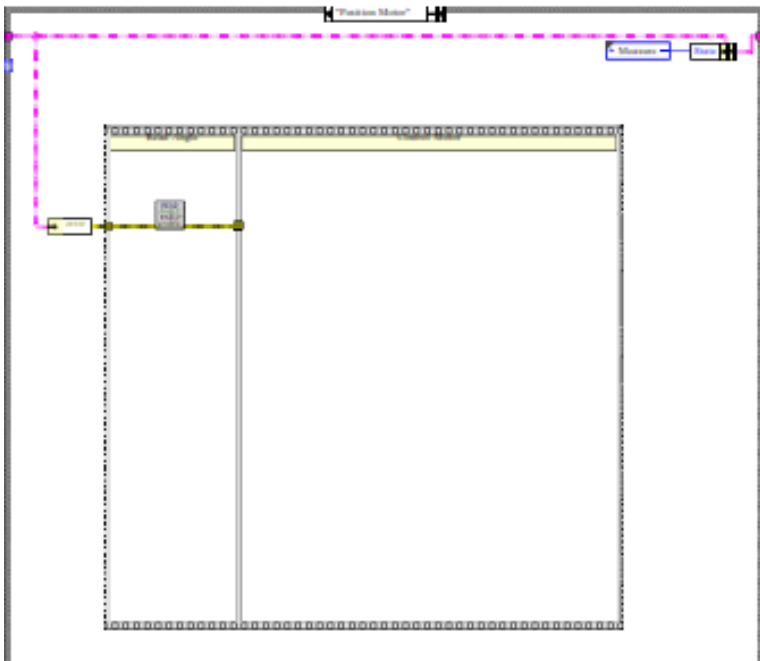






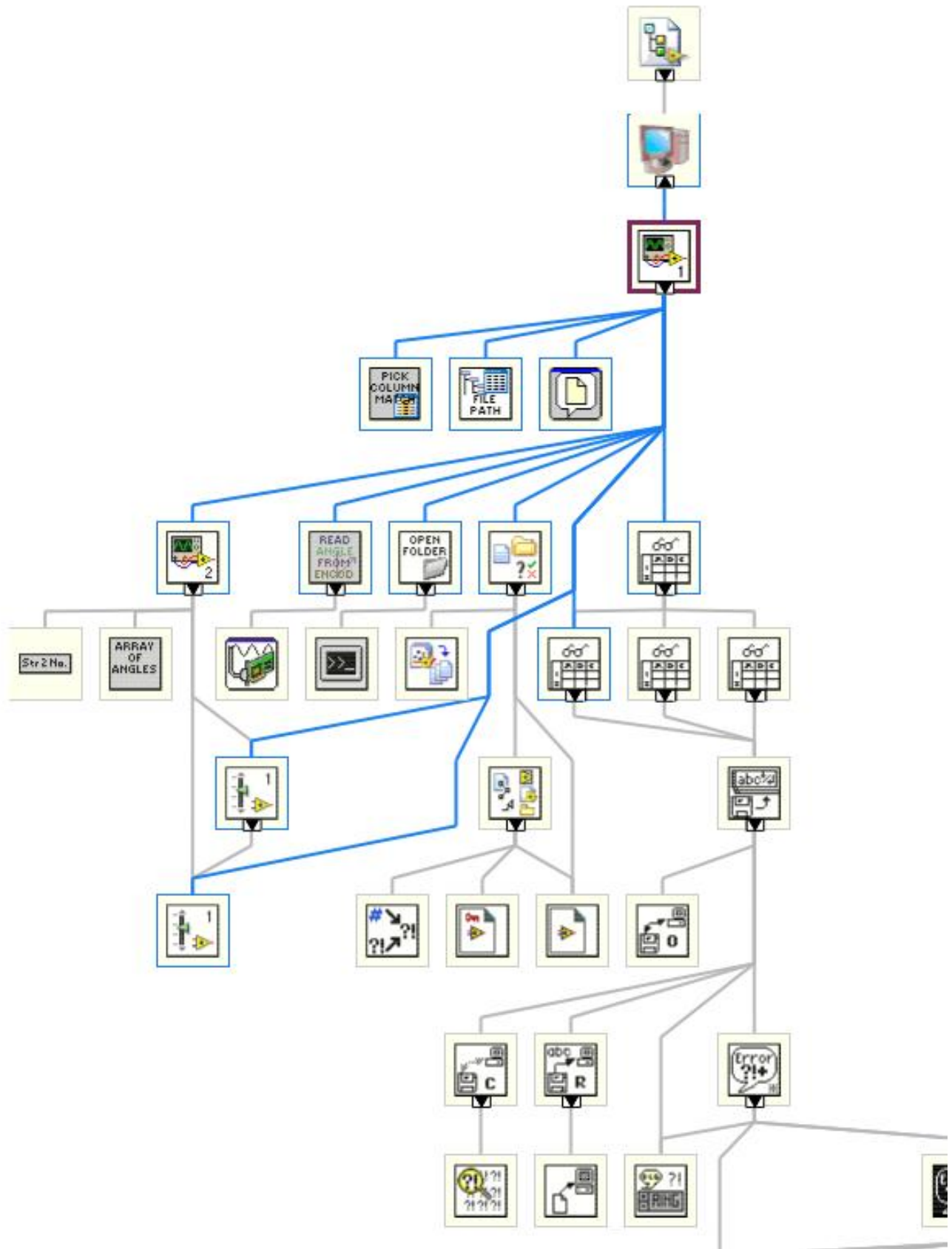


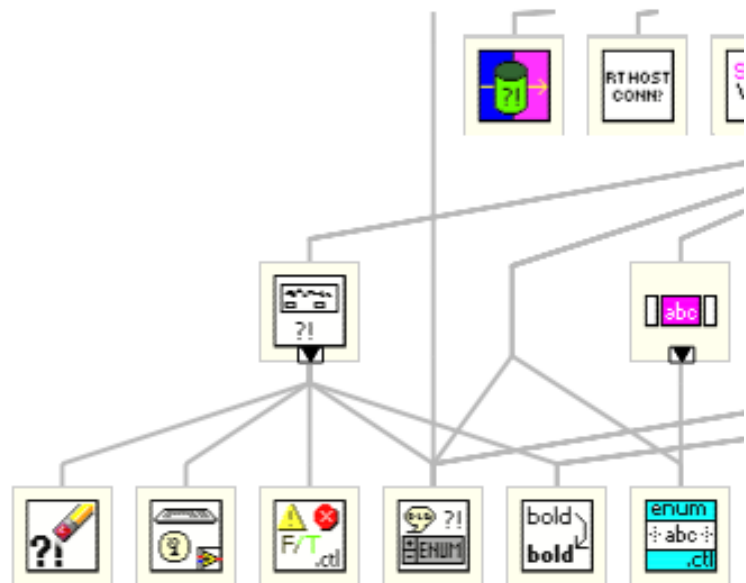






1. Save script and simulate into files
2. Save graph as image
3. Check -> next -> report





- 

 States.ctl
 C:\Users\Rajshekar\Google Drive\Plymouth\Projects\Nasih\SPR Version 3\Controls\States.ctl
- 

 State.ctl
 C:\Users\Rajshekar\Google Drive\Plymouth\Projects\Nasih\SPR Version 3\Controls\State.ctl
- 

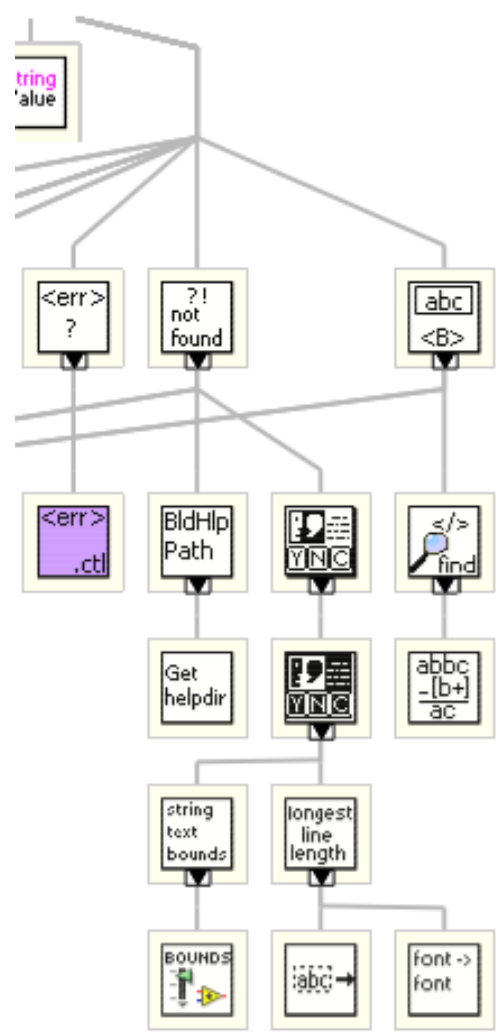
 Simulation.vi
 C:\Users\Rajshekar\Google Drive\Plymouth\Projects\Nasih\SPR Version 3\SubVI\Simulation.vi
- 

 Read Angles.vi
 C:\Users\Rajshekar\Google Drive\Plymouth\Projects\Nasih\SPR Version 3\SubVI\Read Angles.vi
- 

 Read From Spreadsheet File (string).vi
 C:\Program Files (x86)\National Instruments\LabVIEW 2013\vi.lib\Utility\file.llb\Read From Spreadsheet File (string).vi
- 

 Check if File or Folder Exists.vi
 C:\Program Files (x86)\National Instruments\LabVIEW 2013\vi.lib\Utility\libraryn.llb\Check if File or Folder Exists.vi
- 

 PickMatchingColumn.vi
 C:\Users\Rajshekar\Google Drive\Plymouth\Projects\Nasih\SPR Version 3\SubVI\PickMatchingColumn.vi





Read From Spreadsheet File.vi

C:\Program Files (x86)\National Instruments\LabVIEW 2013\vi.lib\Utility\file.llb\Read From Spreadsheet File.vi



LogFilePath.vi

C:\Users\Rajshekar\Google Drive\Plymouth\Projects\Nasih\SPR Version 3\SubVI\LogFilePath.vi



OpenFolder.vi

C:\Users\Rajshekar\Google Drive\Plymouth\Projects\Nasih\SPR Version 3\SubVI\OpenFolder.vi



File Dialog2

File Dialog

Displays a dialog box with which you can specify the path to a file or directory.

This Express VI is configured as follows:

Selection Mode:

Existing file



File Dialog

File Dialog

Displays a dialog box with which you can specify the path to a file or directory.

This Express VI is configured as follows:

Selection Mode:

New or existing file

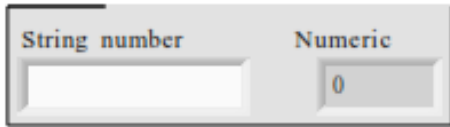
"Main VI v4.vi History"

Current Revision: 110



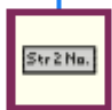
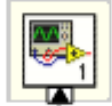
String2Number.vi

String number Str 2 No. Numeric



abc String number

0BL Numeric



"String2Number.vi History"

Current Revision: 2

Page 1

Simulation.vi



Cluster K0

ATR Sim

ATR Expt

ATR Comp

Angle

Current Angle

Phase

Intensity

Start Angle

Step size

End Angle

State

Simulation Data

Run Sim

Run Expt

Comp file Path

Log Folder Path

Repeat Experiment?

error

status	code
<input checked="" type="checkbox"/>	<input type="text" value="0"/>

source

Substrate

Sample













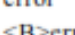

Display Graph

Y

Y

Angle File



	Cluster
	ATR Sim
	>Left M> out
	ATR Expt
	>Left M> out
	ATR Comp
	>Left M> out
	Angle
	>Left M> out
	Current
	Angle
	Phase
	>Left M> out
	Intensity
	>Left M> out
	Start Angle
	Step size
	End Angle
	State
	Simulation Data
	String
	Run Sim
	Run Expt
	Comp file Path
	Log Folder Path
	Repeat Experiment ?
	Numeric
	error

error in can accept error information wired from VIs previously called. Use this information to decide if any functionality should be bypassed in the event of errors from other VIs.

Right-click the error in control on the front panel and select Explain Error or Explain Warning from the shortcut menu for more information about the error.



status

`status` is TRUE (X) if an error occurred or FALSE (checkmark) to indicate a warning or that no error occurred.

Right-click the `error in` control on the front panel and select `Explain Error` or `Explain Warning` from the shortcut menu for more information about the error.



code

`code` is the error or warning code.

Right-click the `error in` control on the front panel and select `Explain Error` or `Explain Warning` from the shortcut menu for more information about the error.



source

`source` describes the origin of the error or warning.

Right-click the `error in` control on the front panel and select `Explain Error` or `Explain Warning` from the shortcut menu for more information about the error.



Substrate



Sample



Display Graph



Y



Y



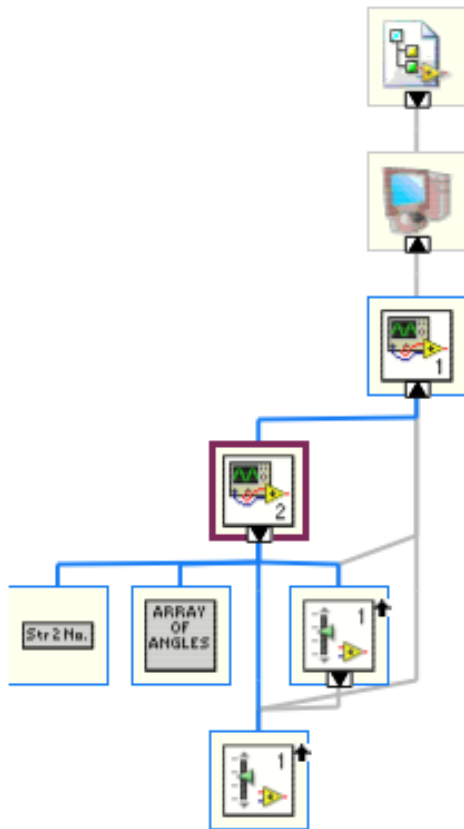
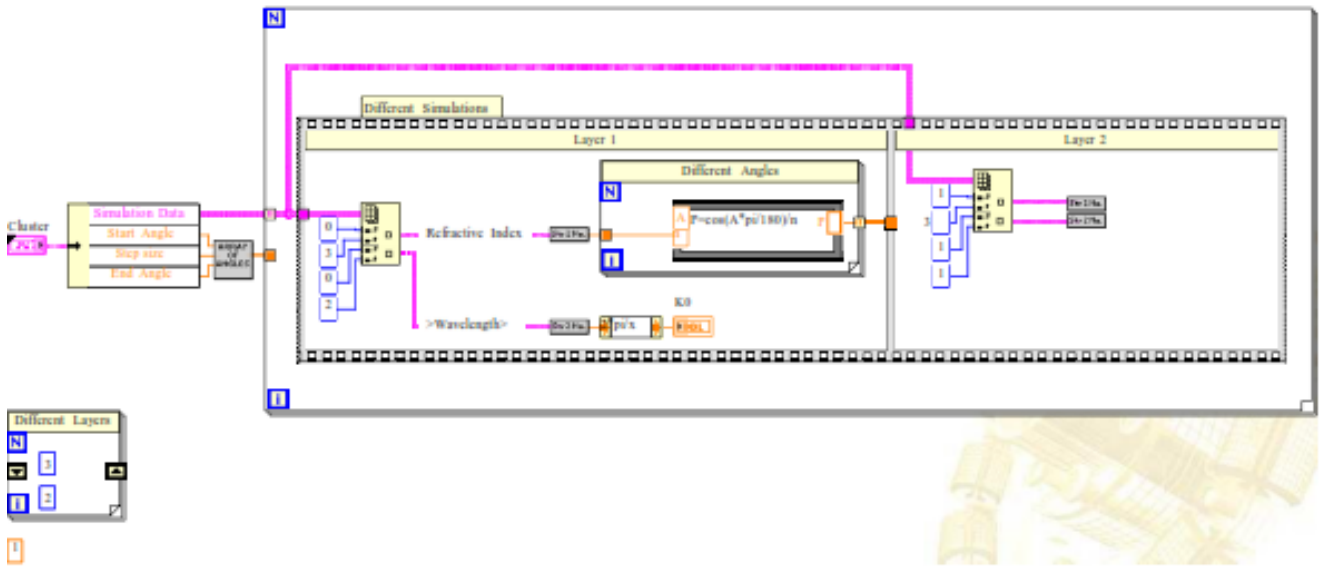
Angle File





>Left M> out



K0



-  1 State.ctl
C:\Users\Rajshekar\Google Drive\Plymouth\Projects\Nasih\SPR Version 3\Controls\State.ctl
-  1 States.ctl
C:\Users\Rajshekar\Google Drive\Plymouth\Projects\Nasih\SPR Version 3\Controls\States.ctl
-  String2Number.vi
C:\Users\Rajshekar\Google Drive\Plymouth\Projects\Nasih\SPR Version 3\SubVI\String2Number.vi



Create Array of Angles.vi

C:\Users\Rajshekar\Google Drive\Plymouth\Projects\Nasih\SPR Version 3\SubVI\Create Array of Angles.vi

"Simulation.vi History"

Current Revision: 1

Page 1



Read Angles.vi



READ ENCODER VALUES AND CALIBRATE ANGLES

INPUT	OUTPUTS
<div style="border: 1px solid gray; padding: 5px; margin-bottom: 10px;"> <p>error in</p> <p>status <input checked="" type="checkbox"/> code <input type="text" value="0"/></p> <p>source <input type="text"/></p> </div>	<div style="margin-bottom: 10px;"> <p>Laser Angle (Degrees)</p> <p><input type="text" value="0"/></p> </div> <div style="margin-bottom: 10px;"> <p>Detector Angle (Degrees)</p> <p><input type="text" value="0"/></p> </div> <div style="border: 1px solid gray; padding: 5px;"> <p>error out</p> <p>code <input type="text" value="0"/> status <input checked="" type="checkbox"/></p> <p>source <input type="text"/></p> </div>



error in[error in]

error in can accept error information wired from VIs previously called. Use this information to decide if any functionality should be bypassed in the event of errors from other VIs.

Right-click the error in control on the front panel and select Explain Error or Explain Warning from the shortcut menu for more information about the error.



status

status is TRUE (X) if an error occurred or FALSE (checkmark) to indicate a warning or that no error occurred.

Right-click the error in control on the front panel and select Explain Error or Explain Warning from the shortcut menu for more information about the error.



code

code is the error or warning code.

Right-click the error in control on the front panel and select Explain Error or Explain Warning from the shortcut menu for more information about the error.



source

source describes the origin of the error or warning.

Right-click the error in control on the front panel and select Explain Error or Explain Warning from the shortcut menu for more information about the error.



Detector Angle (Degrees)



Laser Angle (Degrees)



error out[error out]

error out passes error or warning information out of a VI to be used by other VIs.

Right-click the error out indicator on the front panel and select Explain Error or Explain Warning from the shortcut menu for more information about the error.



status

status is TRUE (X) if an error occurred or FALSE (checkmark) to indicate a warning or that no error occurred.

Right-click the error out indicator on the front panel and select Explain Error or Explain Warning from the shortcut menu for more information about the error.



code

code is the error or warning code.

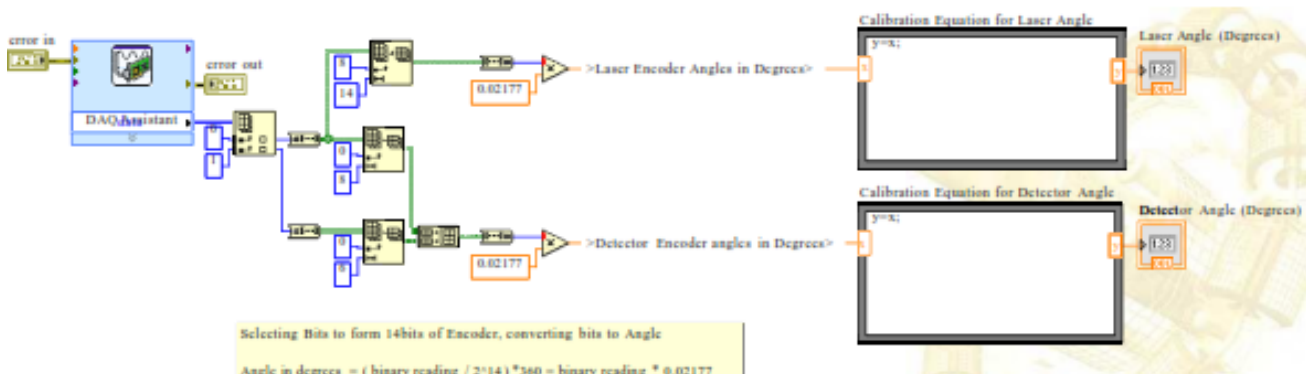
Right-click the error out indicator on the front panel and select Explain Error or Explain Warning from the shortcut menu for more information about the error.



source

source string describes the origin of the error or warning.

Right-click the error out indicator on the front panel and select Explain Error or Explain Warning from the shortcut menu for more information about the error.





DAQ Assistant

DAQ Assistant

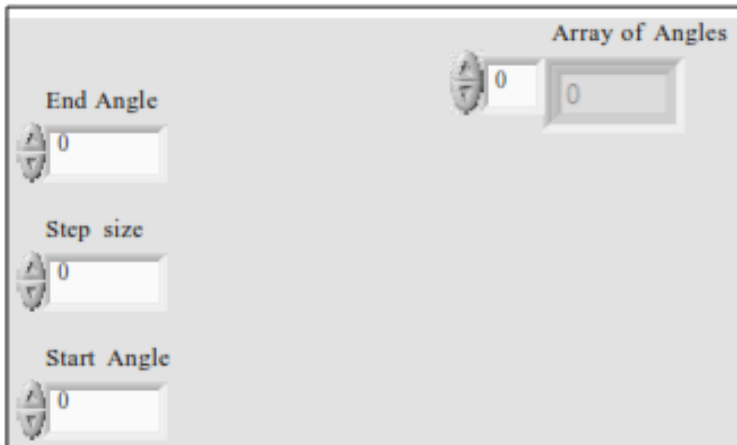
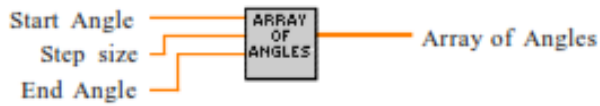
Creates, edits, and runs tasks using NI-DAQmx. Refer to the NI-DAQmx Readme for a complete listing of devices NI-DAQmx supports.

When you place this Express VI on the block diagram, the DAQ Assistant launches to create a new task. After you create a task, you can double-click the DAQ Assistant Express VI to edit that task. For continuous measurement or generation, place a while loop around the DAQ Assistant Express VI.

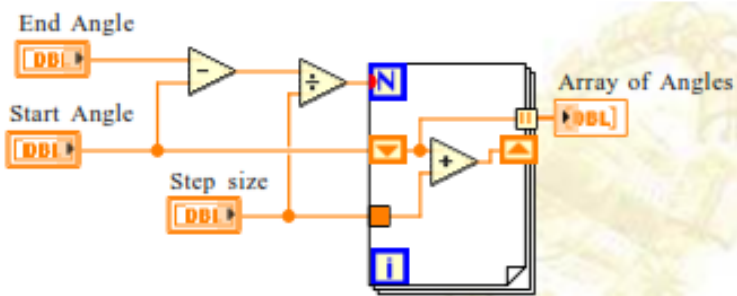
For continuous single-point input or output, the DAQ Assistant Express VI might not provide optimal performance. Refer to the Cont Acq&Graph Voltage-Single Point Optimization VI in examples\DAQmx\Analog In\Measure Voltage.llb for an example of techniques to create higher-performance, single-point I/O applications.

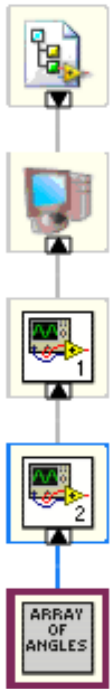
"Read Angles.vi History"

Current Revision: 12

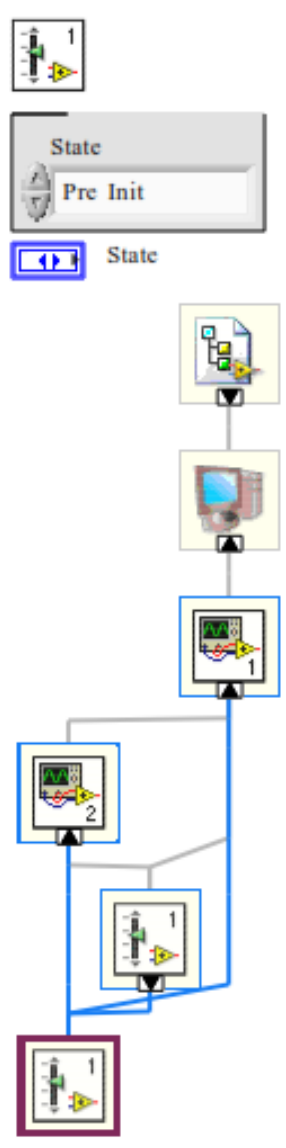


- Step size
- Start Angle
- End Angle
- Array of Angles
- Start Angle





"Create Array of Angles.vi History"
Current Revision: 3



"State.ctl History"
Current Revision: 1



Cluster

ATR Sim
0 0

ATR Expt
0 0

ATR Comp
0 0

Angle
0 0

Current
Angle
0

Phase
0 0

Intensity
0 0

Start Angle
0

Step size
0

End Angle
0

State
Initialize

Simulation Data
0
0
0

Run Sim

Run Expt

Comp file Path

Log Folder Path

Repeat Experiment ?
0 0

error
status code
 0
source

Substrate

Sample

Display Graph
0
Y
0 0
Y
0 0

Angle File
0 0

-  Cluster
 -  ATR Sim
 -  >Left M> out
 -  ATR Expt
 -  >Left M> out
 -  ATR Comp
 -  >Left M> out
 -  Angle
 -  >Left M> out
 -  Current Angle
 -  Phase
 -  >Left M> out
 -  Intensity
 -  >Left M> out
 -  Start Angle
 -  Step size
 -  End Angle
 -  State
 -  Simulation Data
 -  String
 -  Run Sim
 -  Run Expt
 -  Comp file Path
 -  Log Folder Path
 -  Repeat Experiment ?
 -  Numeric
 -  error

error in can accept error information wired from VIs previously called. Use this information to decide if any functionality should be bypassed in the event of errors from other VIs.

Right-click the **error in** control on the front panel and select **Explain Error** or **Explain Warning** from the shortcut menu for more information about the error.



status

status is TRUE (X) if an error occurred or FALSE (checkmark) to indicate a warning or that no error occurred.

Right-click the **error in** control on the front panel and select **Explain Error** or **Explain Warning** from the shortcut menu for more information about the error.



code

code is the error or warning code.

Right-click the **error in** control on the front panel and select **Explain Error** or **Explain Warning** from the shortcut menu for more information about the error.



source

source describes the origin of the error or warning.

Right-click the **error in** control on the front panel and select **Explain Error** or **Explain Warning** from the shortcut menu for more information about the error.



Substrate



Sample



Display Graph



Y



Y




Angle File



>Left M> out

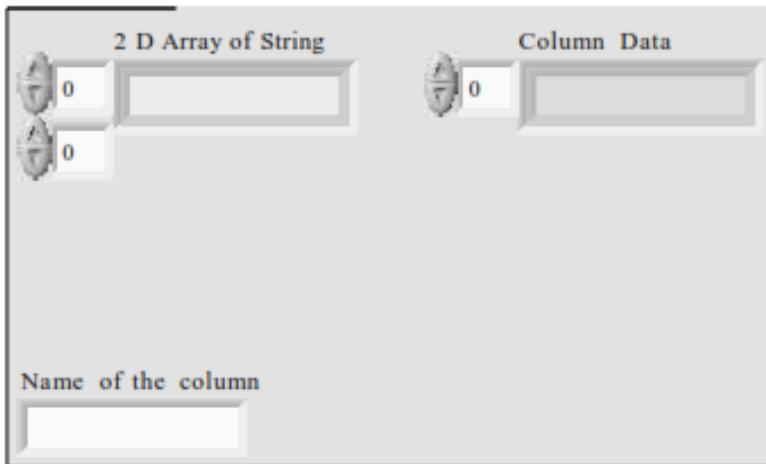


 State.ctl
C:\Users\Rajshekar\Google Drive\Plymouth\Projects\Nasih\SPR Version 3\Controls\State.ctl

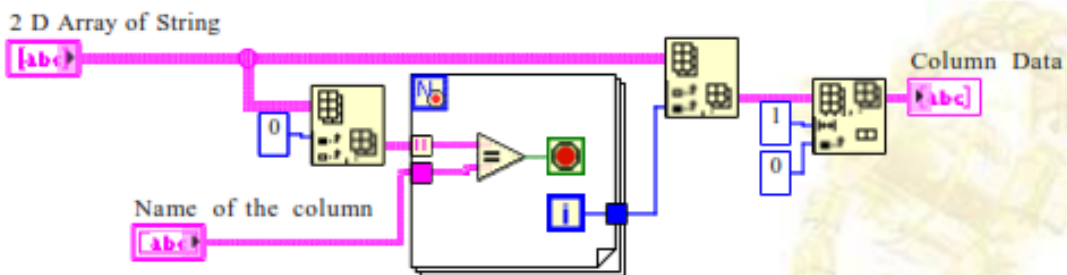
"States.ctl History"
Current Revision: 7



PickMatchingColumn.vi



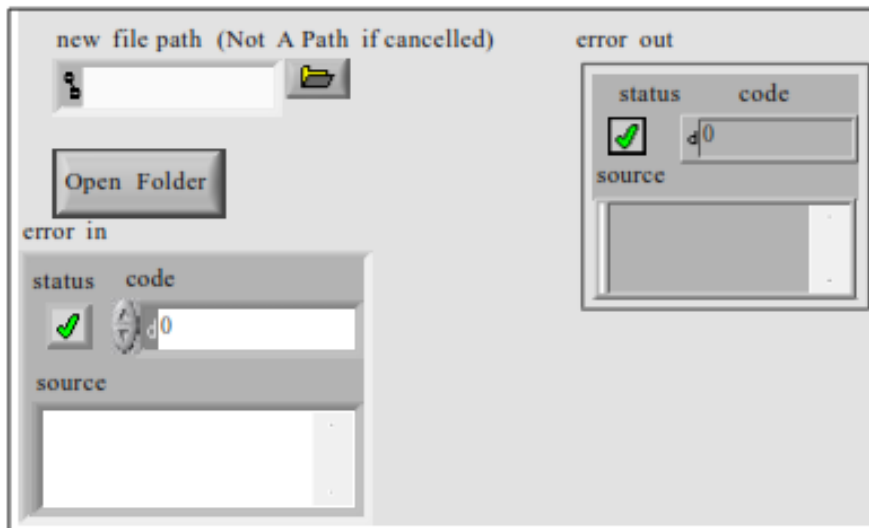
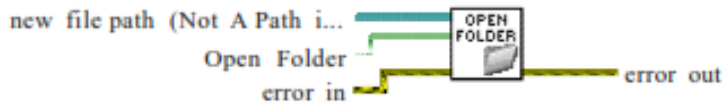
- Name of the column
- 2 D Array of String
 - String
- Column Data
 - String








"PickMatchingColumn.vi History"

Current Revision: 5




-  Open Folder
-  new file path (Not A Path if cancelled)
-  error in

error in can accept error information wired from VIs previously called. Use this information to decide if any functionality should be bypassed in the event of errors from other VIs.


Right-click the **error in** control on the front panel and select **Explain Error** or **Explain Warning** from the shortcut menu for more information about the error.

 **status**
status is TRUE (X) if an error occurred or FALSE (checkmark) to indicate a warning or that no error occurred.


Right-click the **error in** control on the front panel and select **Explain Error** or **Explain Warning** from the shortcut menu for more information about the error.

 **code**
code is the error or warning code.

Right-click the **error in** control on the front panel and select **Explain Error** or **Explain Warning** from the shortcut menu for more information about the error.

 **source**
source describes the origin of the error or warning.

Right-click the **error in** control on the front panel and select **Explain Error** or **Explain Warning** from the shortcut menu for more information about the error.

 **error out**
error out contains error information. This output provides standard error out functionality.



TF status

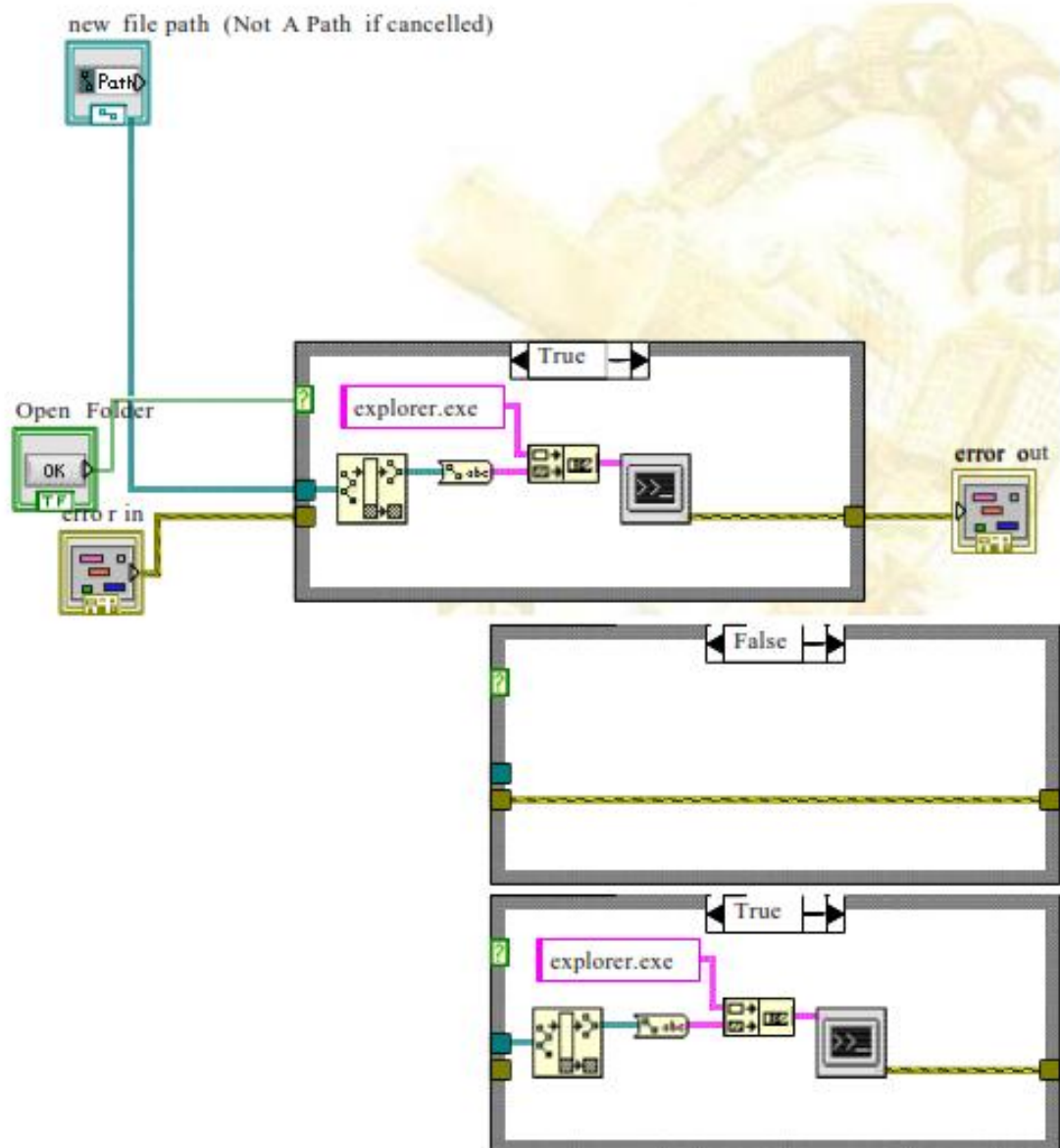
status is TRUE (X) if an error occurred or FALSE (checkmark) to indicate a warning or that no error occurred.

I32 code

code is the error or warning code.

abc source

source describes the origin of the error or warning and is, in most cases, the name of the node that produced the error or warning.





System Exec.vi

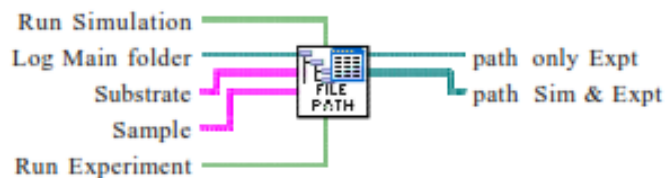
C:\Program Files (x86)\National Instruments\LabVIEW 2013\vi.lib\Platform\system.llb\System Exec.vi

"OpenFolder.vi History"

Current Revision: 3



LogFilePath.vi



Substrate

Sample

Log Main folder

Run Simulation

Run Experiment

path only Expt

path Sim & Expt

error out

status	code
	0

source

error out 2

status	code
	0

source

- Log Main folder
- Substrate
- Sample
- Run Simulation
- Run Experiment
- path only Expt



path Sim & Expt



error out

error in can accept error information wired from VIs previously called. Use this information to decide if any functionality should be bypassed in the event of errors from other VIs.

Right-click the **error in** control on the front panel and select **Explain Error** or **Explain Warning** from the shortcut menu for more information about the error.



status

status is TRUE (X) if an error occurred or FALSE (checkmark) to indicate a warning or that no error occurred.

Right-click the **error in** control on the front panel and select **Explain Error** or **Explain Warning** from the shortcut menu for more information about the error.



code

code is the error or warning code.

Right-click the **error in** control on the front panel and select **Explain Error** or **Explain Warning** from the shortcut menu for more information about the error.



source

source describes the origin of the error or warning.

Right-click the **error in** control on the front panel and select **Explain Error** or **Explain Warning** from the shortcut menu for more information about the error.



error out 2

error in can accept error information wired from VIs previously called. Use this information to decide if any functionality should be bypassed in the event of errors from other VIs.

Right-click the **error in** control on the front panel and select **Explain Error** or **Explain Warning** from the shortcut menu for more information about the error.



status

status is TRUE (X) if an error occurred or FALSE (checkmark) to indicate a warning or that no error occurred.

Right-click the **error in** control on the front panel and select **Explain Error** or **Explain Warning** from the shortcut menu for more information about the error.



code

code is the error or warning code.

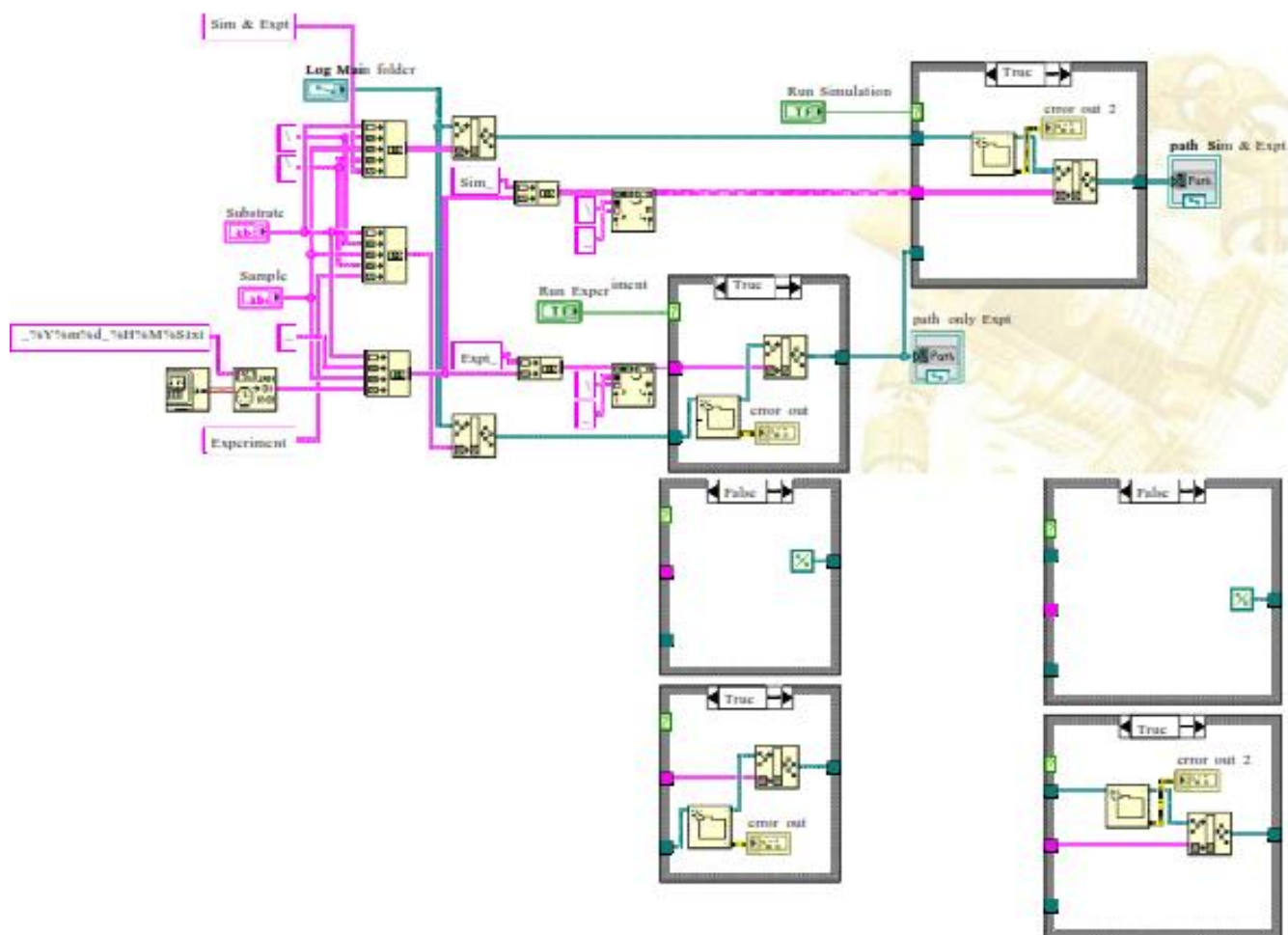
Right-click the **error in** control on the front panel and select **Explain Error** or **Explain Warning** from the shortcut menu for more information about the error.



source

source describes the origin of the error or warning.

Right-click the **error in** control on the front panel and select **Explain Error** or **Explain Warning** from the shortcut menu for more information about the error.



"LogFilePath.vi History"
Current Revision: 8

Appendix D

Mathematica programming –SPR-

(***** Multilayered SPR System Model *****)

```
(*
.....materials used: .....

n1 glass      layer 0          n1 glass(BK7)
-----
n2  x1        layer1 2 nm      nCr
-----
n3  x2        layer 2 49.5     nSilver
-----
n4  x3        layer 3          nGold
-----
n5  x4        layer 4          nSilicon
-----
n6  x5        layer 5          nGr
-----
                                nN          Sensing medium  *)

(*parameter for finding dirivative*)
h = 0.000001;

k0[la_] := 2 Pi / (la 10^(-4)); (*wavevector in vacuum *)

(*glass (1)/medium2 (n2)/medium
3(n3)/medium 4 (n4), /silver particles (N)  *)
n1 = 1.5141; (* glass*)

nGr[la_] := 3 + I (5.446 la) / 3; (* graphine layer*)

(*lambda - table of wavelength values for interpolation,
given in microns*)
lambda = {0.40, 0.50, 0.652, 0.73, 0.850, 0.918, 1.033};
(* data for permittivity and refractive index of gold layer *)
nGoldData = {1.65 + I 1.956, 0.916 + I 1.840, 0.166 + I 3.15,
0.164 + I 4.35, 0.198 + I 5.63, 0.222 + I 6.168, 0.272 + I 7.07};
nGoldTable = Table[{lambda[[i]], nGoldData[[i]]}, {i, 7}];
nGold = Interpolation[nGoldTable];

(*****)
(* data for refractive index and permittivity of silver *)
(*lambda - table of wavelength values for interpolation,
given in microns*)
lambdaS = {0.405, 0.50, 0.664, 0.750, 0.850, 0.918, 1.033};
nSilverData = {0.173 + I 1.95, 0.13 + I 2.974, 0.14 + I 4.15,
0.146 + I 4.908, 0.152 + I 5.721, 0.18 + I 6.183, 0.226 + I 6.99};
nSilverTable = Table[{lambdaS[[i]], nSilverData[[i]]}, {i, 7}];
nSilver = Interpolation[nSilverTable];
epSilver[la_] := nSilver[la]^2;
(*****)
```

```

(*****Cr data*****)

lambdaCr = {0.405, 0.50, 0.664, 0.750, 0.850, 0.918, 1.033};
(*n&kfor Cr**)
nCrData = {1.48 + I 3.54, 2.49 + I 4.44, 3.48 + I 4.36,
           3.84 + I 4.37, 4.31 + I 4.32, 4.42 + I 4.3, 4.5 + I 4.28};
(*n&kfor Titanium**)
(*nCrData={1.55+I 2.15, 1.78+I 2.39,2.29+I 3.05,
           2.65+I 3.24,3.08+I 3.31,3.23+I 3.26,3.35+I 3.3};*)
nCrTable = Table[{lambdaCr[[i]], nCrData[[i]]}, {i, 7}];
nCr = Interpolation[nCrTable];

(* refractive index data for silicon layer *)
nSilicon[la_] :=
  3.44904 + 2271.88813 Exp[-la / 0.058304] + 3.39538 Exp[-la / 0.30384];
(*****
*****
*****effective permittivity
of silver particles *****)

kSilver[la_] := k0[la] nSilver [la];
a = 40 * 10^(-7);
fskin[u_] := 1 / u^2 - 1 / Tan[u] / u;
epParticle[la_] :=
  epSilver[la] (2 fskin[kSilver[la] a] / (1 - fskin[kSilver[la] a]));

(****particles in water *****)
epWater = (1.33126 + 0.00 I)^2;
epD = epWater;
epEff[la_, conc_] :=
  epD + 3 conc epD (-epD + epParticle[la]) / (2 epD + epParticle[la]);
nSen[la_, conc_] := Sqrt[epEff[la, conc]]; (*1.33(1+0.001conc)*)

(*****
*****
(* y is the variable for angle in degrees,
layer thickness is given in nanometers*)
(* start glass prism *****)
pi[y_] := Cos[y Pi / 180] / n1;

(*****layer 1 *****)
n2[la_] := nCr[la]; (* place to change material*)
k2[la_] := k0[la] n2 [la];
sin2[y_, la_] := n1 Sin[y Pi / 180] / n2[la];

```

```

cos2[y_, la_] := Sqrt[1 - sin2[y, la]^2];
beta2[y_, z_, la_] := k2[la] cos2[y, la] z 10^(-7);
p2[y_, la_] := cos2[y, la] / n2[la];
(*****layer 2*****
n3[la_] := nSilver[la]; (* place to change material*)
k3[la_] := k0[la] n3 [la];
sin3[y_, la_] := n1 Sin[y Pi / 180] / n3[la];
cos3[y_, la_] := Sqrt[1 - sin3[y, la]^2];
beta3[y_, z_, la_] := k3 [la] cos3[y, la] z 10^(-7);
p3[y_, la_] := cos3[y, la] / n3[la];

(*****layer3*****

n4[la_] := nGold[la]; (* place to change material*)
k4[la_] := k0[la] n4 [la];
sin4[y_, la_] := n1 Sin[y Pi / 180] / n4[la];
cos4[y_, la_] := Sqrt[1 - sin4[y, la]^2];
beta4[y_, z_, la_] := k4 [la] cos4[y, la] z 10^(-7);
p4[y_, la_] := cos4[y, la] / n4[la];

(***** layer 4*****
n5[la_] := nSilicon[la]; (* place to change material*)
k5[la_] := k0[la] n5 [la];
sin5[y_, la_] := n1 Sin[y Pi / 180] / n5[la];
cos5[y_, la_] := Sqrt[1 - sin5[y, la]^2];
beta5[y_, z_, la_] := k5 [la] cos5[y, la] z 10^(-7);
p5[y_, la_] := cos5[y, la] / n5[la];

(*****layer 5*****
n6[la_] := nGr[la]; (* place to change material*)
k6[la_] := k0[la] n6 [la];
sin6[y_, la_] := n1 Sin[y Pi / 180] / n6[la];
cos6[y_, la_] := Sqrt[1 - sin6[y, la]^2];
beta6[y_, z_, la_] := k6 [la] cos6[y, la] z 10^(-7);
p6[y_, la_] := cos6[y, la] / n5[la];

(*****sensing medium *****
nN[la_, conc_] := nSen[la, conc];
sinN[y_, la_, conc_] := n1 Sin[y Pi / 180] / nN[la, conc];
cosN[y_, la_, conc_] := Sqrt[1 - sinN[y, la, conc]^2];
pN[y_, la_, conc_] := cosN[y, la, conc] / nN[la, conc];
(*****end material
layers *****

matr2[y_, z_, la_] :=
  {{Cos[beta2[y, z, la]], I Sin[beta2[y, z, la]] / p2[y, la]},
   {I Sin[beta2[y, z, la]] p2[y, la], Cos[beta2[y, z, la]}}};
matr3[y_, z_, la_] := {{Cos[beta3[y, z, la]], I Sin[beta3[y, z, la]] /
  p3[y, la]}, {I Sin[beta3[y, z, la]] p3[y, la], Cos[beta3[y, z, la]}}};
matr4[y_, z_, la_] := {{Cos[beta4[y, z, la]], I Sin[beta4[y, z, la]] /
  p4[y, la]}, {I Sin[beta4[y, z, la]] p4[y, la], Cos[beta4[y, z, la]}}};
matr5[y_, z_, la_] := {{Cos[beta5[y, z, la]], I Sin[beta5[y, z, la]] /

```

```

p5[y, la]), {I Sin[beta5[y, z, la]] p5[y, la], Cos[beta5[y, z, la]]});
matr6[y_, z_, la_] := {{Cos[beta6[y, z, la]], I Sin[beta6[y, z, la]] /
p6[y, la]), {I Sin[beta6[y, z, la]] p6[y, la], Cos[beta6[y, z, la]]}};

matrch[y_, x1_, x2_, x3_, x4_, x5_, la_] := matr2[y, x1, la].
matr3[y, x2, la].matr4[y, x3, la].matr5[y, x4, la].matr6[y, x5, la];

startr[y_, r_] := {1+r, -(1-r) p1[y]};
endt[y_, t_, la_, conc_] := t {1, -pN[y, la, conc]};

matrfull[y_, x1_, x2_, x3_, x4_, x5_, t_, la_, conc_] :=
matrch[y, x1, x2, x3, x4, x5, la].endt[y, t, la, conc];

refl1[y_, x1_, x2_, x3_, x4_, x5_, la_, conc_] := r /. Solve[
{startr[y, r] = matrfull[y, x1, x2, x3, x4, x5, t, la, conc]}, {r, t}];
refl[y_, x1_, x2_, x3_, x4_, x5_, la_, conc_] :=
refl1[y, x1, x2, x3, x4, x5, la, conc][[1]];
intentr[y_, x1_, x2_, x3_, x4_, x5_, la_, conc_] :=
Abs[refl[y, x1, x2, x3, x4, x5, la, conc]]^2;
phase[y_, x1_, x2_, x3_, x4_, x5_, la_, conc_] :=
Arg[refl[y, x1, x2, x3, x4, x5, la, conc]];
difintentr[y_, x1_, x2_, x3_, x4_, x5_, la_, conc_] :=
(intentr[y+h, x1, x2, x3, x4, x5, la, conc] -
intentr[y-h, x1, x2, x3, x4, x5, la, conc]) / (2 h);
minangl[y1_, y2_, x1_, x2_, x3_, x4_, x5_, la_, conc_] :=
y /. FindRoot[difintentr[y, x1, x2, x3, x4, x5, la, conc] == 0, {y, y1, y2}];
minangl[65, 74, 2, 49.5, 0, 0, 0, 0.664, 0]
difintentr[60, 2, 49.5, 0, 0, 0, 0.664, 0]
Export["C:\data intencity\min.txt",
minangl[65, 74, 2, 49.5, 0, 0, 0, 0.664, 0]];
>(* (***** output data *****)
ta=
Table[intentr[Y,Cr,Ag,Au,Si,Graphene,Lambda,Np],{Theta,from to ,steps}]*)
t1 = Table[intentr[y, 2, 0, 50, 0, 0, 0.664, 0], {y, 35, 85, 0.2}];
tdif1 = Table[difintentr[y, 2, 35, 0, 0, 0, 0.664, 0], {y, 35, 85, 0.2}];
t2 = Table[intentr[y, 2, 40, 0, 0, 0, 0.664, 0], {y, 35, 85, 0.2}];
tdif2 = Table[difintentr[y, 2, 40, 0, 0, 0, 0.664, 0], {y, 35, 85, 0.2}];
t4 = Table[intentr[y, 2, 45, 0, 0, 0, 0.664, 0], {y, 35, 85, 0.2}];
tdif4 = Table[difintentr[y, 2, 45, 0, 0, 0, 0.664, 0], {y, 35, 85, 0.2}];
t6 = Table[intentr[y, 2, 50, 0, 0, 0, 0.664, 0], {y, 35, 90, 0.2}];
t7 = Table[intentr[y, 2, 0, 35, 0, 0.00, 0.664, 30], {y, 35, 90, 0.2}];
t8 = Table[intentr[y, 2, 0, 0, 0, 0.00, 0.664, 35], {y, 35, 90, 0.2}];
t9 = Table[intentr[y, 2, 0, 0, 0, 0.00, 0.664, 40], {y, 35, 90, 0.2}];
t10 = Table[intentr[y, 2, 0, 0, 0, 1.70, 0.664, 0], {y, 35, 90, 0.2}];
t11 = Table[intentr[y, 2, 0, 0, 0, 1.70, 0.664, 5], {y, 35, 90, 0.2}];
t12 = Table[intentr[y, 2, 0, 0, 0, 1.70, 0.664, 10], {y, 35, 90, 0.2}];
t13 = Table[intentr[y, 2, 35, 0, 0, 1.70, 0.664, 15], {y, 35, 90, 0.2}];
t14 = Table[intentr[y, 2, 35, 0, 0, 1.70, 0.664, 20], {y, 35, 90, 0.2}];
t15 = Table[intentr[y, 2, 35, 0, 0, 1.70, 0.664, 25], {y, 35, 90, 0.2}];
t16 = Table[intentr[y, 2, 35, 0, 0, 1.70, 0.664, 30], {y, 35, 90, 0.2}];
t17 = Table[intentr[y, 2, 35, 0, 0, 1.70, 0.664, 35], {y, 35, 90, 0.2}];
t18 = Table[intentr[y, 2, 35, 0, 0, 1.70, 0.664, 40], {y, 35, 90, 0.2}];

```



```

Export["C:\data intencity\inten 1.txt", t1, "List"];
Export["C:\data intencity\inten 2.txt", tdif1, "List"];
Export["C:\data intencity\inten 3.txt", t2, "List"];
Export["C:\data intencity\inten 4.txt", tdif2, "List"];
Export["C:\data intencity\inten 4.txt", t4, "List"];
Export["C:\data intencity\inten 5.txt", tdif4, "List"];
Export["C:\data intencity\inten 6.txt", t6, "List"];
(*Export["E:\data intencity\inten 7.txt", t7, "List"]*)
Export["E:\data intencity\inten 8.txt", t8, "List"];
Export["E:\data intencity\inten 9.txt", t9, "List"];
Export["E:\data intencity\inten 10.txt", t10, "List"];
Export["E:\data intencity\inten 11.txt", t11, "List"];
Export["E:\data intencity\inten 12.txt", t12, "List"];
Export["E:\data intencity\inten 13.txt", t13, "List"];
Export["E:\data intencity\inten 14.txt", t14, "List"];
Export["E:\data intencity\inten 15.txt", t15, "List"];
Export["E:\data intencity\inten 16.txt", t16, "List"];
Export["E:\data intencity\inten 17.txt", t17, "List"];
Export["E:\data intencity\inten 18.txt", t18, "List"];
Export["E:\data intencity\inten 19.txt", t19, "List"];

(*-----plots-----*)
Plot[{intenr[y, 2, 49.5, 0, 0, 0, 0.664, 0], difintenr[y, 2,
  49.5, 0, 0, 0, 0.664, 0], intenr[y, 2, 49.5, 0, 0, 0.33, 0.664, 0],
  difintenr[y, 2, 49.5, 0, 0, 0.33, 0.664, 0]}, {y, 60, 80},
PlotRange -> All, AxesLabel -> {"Angle (degrees)", "Intensity"},
PlotStyle -> {{Red, Thick}, Blue, Green, Black}]

Plot[{intenr[y, 2, 0, 40, 0, 0, 0.664, 0], intenr[y, 2, 0, 49.5, 0, 0.3, 0.664, 0],
  intenr[y, 2, 0, 35, 0, 0.3, 0.664, 0.0005],
  intenr[y, 2, 0, 50, 0, 0, 0.664, 0.00], intenr[y, 2, 0, 45, 0, 0, 0.664, 0.000],
  intenr[y, 2, 0, 50, 0, 0, 0.664, 0]}, {y, 60, 80},
PlotRange -> All, AxesLabel -> {"Angle (degrees)", "Intensity"},
PlotStyle -> {{Red, Thick}, Blue, Green, Black, Yellow, Red}]
(*-----*)

Plot[{intenr[y, 2, 45, 0, 0, 0, 0.664, 0.001],
  intenr[y, 2, 48, 0, 0, 0, 0.664, 0.001], intenr[y, 2, 45, 5, 0, 0, 0.664, 0.001],
  intenr[y, 2, 48, 5, 0, 0, 0.664, 0.001], intenr[y, 2, 0, 45, 0, 0, 0.664, 0.0001],
  intenr[y, 2, 0, 50, 0, 0, 0.664, 0.001]}, {y, 60, 80},
PlotRange -> All, AxesLabel -> {"Angle (degrees)", "Intensity"},
PlotStyle -> {{Red, Thick}, Blue, Green, Black, Yellow}]
(*-----*)

Plot[{intenr[y, 0, 35, 3, 0, 0, 0.664, 0], intenr[y, 0, 35, 3, 0, 0, 0.664, 0.0025],
  intenr[y, 0, 35, 3, 0, 0, 0.664, 0.005], intenr[y, 0, 35, 3, 0, 0, 0.664, 0.0075],
  intenr[y, 0, 35, 3, 0, 0, 0.664, 0.01]}, {y, 55, 85},
PlotRange -> All, AxesLabel -> {"Angle (degrees)", "Intensity"},
PlotStyle -> {{Red, Thick}, Blue, Green, Black, Yellow}]

(*g3=Plot[intenr[y,30,0,0.633],{y,30,43}]*)
(*intenr[45,20,30]*)

```

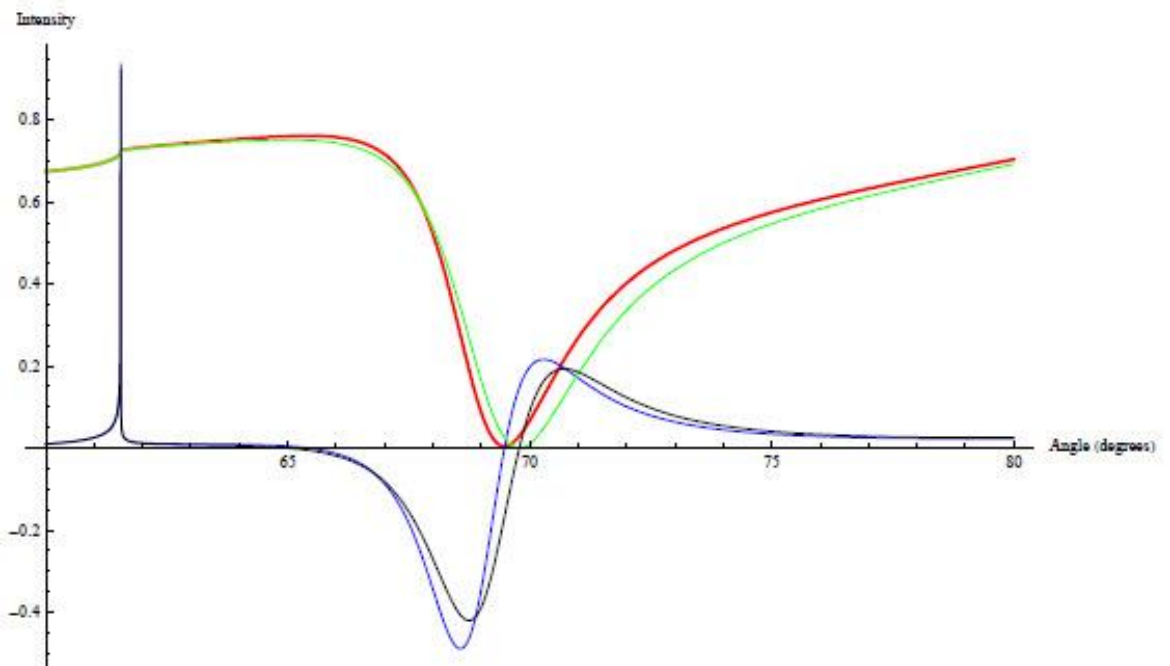
```
Plot[{phase[y, 2, 25, 4, 0, 0, 0.664, 0], phase[y, 2, 30, 4, 0, 0, 0.664, 0],
  phase[y, 2, 35, 4, 0, 0, 0.664, 0], phase[y, 2, 40, 4, 0, 0, 0.664, 0],
  phase[y, 2, 45, 4, 0, 0, 0.664, 0], phase[y, 2, 50, 4, 0, 0, 0.664, 0]},
{y, 40, 85}, PlotRange -> All, AxesLabel -> {"Angle (degrees)", "Phase"},
PlotStyle -> {{Red, Thick}, Blue, Green, Black, Yellow, Red}]
```

```
t20 = Table[phase[y, 2, 35, 0, 0, 0.00, 0.664, 0.0000], {y, 35, 90, 0.2}];
t21 = Table[phase[y, 2, 35, 0, 0, 0.00, 0.664, 0.0050], {y, 35, 90, 0.2}];
t22 = Table[phase[y, 2, 35, 0, 0, 1.02, 0.664, 0.0000], {y, 35, 90, 0.2}];
t23 = Table[phase[y, 2, 35, 0, 0, 1.02, 0.664, 0.0050], {y, 35, 90, 0.2}];
t24 = Table[phase[y, 2, 35, 0, 0, 2.04, 0.664, 0.0000], {y, 35, 90, 0.2}];
t25 = Table[phase[y, 2, 35, 0, 0, 2.04, 0.664, 0.0050], {y, 35, 90, 0.2}];
t26 = Table[phase[y, 2, 35, 0, 0, 1.70, 0.664, 40], {y, 35, 90, 0.2}];
t27 = Table[phase[y, 2, 35, 0, 0, 1.70, 0.664, 45], {y, 35, 90, 0.2}];
t28 = Table[phase[y, 2, 35, 0, 0, 1.70, 0.664, 50], {y, 35, 90, 0.2}];
t29 = Table[phase[y, 2, 35, 0, 0, 1.70, 0.664, 55], {y, 35, 90, 0.2}];
```

```
Export["E:\data phase\phase 1.txt", t20, "List"];
Export["E:\data phase\phase 2.txt", t21, "List"];
Export["E:\data phase\phase 3.txt", t22, "List"];
Export["E:\data phase\phase 4.txt", t23, "List"];
Export["E:\data phase\phase 5.txt", t24, "List"];
Export["E:\data phase\phase 6.txt", t25, "List"];
Export["E:\data phase\phase 7.txt", t26, "List"];
Export["E:\data phase\phase 8.txt", t27, "List"];
Export["E:\data phase\phase 9.txt", t28, "List"];
Export["E:\data phase\phase 10.txt", t29, "List"];
```

```
(*-----plots-----*)
```

```
Plot[{intentr[y, 2, 40, 5, 0, 0, 0.664, 0], difintentr[y, 2, 40, 5, 0, 0, 0.664, 0],
  intentr[y, 2, 40, 5, 0, 0.33, 0.664, 0], difintentr[y, 2, 40, 5, 0, 0.33, 0.664, 0]},
{y, 60, 80}, PlotRange -> All, AxesLabel -> {"Angle (degrees)", "Intensity"},
PlotStyle -> {{Red, Thick}, Blue, Green, Black}]
```



Appendix E

Sputtering System, Nordiko 6”

Considering the illustration photo of the whole system, points describing the necessary steps for the formation of metal films by this machine are given below:

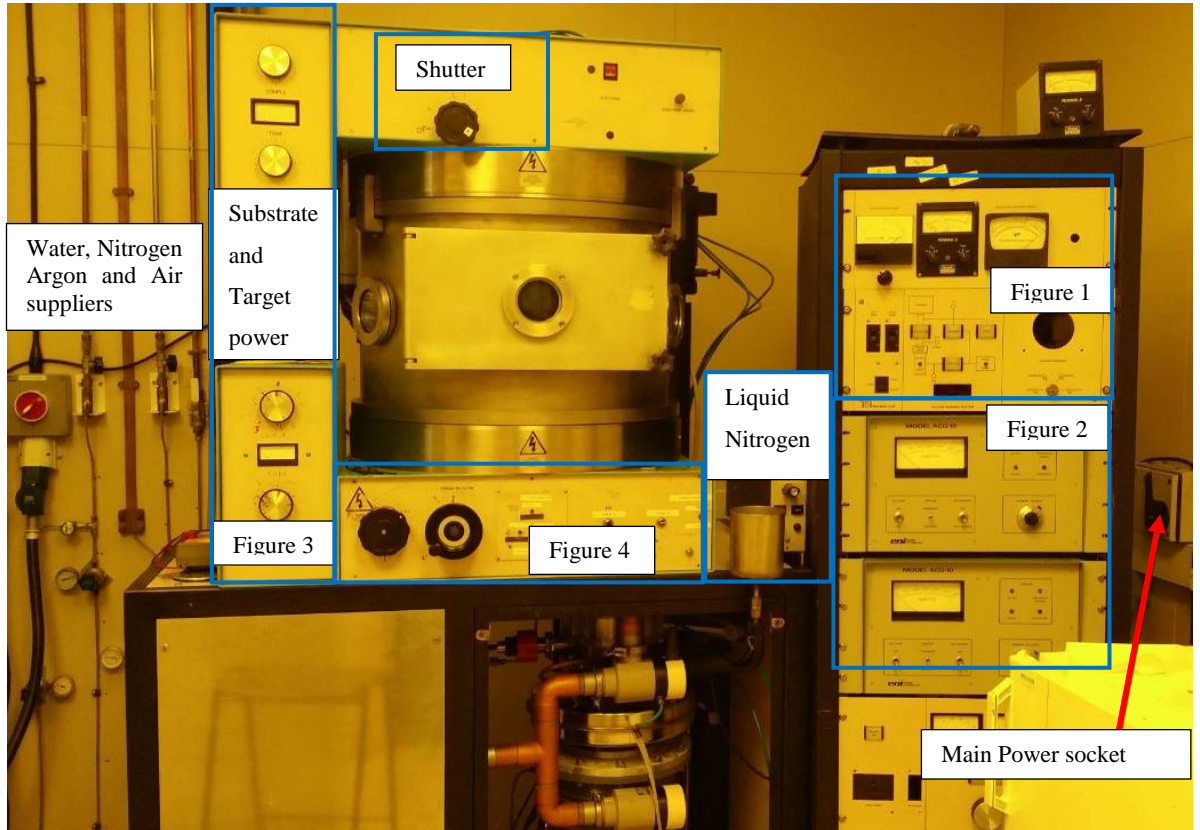


Figure 1, 2, 3 and 4 altogether (whole sputtering system)

Initial steps:

- Rotate the breaker switch present on the left side from the off position to the on position
- Unfasten the pipes containing compressed air, nitrogen, argon and water present on the wall
- Simultaneously activate the mechanical pump and foreline
- Activate the diffusion pump after two minutes



Figure 1 – The mechanical and diffusion pump switches are on the bottom left. The buttons for hi-vac, roughing, vent and foreline are in the bottom centre. The middle and right hand pressure dials are at the top

Prior to loading the substrate, the user has to wait for a time period of 45 minutes to allow the system to start up. During this time, it is ideal to ensure whether or not the amount of liquid nitrogen present in the tank to last throughout the day.

- Conduct ventilation and turn it off when a hissing sound, determining that there is no pressure difference, is heard.
- Slip the substrate platter out of the chamber
- Unfasten the top plate present on the platter, put the substrate underneath the window and fasten the top plate again
- Slide the platter inside the chamber again and use the hand screws to securely shut the door of the chamber
- Turn the foreline off and activate the roughing pump (never simultaneously activate the foreline and the roughing pump)
- Upon obtaining a reading of 50 mbar on the gauge present on the right hand side, turn the roughing pump off and initiate foreline and hi-vac immediately
- When the gauge reading is 20 mbar, switch the throttle on
- Load the flask with two buckets filled with nitrogen

- Activate the middle gauge and ensure that the chamber is pumping downwards. The gauge should have achieved the end of the first range at this time.



Figures 2 and 3 – The two power supplies are on the left. The top is for the substrate and the bottom is for the target. On the right are the tuning and coupling dials. Note the markings for rough positioning



Figure 4 – The target or ‘electrode selector’ is the second wheel to the left. The lights on the panel to the right indicate which target is selected. The first switch on the right turns the argon supply on and off. The knob immediately down and to the right controls the argon pressure. The toggle switch on the far right is the throttle

Until the required level has been achieved, the machine must not be used. It usually takes almost 6-7 hours for a 6×10^{-7} mbar vacuum. In order to make sure that the machine may obtain the lowest vacuums, two buckets of liquid nitrogen have to be incorporated after every 3-4 hours. The process of cleaning and sputtering can be initiated when the vacuum is prepared.

- Warm up both the power supplies by switching on their AC line
- Turn off the middle gauge and throttle
- Turn on the supply of argon (gauge and the throttle and the argon must not be on simultaneously)
- Using the silver dial and the gauge at the right hand side, regulate the pressure of argon. The dial has high sensitivity and this may cause a difference in the dial and the gauge. In order to prevent over and undershooting, make minimal alterations
- Prevent early sputtering by making sure the shutter is closed
- Turn on the RF power present on the top (substrate) power supply
- Rotate the dial until it reaches the substrate setting. Then wait until the plasma appears
- Turn off the high vacuum and wait 10 more seconds if there is no display of plasma. If the plasma does not appear despite this, rotate the tuning dial and target selection wheel slowly till it shows, activating hi-vac if it has been switched off
- Make sure the forward power is 50 W and rotate the tuning and coupling dials to make it 50 W if it isn't
- Using the same procedure, make sure the back power is 0 W
- Set the timer till 1 minute and 30 seconds and allow the substrate to be cleaned
- Turn off RF power and the AC line on the substrate power supply when the time has elapsed (The RF power must not be on for both the supplies simultaneously)
- Adjust the 'electrode selector' wheel by slowly and steadily turning it till it reaches the first target, the correct position of which will be indicated by the stage light turning on
- Turn on RF power present on the lower (target) power supply

- Make adjustments in the tuning dial till it reaches the correct position for the first target material. Then wait for plasma
- Turn off hi-vac and wait for 10 seconds as done previously if plasma is not shown
- Adjust the electrode selector wheel or tuning dial if there is no plasma until it appears. Activate hi-vac if it was turned off
- Using the tuning and coupling dials as done previously, adjust the forward power to the required level (target-specified) and the back power according to GW
- Set the timer according to the time needed to clean the first target
- Set the time needed for sputtering after this
- Initiate sputtering by opening the shutter and starting the timer simultaneously
- As the time finishes, close the shutter
- Turn off the RF power and the AC line for the target power supply

The process of sputtering has been finished. In case of need of extra layers, the procedure has to be repeated for every new target. We can now turn off the machine;

- Turn off the supply of argon first
- Turn off the high vacuum and then the diffusion pump
- Allow the machine to power down for 45 minutes
- Following this, simultaneously turn off the mechanical pump and the foreline
- Lastly, turn off the left hand breaker on the wall and close the gas and water lines

Appendix F

Derivation of the effective medium approximations used

Derivation of Clausius-Mossotti Relation:

Maxwell equations state the relationship (SI Units):

$$\mathbf{P} = 4\pi\epsilon_0\epsilon_r\alpha\mathbf{E}$$

Where P is the polarisation, E is the electric field, epsilon 0 is the permittivity of free space, and ϵ_r is relative permittivity of media. Also it is well known that the polarizability of a sphere is:

$$\alpha = \left(\frac{\epsilon_i - \epsilon_m}{\epsilon_i + 2\epsilon_m} \right) r^3$$

Where r is the radius of the sphere. To convert this to volume we need the relationship:

$$V = \frac{4\pi r^3}{3}$$

Substituting this is, we obtain

$$\alpha = \frac{3V}{4\pi} \left(\frac{\epsilon_i - \epsilon_m}{\epsilon_i + 2\epsilon_m} \right)$$

Next we look at local electric field effects that are affected by polarisation, where the Local electric field \mathbf{E}_L is equal to the external Electric field multiplied by the Polarisation.

$$\mathbf{E}_L = \mathbf{E}_e + \frac{1}{3\epsilon_e} \mathbf{P}$$

Relating this to the permittivities, the relationship holds:

$$\mathbf{P} = N\alpha\mathbf{E}_L$$

$$E_L = E_e + \frac{1}{3\epsilon_e}$$

$$E_e = E_L - \frac{N\alpha E_L}{3\epsilon_e} = E_L \left(1 - \frac{N\alpha}{3\epsilon_e} \right)$$

$$\epsilon_{eff} E_e = \epsilon_e E_e + P$$

$$E_e = \frac{N\alpha E_L}{\varepsilon_{eff} - \varepsilon_e}$$

Hence:

$$E_e = \frac{N\alpha E_L}{\varepsilon_{eff} - \varepsilon_e} = E_L \left(1 - \frac{N\alpha}{3\varepsilon_e}\right)$$

$$\frac{N\alpha}{\varepsilon_{eff} - \varepsilon_e} = \left(1 - \frac{N\alpha}{3\varepsilon_e}\right)$$

Therefore:

$$\varepsilon_{eff} = \varepsilon_e + \frac{N\alpha}{1 - \frac{N\alpha}{3\varepsilon_e}}$$

In this case we treat the external permittivity as the surrounding media $\varepsilon_e = \varepsilon_m$.

$$\alpha = 3\varepsilon_m V \left(\frac{\varepsilon_i - \varepsilon_m}{\varepsilon_i + 2\varepsilon_m}\right)$$

$$\varepsilon_{eff} = \varepsilon_e + \frac{N\alpha}{1 - \frac{N\alpha}{3\varepsilon_e}}$$

$$NV = f = \text{Volume Fraction} \left[\frac{m^3}{m^3}\right]$$

Rearranging the second of these 3 equations, and substituting in the NV and alpha, we obtain the Clausius Mossotti relation:

$$\varepsilon_{eff} \left(1 - \frac{N\alpha}{3\varepsilon_m}\right) = \left(1 - \frac{N\alpha}{3\varepsilon_m}\right) \varepsilon_m + N\alpha$$

$$\varepsilon_{eff} - \varepsilon_m = (\varepsilon_{eff} - \varepsilon_m) \frac{N\alpha}{3\varepsilon_m} + N\alpha$$

$$3\varepsilon_m(\varepsilon_{eff} - \varepsilon_m) = \varepsilon_{eff}N\alpha - \varepsilon_mN\alpha + 3\varepsilon_mN\alpha$$

$$3\varepsilon_m(\varepsilon_{eff} - \varepsilon_m) = \varepsilon_{eff}N\alpha + 2\varepsilon_mN\alpha$$

$$3\varepsilon_m \left(\frac{\varepsilon_{eff} - \varepsilon_m}{\varepsilon_{eff} + 2\varepsilon_m}\right) = N\alpha$$

$$\left(\frac{\varepsilon_{eff} - \varepsilon_m}{\varepsilon_{eff} + 2\varepsilon_m}\right) = f_i \left(\frac{\varepsilon_i - \varepsilon_m}{\varepsilon_i + 2\varepsilon_m}\right)$$

Which is the basis of the Maxwell-Garnett EMT in standardised form.

Taking this further, Bruggeman created a slightly different formula derived from the one above, and can be easily expanded to include multiple materials within one. At very small concentrations they are both very similar.

$$(1 - f_i) \left(\frac{\varepsilon_m - \varepsilon_{eff}}{\varepsilon_m + 2\varepsilon_{eff}} \right) + f_i \left(\frac{\varepsilon_i - \varepsilon_{eff}}{\varepsilon_i + 2\varepsilon_{eff}} \right) = 0$$